

This item was submitted to Loughborough's Institutional Repository (<https://dspace.lboro.ac.uk/>) by the author and is made available under the following Creative Commons Licence conditions.



For the full text of this licence, please go to:
<http://creativecommons.org/licenses/by-nc-nd/2.5/>

Optical Measurement of Shape and Deformation Fields on Challenging Surfaces

by

Tran Nam Nguyen

A Doctoral Thesis

submitted in partial fulfilment of the requirements

for the award of

Doctor of Philosophy of Loughborough University

June 2012

© by Tran Nam Nguyen, 2012

Acknowledgements

I would like to acknowledge the financial support of Airbus UK and Loughborough University. I am in debt with the constant guidance and encouragement of my supervisors: Prof. Jonathan Huntley (Loughborough University), Dr. Russell Coggrave (Phase Vision Ltd) and Dr. Richard Burguete (Airbus UK).

I deeply appreciate the help of Phase Vision Ltd engineers and University staff during my laboratory work. The assistance of engineers and technicians at Airbus UK in Filton and Broughton during my experiments was also much appreciated. The friends at Wolfson School of Mechanical and Manufacturing Engineering – especially Trường Thọ Nguyễn, Taufiq Widjanarko and Tahir Tarvaz – were another fantastic source of encouragement during my time of the research.

Finally, I would like to thank my family for their understanding and particularly my wife for her great love and patience during such a long and difficult time.

Abstract

A multiple-sensor optical shape measurement system (SMS) based on the principle of white-light fringe projection has been developed and commercialised by Loughborough University and Phase Vision Ltd for over 10 years. The use of the temporal phase unwrapping technique allows precise and dense shape measurements of complex surfaces; and the photogrammetry-based calibration technique offers the ability to calibrate multiple sensors simultaneously in order to achieve 360° measurement coverage. Nevertheless, to enhance the applicability of the SMS in industrial environments, further developments are needed (i) to improve the calibration speed for quicker deployment, (ii) to broaden the application range from shape measurement to deformation field measurement, and (iii) to tackle practically-challenging surfaces of which specular components may disrupt the acquired data and result in spurious measurements.

The calibration process typically requires manual positioning of an artefact (i.e., reference object) at many locations within the view of the sensors. This is not only time-consuming but also complicated for an operator with average knowledge of metrology. This thesis introduces an automated artefact positioning system which enables automatic and optimised distribution of the artefacts, automatic prediction of their whereabouts to increase the artefact detection speed and robustness, and thereby greater overall calibration performance.

This thesis also describes a novel technique that integrates the digital image correlation (DIC) technique into the present fringe projection SMS for the purpose of simultaneous shape and deformation field measurement. This combined technique offers three key advantages: (a) the ability to deal with geometrical discontinuities which are commonly present on mechanical surfaces and currently challenging to most deformation measurement methods, (b) the ability to measure 3D displacement fields with a basic single-camera single-projector SMS with no additional hardware components, and (c) the simple implementation on a multiple-sensor hardware platform to achieve complete coverage of large-scale and complex samples, with the resulting displacement fields automatically lying in a single global coordinate system. A displacement measurement

accuracy of $\cong 1/12,000$ of the measurement volume, which is comparable to that of an industry-standard DIC system, has been achieved. The applications of this novel technique to several structural tests of aircraft wing panels on-site at the research centre of Airbus UK in Filton are also presented.

Mechanical components with shiny surface finish and complex geometry may introduce another challenge to present fringe projection techniques. In certain circumstances, multiple reflections of the projected fringes on an object surface may cause ambiguity in the phase estimation process and result in incorrect coordinate measurements. This thesis presents a new technique which adopts a Fourier domain ranging (FDR) method to correctly identifying multiple phase signals and enables unambiguous triangulation for a measured coordinate. Experiments of the new FDR technique on various types of surfaces have shown promising results as compared to the traditional phase unwrapping techniques.

Keywords: 3D shape/displacement/strain measurement, fringe projection, digital image correlation, Fourier transform, automated calibration, multiple sensor, geometrical discontinuity, reflective surface, multiple reflection

Table of contents

Acknowledgements.....	i
Abstract	ii
Nomenclature.....	viii
Chapter 1 Introduction	1
1.1 Background	1
1.2 Aim and objectives.....	3
1.3 Published work.....	4
1.4 Organisation of thesis.....	5
1.5 Figures.....	6
Chapter 2 Literature review	7
2.1 Optical measurement techniques.....	7
2.1.1 Computer vision.....	7
2.1.2 Photogrammetry.....	9
2.1.3 Structured light	10
2.2 Digital image correlation (DIC) for deformation field measurement	11
2.2.1 Two-dimensional DIC	11
2.2.2 Three-dimensional DIC	13
2.2.3 Applications of 3D DIC.....	18
2.3 Fringe projection for shape measurement	19
2.3.1 Phase measurement.....	20
2.3.2 Phase unwrapping	21
2.3.3 Calculation of shape from phase data	22
2.4 Calibration technique	22
2.4.1 Photogrammetry-based model	22
2.4.2 Calibration procedure	25
2.4.3 Bundle adjustment	26
2.5 Post-processing of point clouds	27
2.6 Figures.....	29

Chapter 3 Automated positioning system of calibration artefacts.....	35
3.1 Overview	35
3.2 Implementation of rotation stage	36
3.2.1 Hardware.....	36
3.2.2 Software	36
3.2.3 Practical issues	37
3.3 Algorithm to reduce detection regions	38
3.3.1 Computing tripod-to-world rotation matrix	40
3.3.2 Computing tripod-to-world translation vector.....	41
3.3.3 Computing bar geometry from coordinates of spheres.....	42
3.3.4 Automatic sphere labelling	43
3.3.5 Applying reduced regions of interest to calibration process.....	44
3.4 Results	44
3.5 Summary	46
3.6 Tables	48
3.7 Figures.....	50
 Chapter 4 Shape and deformation measurement with single camera and single projector	 59
4.1 Overview	59
4.2 Measurement and segmentation of 3D point cloud.....	60
4.2.1 Point cloud measurement by SMS.....	60
4.2.2 Discontinuity detection	63
4.2.3 Segmentation of continuous regions	64
4.3 Digital image correlation of discontinuous sub-images.....	65
4.3.1 Discontinuity problem of conventional DIC	65
4.3.2 Improved image correlation algorithm	65
4.3.3 Simulation.....	68
4.4 Measurement of 3D displacement field	69
4.4.1 Measurement procedure.....	69
4.4.2 Interpolation for pixel-resolution displacement field	70
4.5 Implementation of the combined SMS-DIC technique.....	71
4.5.1 Hardware.....	71
4.5.2 Extensible markup language (XML) for input data file	73

4.5.3	Software structure	74
4.5.4	Output file for 3D visualisation with Tecplot.....	76
4.6	Experimental validation	78
4.6.1	Apparatus and procedure	78
4.6.2	Results and discussions.....	80
4.7	Summary	82
4.8	Figures.....	84
 Chapter 5 Multiple-view shape and deformation measurement with multiple sensors.....		
5.1	Overview	97
5.2	Extension to multiple sensors.....	99
5.2.1	Calibration of multiple sensors	99
5.2.2	Management of multiple sensors	100
5.2.3	Combining 3D displacement fields.....	102
5.2.4	Software implementation.....	103
5.3	Experimental results.....	104
5.3.1	Apparatus and procedure	105
5.3.2	Measurement results of the combined SMS-DIC technique	106
5.3.3	Standard stereo-DIC	108
5.3.4	Finite element simulation.....	109
5.4	Discussions.....	110
5.4.1	Point-wise error.....	110
5.4.2	Field-wise comparisons with stereo-DIC and finite element model.....	110
5.5	Summary	112
5.6	Tables	114
5.7	Figures.....	115
 Chapter 6 Applications in the aerospace industry.....		
6.1	Overview	129
6.1.1	Measurement techniques for aerospace applications.....	129
6.1.2	Applications of the SMS at Airbus UK	130
6.2	Fatigue test of metallic wing panel	131
6.2.1	Test description.....	131

6.2.2	Test preparation and execution	132
6.2.3	Camera views alignment.....	134
6.2.4	Measured displacement fields.....	134
6.2.5	Measured strain fields	135
6.3	Buckling test of composite wing panel	138
6.3.1	Test description.....	138
6.3.2	Test preparation and execution	139
6.3.3	Results of displacement fields	140
6.4	Summary	142
6.5	Tables	143
6.6	Figures.....	144
 Chapter 7 Fourier domain ranging technique for shape measurement with		
	multiple reflections	156
7.1	Overview	156
7.1.1	Surface reflection.....	156
7.1.2	Measurement of specular surfaces.....	158
7.1.3	Multiple-reflection problem.....	160
7.2	Fourier domain ranging technique	161
7.2.1	Review of Fourier transform methods for phase estimation.....	162
7.2.2	Improved Fourier domain ranging.....	164
7.2.3	Application to multiple reflection problem	166
7.3	Experimental results.....	170
7.3.1	Proof-of-principle specimen	170
7.3.2	Practical shiny metallic components.....	174
7.4	Summary	175
7.5	Tables	177
7.6	Figures.....	178
 Chapter 8 Conclusions and further work.....		
8.1	Conclusions	196
8.2	Further work.....	198
References		200

Nomenclature

A	signal amplitude
c	focal length
c_x, c_y	image coordinate of principal point of sensor in x - and y -direction
C	image correlation score
\mathbf{d}	3D displacement vector
d_x, d_y, d_z	3D displacement components
d	displacement magnitude
δ	displacement of loading micrometer
ε_1	triangulation error
ε_2	calibration error
ε_d	error of displacement magnitude
ε_{XYZ}	error of measured 3D coordinate
ε_{xx}	longitudinal strain
ε_{yy}	transverse strain
ε_{xy}	shear strain
f	focal length
F	loading force
ϕ, Φ	fringe phase
\mathfrak{F}	Fourier transform operator
$ H $	amplitude of Fourier transform

I	intensity matrix representing a digital image
k	phase step index
$k_1, k_2, k_3 \dots$	lens radial distortion parameters
κ	coefficient of lens distortion, first-order radial term
L	physical size of image sensor
λ	wavelength
μ_x, μ_y	intensity modulation of fringes
N	image size
ω	phase gradient
\mathbf{r}	3D coordinate vector
\mathbf{R}	rotation matrix
s	maximum number of fringe across field of view
s_x, s_y	physical size of an image pixel in x - and y -direction, respectively
σ_x, σ_y	phase error in x - and y -direction, respectively
σ_z	standard deviation of surface roughness
t	time-varying fringe pitch index
\mathbf{T}	translation vector
u, v	horizontal and vertical image displacement, respectively
V	fringe visibility
x, y	image components in horizontal and vertical direction, respectively
X, Y, Z	3D coordinate components
ξ, η	image coordinate of principal point

Chapter 1

Introduction

1.1 Background

Optical techniques for measuring surface profiles of three-dimensional (3D) objects have been developing rapidly over the last ten to twenty years [1], driven by the great demands of industry for rapid and precise measurements of components. Applications of 3D shape measurement include manufacturing quality control, robot control, obstacle detection, mould design, stress/strain measurement, etc. [2]. For example, complex shapes of aircraft wings need measuring with high precision in order to ensure strict compliance with their predicted aerodynamic performance [3]. Non-destructive tests of automotive components require tracking shape changes for evaluating deformations in order to verify finite element analyses [4]. In additional examples, optical measurement techniques were also used to inspect the human body [5–7], mould boundary [8] and surface roughness [9].

Traditionally, the coordinate measuring machine (CMM) [10–12] is used to obtain coordinates of points on an object by moving a measuring probe over its surface. Its advantage is the high precision and resolution; but contacts between the instrument and measured specimens cause various difficulties during setting-up and inspection. Although newer variants of the basic CMM principle use laser scanning to overcome the contact problem, there still persists a short-coming that measurement can only be done for a single point or a single line in one go. As a consequence, measuring a large number of points (or whole field) can be very time-consuming. On the contrary, optical shape measurement techniques can achieve coordinates of millions of points in a short period of time, although their measurement accuracy is less than that of the CMM [1]. Therefore, for applications where performance and convenience are more important than accuracy, optical shape measurement techniques are a strong contender.

There is a wide range of optical shape measurement techniques, including time-of-light, laser stripe, moiré, image correlation, photogrammetry, interferometry and structured

light [1, 2, 13]. These techniques are different in the principle of determining coordinates (i.e. line-of-sight or triangulation), the type of tracking features (i.e. passive features such as printed marker, or active features such as a fringe pattern), the type of light-source (e.g. laser or white light), the measurement precision (e.g. from millimetres to micrometres), the size of measurement volume (e.g. from a circuit board to a car), and the computational performance (e.g. real-time or off-line coordinate processing). Nevertheless, almost all optical techniques use the same fundamental components which are cameras to capture images of tracking features and computers to analyse those images. Since electronic equipment (e.g. cameras, projectors and computers) has become cheaper, smaller and more reliable, many optical measurement techniques have been commercialised so as to transfer the technology to industry. The structured-light ATOS [14], the photogrammetric TRITOP [15] and the image-correlation-based VIC-3D [16] are examples of some commercial competitors.

For the last ten years, a shape measurement system (SMS) based on structured-light technique has been developed at Loughborough University and commercialised by Phase Vision Ltd which is a spin-out company of the university [17, 18]. In this technique, a low-cost projector is used to generate time-varying fringe patterns on an object surface which encode information about the depth (i.e. Z -coordinate) of a dense set of points on the surface. In the meantime, the fringe patterns are recorded by a digital camera in which sensor pixels store implicit information about the other two coordinates of the object points (i.e. X - and Y -coordinate). A computer is then used to compute a *phase* map from the recorded fringes, unwrap the phase map at every image pixel along the time axis, and reconstruct a cloud of 3D object points. With this system, millions of points can be measured at a resolution of up to 1 part in 20,000 of the field of view in just a few seconds [19, 20], and sudden jumps of object profile can also be identified effectively [21]. Recently, a convenient calibration technique for the SMS was developed based on the principle of photogrammetry, which is able to calibrate multiple cameras and projectors and link them into a common global coordinate system [3, 18]. Figure 1 shows a single-camera single-projector SMS being developed at Phase Vision Ltd. The system has been successfully applied for measuring a variety of object types, such as a die-cast pump housing [17], a pair of turbine blades [19] and an aircraft wing panel under compression [3, 18].

1.2 Aim and objectives

The aim of this research is to extend both applicability and accuracy of the shape measurement system, particularly on challenging surfaces. A specific interest is in aerospace applications, such as measuring aircraft wings manufactured at Airbus UK, where the large scale of the measured surfaces raises many challenges. Some problems and solutions were pointed out in the previous research [3]. The key problems addressed in this PhD project are:

- i. Calibration is usually the most laborious process which requires end-users to have good knowledge of the system. Traditionally, calibration artefacts used as a scale reference must be located and rotated manually at many positions within a measurement volume, which is normally very time-consuming. This manual process also has low repeatability, low traceability and high risks of human errors.
- ii. Optical measurement methods have generally developed to address two main areas of application: shape measurement and deformation measurement. Structured-light methods are commonly dedicated to shape measurement; whilst structural deformation measurement is mostly handled with a separate method called “digital image correlation”. In many industrial applications, both shape and deformation are desired; but the use of two separate systems would be costly, complicated for users, difficult in synchronisation, or even restricted by narrow optical access to the samples.
- iii. Metallic, shiny and geometrically-complicated surfaces commonly available in industry introduce many problems in the accuracy and robustness of optical methods, particularly the structured-light method. A serious problem that has not been addressed (at least not thoroughly) by researchers is the “multiple reflection” problem which arises when a partly-reflective surface is present nearby a surface of interest. In these circumstances, light from the projectors may reach the surface of interest both directly and indirectly by scattering from the other surface, thus causing errors in the calculated phase and hence in the computed coordinate.

With the aim of finding a solution for each of the above-mentioned problems, the following objectives are defined:

- i. To introduce an automated positioning stage to mount the calibration artefacts. The benefits of this calibration equipment are convenience, repeatability and speed of operation. In addition, the knowledge of rotation angles of the artefacts can be used to predict their whereabouts in the field of view of each camera, therefore reducing computation time and increasing reliability of the artefact detection process.
- ii. To combine the structured-light and the digital image correlation methods on a single hardware platform for simultaneous measurements of both shape and deformation. In other words, this can be considered as adding the deformation measurement feature to the structured-light shape measurement system currently developed at Loughborough University. Besides a benefit that no extra hardware is required, the new combined system inherits the strengths of both the methods and is able to tackle geometrically-challenging samples, such as discontinuous and large-scale surfaces.
- iii. To develop a novel technique based on the Fourier domain ranging (FDR) technique to tackle the multiple reflection problem by using a Fourier transform to correctly identify light sources, remove disrupting signals and recover affected surface regions to the highest accuracy. When combined with other propriety techniques being developed at Phase Vision Ltd, the FDR technique is able to widen the range of surface types and geometries that can be measured accurately with the structured-light method.

1.3 Published work

The original contributions of this thesis have been published in two peer-reviewed journal papers [22, 23] and two conference papers [24, 25] regarding issue (ii) above. Based on the outcome of this work, the author has also been awarded the second prize of the Young Stress Analyst Competition 2009 organised by the British Society for Strain Measurement (BSSM). The FDR technique regarding issue (iii) is under consideration for a patent application and a journal paper is being prepared.

1.4 Organisation of thesis

Chapter 1 provides an overview of the research project, including general descriptions of the structured-light method currently developed at Loughborough University and Phase Vision Ltd. The main objectives to improve the accuracy, robustness and application range of the shape measurement system are also stated.

Chapter 2 presents a review of various optical methods used for three-dimensional shape measurements. The principles of the structured-light method, together with the calibration technique previously available, are explained in details to provide a foundation for the extension work presented in the following chapters.

Chapter 3 introduces the implementation of an automated artefact positioning system to improve calibration speed, accuracy and robustness. An algorithm to quickly estimate the whereabouts of the artefacts is also described.

Chapter 4 considers the combining of the structured-light method with the digital image correlation technique on a basic system of one camera and one projector. The main focus is on a novel technique to modify the conventional image correlation algorithm for measuring geometrically-discontinuous surfaces. Experimental results of a test sample with a hole and a step that mimic such discontinuities are presented to demonstrate the feasibility of the new technique.

Chapter 5 describes the extension of the combined shape and deformation measurement system to multiple cameras and multiple projectors. Experimental results of a mid-point plate bending test using two cameras and two projectors are presented to demonstrate the capability of the technique to measure different views at the same time and automatically align them to a unified global coordinate system, providing up to 360° coverage of a large-scale object.

Chapter 6 describes two applications of the combined system in the industrial environment of wing R&D at Airbus UK (Filton, Bristol). The first application is the measurement of a smooth metallic A380's wing panel under fatigue loading. The second application is on a highly-discontinuous carbon-fibre wing panel of the next-generation A350XWB aircraft under compressive loading.

Chapter 7 considers the use of the Fourier domain ranging (FDR) technique to solve the multiple reflection problems potentially occurring with partly-reflective mechanical surfaces. The mathematical descriptions and experimental validations are provided.

Chapter 8 presents the conclusions of this thesis and provides a number of suggestions for future work.

1.5 Figures

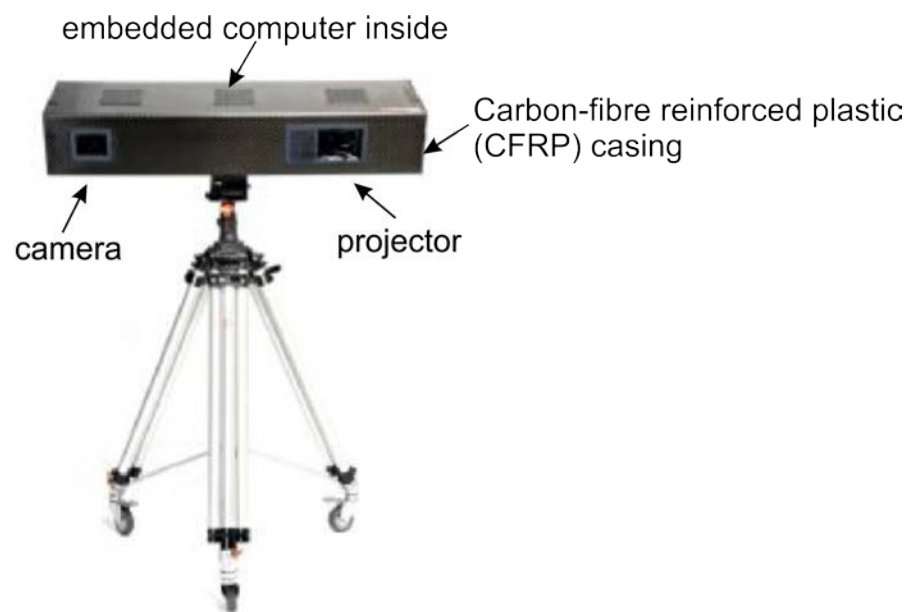


Figure 1: Phase Vision Ltd shape measurement system SMS1200 introduced to the market in 2009.

Chapter 2

Literature review

2.1 Optical measurement techniques

Several optical shape measurement techniques closely-related to the technique used in the present project are introduced briefly in this section, including computer vision, photogrammetry and structured light. The techniques used in this project, which are the computer-vision-based digital image correlation (DIC) and the structured-light fringe projection techniques, are discussed in more detail in the subsequent sections.

2.1.1 Computer vision

Computer vision concerns the extraction of 3D information from images captured by (often low-cost) camera(s) in the most convenient way. Fundamentally, a natural object is reconstructed solely from information available on images of its surface. Those images may be captured by a hand-held video camera or a multi-camera system. Because the amount of information contained in the images is normally low and potentially ambiguous, the accuracy of reconstructed shapes by computer-vision-based systems is relatively low.

Application areas of computer vision include machine control (e.g. industrial robots [26, 27], autonomous vehicle [28, 29]), event detection (e.g. visual surveillance [30, 31]), object modelling (e.g. industrial inspection [32], medical image analysis [33]), human-machine interaction (e.g. 3D interactive games [34, 35]), etc.

Shape-from-shading [36, 37] is a basic method of this class, which uses information about intensity distribution of scattered light due to the slope of a specimen's surface. This method is very sensitive to lightning condition and has limited robustness due to ambiguously shaded patterns.

Shape-from-focus [38] is another method that exploits the relationship between object-to-camera distance and depth-of-field. The method is commonly used for measuring surface roughness.

Stereo-vision is the most popular method, which is sometimes referred to by the name of “computer vision”. This method uses two cameras to capture images of a 3D object from different view angles. From those 2D images, the 3D shape is reconstructed by using triangulation [39]. More accurate and reliable triangulation is achieved if more than two images are analysed by using more than two cameras or a single video camera that moves around the object [40]. Stereo-vision shape measurement techniques were also adapted to deformation measurements in experimental mechanics, where the *digital image correlation* (DIC) technique [41] is a notable variant. The principle of the DIC technique is explained in more detail in Section 2.2.

The pin-hole camera model is commonly used in stereo-vision, which projects a set of 3D points onto 2D points on image sensors of cameras. There arises the problem of determining unknown parameters of the camera model, which is known as calibration. Because calibration strongly affects final accuracy of 3D reconstruction, much work has been done on the development of accurate yet convenient calibration techniques. Tsai [42] was among the first researchers to propose versatile calibration techniques. In his technique, images of a calibration object placed at an arbitrary position are recorded by two cameras; then, unknown camera parameters are computed from the images and the *a priori* knowledge of the calibration object. The beauty of Tsai’s technique is the linearity of his formulation, allowing very fast calibration from a computational point of view. His technique was later improved by many authors, including Heikkila [43] who introduced a nonlinear optimization step for more accurate and robust estimation of camera parameters. Zhang [44] improved this technique for calibrating multiple cameras. Auto-calibration (or self-calibration) [45] is a more convenient technique, in which cameras are calibrated solely based on scene images and a calibration object is not needed; however, a resulting 3D shape is not uniquely determined but scaled to an unknown factor.

Stereo-matching, in which one-to-one correspondence and coordinates of image points are of interest, remains a challenging problem that limits accuracy and performance of stereo-vision systems. For that reason, a large number of matching algorithms have been developed, which were summarised in the taxonomy of Scharstein and Szeliski [46] and in the book chapter of Haralick and Sharipo [26]. Many matching techniques take intensity of images as the primitive and use the cross-correlation or the least-

squared correlation as a merit function of acceptable matches. Although many authors prefer the fast matching technique in which an interrogation window cropped from the reference image is translated and tracked over the objective image, other authors [47, 48] considered the deformation of the interrogation window due to perspective distortion. In particular, the *epipolar geometry* [40] has been widely exploited to reduce the 2D image matching problem to a 1-D problem, which further improves performance and robustness [49]. Besides these, matching techniques using features (e.g. edges) as the primitive are available, offering higher accuracy and robustness but lower spatial resolution.

2.1.2 Photogrammetry

Photogrammetry is a popular optical technique in metrology that aims at higher accuracy than computer vision (which may reach 1 part in 120,000 of object volume [15]), while convenience is not a primary objective. As compared to computer vision, photogrammetry generally requires more precise calibration and suffers from lower level of automation [50]. It is, however, very difficult to distinguish one method from the other, because they share the same principle of triangulation.

In conventional photogrammetry, distinguishable markers are embedded right at the points of interest on the object surface. A single camera is used to capture images of the markers from different views and at arbitrary positions. These arbitrary positions of the camera, which are also known as their external parameters, are computed in the *bundle adjustment* process [51], together with the desired 3D coordinates of the markers. Therefore, the calibration process only involves determination of internal parameters, such as focal length, principal points and lens distortion coefficients. Using the coded markers, the correspondence of the points of interest in different camera images is so obvious that computationally expensive matching techniques can be neglected, although the spatial resolution of measurements is limited and the object surface preparation is usually time-consuming.

Having a long history (dated back to the mid-nineteenth century), photogrammetry has been thoroughly implemented in the forms of commercial software (e.g. PhotoModeler [52]) and industrial inspection systems (e.g. TRITOP by GOM GmbH [15]).

2.1.3 Structured light

Structured light is the active counterpart of computer vision and photogrammetry, where features are generated on object surfaces during the measurement process. In conventional structured-light techniques, a computer-controlled projector is added to a stereo-vision system to produce static/moving stripes on the object surface. These structured stripes form a reliable feature pattern that facilitates the image matching process [53]. Another trend of structured-light techniques evolves from optical interferometry where the *phase* of the stripes/fringes is an important “feature” to establish the correspondence between camera and projector [13]. Although the phase is also computed from image intensity, it is less sensitive to lightning changes than other matching quantities such as correlation, and thus is more robust. In addition, some phase analysis techniques [21] can solve the problem of discontinuities or occlusions of object surfaces much more effectively and efficiently than computer-vision-based or conventional structured-light techniques.

As compared to stereo-vision in general, structured-light has higher accuracy, which may reach 1 part in 20,000 of measurement volume diagonal [54], and faster computational performance (for the same spatial resolution). However, the requirement of fringe projection causes its image acquisition process to be more time-consuming than that of stereo-vision; thus applications of structured light are restricted to relatively static objects. Due to the use of fringe patterns where each pixel can act as an independent range finder, structured light may offer much higher spatial resolution than photogrammetry. Therefore, it is common in metrology to use structured-light and photogrammetry together, where photogrammetry is used to provide measurements at the global length scale and structured-light is used to measure local parts of objects.

The shape measurement system being developed in the present project is of the structured-light type using fringe analysis. An application of a structured-light technique in measuring 3D shape of an engine block is shown in Figure 2. The measurement principles of Phase Vision’s fringe projection SMS are described in more detail in Section 2.3.

2.2 Digital image correlation (DIC) for deformation field measurement

2.2.1 Two-dimensional DIC

Early versions of DIC, starting with 2D versions, were initiated in the 1980's by researchers from the field of experimental solid mechanics [55]. In the conventional 2D DIC technique [56–59], a random speckle pattern is created on the specimen surface by spraying, printing or a chemical process [60], of which the deformation field is then recorded by one digital camera. By comparing the acquired images of the pattern before and after the deformation using an image correlation technique, in-plane displacements and their gradients over a region of interest can be computed.

A mathematical description of the image correlation technique is illustrated in Figure 3. Let us consider a subset of image pixels centred at a point of interest $\mathbf{P}(x_0, y_0)$ which is selected on the reference image I (i.e., the image of the undeformed speckle pattern). Image correlation is the problem of finding that subset on the deformed image \tilde{I} which is centred at a corresponding point $\tilde{\mathbf{P}}(\tilde{x}_0, \tilde{y}_0)$. Vector $\mathbf{P}\tilde{\mathbf{P}}$ thus describes the in-plane displacement of the subset centre, of which the horizontal translation u and the vertical translation v are defined as

$$\begin{aligned} u &= \tilde{x}_0 - x_0, \\ v &= \tilde{y}_0 - y_0. \end{aligned} \tag{1.1}$$

If the deformed subset does not change in size and shape, displacements of all pixels within the subset are identical, and thus the displacement components (u, v) of the centre point are sufficient to represent the whole subset. However, this is not generally the case, and the spatial gradient terms which describe the subset's local deformation must be incorporated in the deformation model. The problem now becomes matching an arbitrary point $\mathbf{Q}(x, y)$ in the reference subset with its corresponding point $\tilde{\mathbf{Q}}(\tilde{x}, \tilde{y})$ in the deformed subset. The location relationship of these two points can be expressed by a Taylor series expansion,

$$\begin{aligned}\tilde{x} &= u + \frac{\partial u}{\partial x}(x - x_0) + \frac{\partial u}{\partial y}(y - y_0) + \frac{\partial^2 u}{\partial x \partial y}(x - x_0)(y - y_0) + \dots, \\ \tilde{y} &= v + \frac{\partial v}{\partial x}(x - x_0) + \frac{\partial v}{\partial y}(y - y_0) + \frac{\partial^2 v}{\partial x \partial y}(x - x_0)(y - y_0) + \dots,\end{aligned}\tag{1.2}$$

where $\frac{\partial u}{\partial x}$ and $\frac{\partial v}{\partial y}$ are the extension/compression terms, $\frac{\partial v}{\partial x}$ and $\frac{\partial u}{\partial y}$ are the shear/rotation terms, and $\frac{\partial^2 u}{\partial x \partial y}$ and $\frac{\partial^2 v}{\partial x \partial y}$ are the perspective (or taper) terms, respectively in x and y directions. Contributions of these local deformation gradients to the deformed shape of a squared subset are depicted in Figure 4. Most deformation models for 2D DIC [56, 61, 62] normally include the first 6 terms only, which are $\{u, v, \frac{\partial u}{\partial x}, \frac{\partial v}{\partial y}, \frac{\partial v}{\partial x}, \frac{\partial u}{\partial y}\}$. Assuming that the reference subset is small enough that its local deformation is homogenous, all the deformation components become constants over the region of interest, which must be calculated in order to find the matching point $\tilde{\mathbf{Q}}(\tilde{x}, \tilde{y})$.

Matching of two windows is done solely based on the intensity values of their corresponding pixels by maximising one of the following correlation scores [61]:

- Magnitude of intensity differences:

$$C(u, v, \frac{\partial u}{\partial x}, \frac{\partial v}{\partial y}, \frac{\partial v}{\partial x}, \frac{\partial u}{\partial y}) = 1 - \sum_{i=-m}^m \sum_{j=-n}^n \left| \tilde{I}(\tilde{x}_i, \tilde{y}_j) - I(x_i, y_j) \right|, \tag{1.3}$$

- Sum of squares of intensity differences:

$$C(u, v, \frac{\partial u}{\partial x}, \frac{\partial v}{\partial y}, \frac{\partial v}{\partial x}, \frac{\partial u}{\partial y}) = 1 - \sum_{i=-m}^m \sum_{j=-n}^n \left[\tilde{I}(\tilde{x}_i, \tilde{y}_j) - I(x_i, y_j) \right]^2, \tag{1.4}$$

- Cross-correlation:

$$C(u, v, \frac{\partial u}{\partial x}, \frac{\partial v}{\partial y}, \frac{\partial v}{\partial x}, \frac{\partial u}{\partial y}) = \sum_{i=-m}^m \sum_{j=-n}^n \tilde{I}(\tilde{x}_i, \tilde{y}_j) I(x_i, y_j), \tag{1.5}$$

- Normalised cross-correlation:

$$C(u, v, \frac{\partial u}{\partial x}, \frac{\partial v}{\partial y}, \frac{\partial v}{\partial x}, \frac{\partial u}{\partial y}) = \frac{\sum_{i=-m}^m \sum_{j=-n}^n \tilde{I}(\tilde{x}_i, \tilde{y}_j) I(x_i, y_j)}{\sqrt{\sum_{i=-m}^m \sum_{j=-n}^n [\tilde{I}(\tilde{x}_i, \tilde{y}_j)]^2} \sqrt{\sum_{i=-m}^m \sum_{j=-n}^n [I(x_i, y_j)]^2}}, \quad (1.6)$$

where the integers m and n define the $(2m+1) \times (2n+1)$ size of the reference window. A nonlinear optimisation algorithm, such as Newton-Raphson and Levenberg-Marquardt [63], is used to maximise one of these correlation scores, and the deformation parameters are obtained.

In general, Equation (1.2) results in a point (\tilde{x}, \tilde{y}) with non-integer coordinates. Therefore, the intensity value of that point must be calculated by interpolation from the intensity values of its surrounding pixel points. A wide range of interpolation functions have been used, including bilinear, bicubic and bicubic-spline [56, 61, 62].

2.2.2 Three-dimensional DIC

To achieve all in-plane and out-of-plane deformation components, the 3D DIC technique was developed [61, 64], in which at least two cameras are used to observe the specimen from different viewing angles. The image matching problem thus involves correlating not only images for different deformation states by the same camera (namely, *temporal-matching*), but also images by different cameras for the same deformation states (namely, *stereo-matching*). A typical cross-image matching strategy is depicted in Figure 5, with two types of deformation to be determined in the image matching process. The *specimen deformation* is caused by loads exerted on the specimen; whilst the *perspective deformation* is induced on the recorded images by the difference in camera viewing angles.

As in stereovision, image matching remains a big challenge to 3D DIC systems; because besides specimen deformation, perspective distortion causes matching windows to distort significantly. Helm et al. [65] introduced a back-projection technique that compensates for these distortions by combining stereo-matching with reconstruction in a nonlinear optimization process similar to the bundle adjustment. Garcia et al. [66] and Luo et al. [67] used matching techniques similar to that in computer vision, in which

matching is divided into easier problems. Using Newton-Raphson algorithms for image correlation [56, 57], matches can be propagated easily from one image to another. A short review of current 3D DIC systems was given by Schreier et al. [64].

Once a complete image correspondence has been achieved, a triangulation technique similar to that used in stereo vision can be used to define the 3D coordinates of any sample point for every deformation state, provided that the cameras have been calibrated beforehand. The 3D displacements are simply the difference between the 3D coordinates of a deformed point and a reference point. The mathematical descriptions of the triangulation based on a pin-hole camera model, as well as the camera calibration procedure, are given below.

Pin-hole camera model

A real camera lens usually consists of a group of lenses to collect light reflected from an object. However, for simplicity, the effective lens is normally modelled as a pinhole with compensation for lens distortions.

With regard to Figure 6, consider a point \mathbf{M} on the specimen surface and in the world coordinate (X,Y,Z) . Its coordinate can be transformed into a camera coordinate (X_C,Y_C,Z_C) by the *rigid-body transformation*,

$$\begin{Bmatrix} X_C \\ Y_C \\ Z_C \end{Bmatrix} = \mathbf{R} \begin{Bmatrix} X \\ Y \\ Z \end{Bmatrix} + \mathbf{T}, \quad (1.7)$$

where \mathbf{R} is a 3-by-3 rotation matrix and \mathbf{T} is a 3-by-1 translation vector.

The point \mathbf{M} , now in the camera coordinate system, can be then projected onto a point \mathbf{m} in the image-plane coordinate (x_I,y_I) by the *projective transformation*,

$$\begin{Bmatrix} x_{I(ideal)} \\ y_{I(ideal)} \\ 1 \end{Bmatrix} = \frac{1}{Z_C} \begin{bmatrix} f & 0 & 0 \\ 0 & f & 0 \\ 0 & 0 & 1 \end{bmatrix} \begin{Bmatrix} X_C \\ Y_C \\ Z_C \end{Bmatrix}, \quad (1.8)$$

where f is the effective focal length (expressed in mm). It can be seen that depth information related to Z_C has been lost after the projective transformation. The resulting

coordinate is ideal in the absence of lens distortion. Real lenses always have curvatures and misalignment of components which respectively result in radial and tangential distortions of images [42, 59]. For modern lenses, only the first term of radial distortion is typically enough for an accurate model. The adjustment of the captured image coordinate for lens distortion is given by [42, 68, 69]

$$\begin{aligned} x_{I(dist)} &= \left[1 + \kappa (x_{I(ideal)}^2 + y_{I(ideal)}^2) \right] x_{I(ideal)}, \\ y_{I(dist)} &= \left[1 + \kappa (x_{I(ideal)}^2 + y_{I(ideal)}^2) \right] y_{I(ideal)}, \end{aligned} \quad (1.9)$$

where κ is the lens distortion coefficient and $(x_{I(dist)}, y_{I(dist)})$ is the image coordinate after correction for lens distortion.

As a digital image is a discrete set of pixels (or picture elements) with the reference coordinate at the top-left corner, the image point \mathbf{m} is represented in the digital image coordinate by

$$\begin{Bmatrix} x \\ y \\ 1 \end{Bmatrix} = \begin{bmatrix} 1/s_x & 0 & c_x \\ 0 & 1/s_y & c_y \\ 0 & 0 & 1 \end{bmatrix} \begin{Bmatrix} x_{I(dist)} \\ y_{I(dist)} \\ 1 \end{Bmatrix}, \quad (1.10)$$

where s_x and s_y are the physical size of a pixel in x - and y - direction, respectively (expressed in mm/pixel); and c_x and c_y represent the position of the principal point \mathbf{I} with respect to the top-left corner (expressed in pixels).

Equations (1.7) to (1.10) are sufficient to map an object point in world coordinates into a point in digital image coordinates using the camera parameters $\{\mathbf{R}, \mathbf{T}, f, s_x, s_y, c_x, c_y, \kappa\}$. The first two parameters are known as the *extrinsic parameters*, because they do not directly involve in the image formation inside the camera, and the last six parameters are called the *intrinsic parameters*.

When the lens distortion coefficient κ in Equation (1.9) is negligible, the mapping from a real point \mathbf{M} to an image point \mathbf{m} becomes linear. Equations (1.7) to (1.10) can thus be combined into the form,

$$\mathbf{m} = \mathbf{K}[\mathbf{R} \mid \mathbf{T}]\mathbf{M}, \quad (1.11)$$

where

$$\begin{aligned} \mathbf{m} &= \lambda\{x, y, 1\}^T, \\ \mathbf{M} &= \{X, Y, Z, 1\}^T, \\ \mathbf{K} &= \begin{bmatrix} f/s_x & 0 & c_x \\ 0 & f/s_y & c_y \\ 0 & 0 & 1 \end{bmatrix}, \\ [\mathbf{R} \mid \mathbf{T}] &= \begin{bmatrix} R_{11} & R_{12} & R_{13} & T_1 \\ R_{21} & R_{22} & R_{23} & T_2 \\ R_{31} & R_{32} & R_{33} & T_3 \end{bmatrix}, \end{aligned} \quad (1.12)$$

with λ being an arbitrary scaling constant.

Camera calibration

Calibration is the process of determining all the intrinsic and extrinsic parameters present in Equation (1.11). To do this, a reference artefact has to be used to give prior knowledge about the 3D coordinates. In early work on the 3D DIC, researchers used precise translation stages to prescribe image displacement and estimated camera parameters as the best fit of prescribed and measured image displacements [67, 68]. Recently, many authors used a calibration grid with precisely known size located at various position in the fields of views of the cameras, and determined the camera parameters as a best fit of the projected and measured images of the grid [66, 70]. This technique is very versatile, because no physical measurement is required and camera setting is unrestricted as long as the cameras can observe a common region on the specimen.

In the first step of the calibration process, each camera is calibrated separately. The world coordinate system is attached to an extreme corner of the chess board, as in Figure 7. Thus, the Z-coordinates of all corners are zero, and Equation (1.11) can be simplified to

$$\lambda \begin{Bmatrix} x \\ y \\ 1 \end{Bmatrix} = \mathbf{K} [\mathbf{R}_1 \quad \mathbf{R}_2 \quad \mathbf{T}] \begin{Bmatrix} X \\ Y \\ 1 \end{Bmatrix} = \mathbf{H} \begin{Bmatrix} X \\ Y \\ 1 \end{Bmatrix}, \quad (1.13)$$

where $\mathbf{R}_i = \{R_{1i}, R_{2i}, R_{3i}\}^T$. From the positions of the corners detected on the images, the mapping matrix \mathbf{H} can be estimated using a maximum likelihood criterion to minimise the metric error [42, 44],

$$\mathbf{H} = \arg \min \sum_{q=1}^{N_q} \sum_{r=1}^{N_r} \left\| \mathbf{m}^{(q,r)} - \tilde{\mathbf{m}}^{(q,r)} \mathbf{H} \right\|^2 \quad (1.14)$$

where $\mathbf{m}^{(q,r)}$ is the digital image coordinate of the corner r detected on the captured image q , $\tilde{\mathbf{m}}^{(q,r)}$ is the digital image coordinate of the corresponding corner on the calibration board projected back onto the image using Equation (1.11), N_q is the number of images, and N_r is the number of selected corners. Matrix \mathbf{H} can then be used to calculate all of the intrinsic and extrinsic parameters [44]. These estimated parameters, together with lens distortion coefficient, are then optimised using a steepest descent algorithm [63].

In the second step, two separate sets of camera parameters, with respect to the same calibration board, are optimised again for consistency. The extrinsic parameters, \mathbf{R} and \mathbf{T} , are now defined as the relative translation (i.e. positions) and the relative rotation (i.e. poses) of the cameras, respectively.

Triangulation

Triangulation is an inverse problem of the projection process described by the camera model in Equation (1.11). Provided that (i) the cameras have been calibrated so that the intrinsic matrix \mathbf{K} and the extrinsic matrices \mathbf{R} and \mathbf{T} are known, and that (ii) correspondence of image points \mathbf{m} have been established using an image correlation technique, the object point \mathbf{M} can be determined explicitly.

Due to noise, 3D coordinates calculated by linear triangulation may suffer from a metric error. This error can be minimised in a nonlinear triangulation scheme. The minimisation problem is formulated in a generic form as

$$\mathbf{M} = \arg \min \left(\left\| \mathbf{m}_{I(1)} - \Phi_{(1)}(\mathbf{M}) \right\|_{(1)} + \left\| \mathbf{m}_{I(2)} - \Phi_{(2)}(\mathbf{M}) \right\|_{(2)} \right), \quad (1.15)$$

where \mathbf{M} is the 3D coordinate to be found, $\mathbf{m}_{I(1)}$ is the coordinate of a point on the image from camera 1, $\mathbf{m}_{I(2)}$ is the coordinate of the corresponding point on the image from camera 2, and Φ is the operator representing all the equations of the camera model (i.e., Equations (1.7) to (1.10)). The Levenberg-Marquardt algorithm is normally used to solve this nonlinear optimisation problem, where the 3D coordinate predicted by the linear triangulation from Equation (1.11) is used as an initial guess.

2.2.3 Applications of 3D DIC

The 3D form of DIC has a very wide range of applications, including material testing, strength assessment, damage inspection, etc. It essentially covers all applications of 2D DIC. Luo et al. [68] applied their method to measure the deformation field of a cracked specimen under mode II loading. Garcia et al. [66] applied their method to metal forming, for which the deformation is large and highly nonlinear. Peters et al. [71] measured the deformation of an internally pressurized composite cylinder. Similarly, Meng et al. [72] investigated the deformation of a fibre-composite vessel, using their so-called digital speckle correlation method.

In the last ten to twenty years, many 3D DIC techniques have been commercialised. The systems are capable of automated calibration using the technique of computer vision presented above, and have user-friendly interfaces. Some commercial systems are equipped with high-speed cameras for dynamic measurements. The most popular products may be VIC-3D [16] by Correlated Solutions Inc. (with claimed strain accuracy down to 0.05%), ARAMIS [73] by GOM GmbH (with claimed strain accuracy down to 0.01%), and Q-400 [74] by Dantec Ettemeyer GmbH (with claimed strain accuracy down to 0.01% and displacement accuracy up to 0.01 pixel).

The accuracy of 3D DIC techniques is often stated in different ways and with correspondingly different values. While some authors validated their methods with pre-defined in-plane and out-of-plane translations of a rigid specimen [66, 69, 75, 76], others conducted simple bending experiments of a plate or a shell and compared their measurements with theoretical predictions [67] or with point-wise measurements [72, 77]. According to Kahn-Jetter and Chu [69], their in-plane displacements have a mean

error percentage of -0.67% with standard deviation of 2.91% (for displacements from 4.4 mm to 10.8 mm) and their out-of-plane displacements have a mean error percentage of -0.79% with standard deviation of 4.53% (for displacements from 3.4 mm to 9.2 mm). Synnergren and Sjö Dahl [75] reported standard deviations of small displacements (less than 0.50 mm) as low as 0.01 pixel for in-plane components and 0.06 pixel for out-of-plane component. Becker et al. [76] conducted an in-plane translation test (with prescribed translations up to 50 mm) and reported displacement errors less than 0.02 pixel. Garcia et al. [66] stated an accuracy of 0.01 pixel (in addition, accuracy of shape measurement was 1 part in 50000 of object size). Tournas et al. [70] reported an accuracy in the order of 0.1 μm , for an object size of 30 cm and an object-camera distance of 30 cm.

As compared to the Electronic Speckle Pattern Interferometry (ESPI) technique [78] which is mature and popular in structural testing, 3D DIC generally has much lower measurement sensitivity. This was shown by an experimental comparison made at Dantec Dynamics GmbH [74]. Furthermore, the sensitivity of 3D ESPI is not dependent on the field-of view (i.e. specimen size), since measured displacements are independent of camera magnification. In contrast, 3D DIC covers a broader range of displacement, and its reduced sensitivity may be an advantage in industrial situations where noise and vibration can prevent useful data from being acquired with ESPI.

2.3 Fringe projection for shape measurement

Like other optical measurement techniques, a structured-light SMS calculates the required physical quantities indirectly from information encoded in recorded images. This information is the phase of the fringe patterns which are projected from a spatial light modulator (SLM) onto the object surface and recorded by a digital camera in the first step called *data acquisition*. In the second step called *data analysis*, a phase value is computed at every image pixel using a phase-stepping algorithm. This phase is ‘wrapped’ to an interval of $[-\pi, \pi]$, as a result of an arctangent function. A process known as phase unwrapping is carried out to unwrap the phase back onto the valid range, and then shape information is computed from this unwrapped phase. The last step involves *data representation*, in which the resulting point cloud is processed, visualised and saved in desired formats. Because the technique is based on a model, unknown

parameters of the model must be determined before being used in the above-mentioned steps, which is the task of *calibration*.

2.3.1 Phase measurement

In the single camera-projector set-up of Phase Vision's SMS [19, 79], an SLM is used to generate fringes so that the intensity of the light passing through the SLM pixel coordinate (i, j) is given by a sinusoidal profile:

$$I_{SLM}(i, j, k, t) = I_0 \left(1 + V \cos \left\{ 2\pi \left[\frac{t(i - N/2)}{N} + \frac{k-1}{4} \right] \right\} \right), \quad (1.16)$$

where I_0 is the constant mean intensity, V is the constant fringe visibility, k is the phase step index ($k=1,2,3,4$), t is the fringe pitch index defining the number of fringes across the array ($t=1,2,\dots,s$), and N is the number of pixels across the array.

In order to implement the temporal phase unwrapping method described in the next section, the fringe pitch is changed over time. Initially ($t=1$), a single fringe is projected so that the fringe phase ranges from $-\pi$ to $+\pi$ across the field of view. For subsequent time values ($t=2,3,\dots,s$), the number of fringes is set equal to t so that the phase range increases to $(-t\pi, +t\pi)$. As a consequence, Equation (1.16) results in planes of constant fringe phases fanning out from the centre of the projector lens, as shown in Figure 8.

A scattering point \mathbf{P} in Figure 8 is imaged onto the pixel (m, n) of the camera. The phase value at this point as measured by the camera can be calculated by the four-frame phase-stepping technique as follows [79]:

$$\Phi(m, n, t) = \tan^{-1} \left[\frac{I(m, n, 4, t) - I(m, n, 2, t)}{I(m, n, 1, t) - I(m, n, 3, t)} \right], \quad (1.17)$$

where $I(m, n, k, t)$ denotes the intensity measured at the pixel (m, n) of the camera.

2.3.2 Phase unwrapping

Due to the nature of the arctangent function in Equation (1.17), the measured phase values are *wrapped* onto the range $(-\pi, \pi)$ instead of the range $(-t\pi, t\pi)$ as produced by the SLM. Therefore, it is necessary to *unwrap* the measured phase by adding/subtracting its value by an integral multiple of 2π , as illustrated in Figure 9.

In Phase Vision's SMS, the *temporal phase unwrapping* technique is used, in which the phase is unwrapped independently at each pixel and as a function of time. Therefore, the horizontal axis in Figure 9 is labelled as time, rather than position as in *spatial phase unwrapping* techniques. The main advantages of temporal phase unwrapping are that it is inherently simple to implement and that phase maps with discontinuities are unwrapped correctly, but the main drawbacks are that computational effort is significant and that it requires rapid sampling of the phase as a function of time [80].

Implementation of the temporal phase unwrapping depends on the fringe sequence used for the SLM which is the parameter t in Equation (1.16). If a linear sequence ($t = 1, 2, 3, \dots, s$) is used, the unwrapping is carried out simply by summing the wrapping incremental phase changes,

$$\Phi_u(m, n) = \sum_{t=1}^s [\Phi(m, n, t) - \Phi(m, n, t-1)] \quad (1.18)$$

where $\Phi_u(m, n)$ is the unwrapped phase computed at pixel (m, n) of the camera. However, the linear sequence may cause data acquisition and computation to be very time-consuming. Two other methods to reduce data acquisition time are the so-called *forward exponential fringe sequence* and *reversed exponential fringe sequence* [80], which are depicted in Figure 10. In the former method, the wrapped phase value calculated for $t = 1$ is added to that for $t = 2$, and the result is used to unwrap the phase change on going from $t = 2$ to $t = 4$. The latter method involves starting at the maximum fringe density ($t = s$), and reducing the number of fringes by $1, 2, 4, \dots, s/2$. The intermediate phase values can also be usefully employed to reduce the measurement uncertainty by performing a least-squares straight-line fit to the Φ versus t graph for each pixel. The best-fit gradient is denoted ω . The reverse exponential sequence performs better than the forward exponential sequence in that the calculated ω

values have lower standard deviation for a given level of phase noise, because measured phase values are clustered at the high- t end of the Φ - t graph [19].

2.3.3 Calculation of shape from phase data

After phase unwrapping, the phase gradient ω_p for point \mathbf{P} can be obtained from the linear relationship between unwrapped phase $\Phi_u(t)$ and fringe pitch t as discussed in the previous section. As seen in Figure 8, the phase gradient defines a plane of constant phase $\omega_p t$ in space that goes through the scattering point \mathbf{P} . Therefore, 3D coordinates of point \mathbf{P} can be recovered by intersecting/triangulating the ray emanating from the camera pixel (i.e. ray $\mathbf{A-B}$ in the figure) and the plane with measured phase gradient ω_p .

Relative positions and angles of the camera and the projector, as well as their internal parameters, have to be known explicitly in order to be able to implement the triangulation. All of these parameters are determined in the calibration task described in the next section.

2.4 Calibration technique

2.4.1 Photogrammetry-based model

Based on the work of Schreiber and Notni [81], a photogrammetry-based calibration technique was developed for Phase Vision's SMS by Ogundana [18]. In this technique, two perpendicular sets of fringe patterns are generated on the projector's SLM. As a result, a plane of constant phase ω_x and its perpendicular counterpart of constant phase ω_y intersect along a line that emanates from a point on the SLM and goes through the lens of the projector into the measurement volume (see Figure 11). The triangulation problem now becomes the determination of the point of intersection of that line with a line coming from the camera pixel that has the phase gradient (ω_x, ω_y) and that passes through the camera lens pin-hole.

For the sake of convenience, three types of coordinate system are introduced:

- *Image coordinate systems*, including the CCD coordinate system (ξ_c, η_c) for the camera and the SLM coordinate system (ξ_p, η_p) for the projector, which are originated at the principal points of the sensor planes. Principal point is defined as the intersection point of the optical axis and the image plane.
- *Sensor coordinate systems*, including the camera coordinate system (x_c, y_c, z_c) and the projector coordinate system (x_p, y_p, z_p) , which are originated at the pin-holes and have the x - y planes parallel to the corresponding sensor planes, and
- *World coordinate system*, an arbitrary global frame in which coordinates (X, Y, Z) of resulting point clouds are defined.

Any camera pixel with the integral indices (m, n) can be converted to the camera's image plane coordinates (ξ_c, η_c) , and the measured phase gradient vector at that pixel, (ω_x, ω_y) , can be converted to the projector's image plane coordinates (ξ_p, η_p) , by using the following equations:

$$\begin{aligned}\xi_c &= \left(\frac{m-1}{N_{\xi,c}-1} - 0.5 \right) L_{\xi,c}, \\ \eta_c &= \left(\frac{n-1}{N_{\eta,c}-1} - 0.5 \right) L_{\eta,c},\end{aligned}\tag{1.19}$$

and

$$\begin{aligned}\xi_p &= \left(\frac{\omega_x}{2\pi} \right) L_{\xi,p}, \\ \eta_p &= \left(\frac{\omega_y}{2\pi} \right) L_{\eta,p},\end{aligned}\tag{1.20}$$

where $N_{\xi,c}$ and $N_{\eta,c}$ are the number of pixels along the ξ - and η -axis of the camera, respectively; $L_{\xi,c}$ and $L_{\eta,c}$ are the physical lengths of the camera's CCD along the ξ -

and η -axes, respectively; and $L_{\xi,p}$ and $L_{\eta,p}$ are the corresponding physical lengths for the projector's SLM.

Transformations between the three types of coordinate systems follow the classical photogrammetry theory. For instance, for the camera, transformation between image coordinates and sensor coordinates is the projective transformation [18]:

$$\begin{Bmatrix} \xi_c \\ \eta_c \end{Bmatrix} = \frac{c}{z_c} \begin{Bmatrix} x_c \\ y_c \end{Bmatrix} + \begin{Bmatrix} \xi_{H,c} \\ \eta_{H,c} \end{Bmatrix} + \begin{Bmatrix} d\xi_c \\ d\eta_c \end{Bmatrix}, \quad (1.21)$$

where c is the focal length of the camera, $(\xi_{H,c}, \eta_{H,c})$ are the coordinates of the camera's principal point, and $d\xi_c$ and $d\eta_c$ are correction terms for lens distortion which are approximated by:

$$\begin{aligned} d\xi_c &= (\xi_c - \xi_{H,c}) (k_{1,c} r_c^2 + k_{2,c} r_c^4 + k_{3,c} r_c^6 + \dots), \\ d\eta_c &= (\eta_c - \eta_{H,c}) (k_{1,c} r_c^2 + k_{2,c} r_c^4 + k_{3,c} r_c^6 + \dots), \end{aligned} \quad (1.22)$$

with $r = \sqrt{(\xi_c - \xi_{H,c})^2 + (\eta_c - \eta_{H,c})^2}$ and the terms $k_{1,c}$, $k_{2,c}$, $k_{3,c} \dots$ are the lens radial distortion parameters of the camera. Tangential parameters have recently been added to the lens distortion model of the Phase Vision SMS; however, the results presented in this thesis were obtained using only radial parameters. The camera parameters appearing in this transformation are known as *intrinsic parameters*.

Then, a point defined in a sensor coordinate system can be transformed into the world coordinate system by the rigid-body transformation, for the camera,

$$\begin{Bmatrix} x_c \\ y_c \\ z_c \end{Bmatrix} = \mathbf{R} \begin{Bmatrix} X \\ Y \\ Z \end{Bmatrix} + \mathbf{T}, \quad (1.23)$$

where \mathbf{R} is the *rotation matrix* usually described by three Euler-angles (ω, ϕ, κ) as

$$\mathbf{R} = \begin{bmatrix} \cos \phi \cos \kappa & \cos \omega \sin \kappa + \sin \omega \sin \phi \cos \kappa & \sin \omega \sin \kappa - \cos \omega \sin \phi \cos \kappa \\ -\cos \phi \sin \kappa & \cos \omega \cos \kappa - \sin \omega \sin \phi \sin \kappa & \sin \omega \cos \kappa + \cos \omega \sin \phi \sin \kappa \\ \sin \phi & -\sin \omega \cos \phi & \cos \omega \cos \phi \end{bmatrix}, \quad (1.24)$$

and \mathbf{T} is the *translation vector* that brings the pin-hole \mathbf{O}_c to the origin of the world coordinate system, which is defined as

$$\mathbf{T} = \begin{Bmatrix} X_0 \\ Y_0 \\ Z_0 \end{Bmatrix}. \quad (1.25)$$

The rotation matrix and the translation vector are also constant parameters of the camera; therefore, they are known as *extrinsic parameters*.

Equations (1.19) to (1.25) are sufficient to model the whole system. Nevertheless, the sensor parameters must be determined explicitly. The 12 parameters for a sensor (either camera or projector) are summarised as follows:

- Extrinsic parameters: X_0, Y_0, Z_0 (pin-hole coordinates), ω, ϕ, κ (Euler-angles describing orientation of sensor),
- Intrinsic parameters: ξ_H, η_H (offset of principal point from the top-left corner of image), c (focal length), and k_1, k_2, k_3 (lens radial distortion coefficients).

2.4.2 Calibration procedure

The calibration process consists of two major steps: *initialisation* and *refinement*. In the initialisation step, using each camera-projector pair, a single pose of a planar artefact is measured. The circles on the artefact are detected from the acquired image using an ellipse-fitting algorithm [82] and used by a *direct linear transformation* (DLT) method [83, 84] to obtain initial estimates of the respective camera and projector parameters.

In the refinement step, two spherical artefacts mounted on a bar are measured in different poses in the measurement volume using all camera-projector pairs. For each camera-projector pair, measured data are converted to a point cloud using the above-mentioned triangulation model which is initialised with the sensor parameters estimated in the first step. The artefacts are then detected from the point cloud by a 3D Hough

transform [85], and then their centre coordinates are used as inputs for the following bundle adjustment, together with the estimated sensor parameters. The bundle adjustment refines the parameters for all cameras, projectors and artefact poses, by minimising an objective function describing the calibration model.

Several types of calibration artefacts for the refinement step were investigated in the work of Ogundana [18], including ball bar, multi-sphere board and parallel plane. Considerations of induced calibration errors, visibility and structure of artefacts were also taken. It is concluded from his work that the ball bar is the most suitable artefact for calibrating multiple camera-projector systems.

2.4.3 Bundle adjustment

Bundle adjustment is the problem of refining a visual reconstruction to produce jointly optimal 3D structure (real world coordinates) and viewing parameter (external and/or internal) estimates [51]. For the sensor calibration, bundle adjustment is used to minimise the intersection closest distance of light rays coming from the camera and the projector in the object space. The intersection closest distance is a geometric measure of how good two rays intersect in space, which should ideally be zero. Provided that good initial estimates of sensor parameters and coordinates of intersection points are available, the bundle adjustment refines all of them in a global optimisation scheme.

In Phase Vision's SMS, a novel bundle adjustment strategy is used [86], in which a cost function is built on triangulation error in object space instead of image space as in conventional strategies. The vector model for the triangulation problem is shown in Figure 12. The points \mathbf{R}_1 and \mathbf{R}_2 represent the pin-holes of camera and projector, and the vectors \mathbf{u}_1 and \mathbf{u}_2 represent the two triangulation rays. The cost function is constructed based on the distance of closest approach ε_1 between the two rays:

$$F = \sum_i \varepsilon_{1,i}^2. \quad (1.26)$$

where the index i refers to an image pixel and thereby to an object point. In this way, the number of optimisation variables is always limited to the number of sensor parameters. Minimisation of F defined by Equation (1.26) with respect to the

camera/projector parameters is however not sufficient to produce a unique solution for those parameters.

An additional error term ε_2 related to the position of the triangulation point with respect to that of a locally known control point, is therefore introduced which provides a length scale for the problem and hence allows a unique solution to be obtained for the camera and projector parameters. For the spherical calibration artefacts ε_2 is defined as the distance of the current point to the centre of the relevant sphere minus the radius of the sphere. The cost function is thus modified to:

$$F = \gamma_1 \sum_i \varepsilon_{1,i}^2 + \gamma_2 \sum_i \varepsilon_{2,i}^2, \quad (1.27)$$

where γ_1 and γ_2 are scalars defining the relative weights of the two error terms. The standard Gauss-Newton optimisation technique is then used to minimise the cost function.

2.5 Post-processing of point clouds

Using Phase Vision's SMS, the point clouds resulting from all camera-projector pairs automatically lie in the same coordinate system without using a post-processing step to patch them together because of the calibration procedure described in the previous section. The common coordinate system is defined to be the one attached to the planar calibration board which is placed inside the measurement volume during the initialisation step. Therefore, the underlying assumption is that the planar calibration board can be observed by all of the cameras and projectors.

Arising from industrial applications, a practical requirement for visualisation purposes is to tessellate a measured point cloud to a mesh of surfaces that can be saved in standard formats. In Ogundana's work [18], this task has been done for two standard formats which are STL and OBJ.

Another requirement is to compare the measured point cloud of an object (say, a mechanical component) with its computer-aided design (CAD) model, in order to evaluate the manufacturing quality. Since the measured point cloud and the CAD model

lie on two independent coordinate systems, a rigid-body transformation (i.e. rotation and/or translation) has to be computed to align the two coordinate systems. Once the common coordinate system is established, manufacturing errors can be visualised simply by differencing coordinates of the point cloud and the CAD model. The *iterative closest point* (ICP) algorithm was used to find the optimum rotation and translation by minimising the alignment cost function [40]:

$$F_{ICP} = \sum_i [(\mathbf{R}\mathbf{M}_i + \mathbf{T}) - \mathbf{C}_i]^2, \quad (1.28)$$

where \mathbf{R} and \mathbf{T} , respectively, are the rotation matrix and translation vector to be found; \mathbf{M}_i is the position vector of point i in the measured point cloud; and \mathbf{C}_i is the position vector of the corresponding point in the CAD model. Because the ICP is a global iterative algorithm in nature, it is very computationally demanding and may be trapped in local optima. To improve the efficiency and robustness of the ICP, Ogundana [18] implemented the ICP algorithm using pre-computed look-up tables that store displacements of each point from its closest surface.

2.6 Figures

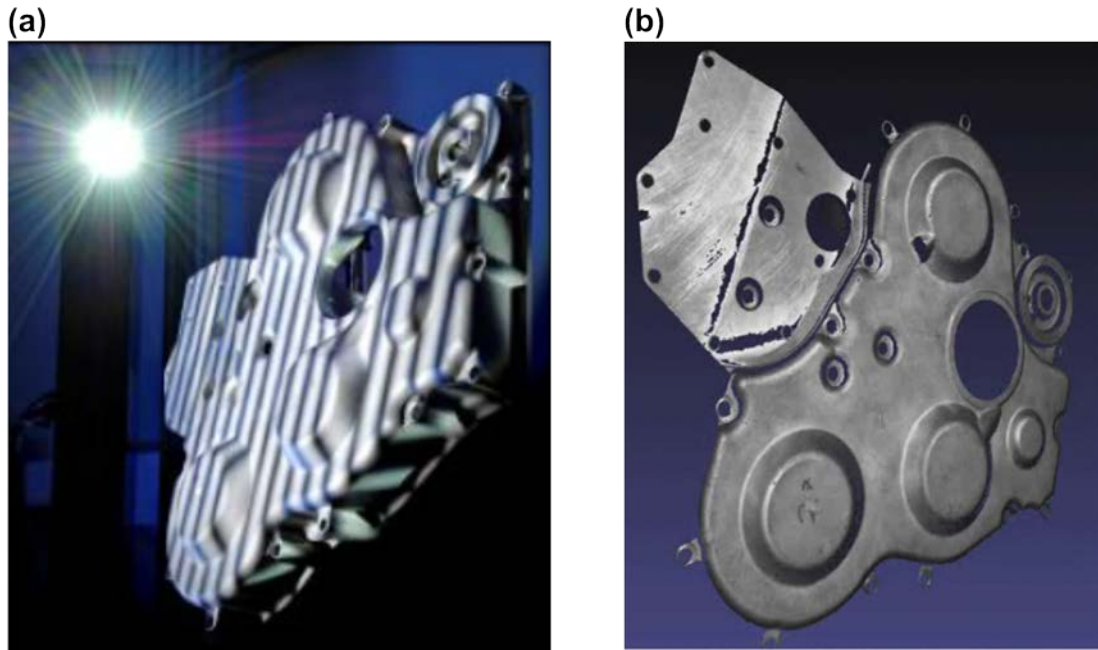


Figure 2: Structured-light fringe projection SMS used in this work. (a) Fringes projected onto sample surface are deformed by the surface profile. (b) Reconstructed 3D model.

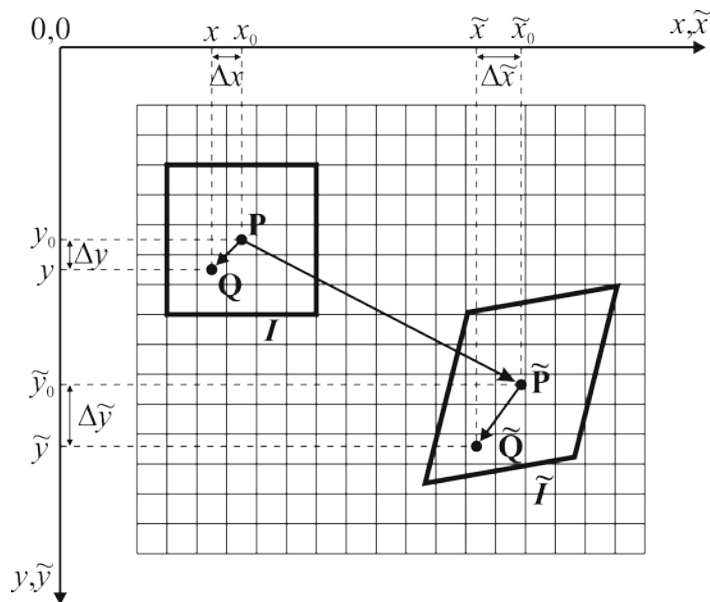


Figure 3: Schematic of the deformation process on the reference image I and the deformed image \tilde{I} .

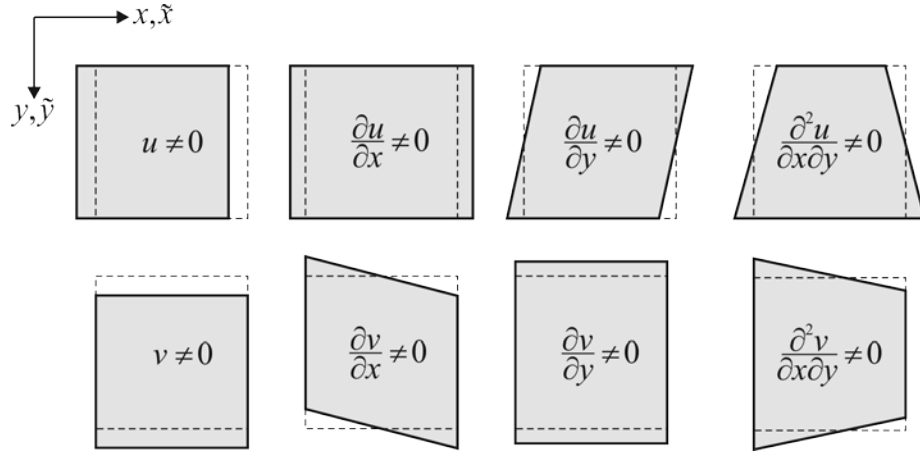


Figure 4: Deformation components of a correlation subset. Dashed boxes represent original shape, and shaded boxes represent deformed shape.

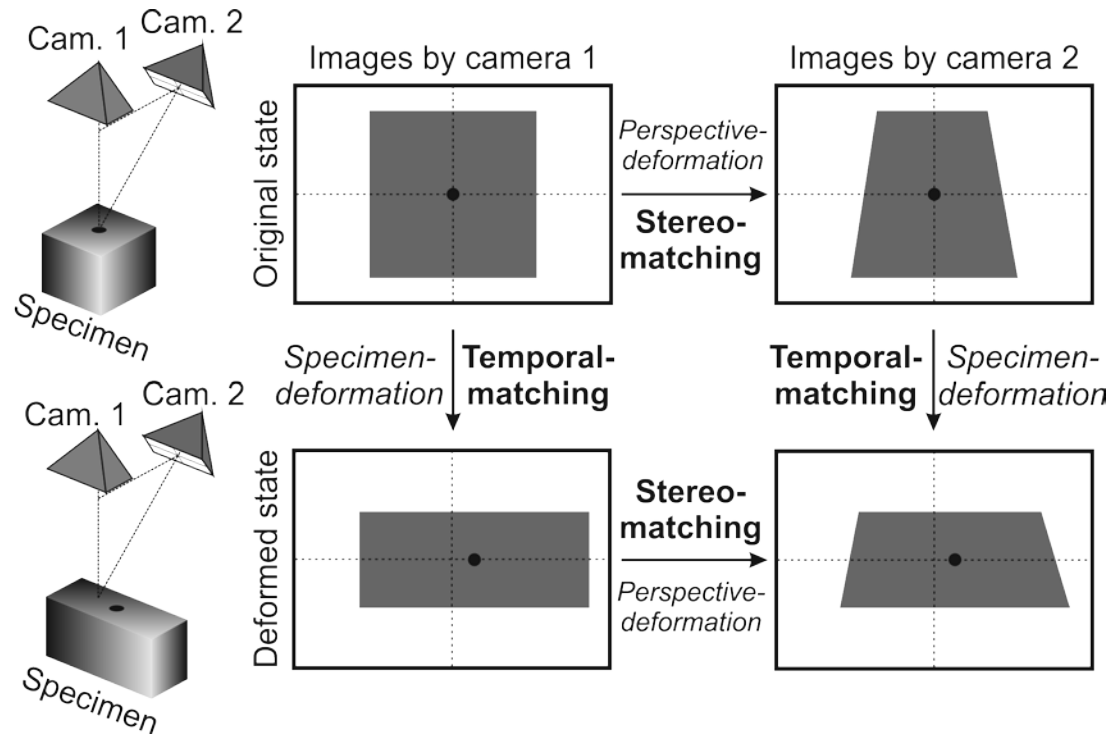


Figure 5: Image matching strategy of a typical 3D DIC technique.

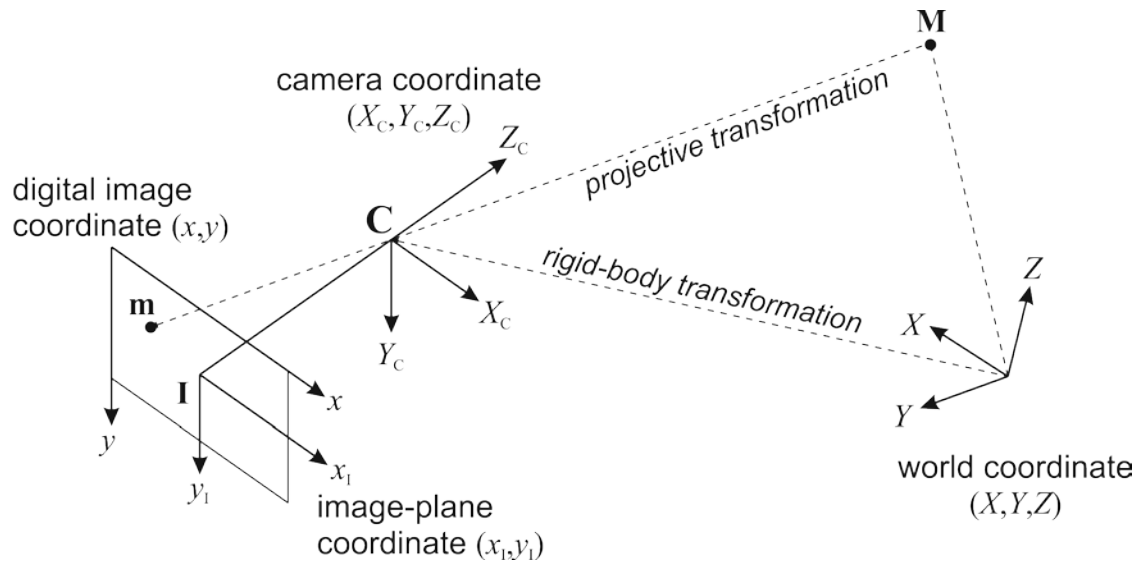


Figure 6: Pin-hole camera model with coordinate systems.

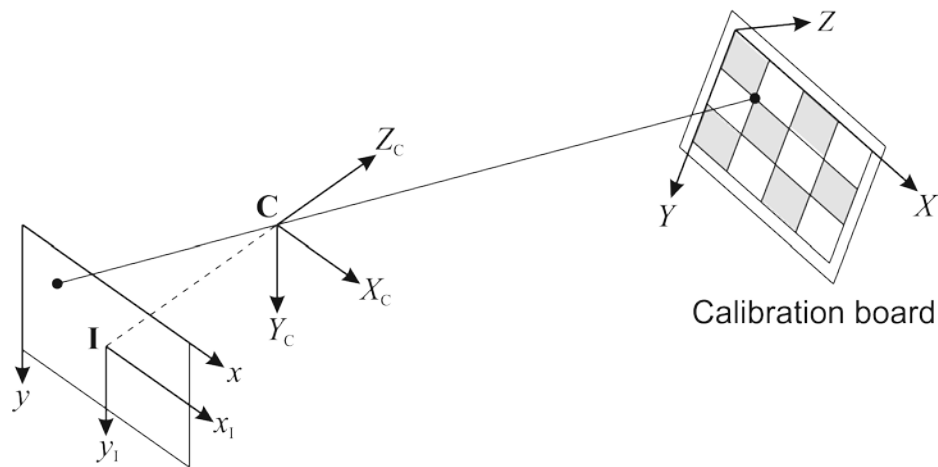


Figure 7: Calibration checkerboard defined in the coordinate system of a camera.

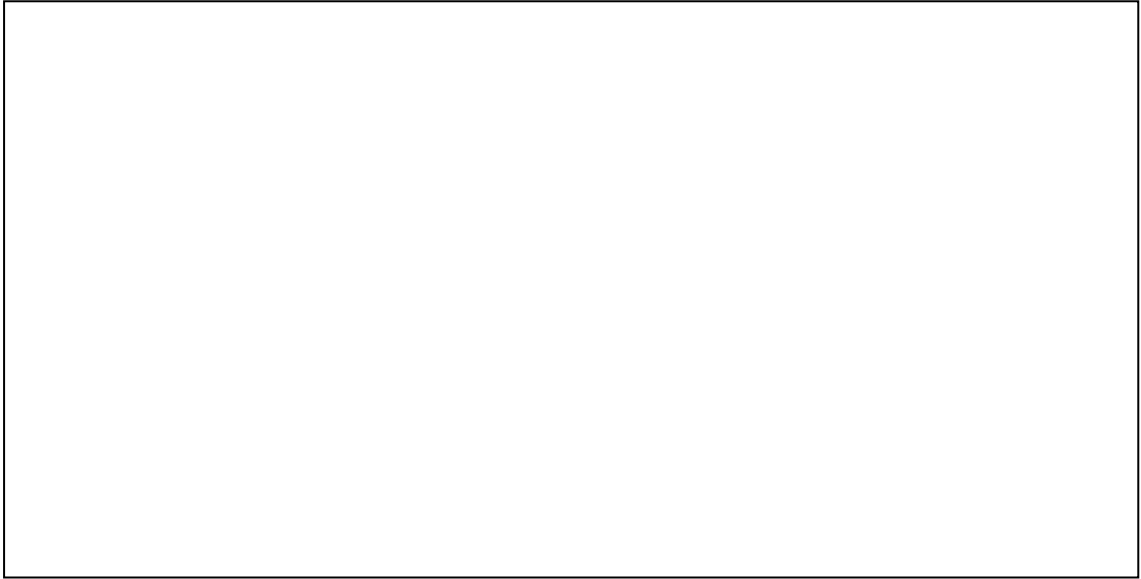


Figure 8: Set-up of a fringe projection technique [19].



Figure 9: Phase unwrapping in one dimension. The wrapped phase sequence is converted into an unwrapped sequence by the addition of integral multiples of 2π [80].



Figure 10: Efficient phase unwrapping methods: (a) forward exponential fringe sequence, and (b) reverse exponential fringe sequence. Both methods give the same unwrapping reliability for a given level of phase noise, but the latter has less variability in the least-squares fitted gradient ω_P [19].

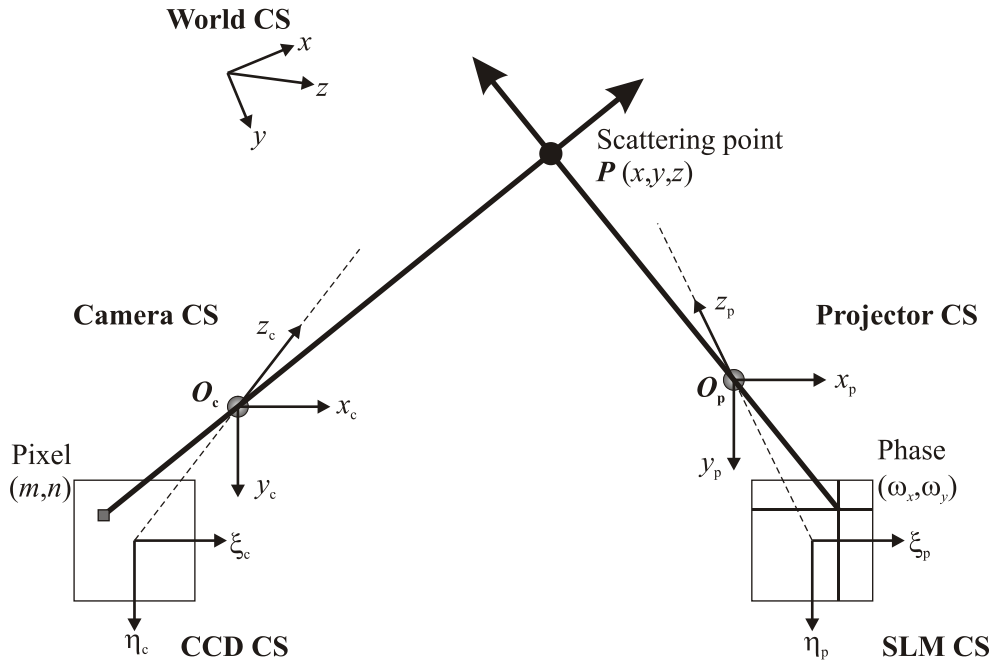


Figure 11: Pin-hole model and coordinate systems. CCD CS (ξ_c, η_c) is the coordinate system attached to the centre of the camera's CCD sensor. Camera CS (x_c, y_c, z_c) is the coordinate system attached to the camera's pin-hole lens. SLM CS (ξ_p, η_p) is the coordinate system attached to the centre of the projector's SLM. Projector CS (x_p, y_p, z_p) is the coordinate system attached to the projector's pin-hole lens. World CS (x, y, z) is the global coordinate system in which any scattering point \mathbf{P} is defined.



Figure 12: Vector model in object space of triangulation problem. \mathbf{R}_1 and \mathbf{R}_2 are the locations of the pin-holes, from which two tracing rays \mathbf{u}_1 and \mathbf{u}_2 emanate. The distance error ε_1 is used as part of the cost function within the bundle adjustment, as \mathbf{s} defines the computed position vector of the scattering point [86].

Chapter 3

Automated positioning system of calibration artefacts

3.1 Overview

In the previous work of Ogundana [18], calibration artefacts for the refinement step were mounted on a manually-operated stage (see Figure 13), i.e. human input was needed in positioning the artefacts. With typically tens or more artefact poses to measure, the calibration process was time-consuming, and its repeatability and traceability were relatively low. In addition, it was difficult to achieve a uniform distribution of the artefacts in the measurement volume in order to obtain accurate and reliable estimates of sensor parameters.

In this work, the manually-operated positioning stage is replaced by an automated robot arm that has two rotational degrees of freedom (DOF). Because the robot arm, which is also referred to as a *pan-tilt stage*, is completely controlled by a computer, the calibration process can be more convenient and faster. Optimal positions of the artefacts can also be computed for the best coverage of measurement volume. Furthermore, the knowledge of rotation angles of the pan-tilt stage can be used to predict the whereabouts of the artefacts on their captured images. Therefore, regions of interest (ROI) on measured phase maps can be filtered so that computational time spent for unwrapping and point cloud calculation are reduced significantly.

The objectives of this work were:

- To develop library functions to control the pan-tilt stage in C++ and integrate them to the SMS, and
- To implement an algorithm to reduce the ROI in the detection of calibration artefacts and to carry out experiments on the system performance.

3.2 Implementation of rotation stage

3.2.1 Hardware

A pan-tilt wrist provided by SCHUNK's Amtec Robotics was used in this work. The wrist has a compact and light-weight design (1.8 kg), which is suitable for developing a portable system. It consists of two rotation axes (i.e. pan and tilt) that can be controlled independently by computer. The axes have large position ranges (i.e. 120° for the pan axis and 108° for the tilt axis) which can cover a large portion of the measurement volume. Additionally, the embedded servo control and the automatic brake for tilt axis can provide accurate and stable positions. Its harmonic gears also give high torques to the axes, which is suitable for carrying heavy artefacts. Basic specifications of the pan-tilt stage are given in Table 1.

An electrical connection diagram for a generic system is shown in Figure 14. The pan-tilt stage is connected to a power supply unit (PSU) by a single cable that encapsulates power and RS232 wires. If multiple stages are used, a terminal switch can be incorporated to connect the stages to multiple power supply units. Since a single stage and a single PSU are used in the current work, the pan-tilt stage is connected directly to the PSU. Next, the PSU is connected to a computer using an RS232 interface.

As shown in Figure 15, the pan-tilt stage is mounted on a rigid tripod and supports the calibration artefacts bar (also known as the *ball-bar*) through a clamping block. The bar can move axially to offset the spheres relative to the clamping block. According to the numerical simulations of Huntley and Coggrave [87], a limited offset of the spheres from the midpoint clamping position can result in a minor improvement in measurement accuracy, because the two spheres can form two different spherical coverages of the measurement volume.

3.2.2 Software

The software was implemented in the C++ language in three levels: low, medium and high.

The low level involves building up customised C++ library functions based on the C library provided by the manufacturer. Low-level functions provide access and control to any available hardware set-up, such as a system composed of more than one stage (i.e.

device) with more than two rotation axes (i.e. module or axis). The diagram of low-level implementation is given in Figure 16. These low-level functions include basic operations, such as opening and closing devices, querying status and position of each module, moving a module to a desired position, and bringing a module to its initial or “home” position. Unlike the C functions provided by the manufacturer, the low-level functions implemented in this work are able to detect and resolve communication errors. Furthermore, modules can be controlled in synchronous, asynchronous and all-synchronous modes. This means that modules can move simultaneously or consecutively and that commands can be issued at the same time or one after another.

In the mid-level implementation, necessary functions for the objective pan-tilt stage with two rotation axes (namely, axis 0 for the pan module and axis 1 for the tilt module) were built based on low-level functions. An important mid-level function involves automatically generating optimal sequence of movements in the form of a table as shown in Table 2. The desired number of poses can be input by high-level functions or by the user via an XML configuration file. Optimal values of pan and tilt angles are computed so that valid position ranges are divided uniformly, and ordered in either a random sequence or a linear sequence that minimises the axes’ movements. In addition, after this implementation stage, the pan-tilt system is integrated into the currently available system so that library functions for the pan-tilt stage can be executed by any higher-level function in the system. Figure 17 illustrates the position of the pan-tilt stage in the system among other hardware components.

In the high-level implementation, a movement sequence of the pan-tilt stage can be incorporated with fringe projections, image acquisitions, phase computation, etc. Operation history of the pan-tilt system, together with those of other components, is exported into a *log* file for debugging purposes.

3.2.3 Practical issues

During the implementation of the pan-tilt system for calibration purposes, there arose several practical issues that affect stability, accuracy, robustness and integrity of the system. Some of the issues, together with the solutions, are as follows.

- Collision of the spheres and the tripod. The facts that the tilt angle can reach 120° and the length of the ball bar is usually comparable to other dimensions of

the positioning system mean that there may be some positions at which a sphere crashes with a tripod leg. The situation is illustrated in Figure 18. If the collision happens, it may damage the bar or the spheres. To avoid such a problem, tilt angle is restricted to values below a certain maximum which is computed from the geometry of the ball bar and the tripod. These geometry dimensions are conveniently defined in the system configuration file in XML format.

- Unstable positioning due to servo hunting. The servo motors of the axes are designed to dynamically adjust positioning errors, which work very well in most cases. However, for some unknown reason, the axes may slightly drift about its programmed position for quite a long period of time. A solution is to monitor the positioning error (i.e., the drift) and have the system wait until the error is less than a prescribed tolerance before executing subsequent commands.
- Vibration due to changes in angular momentum of the bar and the spheres. At the beginning and in the end of some movements, the spheres may “shake” strongly due to changes in angular velocity. Therefore, a nonlinear velocity profile, as shown in Figure 19, is applied to all movements, where velocity gradually increases up to a safe constant value and then decreases again at the end until the axis reaches its desired position.
- Coiling of electrical cable around pan axis. Pan rotation can reach more than two revolutions, and as a result the electrical cable may be twisted around the tripod, which may cause a coil-spring effect that retards the positioning process. The coiling problem can be solved simply by restricting the pan angle to 360° . Furthermore, after measuring the last pose, the “home” process of the pan axis must be done as a backward movement to the initial/“home” position, in order to uncoil the cable.

3.3 Algorithm to reduce detection regions

The *a priori* knowledge of Euler angles introduced by the pan-tilt stage can be used to predict the whereabouts of the calibration artefacts, and is therefore useful for reducing the size of the regions of interest within which the spheres centres are detected by the

Hough transform [85]. Additionally, this information can be used to label the spheres unambiguously.

For convenience, three types of coordinate systems are introduced as shown in Figure 20.

- **World coordinate system** (World CS) is the fixed CS used by the shape measurement system.
- **Tripod coordinate system** (Tripod CS) is defined to have its x'' -axis aligned with the pan axis, y'' -axis aligned with the tilt axis and z'' -axis aligned with the carbon-fibre bar where the pan-tilt stage is at the *home* position (i.e. reference position). Therefore, the Tripod CS is a fixed frame attached to the tripod. Coordinates of a point \mathbf{r}'' in the Tripod CS can be transformed into the World CS by using the rigid-body transformation,

$$\mathbf{r} = \bar{\mathbf{R}}\mathbf{r}'' + \bar{\mathbf{d}}, \quad (2.1)$$

where $\bar{\mathbf{R}}$ is the so-called tripod-to-world rotation matrix and $\bar{\mathbf{d}}$ is the tripod-to-world translation vector.

- **Bar coordinate system** (Bar CS) is attached to the artefacts with its z' -axis going from sphere 1 to sphere 2 and its x' -axis going along the clamping stalk. Its origin is defined to coincide with that of the Tripod CS in order to avoid the need for an additional translation term. Therefore, the transformation from the Bar CS into the Tripod CS is defined completely from the Euler angles introduced by the pan-tilt stage,

$$\mathbf{r}'' = \tilde{\mathbf{R}}\mathbf{r}', \quad (2.2)$$

and

$$\tilde{\mathbf{R}} = \begin{bmatrix} \cos \phi & 0 & \sin \phi \\ \sin \omega \sin \phi & \cos \omega & -\sin \omega \cos \phi \\ -\cos \omega \sin \phi & \sin \omega & \cos \omega \cos \phi \end{bmatrix}, \quad (2.3)$$

where ω is the pan angle and ϕ is the tilt angle.

Therefore, any known coordinates of the calibration spheres can be transformed from the Bar CS into the World CS, once the tripod-to-world rotation matrix $\bar{\mathbf{R}}$ and translation vector $\bar{\mathbf{d}}$ are known. These terms can be computed from 3 special poses:

- Home pose (0,0) with the pan angle $\omega=0$ and the tilt angle $\phi=0$,
- Pan pose ($\omega,0$) with the pan angle $\omega \neq 0$ and the tilt angle $\phi=0$, and
- Tilt pose (0, ϕ) with the pan angle $\omega=0$ and the tilt angle $\phi \neq 0$.

3.3.1 Computing tripod-to-world rotation matrix $\bar{\mathbf{R}}$

As shown in Figure 21, the directional vector $\mathbf{n}_{x''}$ of the x'' -axis of the Tripod CS can be defined in the World CS as a cross-product of two vectors aligning with the artefact bar at the home pose (0,0) and the pan pose ($\omega,0$),

$$\mathbf{n}_{x''} = [\mathbf{r}_2(0,0) - \mathbf{r}_1(0,0)] \times [\mathbf{r}_2(\omega,0) - \mathbf{r}_1(\omega,0)], \quad (2.4)$$

where \mathbf{r}_j is the coordinate of sphere centre j specified in the World CS as a result of the Hough transform. This directional vector can be normalised as

$$\hat{\mathbf{n}}_{x''} = \frac{\mathbf{n}_{x''}}{\|\mathbf{n}_{x''}\|}, \quad (2.5)$$

where $\|\cdot\|$ denotes the norm (or magnitude) of the enclosed vector.

Similarly, the directional unit vector $\hat{\mathbf{n}}_{y''}$ of the y'' -axis of the Tripod CS can be computed in the World CS from the home pose (0,0) and the tilt pose (0, ϕ) as shown in Figure 22,

$$\mathbf{n}_{y''} = [\mathbf{r}_2(0,0) - \mathbf{r}_1(0,0)] \times [\mathbf{r}_2(0,\phi) - \mathbf{r}_1(0,\phi)], \text{ and} \quad (2.6)$$

$$\hat{\mathbf{n}}_{y''} = \frac{\mathbf{n}_{y''}}{\|\mathbf{n}_{y''}\|}. \quad (2.7)$$

Therefore, the unit vector $\hat{\mathbf{n}}_{z''}$ of the z'' -axis can be calculated as

$$\hat{\mathbf{n}}_{z''} = \frac{\hat{\mathbf{n}}_{x''} \times \hat{\mathbf{n}}_{y''}}{\|\hat{\mathbf{n}}_{x''} \times \hat{\mathbf{n}}_{y''}\|}. \quad (2.8)$$

Finally, the rotation matrix that defines the Tripod CS in the World CS can be determined by stacking these directional unit vectors together:

$$\bar{\mathbf{R}} = \left([\hat{\mathbf{n}}_{x''}] [\hat{\mathbf{n}}_{y''}] [\hat{\mathbf{n}}_{z''}] \right). \quad (2.9)$$

3.3.2 Computing tripod-to-world translation vector $\bar{\mathbf{d}}$

The position of the origin of the Tripod CS as defined in the World CS can be determined by intersecting two vectors with the directions of the x'' - and y'' -axes and going through a point lying on each of these axes. A function in the triangulation module of the SMS to compute point cloud coordinates is directly applicable to this intersection calculation.

As explained in Figure 23, the x'' -axis is separated from the tangential vector \mathbf{t}_1 by a distance,

$$h_{x''} = \frac{\|\mathbf{t}_1\|}{2 \tan(\omega/2)} = \frac{\|\mathbf{r}_1(\omega, 0) - \mathbf{r}_1(0, 0)\|}{2 \tan(\omega/2)}, \quad (2.10)$$

Thus, the point lying on the x'' -axis can be located by going from the known mid-point of the tangential vector \mathbf{t}_1 by a radial distance $h_{x''}$,

$$\mathbf{r}_{x''} = \frac{[\mathbf{r}_1(\omega, 0) + \mathbf{r}_1(0, 0)]}{2} - h_{x''} \frac{[\mathbf{r}_1(\omega, 0) - \mathbf{r}_1(0, 0)] \times \hat{\mathbf{n}}_{x''}}{\|[\mathbf{r}_1(\omega, 0) - \mathbf{r}_1(0, 0)] \times \hat{\mathbf{n}}_{x''}\|} \quad (2.11)$$

Similarly, the point lying on the y'' -axis can be defined as shown in Figure 24 by

$$h_{y''} = \frac{\|\mathbf{k}_1\|}{2 \tan(\phi/2)} = \frac{\|\mathbf{r}_1(0, \phi) - \mathbf{r}_1(0, 0)\|}{2 \tan(\phi/2)}, \text{ and} \quad (2.12)$$

$$\mathbf{r}_{y''} = \frac{[\mathbf{r}_1(0, \phi) + \mathbf{r}_1(0, 0)]}{2} - h_{y''} \frac{[\mathbf{r}_1(0, \phi) - \mathbf{r}_1(0, 0)] \times \hat{\mathbf{n}}_{y''}}{\|[\mathbf{r}_1(0, \phi) - \mathbf{r}_1(0, 0)] \times \hat{\mathbf{n}}_{y''}\|} \quad (2.13)$$

3.3.3 Computing bar geometry from coordinates of spheres

As can be seen in Figure 20, coordinates of the sphere centres expressed in the Bar CS only depend on the geometry of the sphere bar, which includes the bar length l , the offset f from sphere 1 to the clamping point and the length s of the clamping stalk. Although these parameters can be measured physically, they can also be estimated numerically from the three special poses. The bar length l can be taken to be the average distance between the sphere centres at the special poses,

$$l(0, 0) = \|\mathbf{r}_1(0, 0) - \mathbf{r}_2(0, 0)\|, \quad (2.14)$$

$$l(\omega, 0) = \|\mathbf{r}_1(\omega, 0) - \mathbf{r}_2(\omega, 0)\|, \quad (2.15)$$

$$l(0, \phi) = \|\mathbf{r}_1(0, \phi) - \mathbf{r}_2(0, \phi)\|, \quad (2.16)$$

$$l = [l(0, 0) + l(\omega, 0) + l(0, \phi)] / 3. \quad (2.17)$$

Using basic geometry relationship between the tangential vectors \mathbf{t}_1 and \mathbf{t}_2 (as shown in Figure 23), the offset term f can be computed from the bar length l by

$$f = l / \left(\frac{\|\mathbf{t}_2\|}{\|\mathbf{t}_1\|} + 1 \right). \quad (2.18)$$

Also, the stalk length s can be estimated using geometry relationship presented in Figure 24,

$$s = \sqrt{d_1^2 - f^2}, \quad (2.19)$$

with the distance d_1 between sphere 1 and the origin of the Tripod CS computed by

$$d_1 = \frac{\|\mathbf{k}_1\|}{2 \sin(\phi / 2)}. \quad (2.20)$$

3.3.4 Automatic sphere labelling

Another advantage of the knowledge of the pan and tilt angles at an artefact pose is that it can be used to label the sphere correctly and automatically. In the previous work of Ogundana [18], the two spheres of a calibration artefact must be labelled by separate markers and tracked manually by an operator. Therefore, the operator must keep their eyes on the spheres all the time, which made calibration an inconvenient and stressful task. In this work, the pan and tilt angles controlled by the automated pan-tilt head are used to track the motion of the spheres and label them automatically, thus neglecting the need for human intervention. The idea is to compare the measured angle between the bar at pose (0,0) and that at pose (ω, ϕ) against a known angle computed from the known angles ω and ϕ . If these two angles are similar (usually within a small tolerance), the sphere labelling at pose (ω, ϕ) matches with that at pose (0,0). Otherwise, the sphere labels at pose (ω, ϕ) need to be swapped over to match with that at pose (0,0). Therefore, the sphere labelling at the home pose (0,0) is used as the reference, which can be defined so that the vector going from sphere 1 to sphere 2 has a positive x -component.

The angle of the length bar between pose (0,0) and pose (ω, ϕ) , which is denoted κ in Figure 25, can be computed in two different ways. The first way, which provides an experimental κ value, involves calculating the dot product of the vectors aligned with the length bar,

$$\mathbf{b}_{00} = [\mathbf{r}_2(0,0) - \mathbf{r}_1(0,0)], \quad (2.21)$$

$$\mathbf{b}_{\omega\phi} = [\mathbf{r}_2(\omega, \phi) - \mathbf{r}_1(\omega, \phi)], \quad (2.22)$$

$$\cos \kappa = \frac{\mathbf{b}_{00} \cdot \mathbf{b}_{\omega\phi}}{\|\mathbf{b}_{00}\| \cdot \|\mathbf{b}_{\omega\phi}\|} \quad (2.23)$$

In the second way, the movement of the artefact bar from the home pose (0,0) to a pose (ω, ϕ) is considered to be done in two steps: (i) moving from pose (0,0) to pose $(\omega, 0)$ by the pan angle ω , and (ii) moving from pose $(\omega, 0)$ to pose (ω, ϕ) by the tilt angle ϕ . Therefore, using simple trigonometry, the angle κ can be computed from the known pan and tilt angles by,

$$\cos \kappa = \cos \omega \cos \phi \quad (2.24)$$

The values of the angle κ as computed from Equation (2.23) and (2.24) can now be compared, and if necessary the spheres are relabelled as described above.

3.3.5 Applying reduced regions of interest to calibration process

The procedure to compute reduced regions of interest (ROIs) to detect sphere centres and apply them to the calibration process is explained in Figure 26. In the first step, three special poses are selected from the pose table which includes a list of pan and tilt angles associated with corresponding calibration input data (e.g. texture image and estimated point cloud). These three special poses include a home pose (with both pan and tilt angles equal to 0), a pan pose (with a sufficiently large pan angle and a zero tilt angle) and a tilt pose (with a zero pan angle and a sufficiently large tilt angle). Then, the sphere centres at each special pose are detected from the estimated point cloud using the 3D Hough transform [85]. Coordinates of the detected spheres are then used to estimate the tripod-to-world rotation matrix $\bar{\mathbf{R}}$ and translation vector $\bar{\mathbf{d}}$ as well as the length bar's dimensions (l , s and f), as described in Sections 3.3.1 to 3.3.3. These parameters characterise a complete transformation of the sphere centres from the local Bar CS into the World CS, and are applied to the rest of the non-special poses in the pose table to reduce the detection ROIs.

For every camera-projector pair of every pose in the pose table, reduced ROIs enclosing the spheres of interest can be identified by using the transform computed above. A reduced ROI is represented as a circle centred at the projection of the predicted sphere centre on the image plane. A sphere centre is detected only from the pixels enclosed within this ROI. Additionally, the resulting sphere centres are labelled correctly using the knowledge of the pan and tilt angles as mentioned in the previous section. Finally, this information is used for the bundle adjustment to refine the estimates of calibration parameters.

3.4 Results

A shape measurement system with two cameras and two projectors was calibrated using the pan-tilt stage and the proposed reduced ROI algorithm. The calibration arrangement was similar to the one shown in Figure 27. The cameras (Vosskuhler CCD1300QFB)

with an image size of 1024×1024 pixels were connected to a Matrox Solios image frame-grabber installed in a desktop computer. The effective image size of the projectors (Vision Plus V1100Z) was 1024×768 pixels. All the imaging devices were connected to a synchronisation board. The cameras and the projectors were mounted on an aluminium frame. The sensors were set to observe a common measurement volume of approximately $400 \times 400 \times 400 \text{ mm}^3$, within which the artefact was placed. The artefact consisted of two spheres that had a nominal separation of 200 mm and were supported by a carbon-fibre reinforced plastic (CFRP) bar. The exact value of the spheres separation was measured beforehand on a CMM. The bar was clamped on the PowerCube PW070 pan-tilt stage which was connected to a power supply unit (PSU) and controlled by the computer. A circle board was used to achieve the initial calibration parameters of the sensors, which were later refined using the two-sphere artefact. These initial calibration parameters were stored in an input file structured in the extensible markup language (XML) format, together with all the geometry parameters of the artefact and the pan-tilt stage.

To populate sample points within the measurement volume, the pan-tilt stage was located nearly at the centre and 5 angle values were specified for each pan and tilt axis, resulting in a total of 25 poses. The list of the poses is given in Table 3 below. For each of the poses, the artefact was illuminated with sinusoidal fringes, of which the fringe density followed a reverse exponential sequence ($t = 32, 31, 30, 28, 24$ and 16 fringes across the projector's field of view), and the images were captured the cameras. In this experiment, the average time for both positioning the artefact and acquiring its fringe images was approximately 36 seconds per pose (i.e., about 15 minutes for all the 25 poses). The corresponding time needed by Ogunada's manual stage [18] was reported to be approximately 170 seconds per pose (i.e., 17 minutes for a total of 6 poses). Therefore, it can be seen that the proposed automated positioning system has reduced the acquisition time by nearly 5 times. After the acquisition of the two-sphere artefact finished, a temporal phase unwrapping technique was used to estimate phase gradients from the acquired fringe images, and the corresponding results were saved on files.

The MATLAB code for calibration refinement developed by Ogunada [18] was executed, taking the measured phase gradient maps of all the poses and the initial calibration parameters as the main inputs. The code estimated a point cloud for each of

the poses, from which the locations of the sphere centres were detected using a 3D Hough transform [85] and then passed to the bundle adjustment algorithm for refining the calibration parameters. Figure 28 shows the result of an estimated point cloud for pose 8 (i.e., tilt pose) and for all of the four available camera-projector pairs. The spheres are visible together with other distracting features such as the background and the tripod legs. Figure 29 shows the corresponding result with the proposed reduced ROI algorithm activated. It can be seen that the regions of interest have been successfully reduced to two circles each enclosing one of the spheres, and almost all distracting features (corresponding to about 4/5 of the original data) have been removed. For comparison, Table 3 shows the processing time needed for the 3D Hough transform module to detect the sphere centres for each pose, with and without using the reduced ROI algorithm. It can be seen that the reduced ROI algorithm is able to reduce the sphere detection time by nearly a half (i.e., about 6 seconds rather than 10 seconds). A further advantage of using the reduced ROI is that sphere detection reliability is improved. This is because large portions of the point cloud that could not contain the spheres, but nevertheless contribute noise to the Hough space, are removed.

Figure 30 presents the results of detected spheres for all of the poses. It can be seen that the poses are populated fairly uniformly within the measurement volume, which may help improve the overall accuracy of the subsequent bundle adjustment. The spheres are also labelled consistently with the automatic sphere labelling described in the previous section.

3.5 Summary

An automated rotation stage with two rotation axes (i.e. pan and tilt) has been introduced to position the calibration artefact. Software to control the rotation stage has been successfully implemented in the C++ language and integrated into the present shape measurement system as an optional module. It is observed that the use of the rotation stage has reduced the acquisition time by nearly 5 times as compared to the manual positioning device.

A technique to employ the knowledge of rotation angles of the artefacts to improve the calibration process has been introduced and implemented into the current calibration module (in the MATLAB environment). This technique is shown to reduce artefact

detection time by 2 times by limiting detection regions significantly. The spheres are also labelled correctly using the knowledge of the rotation angles. The rotation stage has been used intensively at Phase Vision Ltd for calibration processes of the shape measurement system.

3.6 Tables

Table 1: Specifications of the PowerCube PW070 pan-tilt stage.

Specifications	Pan axis	Tilt axis
Resolution ($^{\circ}$)	1/672	1/561
Positioning range ($^{\circ}$)	± 120	± 108
Nominal torque (Nm)	12	2
Max. angular velocity ($^{\circ}/s$)	248	356
Weight (kg)	1.8	

Table 2: An example movement sequence automatically generated by a mid-level function. The required number of poses (i.e. 9 in this example) is read from an XML configuration file. Pan and tilt angles are computed for the most uniform distribution of the spheres in the measurement volume and ordered in a linear sequence that minimises movement of the axes (although a random sequence can also be used).

Pose	Pan angle ($^{\circ}$)	Tilt angles ($^{\circ}$)
1	0	-90
2	0	0
3	0	90
4	120	90
5	120	0
6	120	-90
7	240	-90
8	240	0
9	240	90

Table 3: Pose table and corresponding time required for spheres detection (for pair C0P0).

Pose	Pan angle ω (°)	Tilt angle ϕ (°)	Sphere detection time without Reduced ROI (s)	Sphere detection time with Reduced ROI (s)
1	315	-45	9.5	5.5
2	337.5	-45	9.4	5.9
3	0	-45	10.8	5.6
4	22.5	-45	10.5	5.7
5	45	-45	9.4	5.3
6	45	-22.5	9.3	5.9
7	22.5	-22.5	9.4	5.7
8 (Tilt)	0	-22.5	10.2	5.6
9	337.5	-22.5	10.4	5.9
10	315	-22.5	9.7	6.1
11	315	0	9.9	6.3
12	337.5	0	10.1	5.6
13 (Home)	0	0	10.0	5.9
14 (Pan)	22.5	0	9.7	6.0
15	45	0	9.5	6.3
16	45	22.5	9.6	5.9
17	22.5	22.5	10.1	5.7
18	0	22.5	9.6	5.8
19	337.5	22.5	9.5	5.6
20	315	22.5	9.3	6.1
21	315	45	9.3	5.6
22	337.5	45	9.4	6.0
23	0	45	10.5	5.4
24	22.5	45	10.2	5.5
25	45	45	9.4	5.8

3.7 Figures



Figure 13: Two-sphere artefact mounted on a manually-operated stage [18].

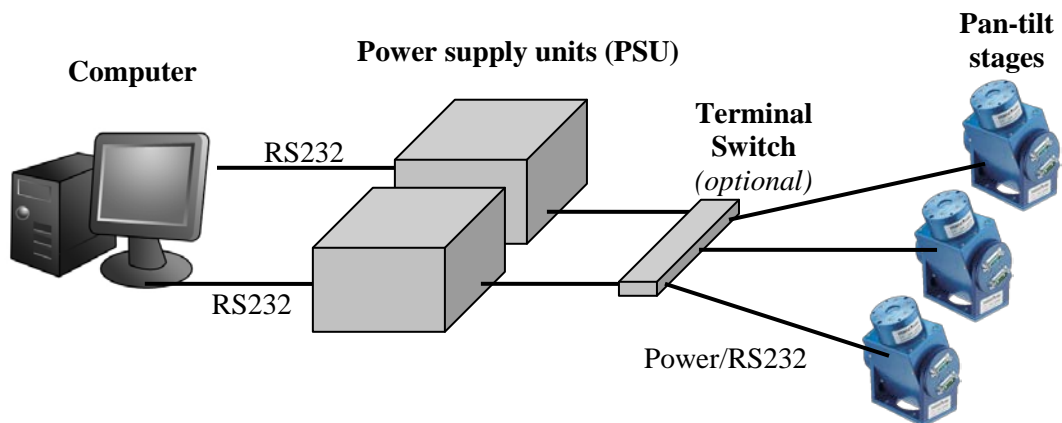


Figure 14: Circuit diagram for electrical connections. A generic system with more than one power supply unit (PSU) and pan-tilt stage is shown. In the present work, only one PSU and one pan-tilt stage are used; thus the terminal switch is not used.

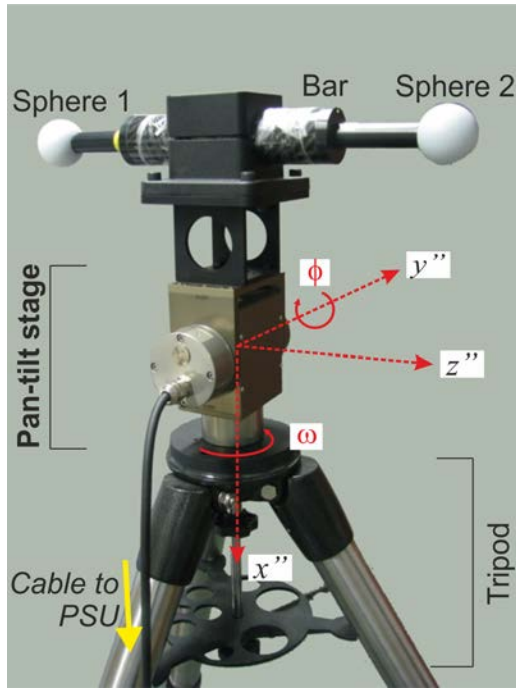


Figure 15: Configuration of the artefact positioning system.

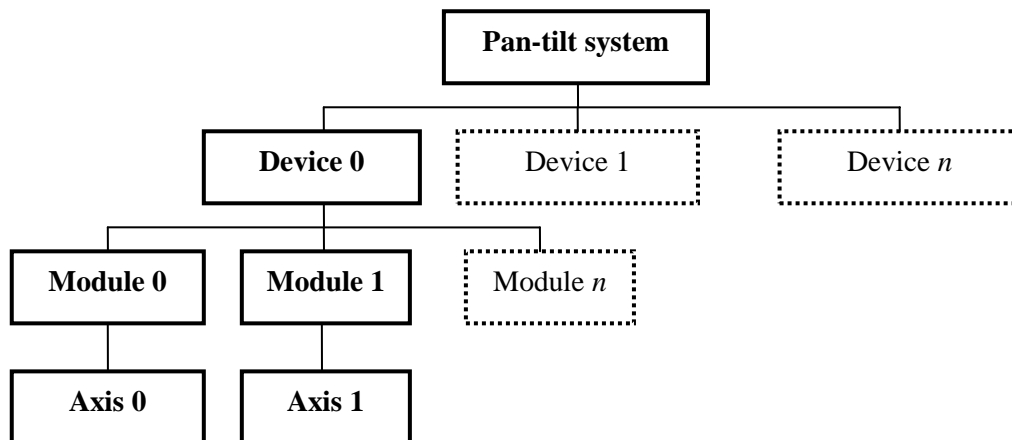


Figure 16: Low-level implementation of the software to control the pan-tilt stage. The items in bold are used in the current two-DOF pan-tilt stage. However, it is possible to use multiple stages with more than two rotation axes. “Device” corresponds to a stage, and “Module” and “Axis” correspond to a DOF.

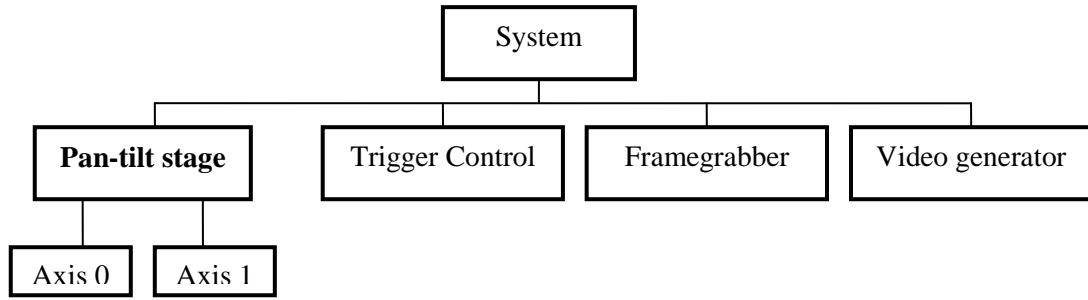


Figure 17: Hierarchical system diagram for mid-level and high-level implementations.

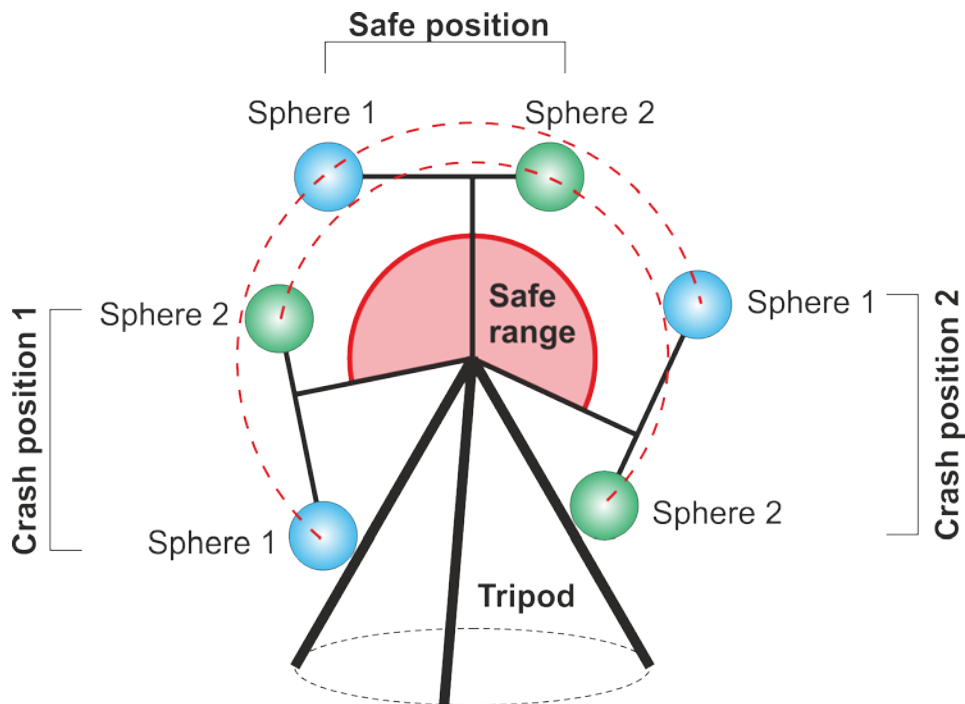


Figure 18: Collision of spheres with tripod. To avoid damage to the artefact, tilt angle is restricted to a safe range defined by the artefact and tripod geometries.

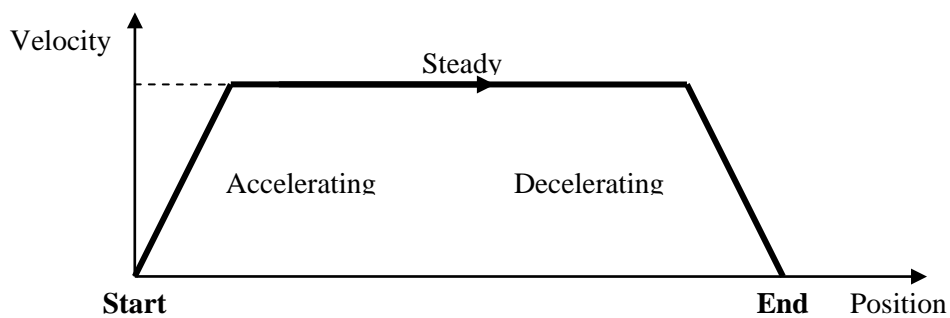


Figure 19: Velocity profile of a movement of an axis.

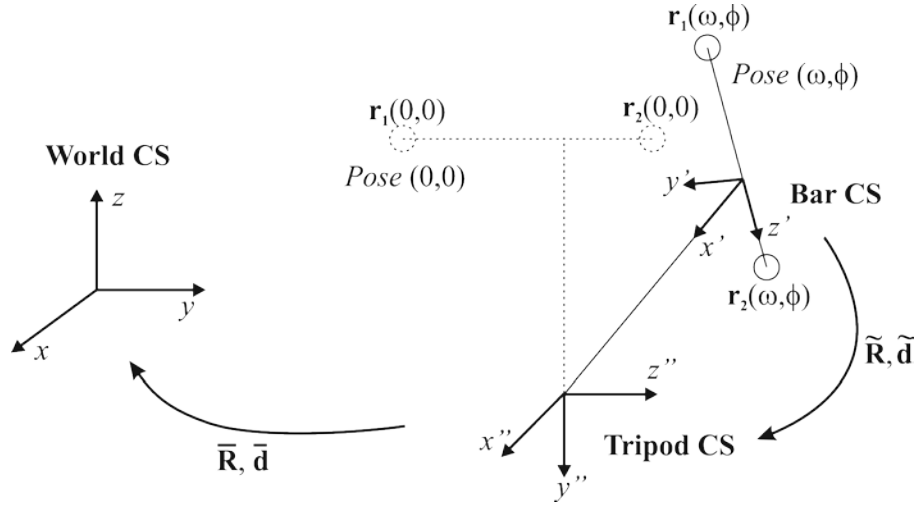
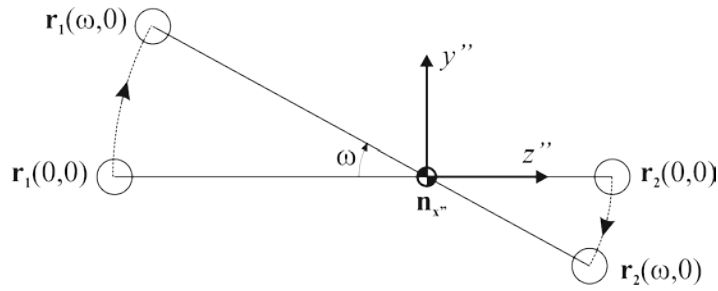
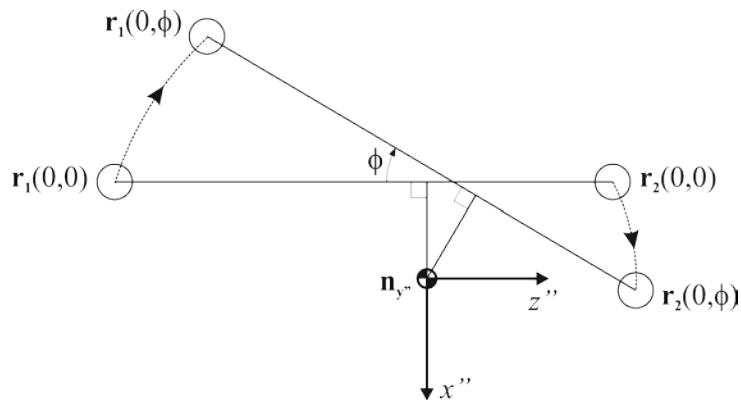


Figure 20: Coordinate systems defined for the pan-tilt stage.


 Figure 21: Derivation of directional vector of the x'' -axis from home pose (0,0) and pan pose ($w,0$).

 Figure 22: Derivation of directional vector of the y'' -axis from home pose (0,0) and tilt pose (0, ϕ).

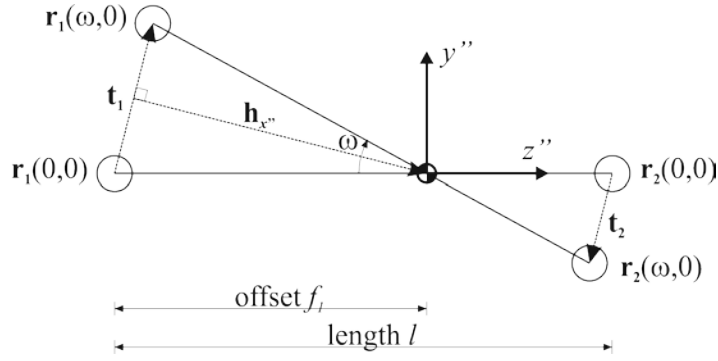


Figure 23: Determining a point on the x'' -axis from home pose (0,0) and pan pose ($\omega,0$).

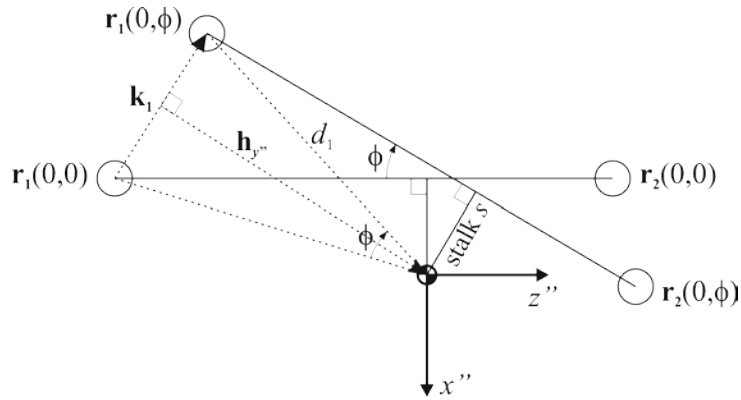


Figure 24: Determining a point on the y'' -axis from home pose (0,0) and tilt pose (0, ϕ).

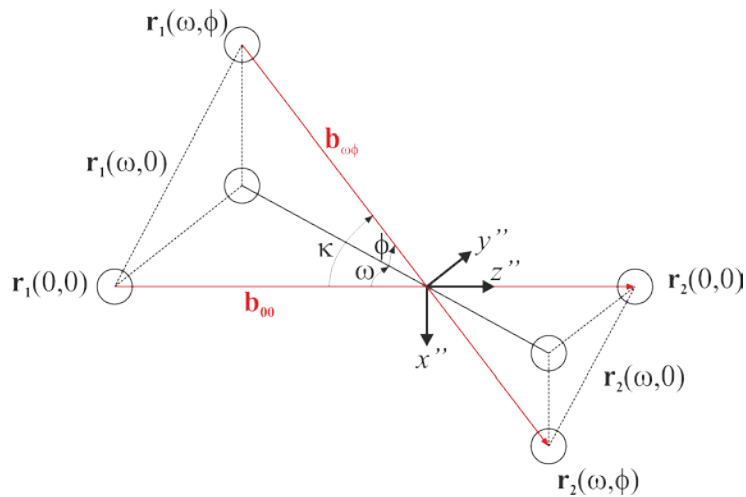


Figure 25: Labelling spheres at arbitrary pose (ω,ϕ) based on angles with respect to home pose (0,0).

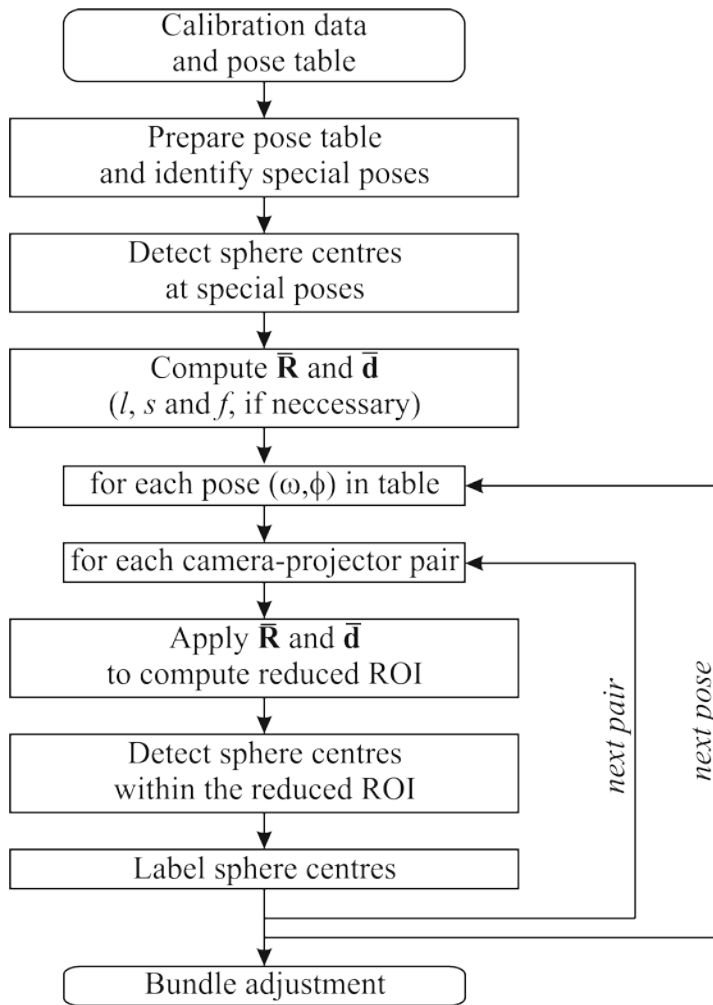


Figure 26: Procedure to apply reduced ROIs to calibration process.

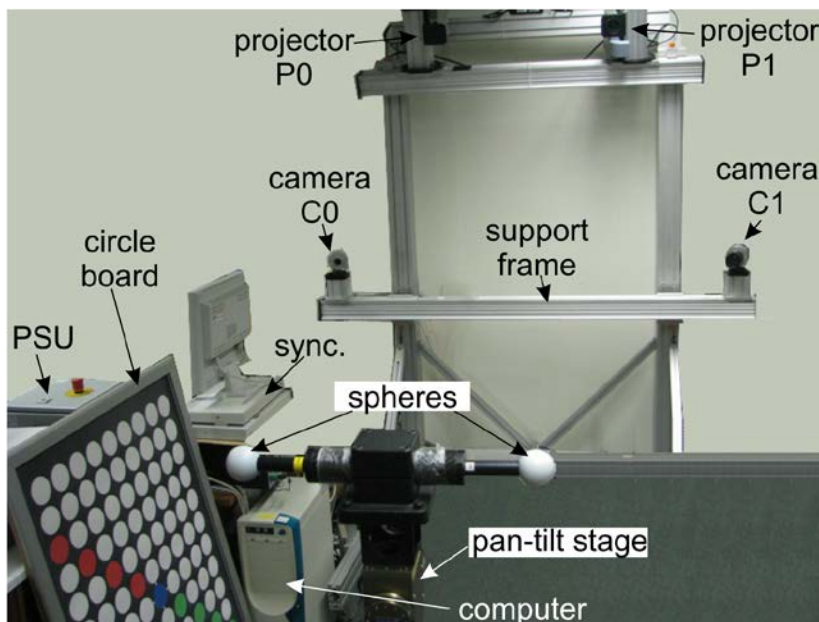


Figure 27: Calibration setup using the pan-tilt stage to position a two-sphere artefact.

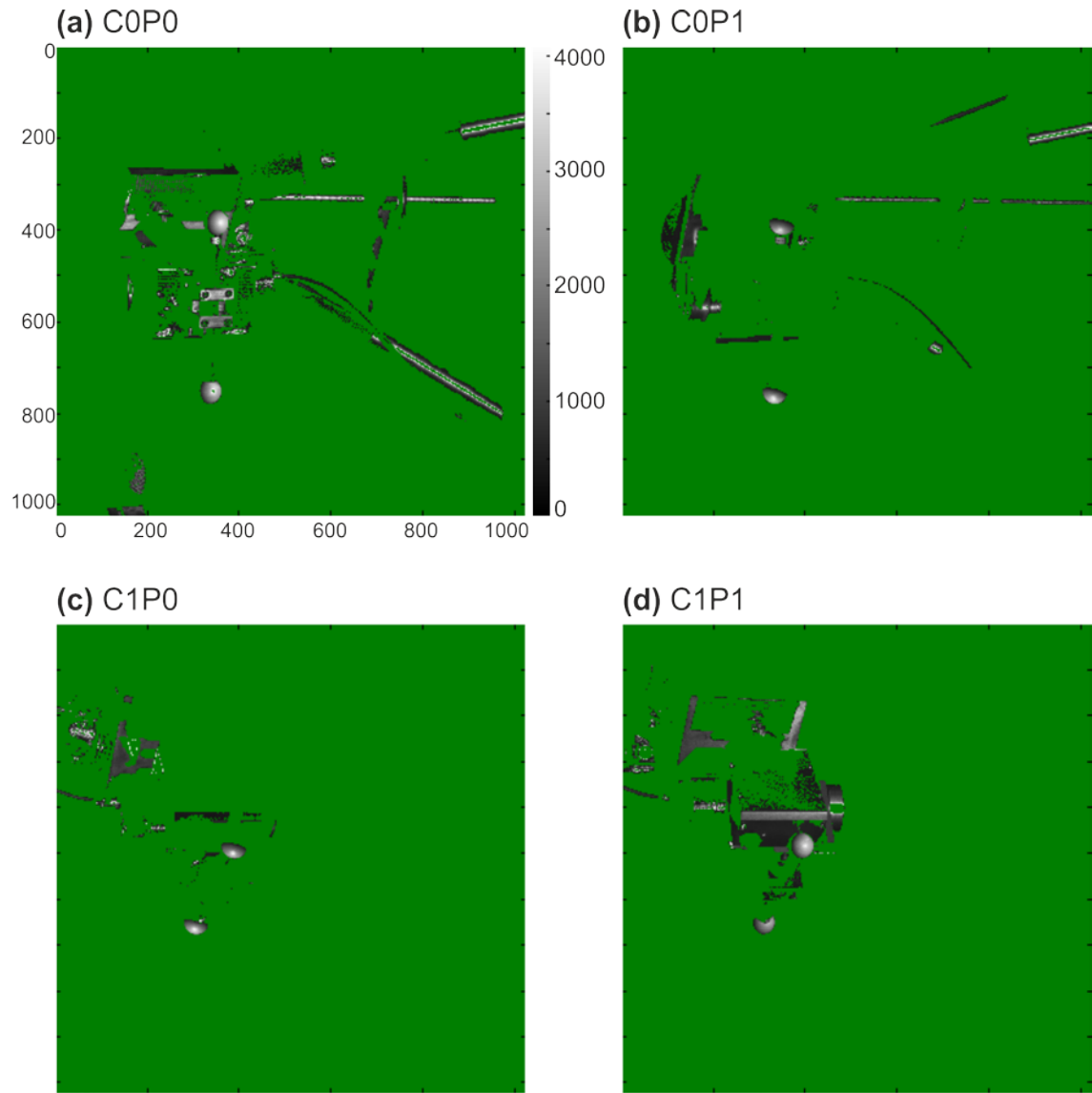


Figure 28: Original regions of interest to detect sphere centres as observed by each camera-projector pair. The presented data are of pose 8 specified in Table 3.

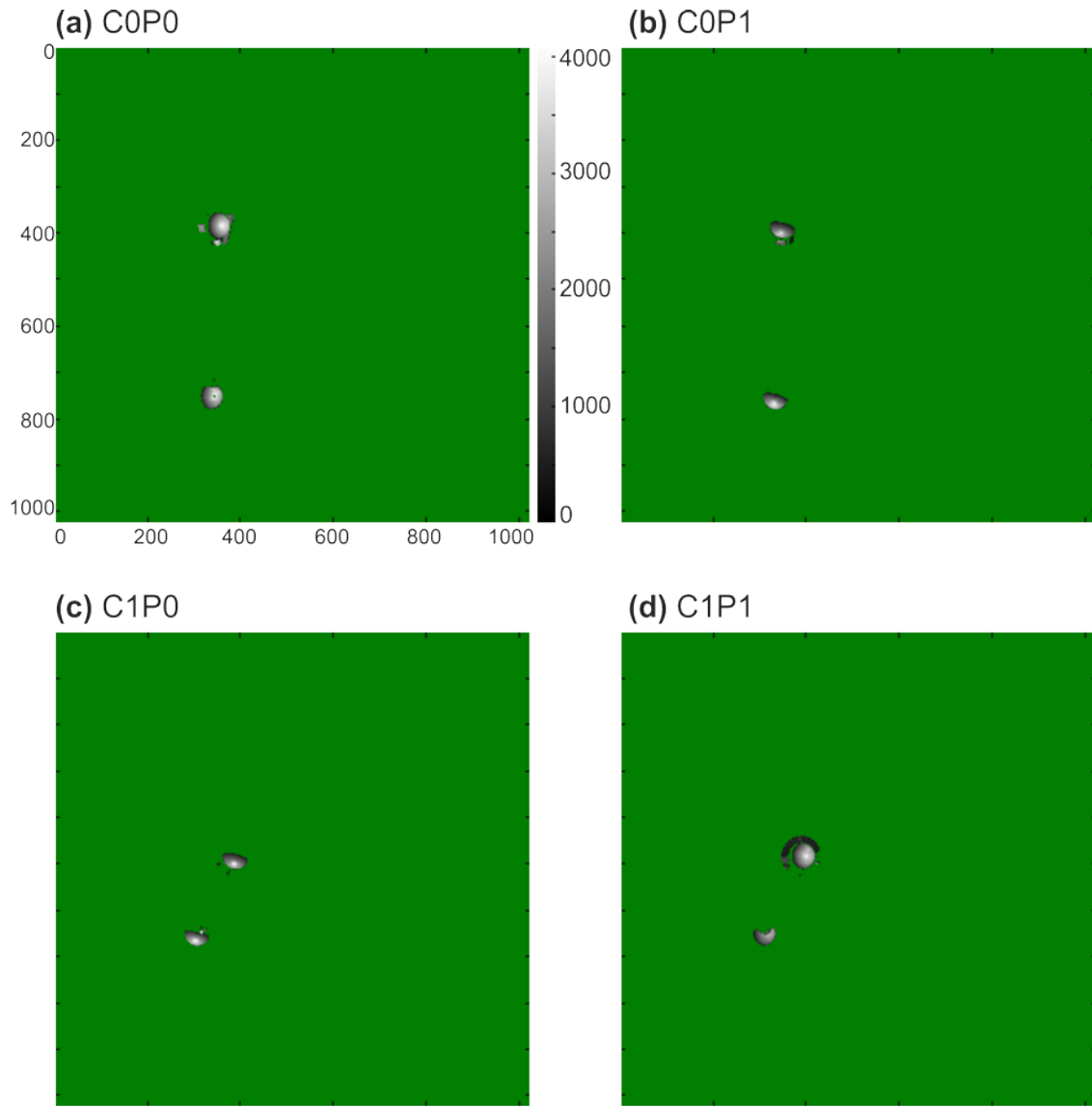


Figure 29: Reduced regions of interest to detect sphere centres as observed by each camera-projector pair. The presented data are of pose 8 specified in Table 3. The reduced ROIs algorithm is turned on.

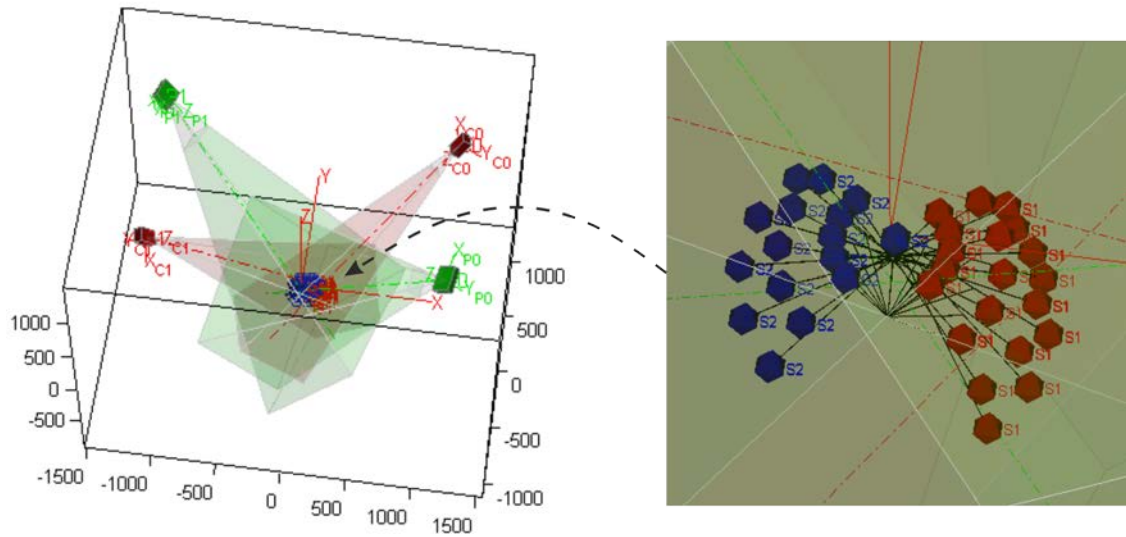


Figure 30: Distribution of spheres in measurement volume, determined by the procedure described in Section 3.3.

Chapter 4

Shape and deformation measurement with single camera and single projector

4.1 Overview

Among the optical methods available to measure shape and deformation of 3D surfaces, fringe projection and digital image correlation are two well-established techniques that have been widely used in industry. Fringe projection is recognised for its high accuracy and spatial resolution in measuring shape and out-of-plane displacement fields [3], but it cannot identify in-plane displacements on smooth surfaces. On the other hand, 2D DIC is a proven technique for accurately measuring in-plane deformation, which has later been extended to 3D DIC for 3D deformation measurements [61]. However, the performance of 3D DIC in surface profiling is inferior to that of the fringe projection technique due to the lower spatial resolution associated with a finite correlation window size. Many applications require fast, accurate and concurrent measurements of both surface profile and deformation for manufacturing quality control and structural testing purposes. Therefore, it is desirable to combine the strengths of the fringe projection and DIC techniques on one measurement system.

The literature contains a small number of papers that describe combinations of fringe projection and DIC techniques. Weber et al [88] presented a method using two projectors and two cameras equipped with colour filters to separately capture fringe patterns and speckle patterns that are simultaneously present on the object surface. The fringe projection technique is then applied to estimate surface profile and out-of-plane displacements, and 2D DIC is used to determine in-plane displacements. References [89] and [90] describe a simpler system using one camera and one projector, in which the fringe pattern is isolated from the speckle pattern during the computation stage using a Fourier transform. In reference [91], sinusoidal fringes and a speckle pattern are captured in two temporally discrete steps and processed in a similar way to the above-mentioned methods. In each of these papers, the authors have described the system performance on continuous surfaces.

One of the main challenges to the DIC techniques is the presence of displacement and geometrical discontinuities across which standard correlation techniques fail to give accurate estimates of image displacements. Several improved DIC techniques have been developed to retrieve the discontinuous displacement field along a crack. Jin and Bruck [92] proposed a point-wise correlation method in which the image displacement at each pixel within a subset is determined independently. Réthoré et al [93] presented an extended DIC approach that includes a model of the crack in the displacement function. Neither method requires the crack's position to be known prior to the optimisation of the correlation score, but they suffer from expensive computational effort due to the large number of unknowns in the modelled displacement function. More recently, Sjödaahl [94] exploited the property of the Hessian term of the correlation score to predict the position of the displacement discontinuity and then remesh the subset grid accordingly. Poissant et al [95] proposed a two-stage approach using a standard DIC calculation first to predict the discontinuity as a line connecting pixels of low correlation scores. This line effectively splits the subset of interest into two continuous regions, whose position can be iteratively refined. All of these techniques work out the discontinuities solely from the intensity images.

In this work, a one-camera one-projector system based on projected fringes and temporal phase unwrapping techniques is used to measure the shapes of surfaces with complex discontinuities. The geometrical discontinuities are detected from the measured point-cloud in the object space rather than the image space, which then allows the 3D displacement field to be estimated correctly around the discontinuities. In order to achieve this, the conventional image correlation technique is modified to cope with discontinuities. The accuracy of the new approach has been validated with an experiment on a geometrically discontinuous specimen undergoing rigid-body deformation.

4.2 Measurement and segmentation of 3D point cloud

4.2.1 Point cloud measurement by SMS

A fringe projection system consisting of one camera and one projector was used to estimate the surface profile. A pattern consisting of t sinusoidal intensity fringes was projected onto the surface to be measured. The shape information of the surface was therefore encoded as phase variations of the fringe patterns observed by the camera. A

four-step phase-shifting algorithm was used to estimate the phase values from the intensity images of the captured fringe patterns. To eliminate ambiguities caused by the discontinuous geometry and to optimise the phase estimation accuracy, the temporal phase unwrapping technique [21] was used to obtain an unambiguous phase value for each pixel, which requires the fringe density t to change over time. For the results presented in this section, a ‘reverse exponential’ sequence of fringe patterns [96] was used, in which the fringe density decreases exponentially from the maximum of $s=32$ fringes across the field of view (i.e. using the values $t=s, s-1, s-2, s-4, s-8, s-16$). A great advantage of using the temporal phase unwrapping method is that each pixel is analysed independently of its neighbours, allowing surfaces with complex discontinuities to be measured as easily as smooth ones. In addition, the use of both horizontal and vertical fringe patterns [81] has been adopted to improve the accuracy of the point cloud estimation.

Figure 31 shows the shape measurement process of a geometrically-discontinuous sample which is a flat glass panel to which is attached a smaller glass step. Horizontal and vertical fringes projected onto the sample can be seen to change in phase suddenly across the discontinuities (i.e. the edges of the step). The results of such a measurement are ultimately a cloud of points on the sample’s surface of which X -, Y - and Z -coordinate are determined explicitly in a world coordinate system. Figure 32 shows the 2D and 3D presentations of the point cloud. Each point in the cloud corresponds to a pixel on the camera’s image. The step can be seen to be separate from the rest of the point cloud.

Together with the final results of X , Y and Z coordinates, the intermediate results of the phase estimation process are also stored and used to quantify the measurement confidence at every pixel. These results include:

- Phase error, σ_x and σ_y : a measure of the deviation of the phase from the expected linear relation with t as it is unwrapped along the time axis, for the vertical and horizontal fringes, respectively. Phase error arises from systematic error sources such as mis-calibration of the camera or mis-synchronisation of the electronic devices, or due to contributions from multiply scattered light. By

setting a threshold σ_0 for the phase errors, a mask of low phase error can be determined for each pixel (m,n) as

$$\begin{aligned} M_{\sigma,j}(m,n) &= 1, \text{ if } \sigma_j(m,n) < \sigma_o \\ M_{\sigma,j}(m,n) &= 0, \text{ if } \sigma_j(m,n) \geq \sigma_o \end{aligned} \quad (3.1)$$

where the subscript j refers to the x or y component.

- Intensity modulation, μ_x and μ_y : the modulation magnitude of the vertical and horizontal fringes, respectively, as captured on the images. Dark texture on the surface and low light received from the projector are the main causes of a low modulation. A mask of high phase modulation can be defined for each pixel (m,n) as

$$\begin{aligned} M_{\mu,j}(m,n) &= 1, \text{ if } \mu_j(m,n) \geq \mu_o \\ M_{\mu,j}(m,n) &= 0, \text{ if } \mu_j(m,n) < \mu_o \end{aligned} \quad (3.2)$$

where μ_0 is the modulation threshold value, and the subscript j refers to the x or y component.

In addition, the measurement volume of a calibrated system, in which the object is placed, has a known depth and is set at a known distance from the system. Therefore, uninteresting features (e.g. walls and doors in the background) can be masked out by setting a limit on the Z -coordinates. Thus, a depth mask is defined for each pixel (m,n) as

$$\begin{aligned} M_Z(m,n) &= 1, \text{ if } Z_{\min} \leq Z \leq Z_{\max} \\ M_Z(m,n) &= 0, \text{ otherwise} \end{aligned} \quad (3.3)$$

where the constants Z_{\min} and Z_{\max} specify the nearest and furthest planes of the calibrated measurement volume.

Combining all of the above-mentioned masks results in a total mask M_V containing only valid pixels with high confidence, which is defined as

$$M_V = M_{\sigma,x} \circ M_{\sigma,y} \circ M_{\mu,x} \circ M_{\mu,y} \circ M_Z \quad (3.4)$$

where the operator \circ denotes the element-wise multiplication. An example of the mask M_V is illustrated in Figure 32-b, where the masked-out areas labelled in white colour correspond to the background and the shadow of the step.

4.2.2 Discontinuity detection

Once the 3D shape is obtained, it is straightforward to detect discontinuities and then segment discrete continuous regions of the surface ready for application of the modified DIC algorithm. Using a flood-fill strategy to detect the region's edges, every valid pixel is compared to a neighbouring pixel along each image axis (i.e., the i -axis and j -axis). Thus, a pixel can be identified as adjacent to a discontinuity if it satisfies one of the first two plus the third of the following conditions,

$$|\mathbf{r}_{i,j} - \mathbf{r}_{i-1,j}| \geq \rho_i, \quad (3.5)$$

$$|\mathbf{r}_{i,j} - \mathbf{r}_{i,j-1}| \geq \rho_j, \quad (3.6)$$

$$M_V(i, j) = 1, \quad (3.7)$$

where i and j are respectively the horizontal and vertical image indices of the pixel; $\mathbf{r}_{i,j}$ denotes the 3D coordinate corresponding to a pixel (i,j) ; the constants ρ_i and ρ_j are the thresholds of geometric distance between two neighbouring pixels in the horizontal and vertical directions, respectively; and M_V is the logical mask defined in Equation (3.4) and specifying whether or not a pixel contains a valid 3D coordinate.

The previous flood-fill strategy using geometric distance has an advantage of being easy to implement; but it is highly sensitive to noise and particularly inaccurate for sharp edges where geometric distances of neighbouring points may be smaller than the threshold. Alternatively, a more generic criterion based on the surface gradient is implemented for better robustness; and Equations (3.5) and (3.6) are replaced by

$$|\delta \mathbf{r}_{m,n} / \delta i| \geq \lambda_i \quad (3.8)$$

$$|\delta \mathbf{r}_{m,n} / \delta j| \geq \lambda_j \quad (3.9)$$

where λ_i and λ_j are the thresholds for surface gradient magnitude computed along the i - and j -axis respectively. To suppress the local data noise, the gradient terms are computed from the X , Y and Z coordinates of a number of $2p$ points surrounding the point of interest (m,n) with $p \geq 2$, instead of only one neighbouring point as in Equations (3.5) and (3.6). Each gradient component, for example $\delta X / \delta i$, is computed as the slope of a line that best fits those $2p+1$ points in a least-squares sense. A least-squares fitting procedure based on that of Press et al [63] is adopted and modified so that only valid data points are fitted (i.e., Equation (3.7) is incorporated). Figure 33 demonstrates the least-squares fitting process through several points with the data size of $p=2$. The gradient is low at point A which is far away from any discontinuity, but suddenly increases at point B which lies on a very sharp edge. The fact that the least-squares fitting is linear allows the gradient computation to be implemented efficiently using linear matrix manipulations.

Figure 34 shows an example result of the discontinuity detection applied for the point cloud presented in Figure 32. The jumps in gradient magnitudes can be seen clearly around the edges of the step, showing the positions of the discontinuity detected by using Equations (3.8) and (3.9). It is noted that pixels that have been masked out in the confidence mask M_V (by Equation (3.4)) are considered to be lying on a discontinuity, and are not incorporated in subsequent image processing stages. All pixels with high measurement confidence and not lying on a discontinuity are labelled in the mask D .

4.2.3 Segmentation of continuous regions

Discontinuities identified in the previous stage may define closed boundaries between continuous surface regions that can then be segmented and labelled using standard image processing techniques, such as the two-pass connected region labelling presented in [97–99]. The idea of this technique is to scan through every valid pixel (i.e., masked-out pixels are considered as background), check if it is connected to any of the 8 neighbouring pixels, and assign a region label accordingly. The segmentation result is achieved in the form of an image whose values are the label of continuous regions, as shown in Figure 34-d. The label of a region is assigned in the order of its area and centroid position, so that any labelled region can be identified and retrieved quickly across different deformation stages. Furthermore, regions with insufficient area can be

considered as outliers and removed by setting their label values to zero (i.e. background).

4.3 Digital image correlation of discontinuous sub-images

4.3.1 Discontinuity problem of conventional DIC

The 2D DIC technique is used here to estimate the displacement vectors of sub-images within the region of interest during the deformation process. A small region of a reference image (called the reference sub-image) is matched against a region of a deformed image (called the deformed sub-image). In practice, the specimen surface is prepared with a high-contrast random speckle pattern to aid the matching algorithm. A successful match of two sub-images is obtained when their cross-correlation score meets some predefined criterion.

In conventional DIC techniques [61], the average relative displacement of the matched sub-images is assumed to be the displacement of the pixel at the centre of the reference sub-image. As a consequence, all pixels within the sub-images are assumed to lie on the same continuous region. However, this assumption may be invalid for a sub-image that intersects multiple continuous regions as each region may undergo a different deformation that is generally not the same as that of the other regions in the sub-image.

Figure 35-a illustrates this point with a simulated sub-image that has the lower and upper halves undergoing different horizontal displacements u_1 and u_2 with respect to the corresponding regions in the reference sub-image. When applied to this type of sub-image, the conventional DIC technique results in a correlation field with two ambiguous peaks, as seen in Figure 35-b, which interact with each other and cause the average computed displacement u^* of the sub-image to be erroneous. The speckle patterns shown in Figure 35 were generated using the algorithm described in Ref. [100], which simulates the formation of laser speckle patterns with the correct first and second speckle statistics.

4.3.2 Improved image correlation algorithm

In this work, the image correlation algorithm has been modified so that the correlation score is computed for each of the labelled regions independently. Therefore, provided that the object deformation is not too large, the correlation field is always assured to

have a single strong peak that gives an accurate estimate of image displacement of each continuous region (see Figure 35-c and -d). The cross-correlation score of a displacement candidate (u, v) for region R_k of a reference and deformed sub-image can be computed by

$$C(u, v, k) = \sum_{i, j \in R_k} I_1(i, j, k) I_2(i + u, j + v, k), \quad (3.10)$$

where I_1 and I_2 are respectively the reference and deformed sub-images whose DC terms have been removed, and (i, j) specifies a pixel indices within R_k . To improve the computational efficiency, Equation (3.10) is done in the frequency domain by using

$$C(u, v, k) = \mathfrak{F}^{-1} \left\{ \mathfrak{F}(I_1')^* \mathfrak{F}(I_2') \right\} \quad (3.11)$$

with

$$\mathfrak{F}(I_1') = \sum_{m=0}^{N-1} \sum_{n=0}^{N-1} I_1'(m, n, k) \exp[-2\pi i \tilde{i}(um + vn) / N_w], \text{ and} \quad (3.12)$$

$$\mathfrak{F}(I_2') = \sum_{m=0}^{N-1} \sum_{n=0}^{N-1} I_2'(m, n, k) \exp[-2\pi i \tilde{i}(um + vn) / N_w], \quad (3.13)$$

where \mathfrak{F} and \mathfrak{F}^{-1} are the forward and inverse 2D Fourier transform operators, respectively; the asterisk indicates complex conjugate; I_1' and I_2' are respectively the sub-images I_1 and I_2 padded with zeros around their edges to avoid aliasing errors; m and n are the indices of the sub-image pixels, $\{m, n\} = 0, 1, 2, \dots, N_w-1$; N_w is the size of the reference sub-image; and $\tilde{i}^2 = -1$. To deal with irregular (i.e. non-rectangular) shape of the sub-images, zero padding is used, in which pixels that belong to other regions and the background are set to zero in I_1' and I_2' so that they do not contribute to the correlation score.

An optimised correlation procedure based on that described in reference [101] is used to compute the image displacement (u, v) with a sub-pixel accuracy that can be as small as one-hundredth of a pixel. The objective is to find the displacements u and v so that

$$\frac{\partial}{\partial u} |C(u, v, k)|^2 = 0, \quad (3.14)$$

$$\frac{\partial}{\partial v} |C(u, v, k)|^2 = 0. \quad (3.15)$$

The 2D discrete Fourier transform applied to the two sub-images in Equation (3.11) can be transformed into a 1D discrete function by rows and then by columns if v is considered as a constant, or by columns and then by rows if u is considered as a constant. By exploiting this property, the two-variable differential equations (3.14) and (3.15) can be reduced to a one-variable problem.

For each reference sample point located at (i, j) , the optimisation procedure consists of two steps: (i) finding approximate estimates of $u = u_0$ and $v = v_0$, where u_0 and v_0 are both integers, by correlating the sub-images $I_1'(i, j, k)$ and $I_2'(i, j, k)$, and (ii) refining u and v by correlating the sub-images $I_1'(i, j, k)$ and $I_2'(i + u_0, j + v_0, k)$. The reason for the second step is that it removes many of the speckles around the edge of the sub-image that are not common to both sub-images, thereby improving the signal to noise ratio of the correlation peak. In the first step, v is initially treated as a constant, and the displacement u can be found as the solution of

$$\frac{\partial}{\partial u} |C(u, k)|^2 = 0 \quad (3.16)$$

A gradient-based Newton-Raphson algorithm is used to search for the minimum of this function and the associated solution of $u = u_0$. Similarly, as u is assigned to the constant value of u_0 , the displacement v is the solution v_0 of

$$\frac{\partial}{\partial v} |C(v, k)|^2 = 0 \quad (3.17)$$

In the second step, the estimated displacements (u_0, v_0) are used to determine a “better” location of the objective sub-images which gives the LHS terms of Equations (3.16) and (3.17) smaller minimum values. The procedure in the first step is repeated and final solution of displacements (u, v) can be found with sub-pixel accuracy of down to 0.01 pixel.

The current implementation assumes that a sub-image undergoes only rigid-body translation. However, it is possible to introduce higher-order terms, such as extension and shear, into the deformation model of the sub-image as described in Equation (1.2), following the algorithm presented in [61].

4.3.3 Simulation

Simulated images have been used to validate the accuracy of the correlation method described above. Using simulated images helps to avoid the influence of the image-acquisition and phase-measurement errors, and thus quantifies the accuracy of the improved image correlation module itself. A pattern of speckles with random size, distribution and intensity was generated by using the method reported in [100] in which light backscattering on a surface with uniformly-distributed roughness creates varying speckle intensity.

A square and regular grid of pixels to store final intensity values is generated so that the origin of the image coordinate system Oxy is located at its centre, i.e., $\{x, y\} = -(N-1), \dots, -1, 0, 1, \dots, (N-1)$ and $(2N-1)$ is the size of the grid. A complex function describing the light amplitude is given by

$$A_1(x, y) = \begin{cases} \exp(i4\pi\sigma_z R_{\mu,\sigma}(x, y) / \lambda) & \text{if } \sqrt{x^2 + y^2} \leq r_0 \\ 0 & \text{otherwise} \end{cases} \quad (3.18)$$

where r_0 is the size of the illuminated area; λ is the light wavelength; σ_z is the standard deviation of the surface roughness; and $R_{\mu,\sigma}$ is a function returning a random number from a Gaussian distribution with a mean μ of 0 and a standard deviation σ of unity. The speckle pattern I_1 is the modulus squared of this amplitude distribution,

$$I_1 = \left| \mathfrak{T}^{-1}(W \cdot \mathfrak{T}(A_1)) \right|^2 \quad (3.19)$$

where W is a window function.

To introduce an image displacement (u, v) to the speckle pattern, the reference image is shifted using the Fourier shift theorem, and the deformed image can be obtained as

$$I_2 = \left| \mathfrak{T}^{-1}(W \cdot S \cdot \mathfrak{T}(A_1)) \right|^2. \quad (3.20)$$

with $S = \exp[-i2\pi(ux + vy) / N]$.

An example of two simulated speckle images generated by this method is given in Figure 36. The parameters to control the speckle pattern characteristics are image size $N = 256$ pixels, surface roughness $\sigma_z = 20 \mu m$, wavelength $\lambda = 0.532 \mu m$ and illuminated area size $r_0 = N / 16$. The deformation is a translation in the x -direction by $u = 39.25$ pixels and in the y -direction by $v = 14.19$ pixels. Besides being diverse in shape and size, the resulting speckles have a broad intensity range varying from 0 (black) near the edge to 255 (white) towards the centre.

Figure 37 shows the results of horizontal image displacements estimated for the example sub-image given in Figure 35-a. The horizontal displacement u_1 and u_2 of each half of the sub-image is varied by increments of 0.2 pixels and 0.4 pixels, respectively. It can be seen that the displacements computed by the new method are accurate to ~ 0.05 pixel.

4.4 Measurement of 3D displacement field

4.4.1 Measurement procedure

Figure 38 shows the proposed new procedure to calculate 3D displacements from the measured point clouds and image displacements. Whilst in the reference state, the object surface is measured with the shape measurement system using projected fringes as described in Section 4.2.1, generating a dense cloud of 3D points corresponding to the scattering points imaged onto individual camera pixels. A white-light texture image of the speckle pattern on the object surface is also captured by the camera. From the measured point cloud, discontinuities are detected and continuous regions are segmented. At each subsequent loading state, the deformed 3D point cloud and texture image are also obtained in the same way.

A region of interest is selected in the reference image, in which a grid of reference sample points is populated. Using the correlation technique described in Section 4.3, sub-images centred at those 2D sample points are matched with corresponding 2D sub-image centre points in the deformed texture image.

The 3D coordinates of each of the reference image sample points can be extracted easily from the reference 3D point cloud as they correspond to integer pixels in the reference image. Image coordinates of a deformed sample point are generally non-integers, and hence it is necessary to interpolate 3D coordinates from the neighbouring pixel sites. The results presented in this thesis were obtained using a bicubic interpolation. The systematic error induced by the interpolation process is not usually significant, since the geometric distances between the interpolation points are small due to the high density of the point cloud. Finally, the 3D displacements are computed by direct subtraction of the 3D coordinates of the deformed and reference sample points.

4.4.2 Interpolation for pixel-resolution displacement field

To reduce computation time, the 3D displacements obtained by the procedure above are estimated on a grid of sample points whose spacing is related to the correlation window size. A typical mesh grid of sample points, as shown in Figure 39, is initially seeded at a spacing of 8×8 pixels for a window size of 16×16 pixels, automatically labelled according to the surface regions on which they lie, and redistributed to adapt to the geometrical discontinuities. Based on this labelling and the availability of 3D coordinates for every single pixel, the displacement field can be interpolated with high confidence for all pixels even near the discontinuities, e.g. for the purpose of full-field visualisation or for improving the accuracy of subsequent strain calculation.

Let us consider a pixel (i_0, j_0) , lying within region R_k as illustrated in Figure 40, whose displacement component d needs to be interpolated from known displacement values of the sample points (i, j) . This can be done by fitting a parametric surface $P(i, j)$ going through sample points closest to the pixel. Mathematically, the problem involves finding a parameter set of the surface that minimises the displacement difference from the sample points, which is defined as

$$\sum_{i, j \in R_k} w_{i_0, j_0} \left[d_{i, j} - P(i_0, j_0) \right]^2, \quad (3.21)$$

where $d_{i, j}$ is the displacement value at sample point (i, j) and w_{i_0, j_0} is the weight factor based on both image and 3D distances of the pixel to the sample points. To simplify the optimisation problem to a linear least-square fitting, the surface $P(i, j)$ is chosen to be a plane and only three sample points closest to the pixel are included in Equation (3.21).

4.5 Implementation of the combined SMS-DIC technique

4.5.1 Hardware

The shape measurement systems presented in this thesis have gone through over ten years of development from laboratory prototypes to commercialised products. Figure 41 presents four main versions of a single-camera single-projector system.

- The first prototype developed by Coggrave [17] consisted of a Proxima DP4200 digital mirror device projector and an EEV CAM17 camera fitted with a Nikon standard 35 mm lens with a focal length of 50 mm. The projector had a resolution of 800×600 pixels and a frame-updating speed of 60 fps, and the camera had a CCD sensor of 512×512 pixels and an 8-bit digital image output. The sensors were mounted on a steel support rig that was suitable for laboratory optical table. The measurement accuracy of 1/4,000 of the measurement volume size had been achieved with this system.
- The second prototype also developed by Coggrave and used in the PhD research of Ogundana [18] had a more compact and modular design. The digital light processing (DLP) Vision Plus V-1100Z projector had a resolution of 1024×768 pixels, and the 8-bit Vosskuhler CCD-1300QFB had a resolution of 1024×1024 pixels. The system was supported by a frame of aluminium profiles that can be assembled and disassembled accordingly to required measurement space. A measurement accuracy of 1/5,000 of the measurement volume size was reported.
- The third prototype named SMS1200 developed at Phase Vision Ltd based on the equipment available for the second prototype was used for the experiments presented in this thesis. One significant improvement was the introduction of the carbon-fibre casing for the sensors, which not only provides better protection, but also minimises the effect of thermal expansion due to the heat induced by the operating devices. More details of this version are provided in the following paragraphs.
- The latest commercial SMS scanners have been designed and manufactured with industrial standards. Several high-quality high-power projectors and compact cameras with resolution of up to 8 Mpixels have been introduced. The server

computer has also been embedded inside the carbon-fibre casing, and can be controlled remotely by another client computer via LAN network. An accuracy of 1/20,000 of the measurement volume diagonal has been reached. This system was used for the on-site experiments at Airbus UK which is presented in Chapter 6 of this thesis where a more detailed description can be found.

As shown in Figure 42, a SMS1200 system consists of three main components: (i) a SMS1200 scanner, (ii) a control box, and (iii) peripherals such as LCD monitor, keyboard and mouse. The scanner has the camera-projector separation of 1,200 mm and weighs less than 15 kg. The casing is made of carbon-fibre-reinforced plastic (CFRP) composite, of which the lay-up was designed so that thermal expansion is kept to minimum and thus does not affect the previously-calibrated camera-projector separation. The sensor can be mounted on two tripods for convenient deployment in industrial environments, or on an aluminium frame such as the one shown in the photo background.

A diagram of hardware connections for the SMS1200 scanner is given in Figure 43. The scanner consists of a Vision Plus V-1100Z projector and a Vosskuhler CCD-1300QFB camera. The projector and the camera are connected to the control box respectively via a digital visual interface (DVI) cable and a CameraLinkTM cable that are highly insensitive to noise. The control box consists of a home-built personal computer equipped with the self-developed measurement software, a 128MB ATI Radeon video graphic card to generate sinusoidal fringe patterns, a dual-base Matrox Solios XCL frame grabber to capture the fringe pattern images, a video splitter to distribute the generated fringe patterns to the projector and the monitor, and a trigger controller to synchronise the camera and the projector. The process of projecting a fringe pattern sequence on an object and receiving their reflected images are explained as follows.

- A fringe pattern with sinusoidal intensity profile is generated by the computer and transferred to the graphic card as a digital image.
- The fringe image is then transmitted via a DVI cable to the video splitter which divides the signal for the projector to illuminate the object surface and for the monitor. The video splitter can provide up to 8 output signals, enabling the use of multiple projectors. As the video splitter is also connected to a COM port of the

computer by a serial RS232 cable, the software knows when the fringe pattern is projected.

- Whilst the projector is illuminating the object, the software sends an instruction via an RS232 cable to the trigger controller stating when to trigger the camera acquisition. The fringe image captured by the camera is transmitted via the CameraLink™ cable to an input port of the trigger controller. Then, the synchronised image is transmitted to the frame grabber via another CameraLink™ cable ready for image processing.

4.5.2 Extensible markup language (XML) for input data file

As a common programming practice, an input data file storing information of the hardware and software parameters needs to be kept separately from the software code and the measurement output files. This is to facilitate the effective management of large measurement datasets and the convenience of repeating measurements when needed. The very large number of input parameters controlling the SMS' image acquisition and image processing processes raises a problem of how to store and retrieve these parameters efficiently. Furthermore, if the input file of a measurement is reused for a different application using different hardware devices, it is essential that the documentation rule (or language) of the file must be consistent and expandable. For the present Phase Vision SMS system, the XML format is used for digital representation of the input document. Several important output parameters are also archived in the XML file.

An XML document is a well-formed text file that is both human-readable and computer-readable [102]. It is a hierarchical structure of components, called “elements”, each containing either a parameter value or a logically-lower element (called “child element”). Every element has an attribute that defines the type of value it is storing. An XML file for making measurement should have a structure as follows:

<code><sms></code>	(root element)
<code><hardware> </hardware></code>	(element: device information)
<code><acquisition> </acquisition></code>	(element: fringe size, sequence, etc.)
<code><phase_analysis> </phase_analysis></code>	(element: phase-shift steps, etc.)
<code><filename> </filename></code>	(element: saving folders, etc.)
<code><calibration></calibration></code>	(element: sensor parameters)


```

<dic>
    <correlation_size>8</correlation_size>
    <score_threshold>0.9</score_threshold>
</dic>
</sms>

```

(**element:** correlation parameters)
 (child element: window size)
 (child element: minimum score)

A third-party XML processor developed in Java by JDOM.org [103] is used to parse the text-based XML document into computer-readable format. This parser provides a wide range of commands to read, write and transmit XML elements, and can be invoked by both the C++ and MATLAB languages used in this work.

4.5.3 Software structure

Software to control the hardware components and execute the measurement procedure described in the previous sections can directly affect the system performance and the implementation efficiency. The image acquisition process needs low-level and real-time communication between the software and the hardware, and the phase measurement requires efficient management of a large number of fringe images. Therefore, the C/C++ programming language was used by the engineers at Phase Vision Ltd to develop the computationally-intensive shape measurement module. The deformation measurement module developed by the author of this thesis, on the other hand, can be designed so that only a few images are needed for processing at the same time and the memory overflow problem can be avoided. In practice, on-line (or real-time) measurements of structural deformation are not normally essential, and relatively lower computational speed may be acceptable. For those reasons, MATLAB was chosen as the main programming language for the deformation measurement module, with additional considerations of its readily-available matrix manipulation and representation capabilities. Post-processing of a digitalised 3D point cloud and its associated data (e.g. 3D displacement fields) can be done easily with available commercial software like Polyworks [104], Geomagic [105] and Tecplot [106], or even with a free open-source software like Meshlab [107]. Thus, using these third-party packages for general-purpose post-processing can be more cost-effective in terms of both time and money than developing an in-house counterpart. The overall architecture of the software modules and their data flow are illustrated in Figure 44, with detailed descriptions given in the following paragraphs.

In the C/C++ shape measurement module, the XML input file is first parsed for controlling parameters, such as the phase shifting and phase unwrapping parameters, and then passed into the image acquisition function. A four-step phase shifting is used along with a “reverse exponential” phase unwrapping in which the fringe density decreases exponentially from the maximum of $s=32$ fringes across the field of view (i.e. using the sequence of 32, 31, 30, 28, 24 and then 16 fringes per pattern). Thus, a total of $4 \times 6 = 24$ vertical fringe patterns are projected onto the object surface, followed by another 24 horizontal fringe patterns. At the same time, those fringe images are recorded by the camera, saved on the computer hard-disk and inputted to the phase estimation function. One further image called a white-light texture image is also stored, increasing the total number of images to 49. The phase estimation function then returns three maps (i.e. 2D matrices of the same size as the acquired images) of the resulting phase, phase error and intensity modulation, for each horizontal and vertical projected fringe orientation. Finally, the point-cloud calculation function uses a triangulation algorithm to obtain a 3D point cloud from the previous two phase maps and the calibration parameters available in the XML input file. The point cloud is saved on the hard-disk as three matrices corresponding to the X, Y and Z coordinate components. For efficient file management and house-keeping, all of the necessary output files (i.e. texture image, phase maps, phase errors, phase modulations and point cloud data) are saved in one time-stamped folder named with the date and time that the measurement is taken.

For deformation measurement, the afore-mentioned shape measurement module is repeatedly applied for every deformation state of the object. At the end of the on-line measurement procedure, the content of the XML file is updated with the paths to all of the measurement result folders, and continues to be passed on to the deformation measurement module executed off-line in the MATLAB environment. In the first stage of the deformation image processing, the user is asked to select a region of interest on the texture image of the reference state. Sample points are then automatically seeded on a regular grid with the spacing declared in the XML input file (but adjustable by the user if wanted). This is the only stage where user input is requested (although not essential), the rest being fully automatic. Based on the point cloud data, the phase errors and the phase modulations for the reference state, the point-cloud segmentation function returns a label map that identifies all continuous regions of the reference object surface.

In the same way, measurement result data for the first deformed state are loaded, and another label map is calculated. Then, the two texture images and two label maps are passed to the image correlation function to obtain matched points on the deformed texture image of the sample points specified on the reference image. Within this function, reference sample points that do not have a match are removed from the sample grid, and those that lie near a discontinuity are adjusted so that the grid becomes denser. (Such a refined grid is presented in Figure 39.) Next, the X , Y and Z coordinate of the sample points are extracted from the measured point clouds for both the reference and the deformed state; and the displacement components d_x , d_y and d_z are obtained at those sample points. The interpolation function is applied to achieve a full 3D displacement field at all pixels within the specified region of interest. Finally, the resulting 3D displacement field can be saved either in the image format as with the 3D point cloud or in a structured text file. The procedure is repeated for the subsequent deformed states, and the whole deformation sequence is obtained.

Visualisation of a measured 3D displacement field can be done either on the 2D texture image within the MATLAB environment or using 3D visualisation software such as Tecplot 360 [106]. Therefore, the final shape and deformation measurement results must be saved in a Tecplot-compatible file format. For more sophisticated 3D point cloud inspections, such as extracting surface features and aligning a point cloud with a CAD model, 3D processing software like Polyworks, Geomagic (available at Phase Vision Ltd) or Meshlab (freely available online) can be utilised. Descriptions of how to generate a neutral-format STL or OBJ file can be found in the PhD thesis of Ogundana [18]. Also, a function to generate a Polyworks-format PIF file was implemented by the Phase Vision engineers in the shape measurement module following the reference guide [108].

4.5.4 Output file for 3D visualisation with Tecplot

Tecplot is a visualisation and post-processing software for complex numerical data sets. The software is popular for analyses of computational fluid dynamics (CFD), finite element analysis (FEA) and reservoir simulation. Its main features include display of measured field data, generation of a wide range of engineering plots and mathematical data analysis. As shape and deformation measurement results of the SMS-DIC

technique are in complex forms like FEA data, Tecplot is ideal for both deformation field visualisation and error analysis purposes.

Like many numerical analysis software, Tecplot requires a data set to be tessellated into facets and vertices (or elements and nodes). As illustrated in Figure 45, an element is defined by a connectivity of its surrounding nodes. The connectivity numbering adheres to the “right-hand rule” and is in counter-clockwise order, for consistent definition of the element orientation. A node is specified by its coordinates and associated data. There are two types of Tecplot input data file: a binary file which is readable by both human and the software, and an ASCII file which is only readable by the software. Due to its compressed size, a binary file can be loaded much faster than an ASCII file especially for a very large data set [109]. A typical ASCII file has a structure as below.

```
#File header
TITLE = "Point cloud & displacement field - load case n"
VARIABLES = "X" "Y" "Z" "dX" "dY" "dZ"
ZONE NODES=NumberOfNodes , ELEMENTS=NumberOfElements ,
DATAPACKING=PackingType , ZONETYPE=ZoneType

#Nodes declaration
ValueOfX ValueOfY ValueOfZ ValueOfdX ValueOfdY ValueOfdZ (1st node)
...
ValueOfX ValueOfY ValueOfZ ValueOfdX ValueOfdY ValueOfdZ (Last node)

#Elements declaration
ConnectedNodes (1st element)
...
ConnectedNodes (Last element)
```

The first section of the file is the file header declaring data set title, variable names and node-element structure parameters. The arrangement of an ASCII file depends on the data packing type *PackingType*, which can be either BLOCK or POINT. In BLOCK data packing the data is arranged by variable, whilst in POINT packing the data is arranged by node. The *ZoneType* parameter defines the number of nodes of an element. In this work, triangular finite elements are generated by using an optimised Delaunay

triangulation algorithm based on the one presented in [110]; therefore, the parameter is chosen to be FETRIANGLE.

In the second section of node declaration, each row contains the values of the above-stated variables in a correct order. The variables here are the X , Y and Z coordinates, together with the measured displacement components d_X , d_Y and d_Z . The node number is implicitly indicated by the row number. In the last section, the node-connectivity of an element is declared in a single row and in the incremental numbering order as for the node declaration.

Although Tecplot input files are implemented in the ASCII format in this work, it can be converted into the binary format once imported to Tecplot. The converted binary files are then saved for reuse, and subsequent loading time can be greatly reduced.

4.6 Experimental validation

4.6.1 Apparatus and procedure

An experiment on a discontinuous surface undergoing rigid-body translation was conducted to validate the combined SMS-DIC technique. The experimental arrangement is depicted in Figure 46. The specimen is a planar specimen that is made of plastic and contains a hole and a step to mimic geometrical discontinuities. The SMS1200 equipped with one camera and one projector was used in this experiment. The camera has an image resolution of 1024×1024 pixels, and was calibrated so that it covers a field of view of approximately $700 \times 700 \text{ mm}^2$ (i.e. about the same size as the specimen). The specimen was placed in the centre of the measurement volume at about 2.7 m from the scanner. By definition, this central position is also the origin of the global coordinate system OXYZ. The coordinate system was set so that the Z -axis pointed towards the scanner, the X -axis pointed to the right and the Y -axis pointed upwards. To avoid over-saturated hotspots caused on the camera image by strong specular components of reflected projector light, the specimen was tilted slightly by an angle of about 10° from the XY -plane.

The specimen was supported by a frame assembled from aluminium profiles, as shown in Figure 47. The whole frame was secured to the moving base of an Aerotech ATS 15030 linear translation stage by four M10 bolts. The stationary base of the translation

stage was attached to a steel table by three powerful magnetic locks. The damping pillars of the table helped suppress vibrations from the floor. The moving base of the translation stage was driven by a 0.2 inch pitch leading screw powered by a stepper motor. The stepper motor ensured a stationary position of the specimen for measurement. The translation resolution of the stage was 1/10,000 inch (or 2.5 μm) with a repeatability of 1/2,500 inch (or 10 μm) and a maximum driving range of 12 inches (or 300 mm).

In this experiment, the specimen was translated mostly in its plane and in the X -direction by a series of 18 displacements varying from 0 mm to 1.016 mm with a small increment of 0.127 mm and then from 1.016 mm to 10.160 mm with a larger increment of 1.016 mm. At each increment of the translation stage, the shape measurement module was used to capture a speckle image and measure a 3D point cloud of the specimen. To reduce operation time and workload for the operator, a piece of code written in MATLAB was executed to automatically trigger the shape measurement at the end of every increment.

To assist the image correlation of the deformation measurement module, a speckle pattern was randomly painted on the surface of the specimen before the experiment. Choosing the right speckle size and density is crucial to the accuracy of any image correlation technique. Several authors [111, 112] have tested a large number of real and simulated speckle patterns and suggested that an average speckle should have a diameter of 7-9 pixels in the image plane of the camera. The speckle size distribution is also related to the correlation window size which was suggested to contain at least 3 speckles in each direction. However, a larger window size may increase not only computation time but also matching uncertainty in the presence of sufficiently large local deformation. The process of preparing the speckle pattern followed a trial-and-error approach. First, tiny but dense speckles were sprayed on the specimen as a foundation layer, followed by larger and looser speckles. By checking the captured image against the previous two empirical criteria, it can be decided whether to increase the speckle size and/or the separation. If necessary, several values of window size must be tested, and the one giving highest correlation score without slowing down the computer performance too much can be chosen. For this particular experiment, the window size of 16×16 pixels seemed to be optimal.

4.6.2 Results and discussions

The result of measuring the shape at the reference state is shown in Figure 48. The texture image (i.e., an image captured with spatially uniform illumination from the projector) is shown in Figure 48-a, and the X -, Y - and Z -coordinates of nearly one million scattering points obtained by projecting the full fringe sequence are presented in Figure 48-b, -c and -d, respectively. Within the hole region, measured data correspond to the background instead of the specimen of interest, thus resulting 3D coordinates have been automatically masked out using a depth threshold. The shadow region to the left of the step is automatically detected and omitted from the generated surface model by the intensity modulation threshold. In addition, the dark regions that can be seen around the edges of the texture image have a very low fringe visibility and are also automatically removed from the final result. A mask of valid pixels lying within a region of interest is shown in Figure 49-a. Thus, the resulting 3D model of the specimen has been reconstructed with high confidence despite the presence of the surface discontinuities. The point cloud segmentation label map is given in Figure 49-b, showing two continuous regions: the planar base and the step. The point cloud has also been tessellated, exported as a neutral format OBJ file, and imported to Meshlab software for visualisation. Figure 50 presents the 3D model of the point cloud which consists of nearly 800,000 valid points and 1.5 million faces. The intensity values of the texture image have been assigned as the face grey levels, giving a full 3D “picture” of the specimen.

A 3D displacement field was estimated for each “true” displacement prescribed by the translation stage. Nearly 500 sample points were selected within a region of interest in the reference image (as shown in Figure 48-a). Using the segmentation label map in Figure 49-b, the sample points have been automatically labelled and redistributed to adapt with the discontinuities. Figure 51 shows image displacement fields u and v together with an estimated 3D displacement magnitude field that corresponds to the true displacement of 10.160 mm. The 3D displacement magnitude $|d|$ was computed at a sample point by

$$|d| = \sqrt{d_x^2 + d_y^2 + d_z^2}, \quad (3.22)$$

where d_x , d_y and d_z are respectively the X -, Y - and Z -components of the 3D displacement estimated at the sample point. For visualisation purposes, all displacement fields have been interpolated for each camera pixel from the low-resolution grid of displacement vectors, following the process presented in Section 4.4.2. It can be seen that all regions of the specimen have almost the same displacement magnitude (with a mean difference of about 0.05 mm), as expected for a specimen undergoing rigid-body displacement. By contrast, the 2D image plane displacement field u has two distinct regions due to different magnifications caused by the presence of the step: speckles on top of the step, which is closer to the camera and therefore recorded at a slightly higher magnification than those on the supporting plate, move further for the same sample displacement.

A standard 2D DIC algorithm was implemented without the continuity detection for comparison with the improved DIC algorithm presented in Section 4.3.2. The standard 2D DIC was applied to the same data set and with the same window size, and the resulting image displacement field u is shown in Figure 52. It can be seen that the result of the proposed technique has superior accuracy especially along the edges of the hole and the step. This can be explained by the fact that the 2D DIC technique does not have knowledge about the presence of the discontinuities and thus cannot avoid the peak splitting problem mentioned in Section 4.3.1. In addition, as opposed to the proposed technique which takes into account the 3D shape during the pixel-scale interpolation near the discontinuities, the 2D DIC code interpolates from sample points lying in completely different regions, resulting in erroneous displacement estimation around the hole for example. Therefore, it can be seen that the spatial resolution of the proposed technique can be as small as 1 pixel and it can measure the very sharp edges of the step in Figure 51-a. On the contrary, the standard 2D DIC results in the edges with the width of approximately 20 pixels as seen in Figure 52, thus giving a much lower spatial resolution.

To quantify the accuracy of 3D displacement field measurement at each deformation state, the mean and standard deviation of the estimated displacement magnitudes were computed. The differences of the mean displacement magnitude from the true displacement prescribed by the translation stage are shown in Figure 53, together with the standard deviations represented by the error bars. It can be seen that the estimated

3D displacements have a maximum error of about 0.1 mm (corresponding to about 1 part in 7,000 of the measurement volume side) and a maximum standard deviation of about 0.15 mm, for rigid-body displacements of up to 10.160 mm. There is an apparent periodic error in this plot which may be due to the DIC algorithm, since systematic errors can arise as the speckle displacement varies between integral- and non-integral-pixel image shifts. Other possible explanations are ripple on the measured shape data due to nonlinearities in the projector [20], or periodic errors in the pitch of the leadscrew of the translation stage. The measurement resolution (or precision) of the proposed technique can be related to the standard deviations represented by the error bars, which has the mean value of approximately 0.03 mm (corresponding to about 1 part in 24,000 of the measurement volume side). This measurement resolution is an inherent specification of the proposed system, which is generally affected by noise and, in this experiment, mostly by the low phase extraction accuracy from dark speckles.

4.7 Summary

The fringe projection and digital image correlation techniques can be combined on a one-camera one-projector system to accurately measure both profile and 3D deformation of surfaces with complex geometrical discontinuities. The key original contribution, which differentiates the proposed method from other optical deformation measurement methods, is the use of the fringe projection technique to identify geometrical discontinuities present in the 3D shape and inform the digital image correlation technique about their presence. The algorithm starts with segmentation of a measured point cloud for separate continuous regions. This knowledge is then used to improve the image correlation technique to avoid the existing peak-splitting problem of conventional 2D DIC techniques, thus avoiding erroneous image correlation across the discontinuities. Once accurately matched points are achieved on the image, their corresponding 3D coordinates are extracted from the point cloud, and used to compute 3D displacement components.

Experimental results show that this method currently achieves an accuracy of $\sim 1/7,000$ and a measurement resolution of $\sim 1/24,000$ of the measurement volume side length for rigid-body 3D displacements of up to about 10 mm. The spatial resolution can reach 1 pixel, whereas the standard 2D DIC can only give 20 pixels for areas near the discontinuities. The method can in principle be extended to a multi-camera multi-

projector system to obtain complete 360° measurement. However, the approach is restricted to specimens undergoing relatively static deformations due to the use of the temporal phase unwrapping technique.

4.8 Figures

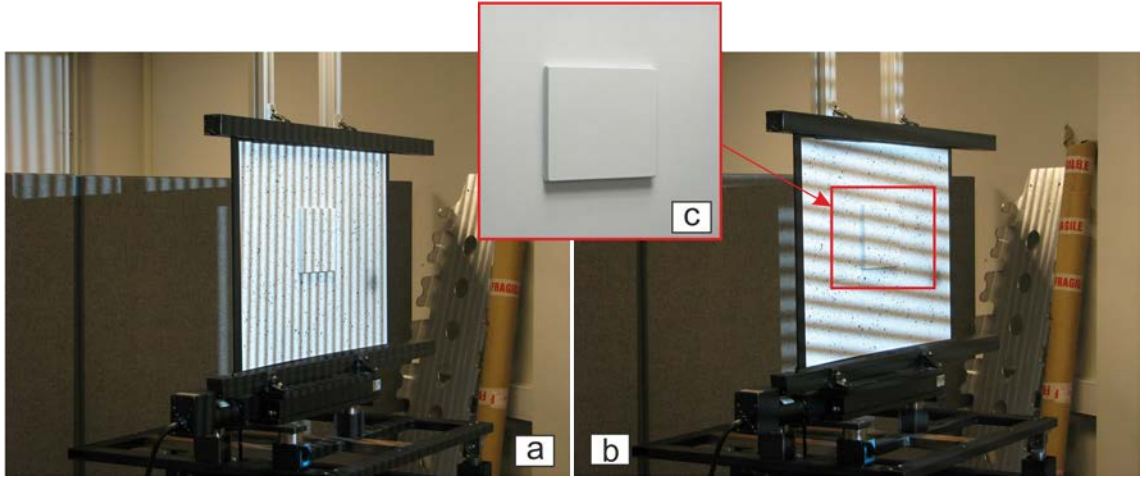


Figure 31: Flat sample with a step being measured by SMS. (a) Projected vertical fringes. (b) Projected horizontal fringes. (c) Close-up view of the step (height = 10 mm) before the surface was sprayed with black speckles.

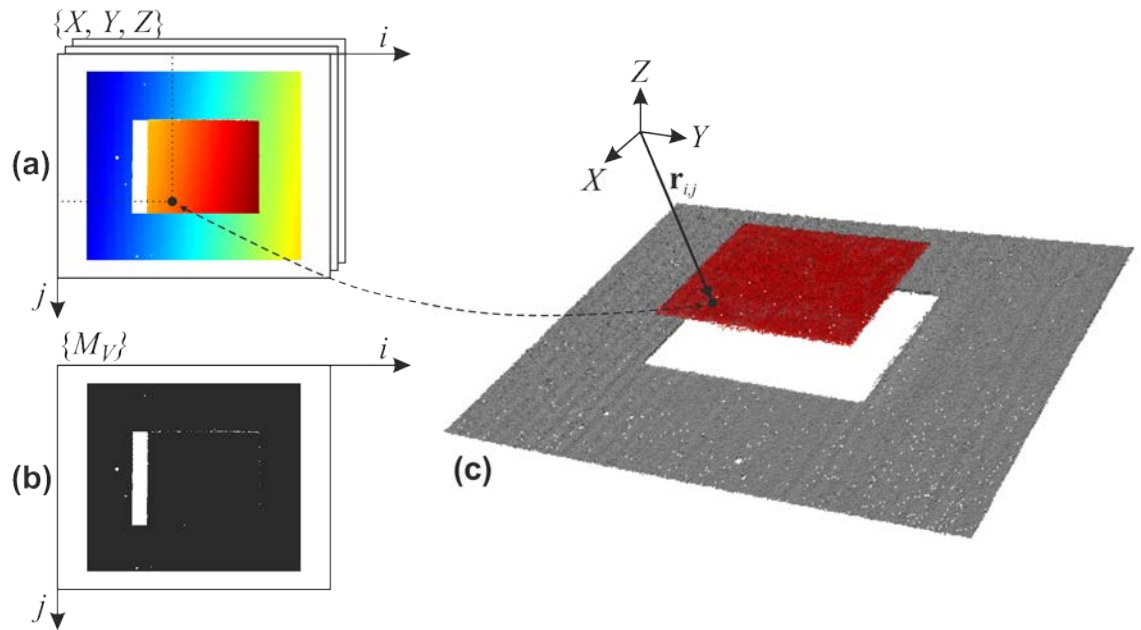


Figure 32: Representation of a measured point cloud. (a) 2D representation on three images – each image stores a coordinate component X , Y or Z . (b) Mask of pixels with high measurement confidence. (c) 3D representation in world coordinate system.

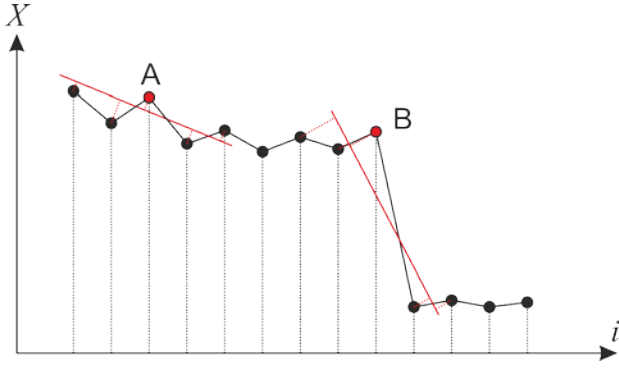


Figure 33: Linear least-square fitting to determine spatial gradient at a data point. Point A represents a normal point far away from discontinuities. Point B lies on a sharp edge that can be considered as a discontinuity.

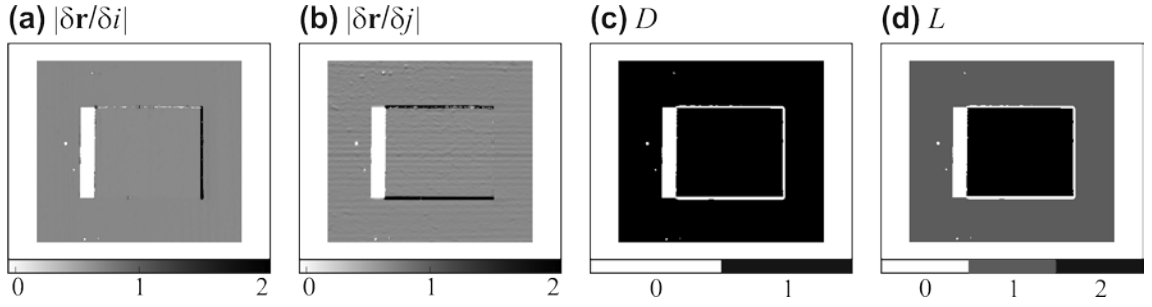


Figure 34: Example segmentation results of the surface presented in Figure 32. (a) Gradient computed along i -axis. (b) Gradient computed along j -axis. (c) Map of pixels not straddling discontinuity. (d) Label map of continuous regions.

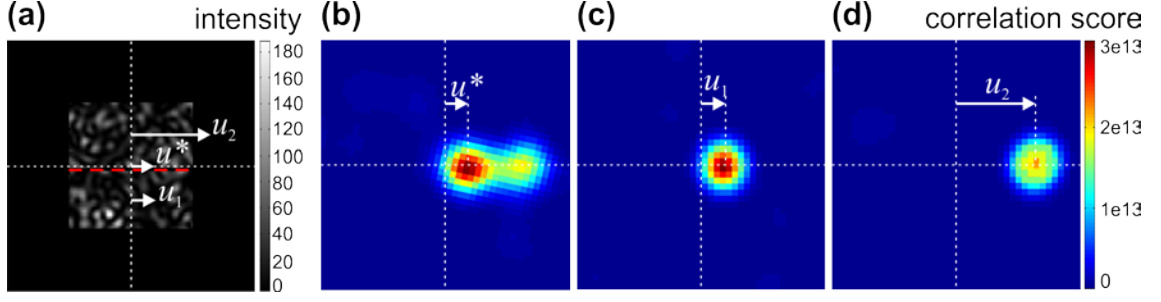


Figure 35: (a) An example simulated sub-image lying across a horizontal discontinuity (shown by the red dashed line) that divides it into two regions with different (constant) image displacements u_1 and u_2 . (b) Correlation field computed by standard DIC containing ambiguous peaks and resulting in erroneous image displacement u^* . (c), (d) Correlation fields computed by the new DIC algorithm for the lower and upper halves, respectively, of the sub-image.

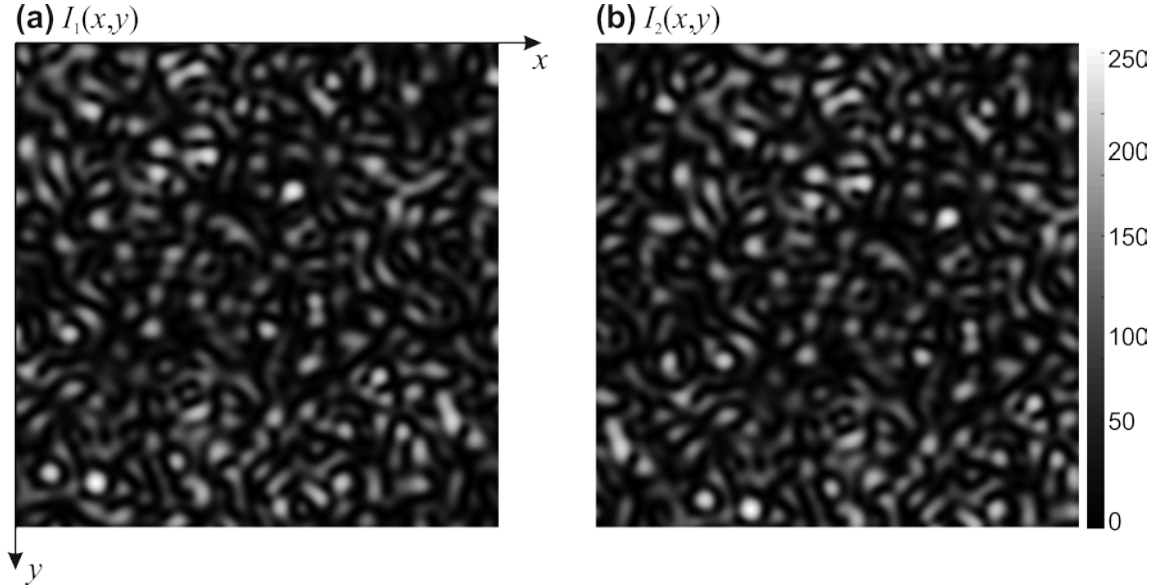


Figure 36: Simulated speckle images. Image size is 256×256 pixels. Translation vector applied is $\{u=39.25 \text{ pixels}, v=14.19 \text{ pixels}\}$.

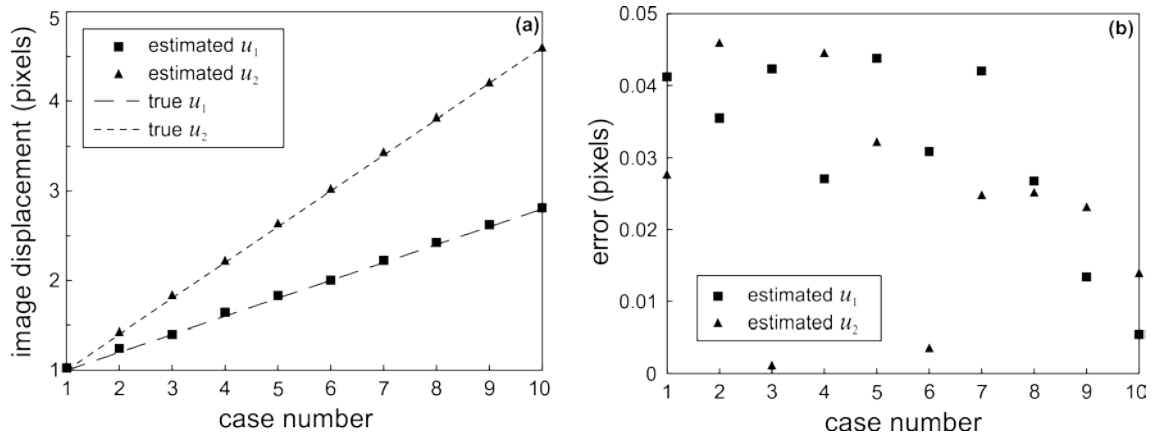


Figure 37: Calculated image displacements from simulated images of the type shown in Figure 35. (a) Estimated horizontal image displacements u_1 and u_2 as compared to a prescribed value. (b) Estimation error of corresponding image displacements.

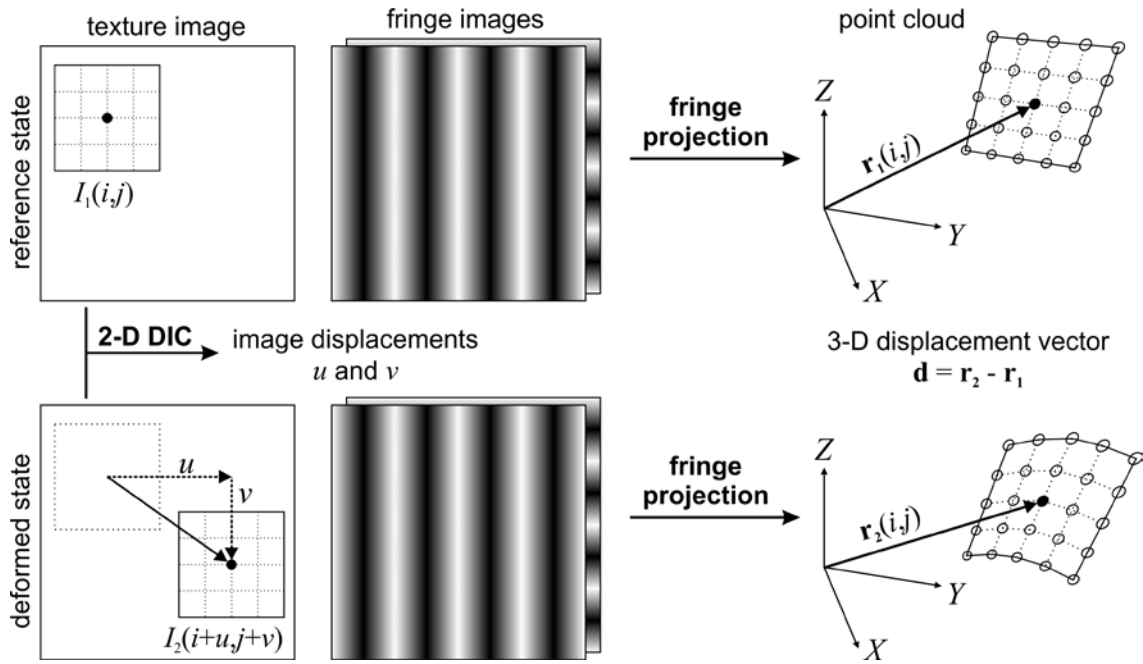


Figure 38: 3D displacement vector estimation procedure using a one-camera one-projector sensor.

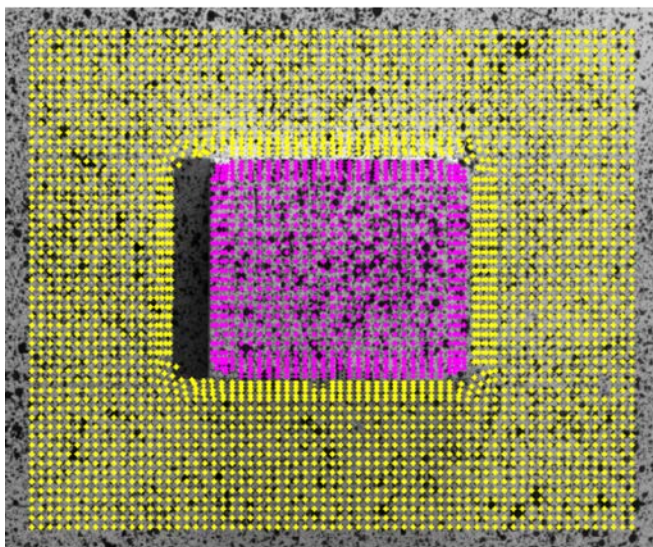


Figure 39: Example grid of sample points seeded on the surface and automatically adjusted to adapt to the surface profile.

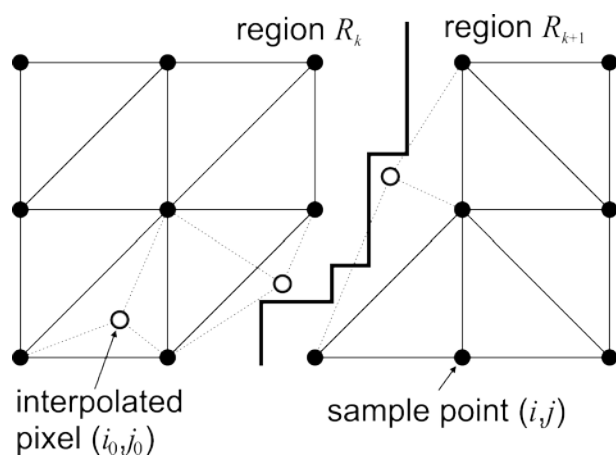


Figure 40: Interpolation of displacement for each pixel from known sample points.

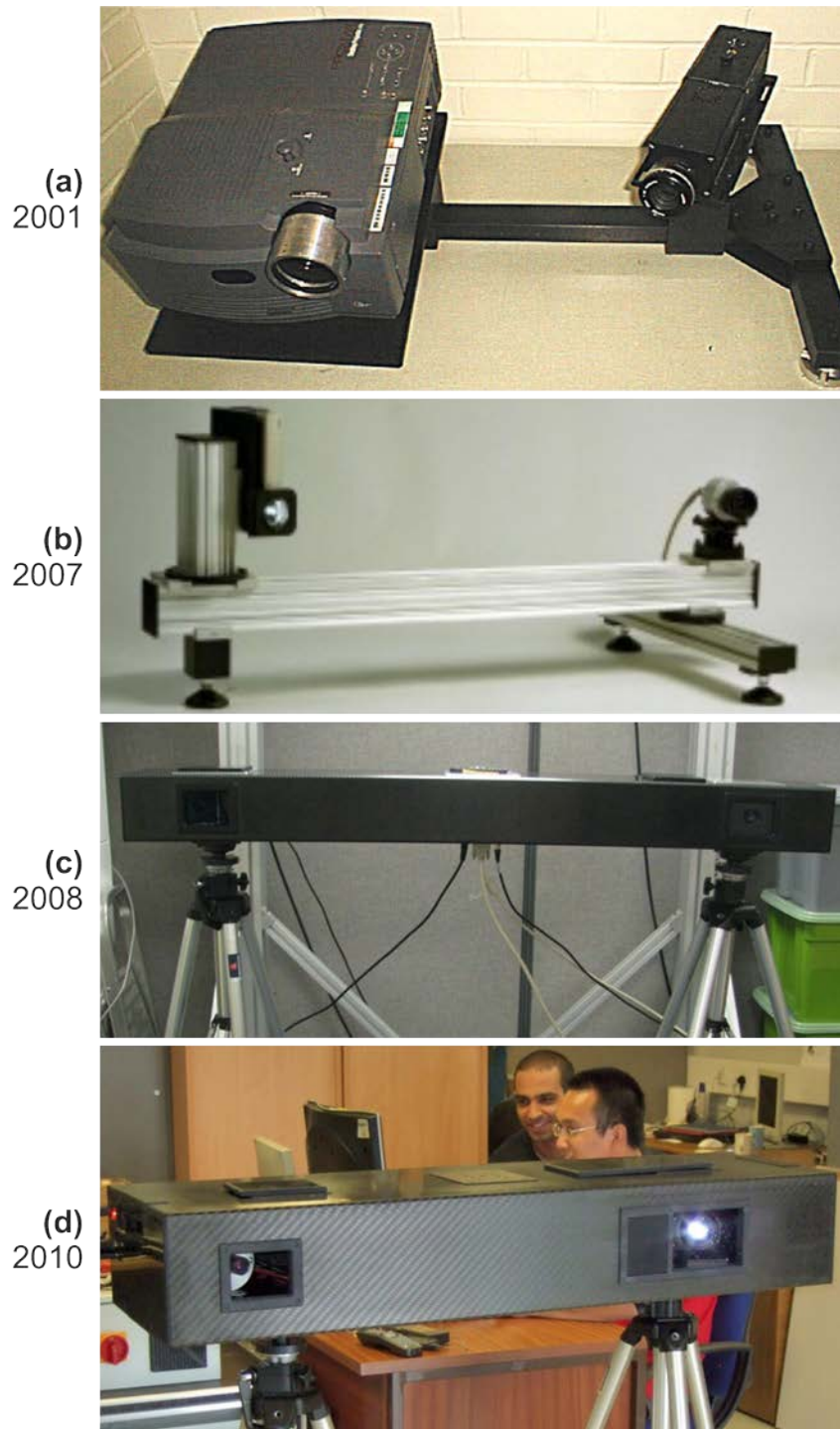


Figure 41: Evolution of SMS developed at Loughborough University and Phase Vision Ltd. (a) First prototype developed by Coggrave [17]. (b) Second prototype used by Ogundana [18]. (c) SMS1200 system used in this thesis. (d) Latest Quartz-DBE system also used in this thesis.

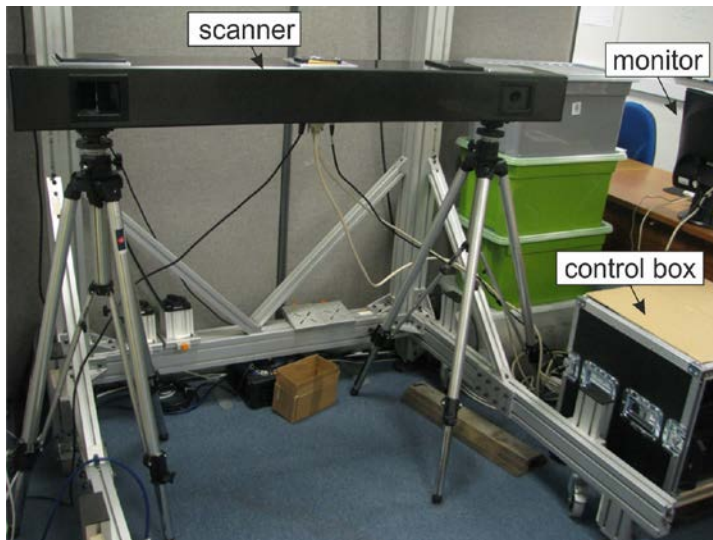


Figure 42: Photo of a SMS1200 scanner used for the experiments presented in Chapter 4 and Chapter 5.

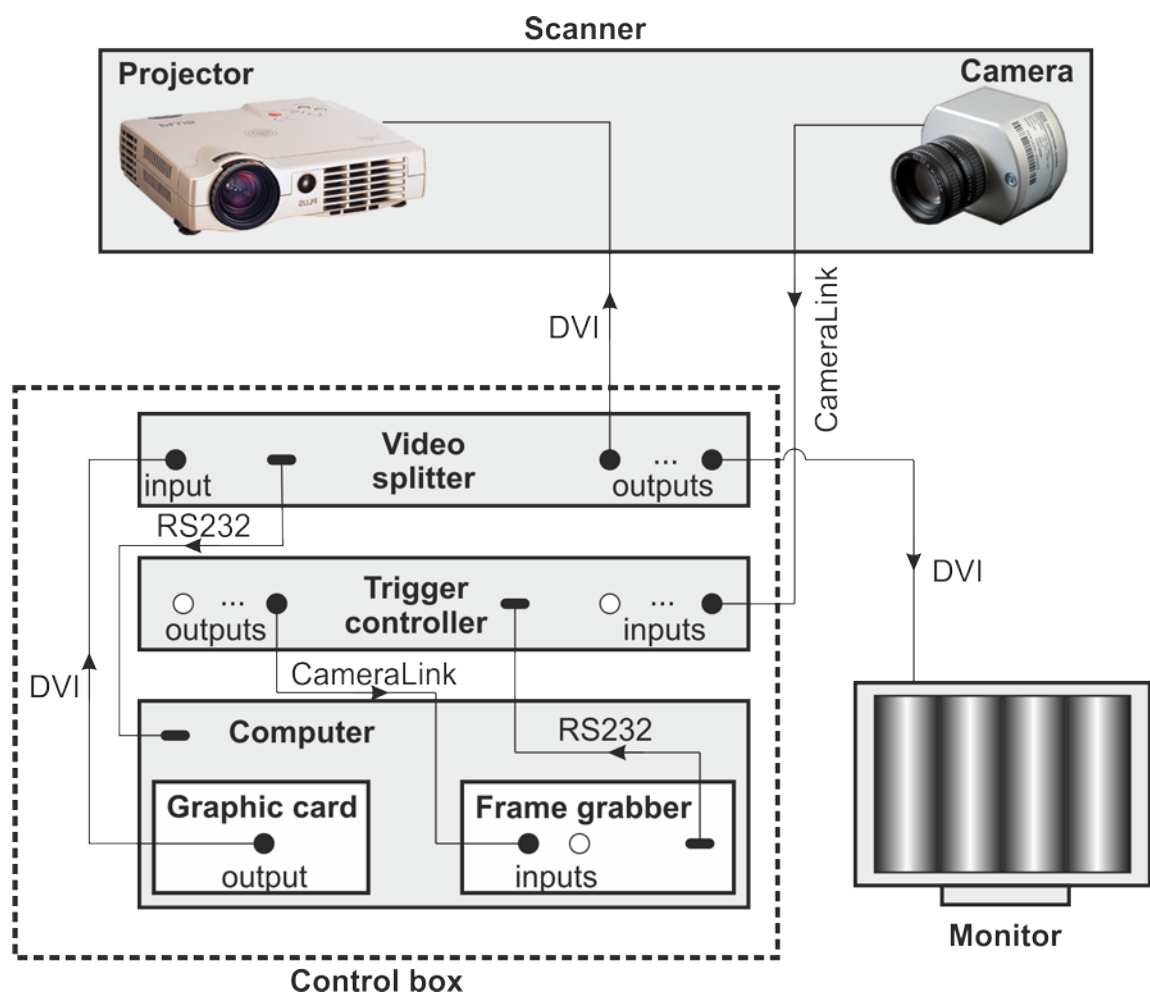


Figure 43: Wiring diagram of electronic devices of a SMS1200 scanner.

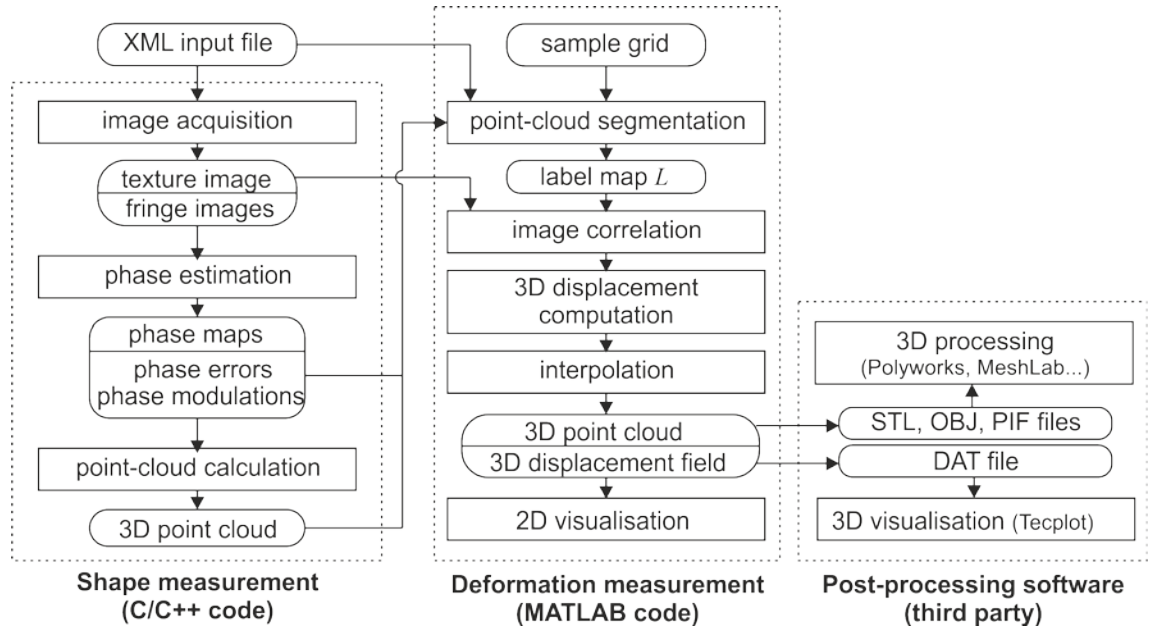


Figure 44: Structure of software modules for 3D point-cloud measurement, 3D displacement field computation and result post-processing.

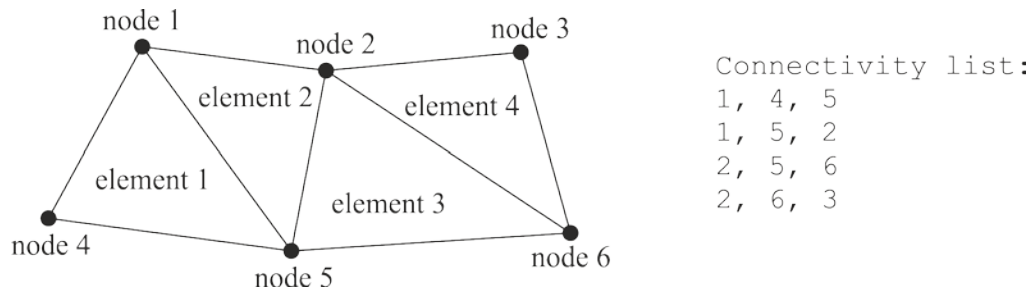


Figure 45: Connectivity arrangement of an unorganised dataset with triangular elements. Connectivity list has 4 rows corresponding to the 4 elements. Each row contains ID numbers of 3 nodes.

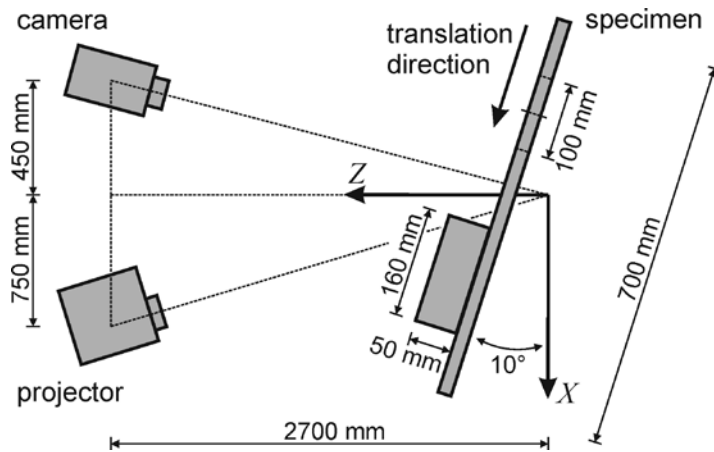


Figure 46: Arrangement of the validation test. The dimensions are approximate and not to scale.

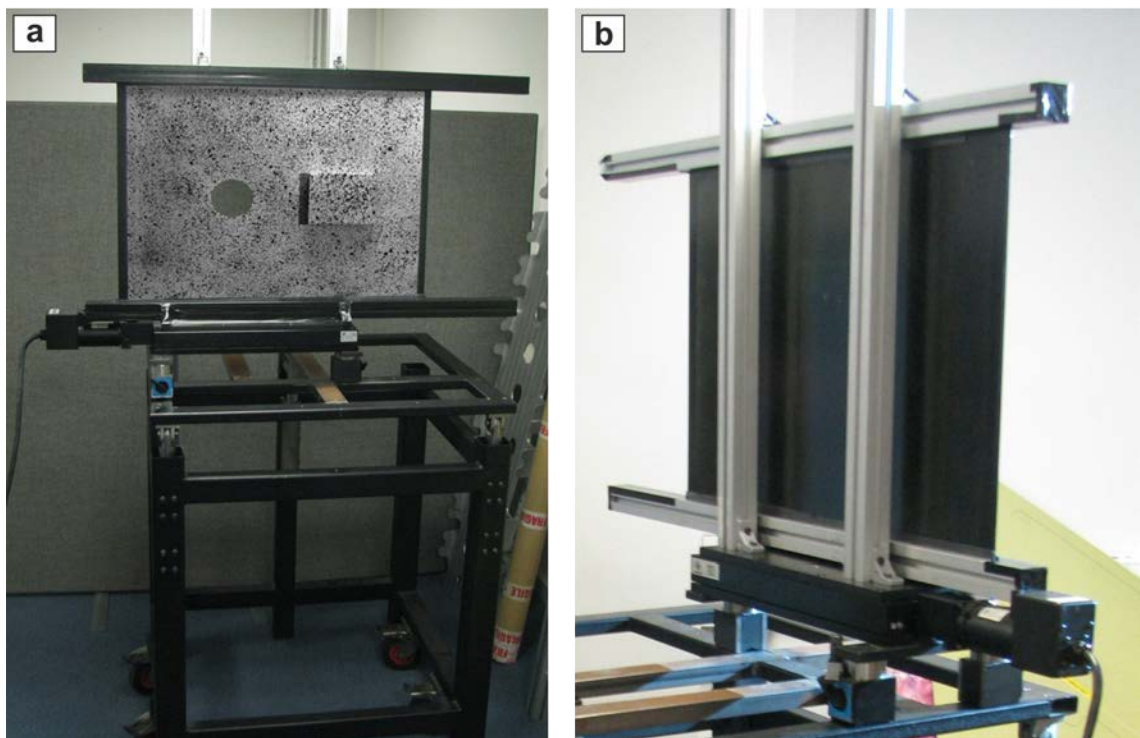


Figure 47: Experimental specimen with a hole and a step mounted on a linear translation stage. (a) Front view showing the speckle pattern spray-painted on the specimen surface. (b) Back view showing the supporting aluminium frame.

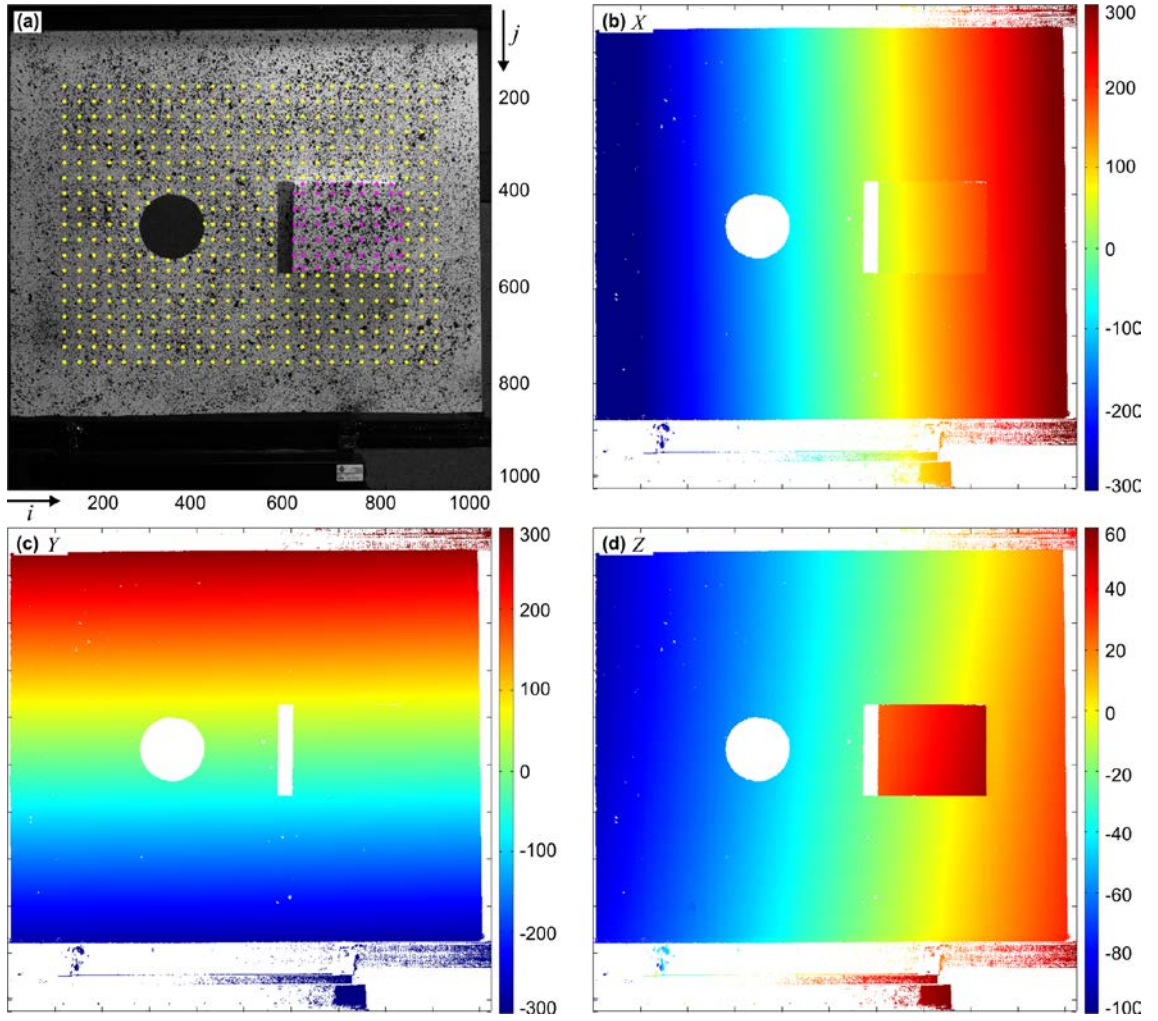


Figure 48: Shape measurement result of reference specimen. (a) 1024×1024 texture image with labelled sample points. (b), (c) and (d) Colour range maps of X-, Y- and Z-coordinates, respectively, of pixels shown in (a), where invalid pixels are displayed in white and colour value is expressed in mm.

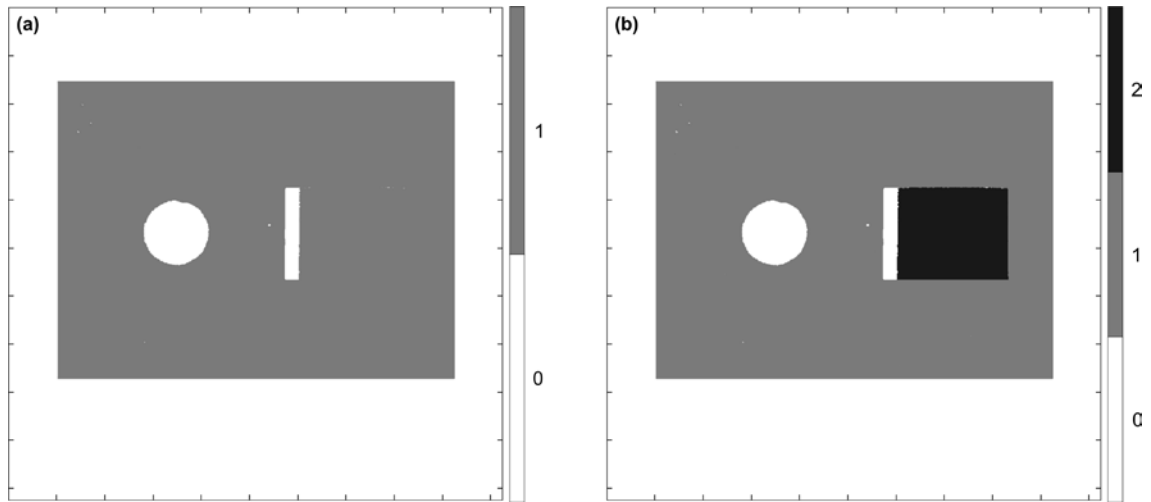


Figure 49: Surface segmentation result. (a) Mask of valid pixels within region of interest. (b) Label map of connected regions.

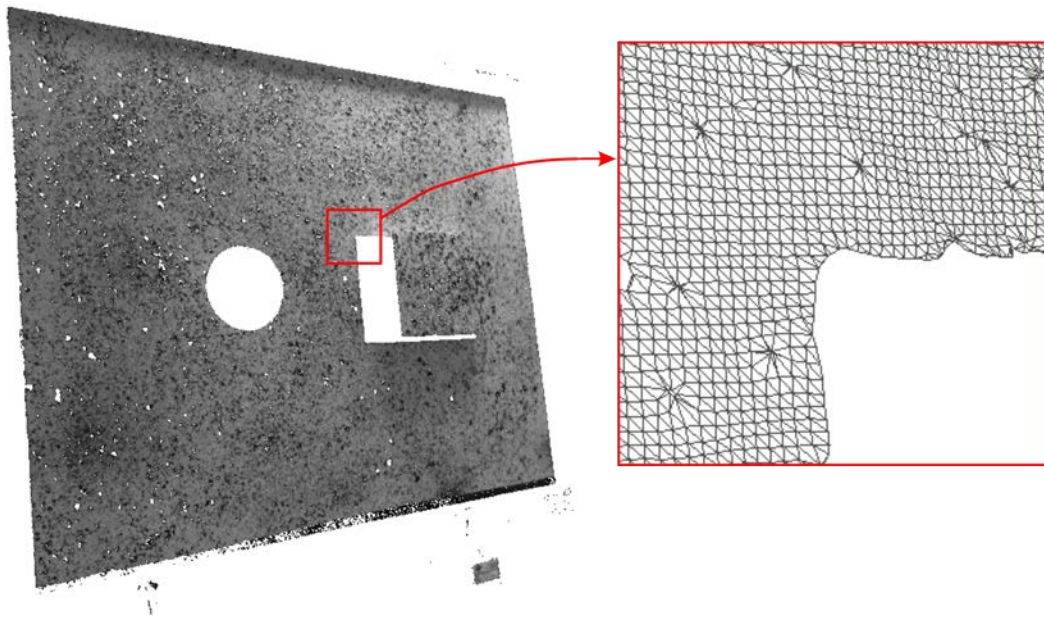


Figure 50: 3D point cloud of the reference surface as visualised in Meshlab software. There are 797,224 vertices and 1,520,875 faces. Missing data points due to poor intensity modulation at some of the dark speckles show up as white dots in the left hand image, and ‘star’ shaped facet arrangements in the right hand plot.

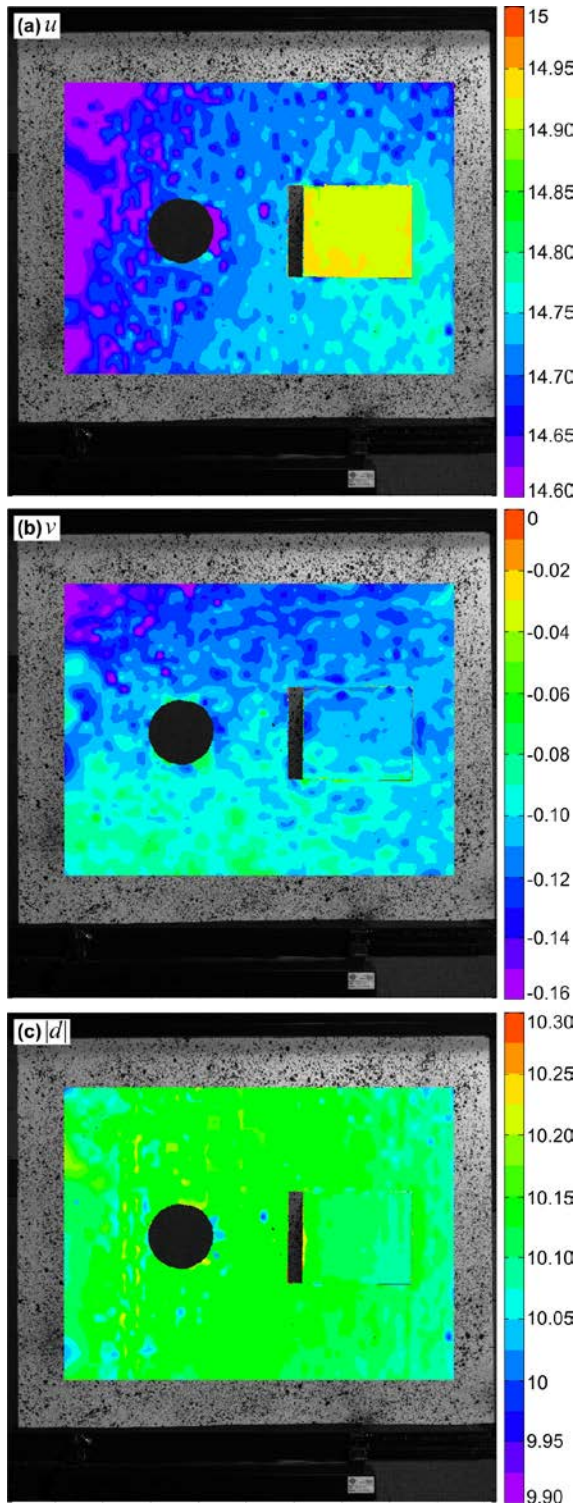


Figure 51: Estimated displacement fields corresponding to the true displacement of 10.160 mm. (a), (b) Horizontal and vertical image plane displacement components u and v , respectively, expressed in pixels. (c) 3D displacement magnitude field $|d|$ expressed in mm.

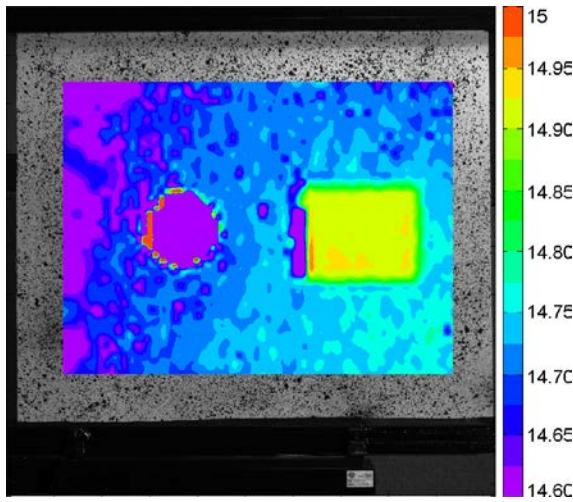


Figure 52: Horizontal image displacement field u estimated by a standard 2D-DIC technique without discontinuity detection for the true displacement of 10.160 mm (unit: pixels).

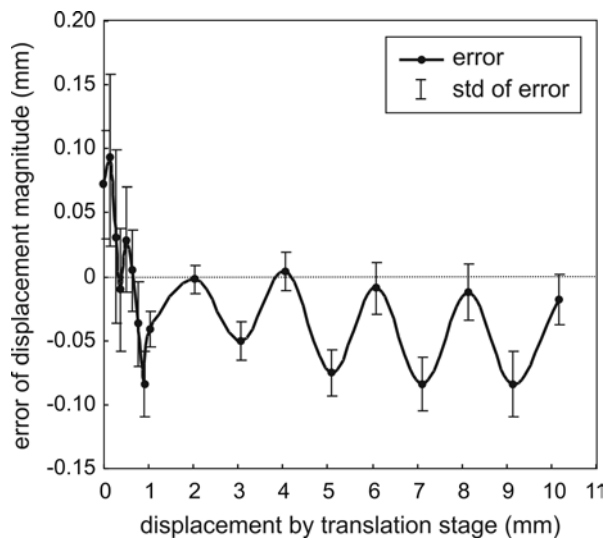


Figure 53: Mean error of displacement magnitude $|d|$ for the translation test. The standard deviation is represented as an error bar.

Chapter 5

Multiple-view shape and deformation measurement with multiple sensors

5.1 Overview

The structured-light fringe projection technique has become popular in industry due to its very high spatial resolution (i.e., one independent measured point per camera pixel) and the ability to measure discontinuous surfaces. For deformation measurement, digital image correlation [61] is widely recognised for its greater robustness in noisy environments and larger maximum measurable displacement than some of the other full-field imaging techniques such as Electronic Speckle Pattern Interferometry (ESPI) and moiré interferometry [113]. Although fringe projection and DIC sensors are available separately from commercial vendors, the common hardware requirements for the two techniques suggests that combining the two on a common platform is a logical direction of development, with benefits to include lower overall system cost and greater ease of use for the end users of the technology. A method to combine the strengths of these two well-known techniques has been developed in this research. This method offers two key advantages over previous work (e.g. [88–91]): (i) the ability to measure complex surfaces with severe discontinuities, and (ii) the ability to achieve up to 360° surface coverage by extending to multiple sensors. The former issue is presented in Chapter 4, and the latter is discussed in this section.

Due to a sensor's field-of-view limit and optical occlusion effects, large-scale and complex objects need to be measured from many different viewing directions, resulting in point clouds defined in different coordinate systems. There are at least three different approaches to connecting the coordinate systems [2]: (i) fixing the sensor and rotating the object on a mechanical stage, (ii) moving the sensor around the fixed object, and (iii) using multiple sensors to observe the fixed object. The first approach [114, 115] is not only expensive for large-scale inspections, but also unfeasible for structural tests where the object must be attached to a loading machine. In the second approach, the position and orientation of the sensor can be determined in several different ways, for

example by using a mechanical positioning system to move the sensor, using a laser tracking system to track the sensor movement, matching overlapping parts of the point clouds by iteratively minimising a least-square error measure [116], or using photogrammetry [117]. When applied to deformation measurements, this approach requires repeated translation of the sensor to exact locations and orientations in space, which is time-consuming and prone to re-positioning errors. Therefore, the third approach of using multiple sensors, which is common in surface profilometry (e.g. [40, 81]), is preferable for deformation measurements of objects with dimensions of order 1 m or above, as typically used in the aerospace industry.

There are currently only a few papers proposing methods to measure a complete 360° deformation field using multiple sensors. They generally involve using a stereovision DIC system to measure the point cloud and the associated displacement field for each view, and then registering them with respect to one another by aligning markers that are common to at least two of the views. Sutton et al. [62] used four cameras to measure simultaneously the front and back surfaces of a cracked plate undergoing bending and compression. The four cameras were grouped into two stereovision sets which were calibrated separately using a reference checker board. To estimate the coordinate transformation between the sets, 3D point clouds of both sides of a metal plate of known thickness, drilled with six holes, were aligned using the holes as the markers. In references [118, 119], the full surface of a cylindrical shell undergoing compression was measured by four sets of stereo-DIC systems. Although not clearly described in the papers, the four sensor sets appear to have been connected by using a photogrammetry system that tracks coded markers distributed on the specimen. Recently, Harvent et al. [120] proposed a method to correlate multiple speckle images captured by multiple cameras so that the speckle pattern itself can be used as the “markers” for the camera alignment. Nevertheless, these stereo-DIC-based methods suffer from at least two of the following three problems. Firstly, the process of matching images of two different views, known as stereo correspondence [121] in the computer vision community, may result in an erroneous point cloud (and thereby an inaccurate displacement field) in the presence of large perspective distortions. Although a deformable correlation window can be used for DIC-based stereo matching and can lead to accurate 3D coordinate measurement, this requires the introduction of additional free parameters in the correlation process which may reduce the measurement accuracy. Secondly, although

the number of points in the point cloud can approach the number of camera pixels by shifting the window position pixel by pixel, the density of independent measured points in the point cloud is restricted by the correlation window size. Thirdly, the alignment accuracy depends strongly on the quality of the markers and the method used to detect them.

This section presents a method that combines fringe projection with the digital image correlation technique on a single hardware platform to measure simultaneously both shape and deformation. The work described here can be considered a natural extension of the single-camera single-projector system presented in Chapter 4 to multiple cameras and projectors, which provides a route to complete 360° coverage of the sample surface. In particular, view alignment is not required as each sensor is automatically defined in a unified global coordinate system by an initial calibration procedure. By using the fringe projection technique, very dense point clouds can be produced. Furthermore, only sub-images recorded on the same camera are correlated with one another, and therefore the stereo correspondence problem is avoided. In many cases, the load-induced distortions between speckle patterns are normally much smaller than the perspective distortions occurring in cross-camera image correlations. Thus, at least for sufficiently small deformations, the complication of additional free parameters to describe the distorting correlation window can be sidestepped.

5.2 Extension to multiple sensors

The shape measurement system presented in this thesis can easily be extended to a multi-camera multi-projector system due to the modular design. More cameras and/or projectors can be added in order to inspect different parts of the object surface, since the present calibration technique is able to automatically bring 3D point clouds measured by different camera-projector pairs together into a unified global coordinate system.

5.2.1 Calibration of multiple sensors

The present calibration technique employs the principle of photogrammetry [81] to determine up to 12 parameters for each camera and projector, including 6 external parameters describing position and orientation of the sensor in the global coordinate system, 3 internal parameters describing principal point and focal length, and up to 3 coefficients of lens distortion. Figure 54 shows the reference artefacts used in two

stages of the calibration process: the circle pattern for the initialisation and the ball bar for the refinement. In the initialisation stage, the circle centres are detected by an ellipse-fitting algorithm and used as reference coordinates to obtain quick estimates of the first 9 calibration parameters with a direct linear transform (DLT). The global coordinate frame, which is virtually attached to some markers on the circle pattern within the measurement volume, is also defined at this stage.

In the refinement stage, the centres of the balls, which are distributed in various positions within the measurement volume, are first estimated from the measured point cloud by using a 3D Hough transform [85]. This allows points belonging to the surfaces of the two spheres to be selected from the full point cloud. A subset of these points is then used within a bundle adjustment calculation to refine the initial estimates of the 12 parameters, under the constraints that (i) camera and projector light rays must intersect in space and that (ii) the ball centres must be separated by the known distance as determined on a suitably calibrated mechanical Coordinate Measuring Machine (CMM).

As presented in Chapter 3, a robotic positioning system has been introduced to move the ball bar in space by two rotation angles ϕ and ω , each to a nominal precision of approximately 50 μ rad. Besides allowing the calibration process to be more automatic and repeatable, the knowledge of the rotation angles can be used to estimate the approximate positions of the ball centres and hence identify smaller regions of interest within the acquired datasets. The automated positioning also allows for significantly larger numbers of artefact poses to be conveniently employed (typically 40 for the experiments reported here), which improves the accuracy of the calibration.

5.2.2 Management of multiple sensors

Multiple sensors can be arranged in either of the two configurations shown in Figure 55. Each pair of camera and projector is enclosed in a carbon-fibre casing for protection. Such a sensor pair, called a scanner, constitutes a basic working system of one camera and one projector that can be used for both shape and deformation measurements (as described in Chapter 4). This modular design allows convenient and versatile extension to a multi-sensor system.

Configuration (a) corresponds to the use of the SMS1200 scanner introduced in Figure 41-c. When the system is extended to multiple scanners, all of the scanners are connected to the control box which performs the tasks of image acquisition control, image processing and result presentation. With regards to the cable wiring shown in Figure 43, the projector of an additional scanner is connected to an output port of the video splitter via a DVI cable, and the camera is linked to a spare input port of the trigger controller via a CameraLinkTM cable. The transmission of synchronised images from that camera to the computer is done via an additional CameraLinkTM cable connecting a spare output of the trigger controller to a spare input of the frame grabber. The multiple-scanner system used for the experiment presented in this chapter was set up in this configuration.

Configuration (b) corresponds to the use of the latest Quartz-DBE scanners presented in Figure 41-d. Within each scanner, a pair of camera and projector is connected to a server computer embedded inside the scanner which performs the first two of the above-mentioned tasks (i.e. image acquisition and image processing). The parallelism of the scanners suggests that the heavy processing of acquired fringe images for 3D shape information can be done more efficiently by parallel computing. A client computer, linked to the servers via Ethernet network cables, is used to retrieve and present the shape measurement results as well as to synchronise the servers. To obtain deformation fields, one simple approach is to gather the point clouds and texture images from all of the scanners in the client PC, and do the processing on this client PC. Another possible approach that exploits the parallel structure of the system to speed up the computation is to distribute the heavy image correlation tasks back to the scanners. However, the latter approach has not been implemented in this work.

In either of the configurations, measurement can be made using a pair of any camera and any projector. For each deformation state, the acquisition starts with projecting a fringe pattern sequence with projector P1 and capturing its images with all of the synchronised cameras (C1, C2,... Cn). Then, projector P2 is activated and the image capturing is repeated, and so forth until the last projector Pn. Although the total numbers of cameras and projectors are chosen to be the same in these configurations, this is generally not essential.

Control parameters of the system, including information about available hardware devices, image acquisition, phase estimation, calibration and image correlation, are stored in one XML input file. The operator can conveniently select which sensors to be used by modifying an XML element that specifies the indices of activated cameras and projectors.

5.2.3 Combining 3D displacement fields

The 3D displacement field measured by every camera-projector pair (using the procedure presented in Section 4.4) is associated with the measured point cloud and thus has already been defined in the global coordinate system due to the calibration technique. As a result, combining 3D displacement fields measured by all camera-projector pairs requires only two simple steps. First, displacement fields corresponding to the same view (i.e. measured by the same camera but different projectors) are merged together. As 2D reference sample points of those pairs are identical, most of their 3D coordinates and displacements have approximately the same values and thus can be statistically combined to improve the estimated point cloud and displacement field. In particular, the combined measurement results for view k of camera C_k are computed for each sample point (i,j) by

$$\begin{aligned}\bar{\mathbf{r}}^{(C_k)}(i, j) &= \sum_{Pl \in V} \mathbf{r}^{(C_k Pl)}(i, j) / N_V, \\ \bar{\mathbf{d}}^{(C_k)}(i, j) &= \sum_{Pl \in V} \mathbf{d}^{(C_k Pl)}(i, j) / N_V,\end{aligned}\tag{4.1}$$

where \mathbf{r} and \mathbf{d} are respectively the 3D coordinate vector and the 3D displacement vector, V indicates the subset of projectors for which a valid point measurement has been obtained at pixel (i,j) of camera C_k , and N_V is the size of that subset.

Then, the point clouds and their associated displacement fields of all camera views are gathered into a combined data set as depicted in Figure 56. The combined point cloud is meshed with triangular faces connecting sufficiently neighbouring measured points by using a Delaunay triangulation MATLABTM function which is based on the algorithms described in [122, 110]. In this way, a surface with several different overlapping views can be digitised with higher spatial resolution. Spatial smoothing was not used for the data presented in this thesis.

5.2.4 Software implementation

The structure of the 3D deformation measurement module using multiple cameras and projectors is presented in Figure 57. This is basically an extension of the MATLAB code for the single-camera single-projector platform described in Section 4.5.3, and thus can be used for any number of sensors. The executing functions are contained in three nested *for* loops over the following indices:

- Loading state index $t = 0, 1, 2, \dots, N_S$, where the case of $t=0$ corresponds to the reference (or undeformed) state of the object and the rest correspond to subsequent deformed states. The last deformed state is referred to as N_S . In the XML input file, a deformation sequence is specified as an ordered list of folders storing measured shape data.
- Camera index $k = 1, 2, \dots, n$, where n is the total number of cameras used.
- Projector index $l = 1, 2, \dots, n$, where n is the total number of projectors used, which is the same as the number of cameras in this implementation.

The code starts with reading the XML input file for necessary parameters, such as the numbers of sensors used in the previous shape measurement stage, the list of measured shape data folders for the whole deformation sequence, and the settings of the image correlation function. In the first iteration corresponding to the reference state ($t=0$), the reference texture image and point cloud are loaded into the computer memory. As the texture images acquired by a specific camera C_k are of the same view k (although illuminated differently by the projectors), the texture image of pair C_kP_1 can represent the view k and is drawn on the screen so that the user can select an area of interest. A regular grid of sample points is then populated within this area of interest. This area also defines a boundary for segmenting reference point cloud of any other pair of the view k (i.e., C_kP_2, \dots, C_kP_n). The resulting label map of segmented continuous regions of the reference point cloud is saved in the memory for later processing.

Then, the texture image and point cloud of a subsequent deformed state acquired by the same pair C_kP_l as in the step above are loaded and segmented for a label map of continuous regions of the deformed point cloud. The image correlation function presented in Section 4.3.2 takes the two texture images and the two corresponding label

maps, and outputs a matched set of the sample points. From these two matched sets of sample points and the two point clouds, the 3D displacements can be computed for the sample points and interpolated for all other pixel points within the area of interest. Before moving to the next projector $P(l+1)$, the obtained 3D displacements as well as the measured 3D coordinates for this pair C_kP_l can be then combined with those for the previously available pair $C_kP(l-1)$ following Equation (4.1) to improve the overall results for view k .

Once the view k has been processed entirely for all of the projectors associated with the camera C_k , its final point cloud and displacement field are meshed with triangular faces and saved in a Tecplot-compatible output file [109]. The process is repeated for the next views and all of the deformation states. The final results comprise of N_s sets of output files for all of the deformation states, each of which contains n files for all of the views.

If combining all views is requested (and instructed in the XML input file), the code can eventually execute a post-processing function that loads the output files, gathers the results of all different views for each deformation state, and remeshes the combined point cloud following the procedure presented in Figure 56. The main reason for keeping this post-processing function separate from the 3D deformation measurement module is to avoid memory overflow due to loading so many data sets at the same time.

It is noted that the present implementation is in a sequential flow such that most variables are stored only temporarily in the memory and overwritten throughout the three *for* loops. The benefit of this approach is that memory usage is kept to minimum and an increase in the numbers of sensors and deformation states does not cause memory overflow. This is suitable for implementation on a single computer as in this case. However, parts of the procedure can be redesigned to be parallel and the processing can be distributed to parallel computers (as in the second configuration in Figure 55-b), since the deformation states and the camera views are independent on each other.

5.3 Experimental results

An experiment on a discontinuous specimen undergoing displacement-controlled mid-point bending was carried out to validate the newly proposed technique using multiple cameras and projectors. The measured 3D displacement fields were compared against

the reference ones and those obtained with an industry-standard DIC system and a finite element model.

5.3.1 Apparatus and procedure

The specimen used for the mid-point bending experiment is illustrated in Figure 58, which is an aluminium sheet of thickness 1 mm bent along four parallel lines into a ‘top hat’ profile to introduce geometrical jumps and perspective occlusions. Two circular holes were also created on the top section to mimic cut-outs that are common in aerospace components. The specimen has a plane-view area of $500 \times 500 \text{ mm}^2$ and a depth of 100 mm. The edges of the specimen were clamped onto a supporting frame. The supporting frame, as shown in Figure 59, was assembled from ready-made aluminium profile bars.

A micrometer with a measurement precision of 0.01 mm was used to introduce a prescribed displacement δ at the centre point from the back of the specimen. To avoid local plastic deformation caused by stress concentration at the centre, the load was distributed through a penny coin of diameter 20 mm that is thicker and stiffer than the specimen.

To assist the image correlation, the front surface was prepared with a high-contrast speckle pattern by spraying black paint onto the white surface. As pointed out by Lecompte et al. [111], the speckle size and density strongly affect the image correlation accuracy. In this experiment, the speckles had an average diameter of effectively 7 pixels and an average density of around 5 speckles in a correlation window of 33×33 pixels.

The specimen was placed in the measurement volume of a shape measurement system configured with two cameras and two projectors as shown in Figure 60. Thus, four camera-projector pairs (i.e. C1P1, C1P2, C2P1 and C2P2) can be used to cover the entire front surface. The sensors were arranged and calibrated so that a measurement volume of $500 \times 500 \times 500 \text{ mm}^3$ included the specimen surface. In this experiment, the calibration RMS error was about 0.08 mm (or $\cong 1/11,000$ of the measurement volume diagonal), which is the RMS deviation of 3D coordinates measured on the surfaces of the calibration artefacts from their reference dimensions measured with a more precise

CMM. It may be noted that the global coordinate system XYZ defined by the calibration process is not necessarily aligned with that of the specimen.

During the acquisition process, a sequence of prescribed displacements δ varying from 0 mm to 10 mm with steps of 1 mm was introduced by the micrometer. At each loading state, the shape and deformation field of the specimen were measured by the system. In the current software implementation, surface profiles are calculated in a few seconds using C++ code, whereas the displacement fields are computed off-line with the software implemented in MATLABTM.

5.3.2 Measurement results of the combined SMS-DIC technique

Example results of image-plane displacement fields u and v , computed for a micrometer displacement $\delta = 5$ mm by camera-projector pairs C1P1 and C2P2, are shown in Figure 61. The coloured contour is visualised at a pixel level by spatially interpolating displacement values of a grid of sample points with a spacing of 16 pixels that is specified by the user on the reference image. As spatial interpolation is restricted to continuous surface regions, it can be seen that the estimated image displacement has been correctly estimated along surface discontinuity boundaries, such as the edges of the circular holes and the bends between the top and base sections.

Figure 62 shows the X -, Y - and Z -components of the 3D displacement field (namely d_x , d_y and d_z , respectively) obtained at the same load state ($\delta = 5$ mm). In this image visualisation, the Y -axis points to the left for pair C1P1 and to the right for pair C2P2. It can be seen that the out-of-plane component (which is approximately aligned with d_z) is dominant. A number of pixels imaging dark speckles have been masked out automatically since low signal modulation reduces confidence in the corresponding phase extraction. Figure 63 shows the magnitude of the 3D displacement field calculated from the three displacement components. As expected, the displacement magnitude is nearly zero along the clamped edges and increases up to a maximum value of approximately 5 mm towards the centre.

Three-dimensional visualisations of the specimen shape and displacement field as measured by all of the four camera-projector pairs at the load state of $\delta = 5$ mm are displayed in Figure 64, together with their combined result. The displacement magnitude field is represented on top of the reference shape of the specimen. The

coordinate system is the same for all of the pairs, which was defined in the calibration process. It can be seen that pair C1P1 (as shown in Figure 64-a) covers the entire left base section, the left side section, the top section and a part of the right base section, whilst pair C2P2 (in Figure 64-b) obtains the entire right base, the right side, the top and a part of the left base. So, even using only these two pairs can provide the entire coverage of the specimen surface of interest. Each of the other two pairs C1P2 and C2P1 (as shown in Figure 64-c and -d) results in two narrow strips of the base section which are adjacent to the clamped edges. In this particular sensors arrangement, the limited coverage of these two pairs is caused by optical obstruction and overexposed illumination on the top section. Considering pair C1P2 for example, although camera C1 can observe the whole left half of the surface (similar to the case of pair C1P1), projector P2 positioned on the right can only project fringes on a small strip near the left edge due to the occlusion caused by the raised top section. (The strip near the right edge can be still be illuminated as for pair C1P1.) Although the top section is visible to both camera C1 and projector P2, their mostly symmetrical position and angle over the perpendicular plane of the top section caused the strong light from P2 to reflect directly to C1 (i.e., reflective illumination was dominant over diffuse illumination) and therefore oversaturate the acquired images of C1. As a result, the achieved data of the top section had very low measurement confidence and were automatically masked out in the final result.

The RMS displacement discrepancy of the pairs is estimated to be 0.10 mm, which is computed from the differences in displacement magnitude of data points available for at least two pairs. Figure 65-a shows the distribution of displacement magnitude differences from pair C1P1 of all the other pairs. It is noted that sample points are identical for the same views (e.g. pairs C1P1 and C1P2 have identical sample grid) but different for different views (e.g. pairs C1P2 and C2P2 have different sample grid). Therefore, to construct this combined error map, nearest-point interpolation was done for sample points of different views. This interpolation in turn has also contributed to the presented error; however, it is only used for the evaluation purpose and should not be considered as an inherent error of the proposed technique. In other words, the pair-to-pair discrepancy is expected to be slightly lower than the presented figure of 0.10 mm. The main source of error comes from the measured 3D coordinates (from which the displacements are computed). Figure 65-b presents the distribution of

coordinate differences with pair C1P1 used as the reference. A coordinate difference is defined as the geometric distance between two measured coordinates of a sample point. The RMS of the coordinate differences is estimated to be around 0.10 mm, which is slightly higher than the calibration error. The repeated pattern of high coordinate differences on the top section suggests that there is systematic error across different sensor pairs.

5.3.3 Standard stereo-DIC

To validate the proposed technique, its measured displacement fields were compared against the results of an industry-standard stereo-DIC code (the Vic-3D 2009 software from Limes GmbH). Vic-3D [16] is well-known for non-contact measurement of 3D shape, displacement and strain fields of mechanical specimens of up to several m² in size. It is stated to achieve up to 50 micro-strain of measurement accuracy. A typical stereo-vision Vic-3D system consists of two digital cameras mounted on a metal bar and connected to a portable computer via Gigabit Ethernet cables. The computer is equipped with the Vic-3D software to capture and process images. In this work, only the Vic-3D software was utilised, whilst present SMS1200 hardware was used to acquire the deformation images. This is to rule out the effects of hardware on the performance comparison.

To ensure strictly the same testing condition, the texture images captured by camera C1 and C2 in the previously-presented procedure were used as the inputs for the stereo-DIC software. The same grid of sample points populated on the reference image of camera C1 in the proposed technique was used again for the stereo-DIC software. The correlation subset size was also chosen to be 33×33 pixels, i.e. the same as for the newly proposed image matching technique. A second-order subset shape function was used. Due to severe perspective disparities between image subsets of the cameras, the user was required to manually specify several matched points between the images to assist the stereo correspondence process. This problem does not arise with the new approach because the image correlation here is always performed between images recorded on the same camera.

The software also required calibrating the cameras by recording a planar circle pattern of known separations at a number of poses (20 in this experiment). Some example calibration images captured by cameras C1 and C2 of the present system are shown in

Figure 66. The calibration circle pattern was generated by Vic-3D's add-on software, printed on a 600dpi laser printer to an A3-size paper and glued to a relatively flat plastic panel. The Vic-3D software read those calibration images, detected the centres of the circles and worked out all intrinsic and extrinsic parameters of the cameras using a bundle-adjustment algorithm similar to the SMS's calibration technique explained in Section 2.3.3. Its resulting calibration parameters are given in Table 4 for comparison with those converted from the camera parameters of the proposed system. It can be seen that the two sets of calibrated camera parameters have slightly different values, which may be caused by the differences in (i) the calibration algorithms, (ii) the calibration artefacts, and (iii) the pixel skew factors. Skew factor represents the "squareness" of a physical pixel on a camera sensor, which has the value of 0 if the pixel corner angle is perfectly 90° . The skew factors of the both cameras were set to 0 in the current calibration model of the proposed SMS whilst being variables in that of the stereo-DIC technique. However, considering their resulting values of 0.052 pixel and 0.307 pixel (corresponding to the skew angles of 89.999° and 89.995° , respectively), the difference is expected to be negligible.

The displacement magnitude field obtained at the micrometer displacement $\delta = 5$ mm is shown in Figure 67. Only the displacements on the top section of the sample can be determined because most of the remaining sections are occluded for one of the two cameras.

5.3.4 Finite element simulation

To achieve more confidence in the 3D displacement distribution over the entire surface, a finite element simulation was also carried out. The finite element model, as depicted in Figure 68, consisted of 1,100 quadrilateral shell elements with a mesh density that increased towards the loaded point. The material was modelled as linear elastic with the properties given in the caption to Figure 58. The two boundaries were clamped by constraining all six degrees of freedom at the relevant nodes. The displacement δ was applied to all nodes lying on the circular edge of the loading block, mimicking the real loading coin. The MSC.NastranTM linear static solver was used to calculate the displacement and stress fields. The resulting stress distributions predicted that the loaded region starts to deform plastically when δ exceeds 8 mm. The results of the simulated displacement fields are discussed in Section 5.4.2.

5.4 Discussions

5.4.1 Point-wise error

The discrepancy of the displacement magnitude d measured at the loaded point from the prescribed micrometer displacement δ is used as a measure of error to compare the proposed system with the stereo-DIC software. Figure 69 shows the displacement error $|d - \delta|$ for various values of δ for pair C1P1 and C2P2 as well as for their combined result in comparison with that of the stereo-DIC software. The displacement error for the combined pairs is generally not a simple average of the two pairs, due to the statistical data gathering and re-meshing. It can be seen that the point-wise error of the combined displacement field varies from $\cong 0.02$ mm to $\cong 0.13$ mm with an RMS of $\cong 0.07$ mm (which is $\cong 1/12,000$ of the measurement volume diagonal). The error tends to increase with the loading displacement due to the increasing distortion of the texture subset around the loaded point which is not included in the current zeroth-order subset deformation model. The error difference of pair C1P1 and C2P2 has an RMS value of $\cong 0.07$ mm, which is mainly due to the propagation of errors from slight imperfections in the camera and projector parameters as estimated during the calibration process.

In comparison, the stereo-DIC code gives lower or comparable displacement error at the first four loading states, which may be attributed to the fact that it incorporates a second-order deformation model of the correlation subset. However, as the deformation increases, the error of the stereo-DIC measurements increases much more dramatically than that of the proposed system. This is possibly due to the increasing disparity of the subsets as observed by the cameras located at large separation. By contrast, the proposed system does not utilise stereo correspondence on texture images from different cameras, and thus has been able to eliminate this important source of error.

5.4.2 Field-wise comparisons with stereo-DIC and finite element model

The magnitude of the 3D displacement fields for the whole deformation process, estimated by the proposed system, the stereo-DIC code and the finite element simulation, are visualised on top of the reference shapes in Figure 70 and Figure 71. The shape and displacement field shown for the proposed system are a combination of all of the active camera-projector pairs. For comparison, the three models have been brought into the same coordinate system.

From a qualitative comparison, it may be observed that the proposed system has been able to provide a full coverage of the surface, whereas only the top section is measured by the stereo-DIC software. It is of course to be expected that surface coverage provided by the proposed system is larger, since it used all four sensors (i.e. two cameras and two projectors) as opposed to only two sensors (i.e. two cameras) by the stereo-DIC. The important point is that, for the top section of the surface where both systems can make valid measurements, the displacement fields seem to be in fairly good agreement. This agreement becomes clearer for the last four deformation steps (i.e., $\delta = 7, 8, 9$ and 10 mm), where the central deformation field is biased to one side of the specimen due to the not perfectly-central loading. As compared to the finite element model, good agreement is observed over most of the surface, although the simulated displacement field seems to be localised closer to the loaded region. The discrepancy between the finite element simulation and the two experimental techniques is possibly due to imperfections of the specimen and the residual deformation induced during manufacture of the specimen and clamping it along two edges, which are not included in the finite element model.

Several advantages of the proposed system over the stereo-DIC approach are demonstrated by the experimental results. Firstly, the areas on the base section near the clamped edges, although visible to both the cameras as shown in Figure 67, are not included in the result of the stereo-DIC. The reason is that their images appear to be too different (due to both perspective distortion and depth-of-field difference) for the stereo correspondence to achieve sufficient correlation scores. These areas, on the other hand, can be measured by the proposed system even with a single sensor pair, such as pair C1P1 as shown in Figure 63-a. Secondly, the proposed system has correctly measured the areas along the discontinuities, such as the bent lines between the top section and the side sections. By contrast, the stereo-DIC approach results in erroneous displacements in these discontinuous areas. As it has no prior knowledge about the 3D scene and occlusions that may occur, an image of the side section has been wrongly correlated with that of the base section. Thirdly, the point cloud is computed at all camera pixels in just a few seconds by the proposed system, whereas the point cloud density by the stereo-DIC is normally restricted to a subset of the camera pixels (1 pixel in 16 along each axis in this experiment) due to the significant computation time (approximately 10 minutes for all the pixels of the 1 Mp images used here).

For a quantitative comparison, a difference field of displacement magnitude (namely ε_d) is computed for each stereo-DIC and FEM result model from the result of the proposed technique. The difference fields for the whole deformation sequence are shown in Figure 72. For the stereo-DIC results, it can be seen that the difference is lower in the loaded area (showing the good agreement with the proposed SMS-DIC technique) and higher around the edges (showing the limitation of the stereo-DIC in dealing with discontinuities). For the FEM, high differences are observed in some part of the base sections, which is due to the imperfection of the specimen's geometry.

A RMS value is computed for each of the above-mentioned difference fields and summarised in Figure 73. The curve of “good data” is computed only from sample points in the loaded area; whilst the curve of “all data” includes other high- difference sample points around the edges. The former curve shows a very good agreement between the stereo-DIC and the FEM. The RMS difference ranges from about 0.05 mm (for $\delta = 1$ mm) to about 0.5 mm (for $\delta = 10$ mm). The fact that the RMS difference increases with the micrometer displacement is consistent with the point-wise comparison in Figure 69.

Although the present experiment has demonstrated many advantages of the proposed SMS-DIC-combined technique, some limitations should also be pointed out. Firstly, due to the use of projected fringes and the temporal phase unwrapping technique, the proposed system requires relatively long acquisition time (which was about 20 seconds for a single deformation state in this experiment) and thus is restricted to specimens undergoing relatively low strain-rate deformations. Stereo-DIC, however, is a single-shot technique that has been applied to dynamic testing (e.g. [62, 118, 119]). Secondly, phase values at dark speckles may not be extracted with high confidence by the fringe projection technique due to low signal modulation. The resulting random shape measurement errors could be reduced by employing a speckle pattern with reduced contrast, although this would also have the effect of increasing the displacement field errors.

5.5 Summary

The fringe projection and digital image correlation techniques have been combined on a hardware platform with multiple cameras and multiple projectors to simultaneously

measure both surface profile and deformation field from multiple views. The proposed approach has an attractive feature of accurately measuring discontinuous surfaces by exploiting the very dense point clouds to assist the image correlation. Another advantage is that results from multiple views of the surface are automatically combined into a unified global coordinate system without an extra alignment step. The experimental results show that the proposed system has currently achieved an accuracy of $\cong 1/12,000$ of the measurement volume diagonal for fully 3D displacements of up to 10 mm. The results have been compared to those produced by a standard stereo-DIC system and a finite element simulation, and good agreement has been observed.

5.6 Tables

Table 4: Calibration parameters of the stereo-DIC system as compared to the proposed system. The notation is adopted from [62].

	Stereo-DIC system	Proposed system
Intrinsic parameters of camera C1		
Principal point $\{c_x; c_y\}_1$, pixels	{520.695; 513.419}	{508.665; 562.773}
Focal length $\{f_x; f_y\}_1$, pixels	{3910.61; 3909.93}	{3912.15; 3912.15}
Pixel skew $\{f_s\}_1$, pixels	0.052	0
Lens distortion $\{\kappa_1; \kappa_2; \kappa_3\}_1$	{-0.084; 0; 0}	{0.001; 0; 0}
Intrinsic parameters of camera C2		
Principal point $\{c_x; c_y\}_2$, pixels	{536.137; 524.398}	{522.480; 566.328}
Focal length $\{f_x; f_y\}_2$, pixels	{3896.33; 3896.05}	{3894.97; 3894.97}
Pixel skew $\{f_s\}_2$, pixels	0.307	0
Lens distortion $\{\kappa_1; \kappa_2; \kappa_3\}_2$	{-0.072; 0; 0}	{0.001; 0; 0}
Relative transform from C1 to C2		
Translation $\{t_x; t_y; t_z\}_{1-2}$, mm	{-1784.390; -9.059; 517.984}	{-1723.244; 14.820; 549.705}
Rotation $\{n_x; n_y; n_z\}_{1-2}$, degrees	{0.589; 34.007; 0.752}	{0.603; 33.972; -1.157}

5.7 Figures

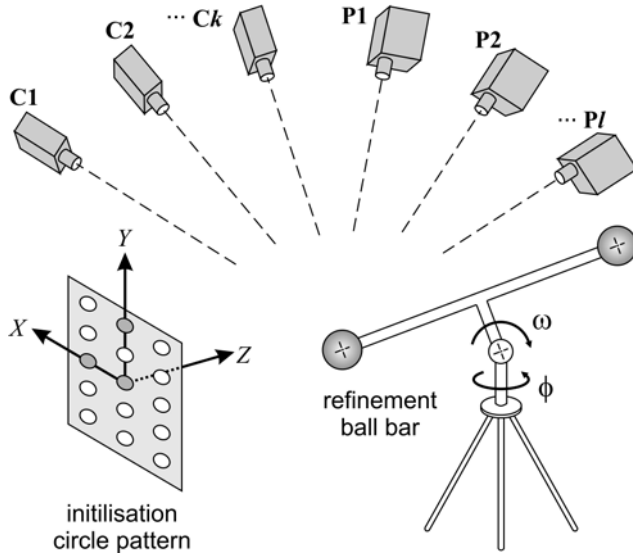


Figure 54: Calibration arrangement for multiple sensors. The cameras are denoted as $C1, C2$ and Ck , and the projectors as $P1, P2$ and Pl .

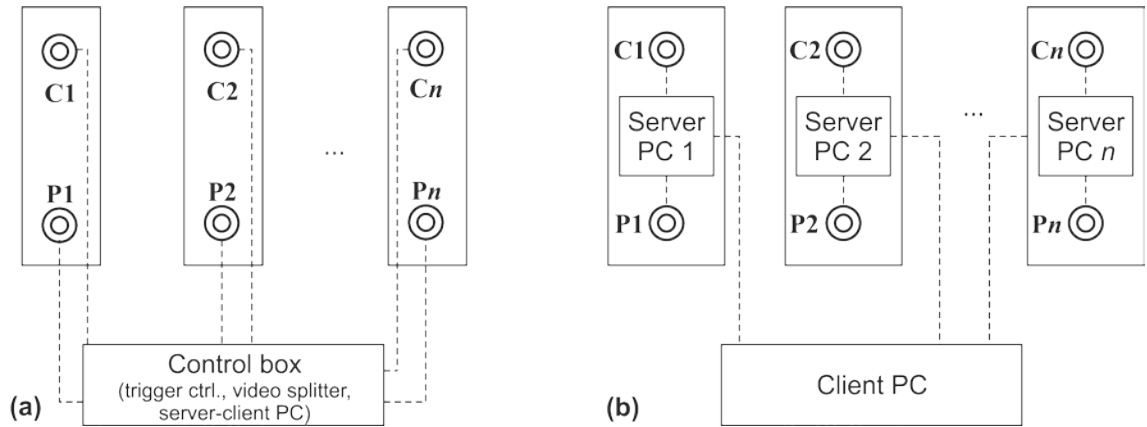


Figure 55: Two configurations for managing multiple sensors.

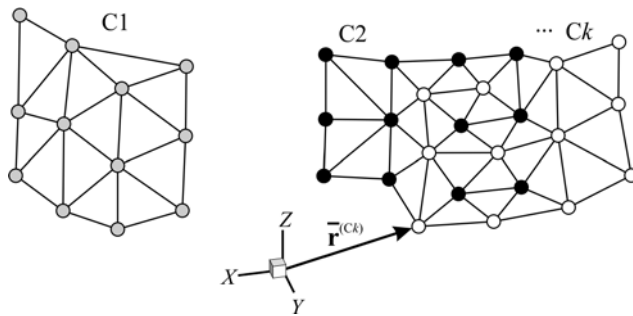


Figure 56: Gathering and meshing of point clouds from multiple camera views.

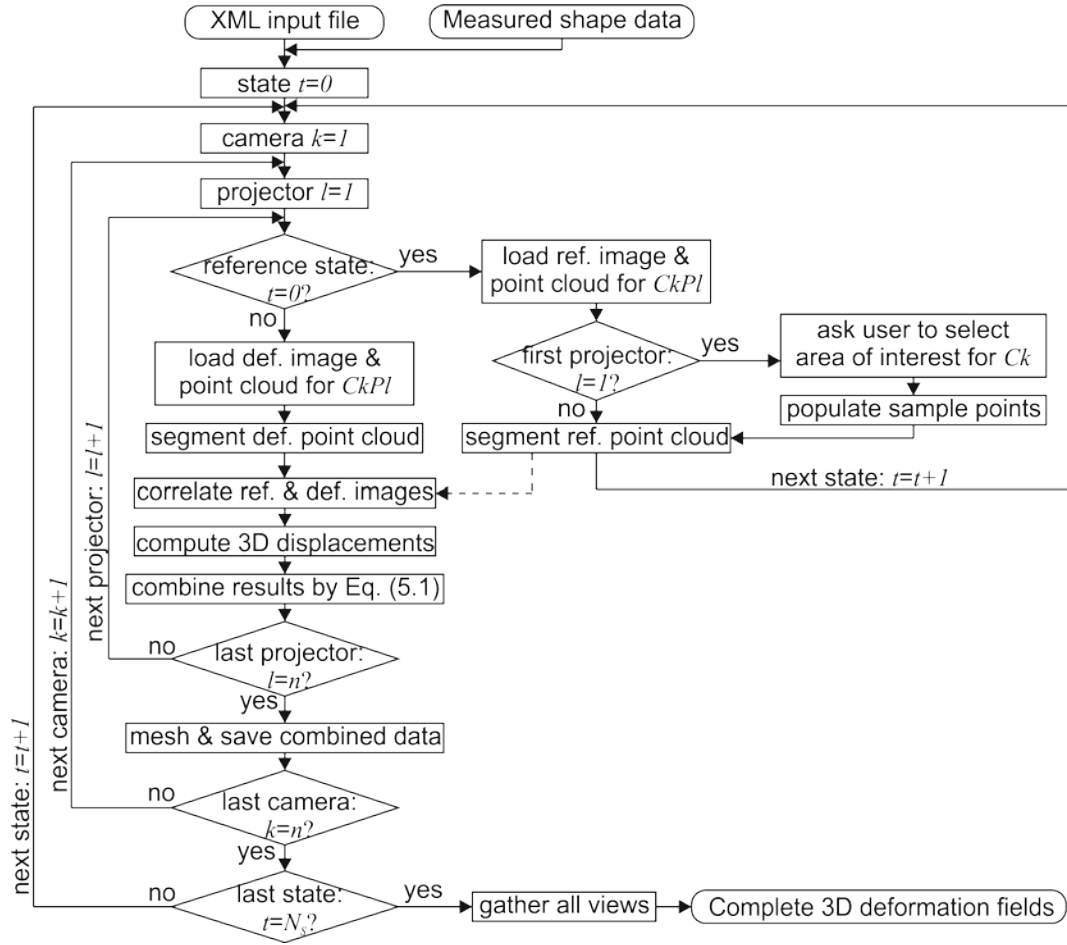


Figure 57: Software structure of 3D deformation measurement module extended to multiple sensors.

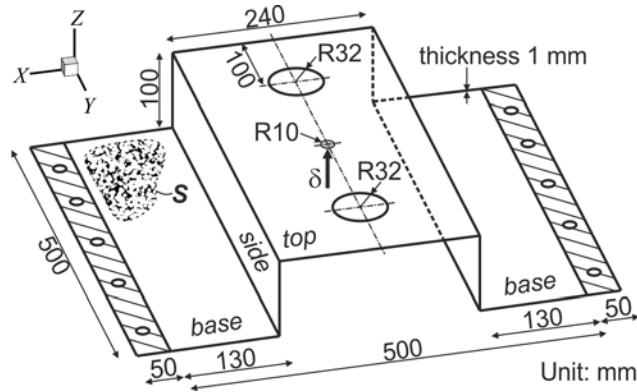


Figure 58: Schematic illustration of test specimen. Material: aluminium alloy 1050 (H14) (Young's modulus 71 GPa; Poisson's ratio 0.33; and tensile strength 115 MPa). Region S represents the speckle pattern painted on the entire specimen surface. The edges are clamped, and the centre is pushed by a micrometer by displacement δ .

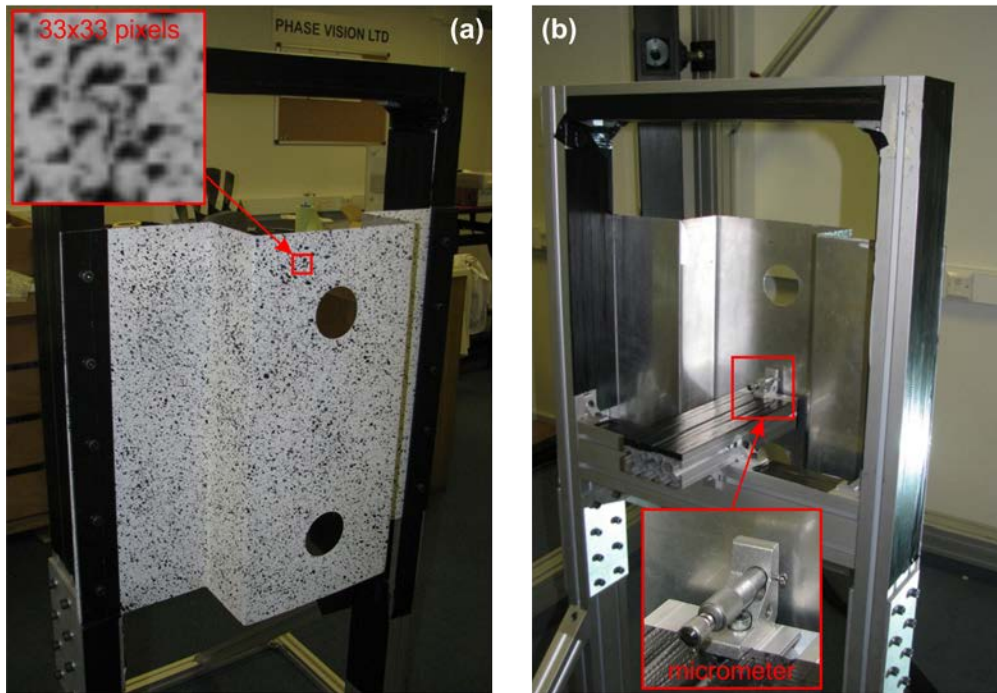


Figure 59: Specimen support frame and loading micrometer. (a) Front view, shown with a 33×33 correlation window. (b) Rear view, shown with the loading micrometer.

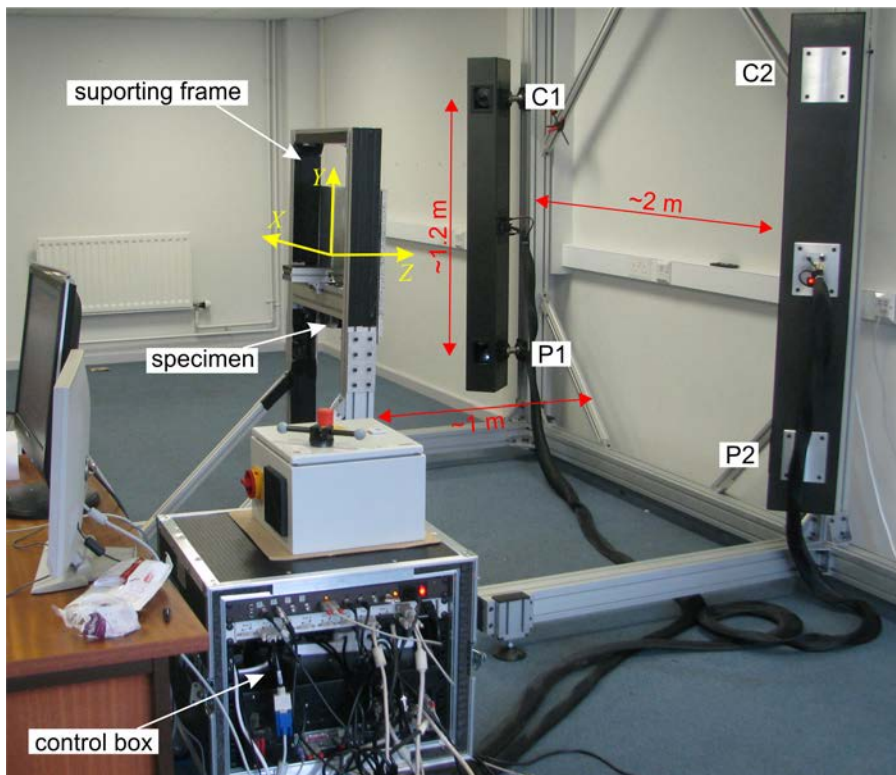


Figure 60: Experimental configuration.

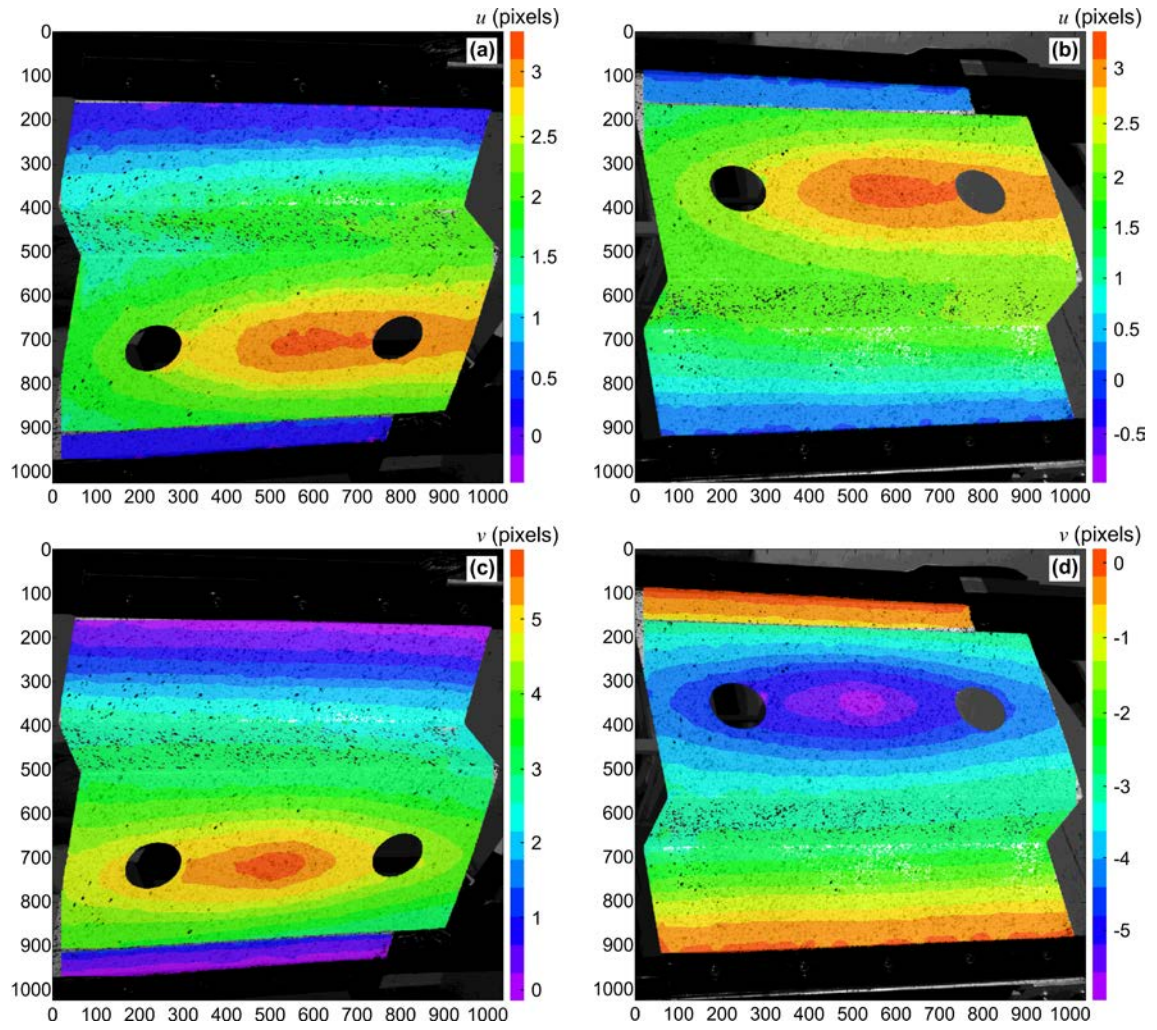


Figure 61: Estimated image-plane displacement fields for a micrometer displacement δ of 5 mm. (a,c) Horizontal and vertical displacements by pair C1P1, respectively. (b,d) Horizontal and vertical displacements by pair C2P2, respectively.

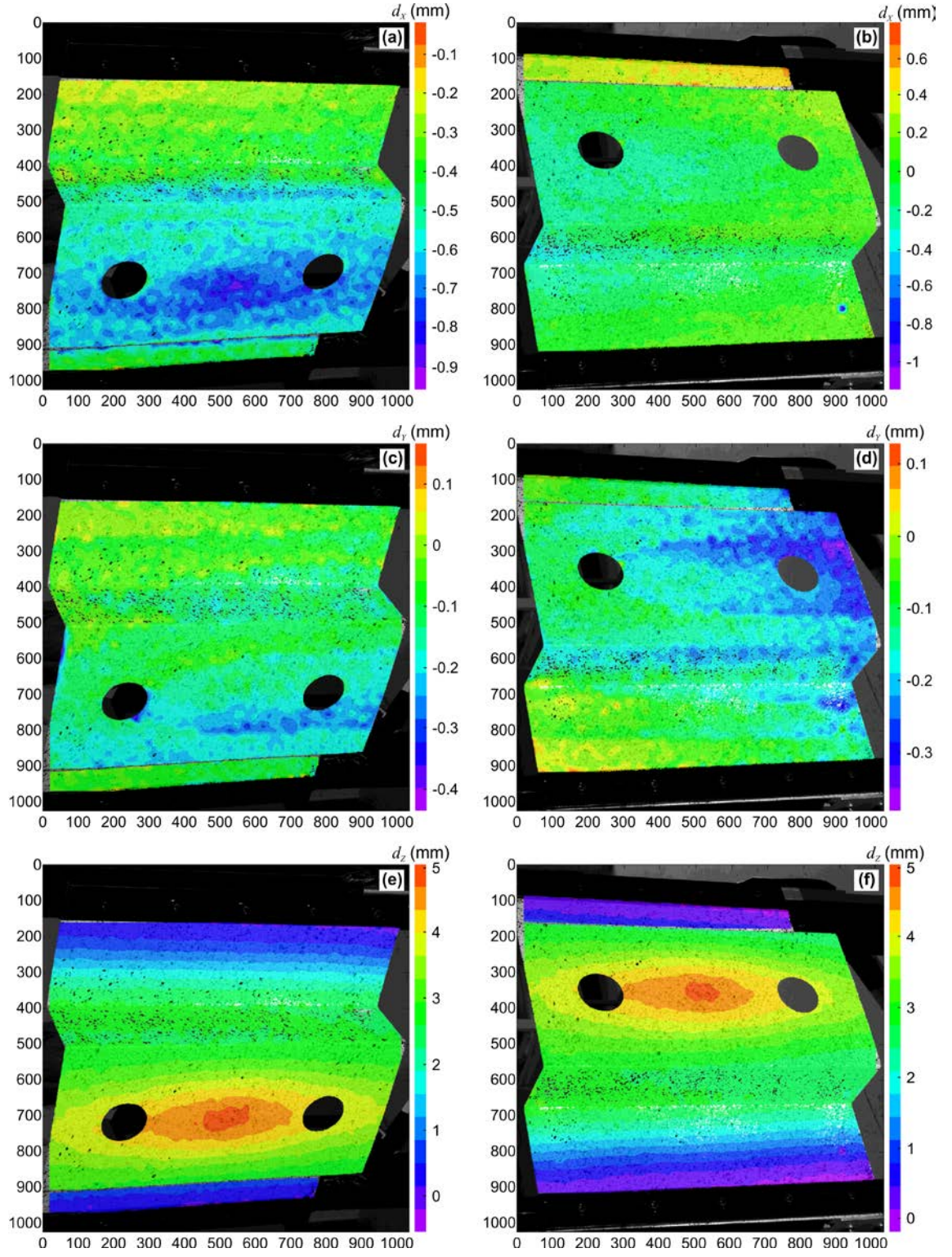


Figure 62: Estimated components of the 3D displacement field for a micrometer displacement δ of 5 mm for pair C1P1 (a,c,e) and C2P2 (b,d,f).

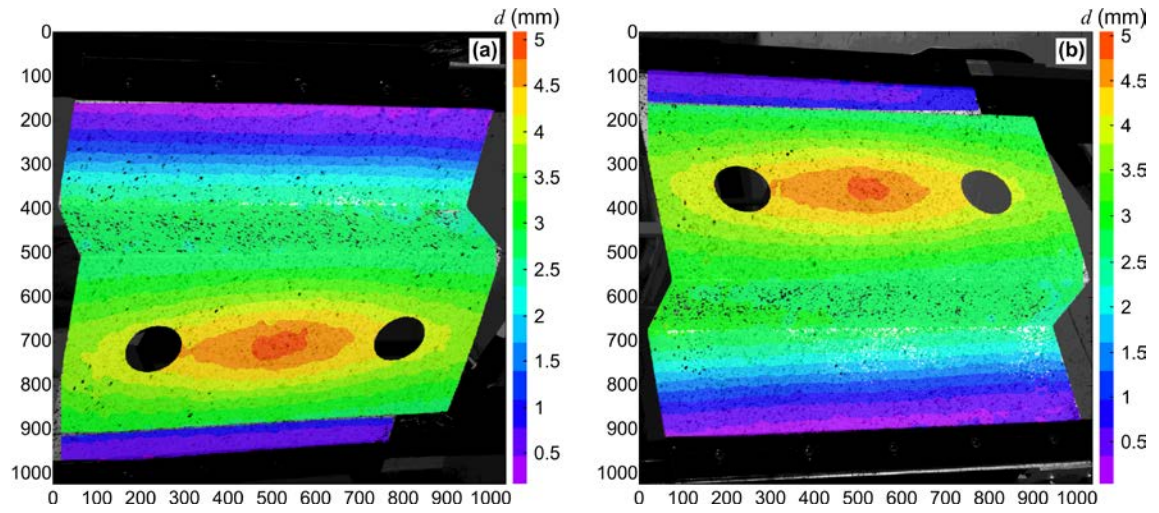


Figure 63: Estimated displacement magnitude field for a micrometer displacement δ of 5 mm for pair C1P1 (a) and C2P2 (b).

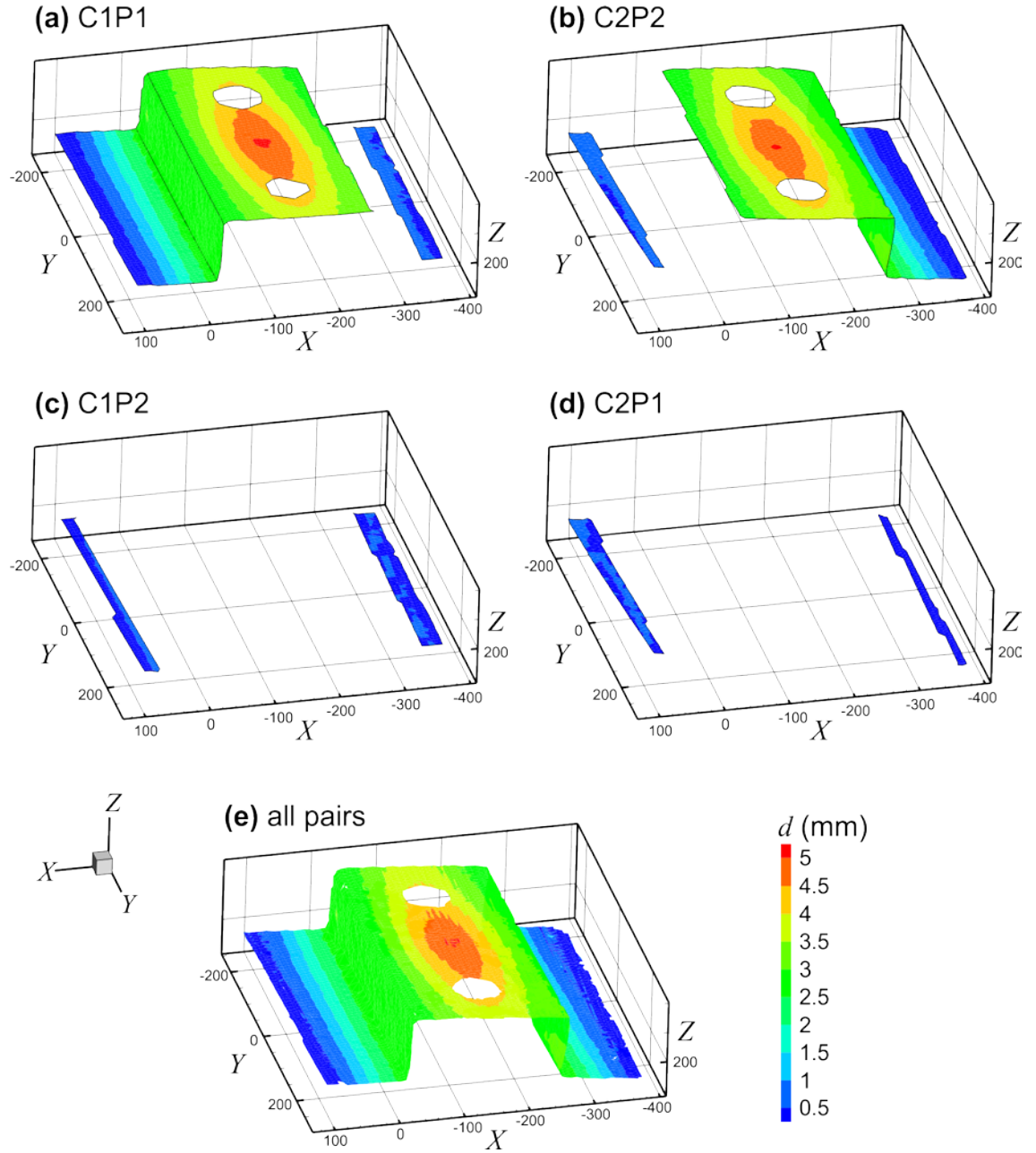


Figure 64: Displacement magnitude fields measured by the four camera-projector pairs (a-d) and the combined results of all pairs (e) for micrometer displacement δ of 5 mm. The fields are displayed on top of the measured specimen at the reference state. The coordinate system is defined in the calibration process and is the same for all pairs.

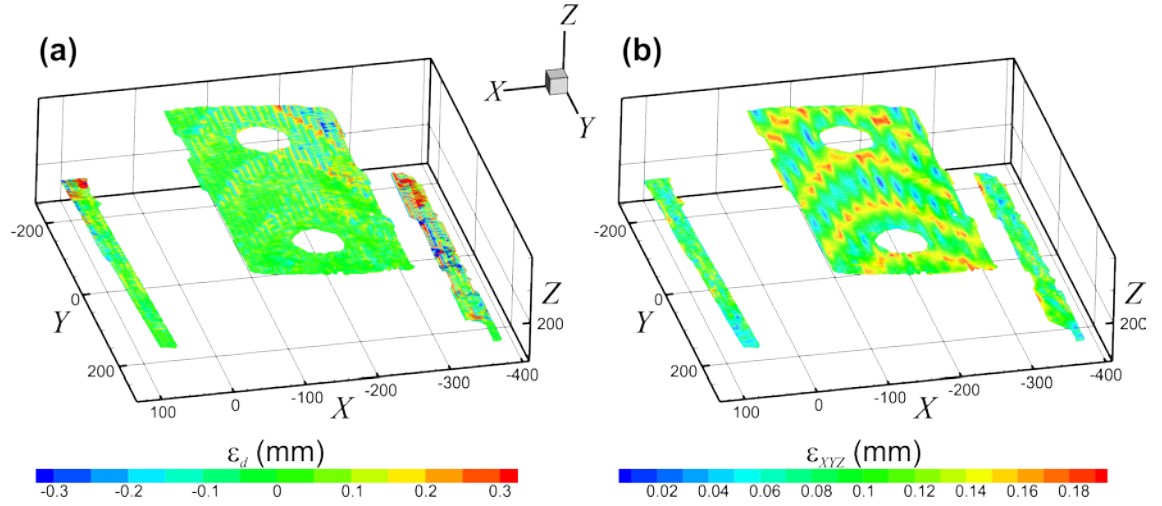


Figure 65: Discrepancies of displacement magnitudes (a) and measured coordinates (b) among the four camera-projector pairs for the micrometer displacement δ of 5 mm. Only data available in at least two pairs are shown.

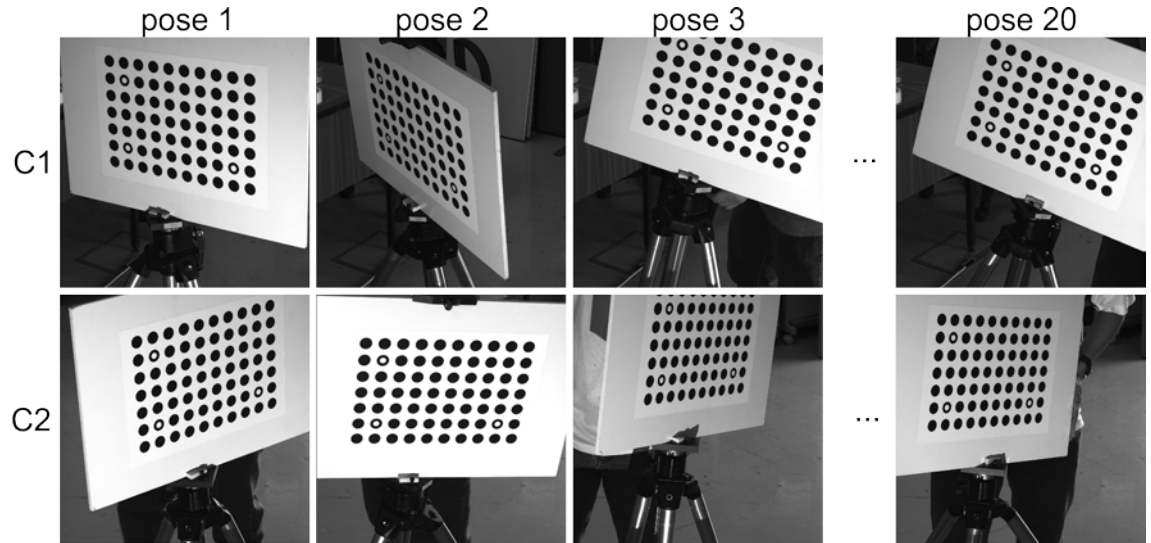


Figure 66: Images used to calibrate the stereo-DIC software. A circle pattern with known circle distance was generated by the software, printed out, attached on a flat panel and orientated at 20 poses in the common view of cameras C1 and C2.

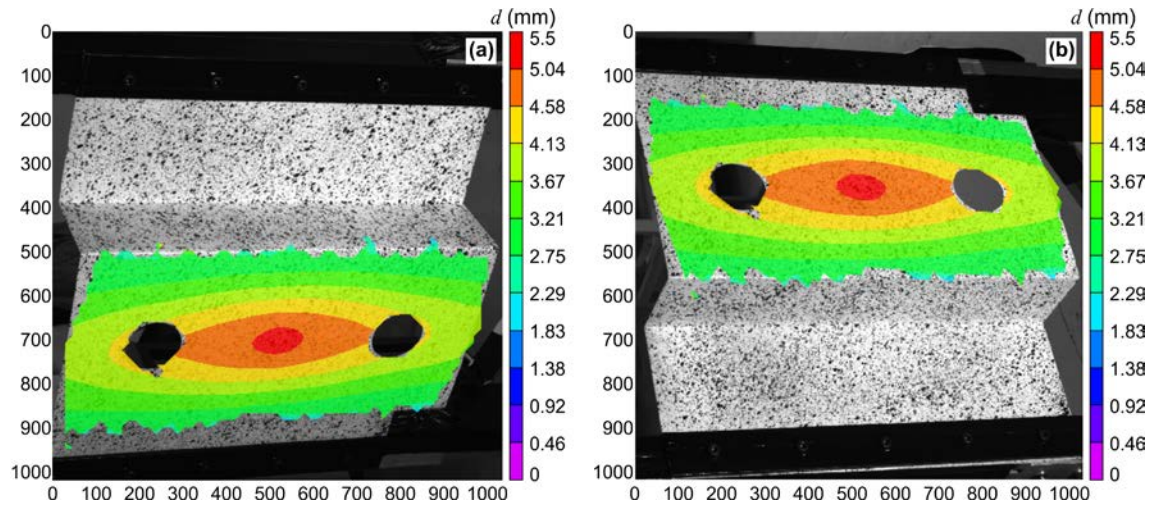


Figure 67: Displacement magnitude field by the stereo-DIC system for a micrometer displacement δ of 5 mm and plotted on the image of camera C1 (a) and C2 (b).

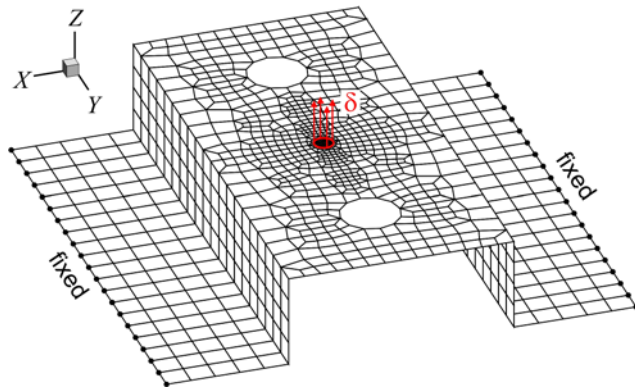


Figure 68: Finite element model of the experimental sample.

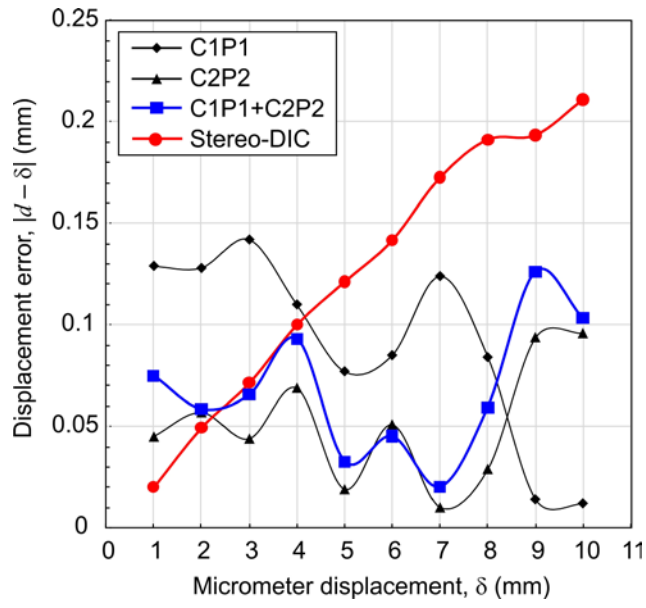


Figure 69: Error of displacement magnitude estimated at the centre point by the new system and the stereo-DIC system for various micrometer displacement values.

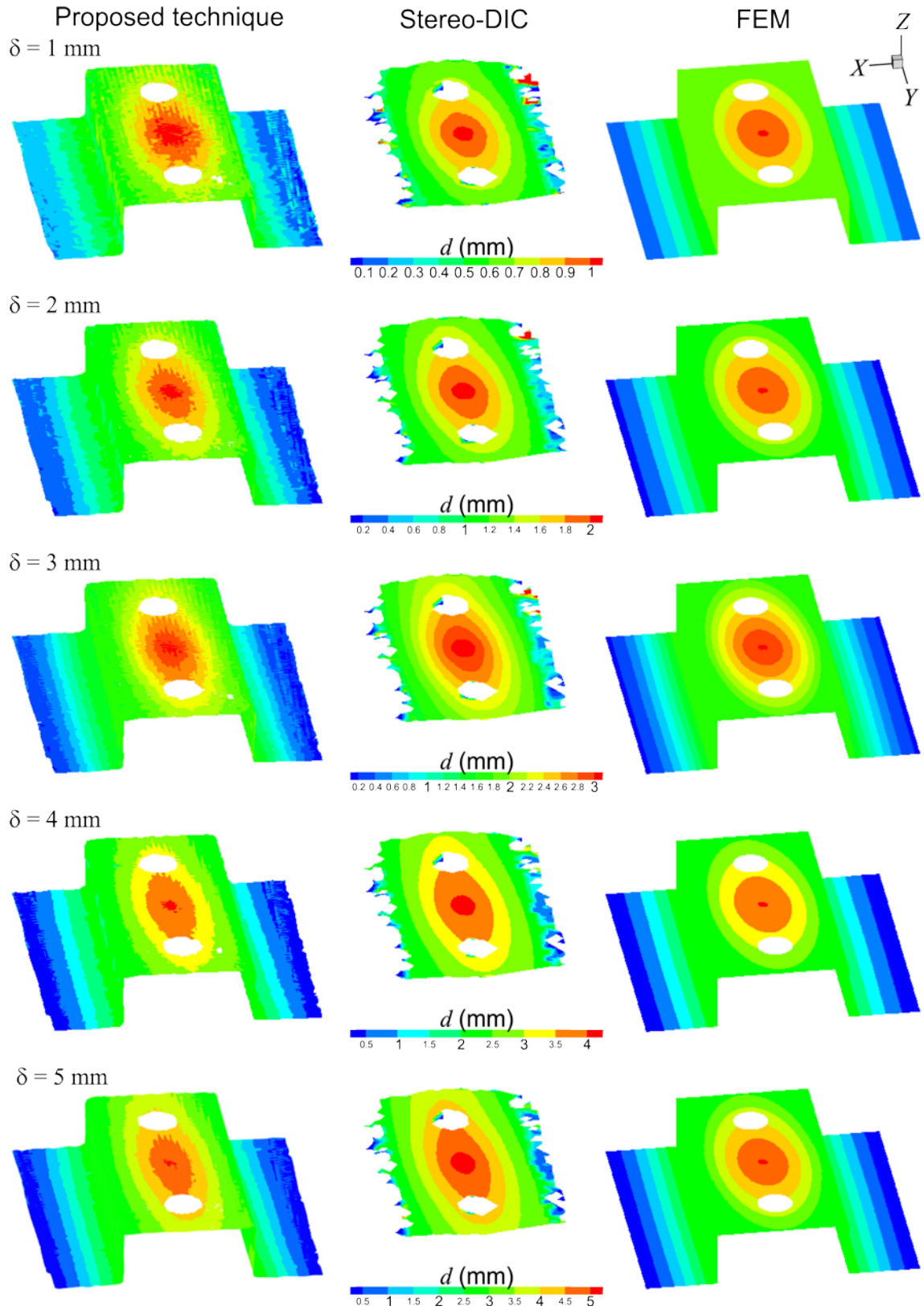


Figure 70: Displacement magnitude fields computed by the proposed technique, the stereo-DIC software and the finite element analysis for micrometer displacement δ ranging from 1 mm to 5 mm. All of the models are in the same coordinate system.

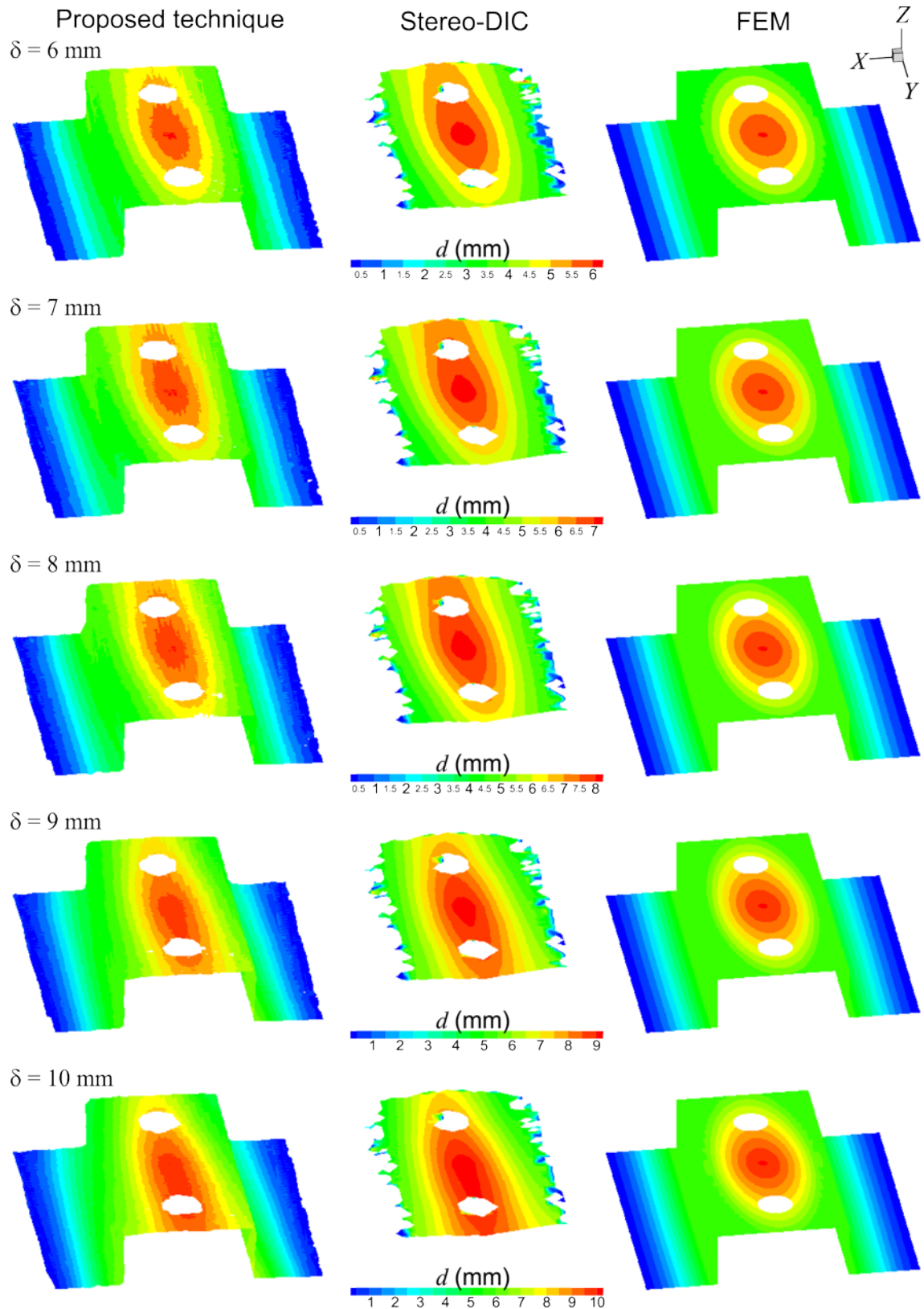


Figure 71: Displacement magnitude fields computed by the proposed technique, the stereo-DIC software and the finite element analysis for micrometer displacement δ ranging from 6 mm to 10 mm. All of the models are in the same coordinate system.

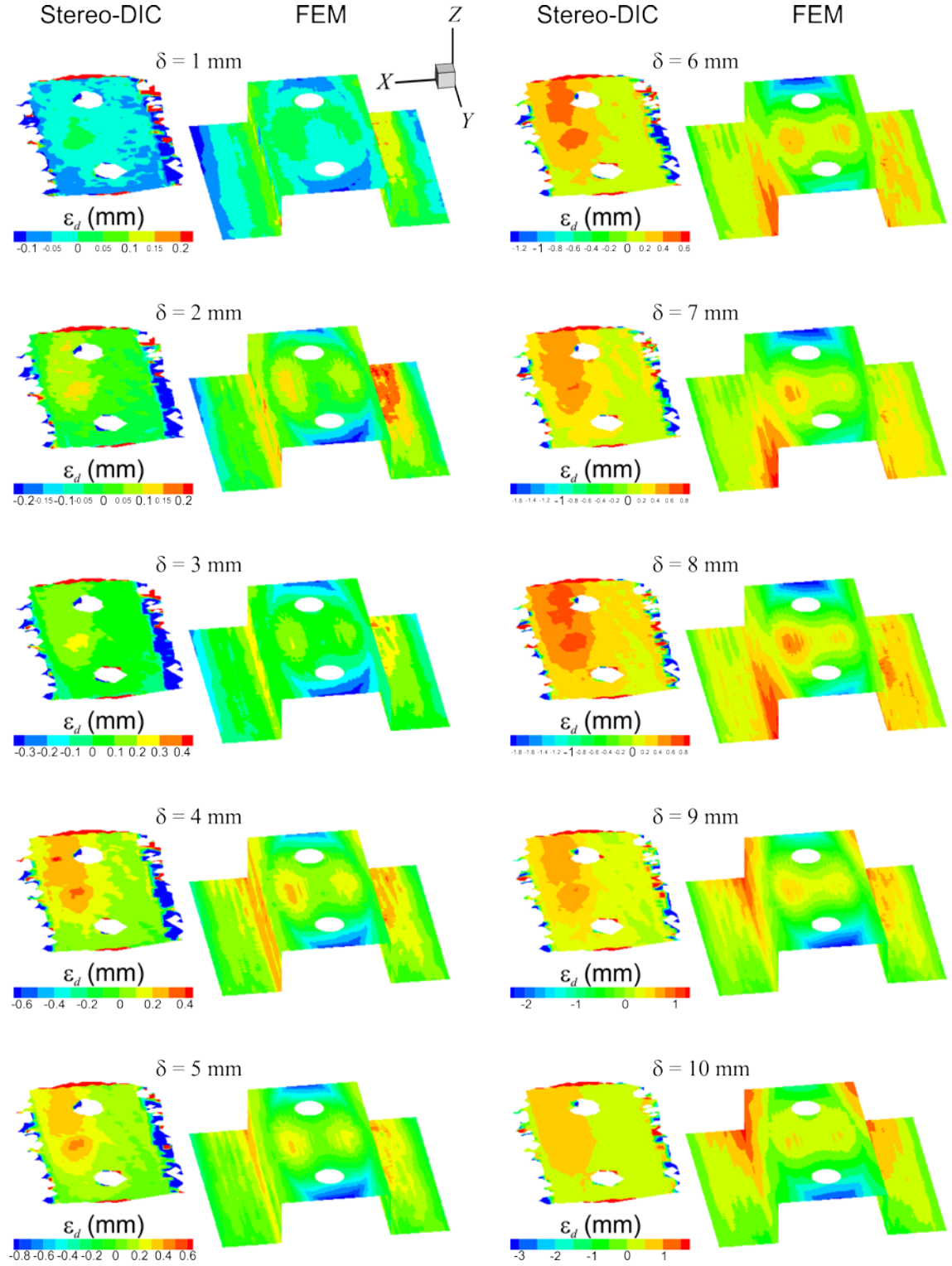


Figure 72: Displacement magnitude errors of the stereo-DIC and the finite element analysis from the proposed technique, for micrometer displacement δ ranging from 1 mm to 10 mm.

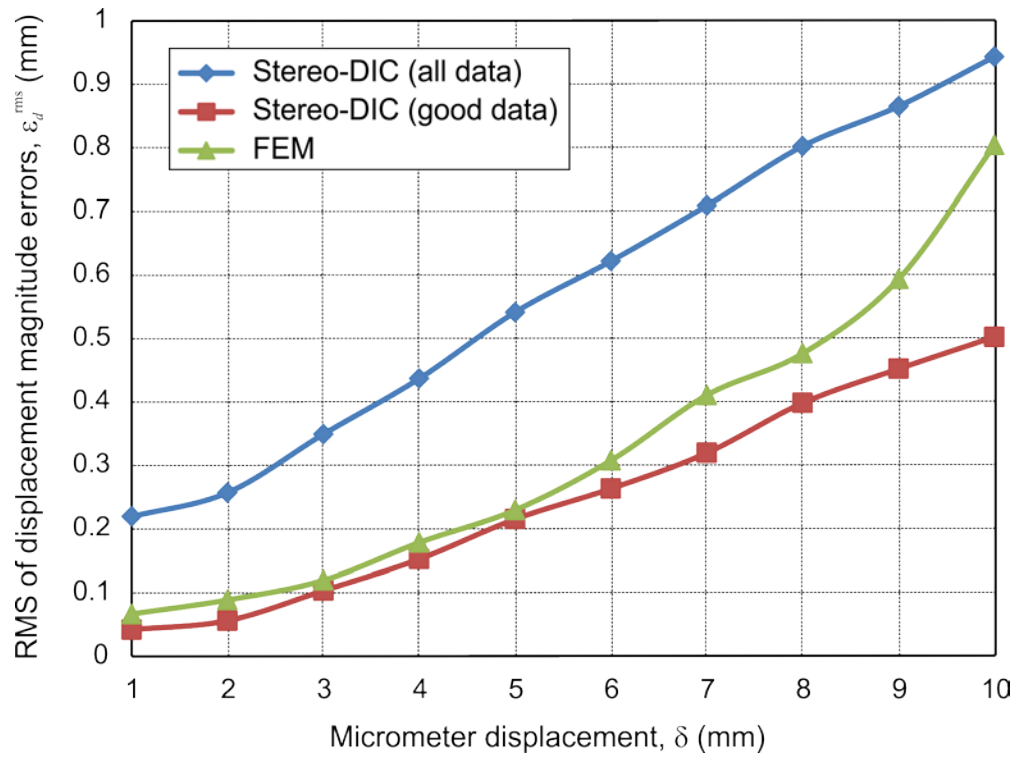


Figure 73: RMS errors of displacement magnitude fields of the stereo-DIC and the finite element analysis as compared to the proposed technique.

Chapter 6

Applications in the aerospace industry

6.1 Overview

6.1.1 Measurement techniques for aerospace applications

Optical 3D shape and deformation measurement techniques are increasingly important across many manufacturing industries. In the aerospace industry, the development process of an aircraft often requires measurement of shape and/or deformation of a component during prototype design, manufacturing and structural testing. Wind-tunnel test models of various aircraft components such as wing, engine and fuselage need to be designed, built and measured with high accuracy in order to optimise the aerodynamic performance. The accurate information of their geometries may be achieved by coordinate measuring machines (CMMs) and laser scanning techniques. Other important aerodynamic parameters such as velocity of the surrounding air flow can also be optically measured by the particle image velocimetry (PIV) technique [123, 124] (which is a counter part of the digital image correlation used for experimental solid mechanics). Likewise, the manufacturing stage requires tools, moulds, fixtures and jigs to be accurately measured for shape and position. For example, the alignment of a Boeing 777's wing panel on a manufacturing jig has been monitored by a photogrammetry system [125]. The manufacturing quality also needs to be controlled by measuring manufactured parts and comparing them against the computer-aided design (CAD) models.

Structural testing is another crucial part of an aircraft development programme. A structural test is carried out for the purposes of certification and/or development. Certification is a regulatory obligation by an aviation authority that requires an aircraft to pass many complex and rigorous tests before it is cleared for take-off, such as coupon tests of material samples for mechanical strengths, element tests of wing panels for structural failures and full-scale test for simulating in-flight failures [126, 127]. Development tests, on the other hand, are driven by the need to optimise the aircraft weight and cost. These include structural tests to understand mechanical properties and

behaviours of new materials and new structures under various types of loading conditions.

For all of the structural testing purposes, almost all available optical methods have been employed by aerospace companies, in addition to the traditional contact methods using strain gauges and linear variable differential transformers (LVDTs) [128, 129]. Popular optical methods include moiré interferometry, photoelasticity, electronic speckle pattern interferometry (ESPI) and digital image correlation. For example, the digital image correlation technique was used to measure the stress intensity factors on a cracked wing panel [130] and investigate the dynamic buckling phenomenon of a stiffened panel [131] at Airbus UK. There are no existing standards to characterise optical measurement techniques. However, a recent European study known as SPOTS supported by the aviation industry proposed a standard design and testing of a reference material for calibration of optical systems for strain measurement [132].

6.1.2 Applications of the SMS at Airbus UK

The first prototype of the fringe projection system developed in the previous PhD research of Ogundana [18] at Loughborough University and Phase Vision Ltd was applied to a structural buckling test at Airbus UK and produced full-field measurement results that were in good agreement with other benchmarking techniques (e.g. digital image correlation). However, only out-of-plane deformation components could be measured with this first prototype.

The present PhD project, being sponsored by Airbus UK, continues to take advantage of the state-of-the-art facilities at Airbus to demonstrate new capabilities of the improved fringe projection system in an industrial environment. The following applications have been done at Airbus UK using the system presented in this thesis:

- Measurements of the leading edges of an A320 and an A330 at Airbus manufacturing site in Broughton. Accurate measurements of the 3D aerodynamic shapes were required in order to evaluate actual deviations of the manufactured wings from designed CAD models. The author was involved with Dr Coggrave of Phase Vision Ltd in using two single-camera single-projector sensors (namely SMS800, with a nominal camera-projector baseline of 800 mm) for this programme. The sensors were calibrated using the automated calibration

system presented in Chapter 3. A wing was captured from many different viewing angles, and then the acquired 3D point clouds were stitched using the Polyworks software [104] based on overlapping coded markers that had been applied over the surface. Due to a non-disclosure agreement between Airbus and Phase Vision, the results of this programme cannot be provided in this thesis.

- Measurements of the wing cover of an A380 at Airbus R&D site in Filton (Bristol). The relatively smooth wing was under cyclic loading during a fatigue test. It was prepared with strain gauges to monitor strains at several critical points. The author was in charge of using a SMS800 system to measure the panel at several views along the wingspan. The final results from different views were then stitched by a home-built technique based on texture images of the surface, and were compared against those from the strain gauges. Details of this test are given in Section 6.2.
- Measurements of the wing panel of an A350XWB at Airbus R&D site in Filton. This next-generation aircraft wing is mostly made of carbon fibre reinforced plastic (CFRP) and has a complex geometry where the ribs and stiffeners introduce discontinuities. Additionally, an initial crack deliberately created for the testing purposes and the compression loading condition caused the panel to deform in a complicated buckling mode which became an interesting challenge to the present shape/deformation measurement system. The test is described in Section 6.3.

6.2 Fatigue test of metallic wing panel

6.2.1 Test description

Fatigue testing examines how an aircraft structure responds to stress over a long period of time and during different operation modes, such as taxiing on the runway, take-off, climbing to an altitude, cruising and landing [127]. To create such conditions in the laboratory, a combination of cyclic loads is applied on the structure by computer-controlled hydraulic jacks. A major fatigue test of the A380 super-jumbo jet accumulates 47,500 flight cycles over a period of 26 months. Fatigue damage is normally associated with the propagation of an initially small crack present in the structure that eventually compromises the load-carrying ability of the whole structure. A

fatigue test can be classified as static or dynamic depending on the strain rates which are induced by the changing rates of the applied loads.

The fatigue test presented in this section is for a part of the lower wing cover of an A380-800 aircraft. As shown in Figure 74, the part comprises of an aluminium skin panel strengthen with stringers and ribs. The overall dimensions are approximately 5 metres in length, 1 metre in width and 0.2 metre in depth. The two ends of the part were clamped on more-rigid metal blocks which were connected to a hydraulic loading machine. The part was loaded in both compression and tension.

The region of interest is a central $900 \times 175 \text{ mm}^2$ area of the part. On the back of this region, there are two stringers with different conditions. As shown in Figure 75, stringer B contains a crack that has propagated along the stringer from the right to the left. It is therefore predicted that the low stress-carrying ability of the stringer will affect the overall stress distribution over the region of interest. The objective of the present test is to measure the displacement and strain field on the front surface during a fatigue loading period. It is noted that the applied load varied so slowly that the fatigue test was relatively static. A total of 42 strain gauges were attached to the front and back of the panel at various critical positions to monitor the strain variations, some of which are used to verify the strain results of the proposed SMS-DIC technique.

6.2.2 Test preparation and execution

The inspection was performed using a Phase Vision SMS800 sensor with a camera-projector separation of about 800 mm and a camera resolution of 1024×1024 pixels. The system was calibrated for a measurement area of approximately $300 \times 300 \text{ mm}^2$ with a point cloud estimation RMS error of 0.035 mm. The global coordinate system attached to the scanner was defined so that the X-axis pointed to rightwards along the panel length, the Y-axis pointed upwards across the panel width and the Z-axis pointed towards the scanner. The origin, which is at the centre of the measurement volume, was located approximately 1.2 m away from the scanner. The main calibration was done at Phase Vision's laboratory in Loughborough using both the initialisation circle pattern and the refinement ball bar described in Section 2.4. Upon being transported to the Airbus site in Filton, the calibration parameters might have changed slightly. Therefore, a quick calibration using the circle pattern and a manual ball bar was done to compensate for any changes. The previous calibration parameters were taken as the

initial guess for the optimisation process. However, it was observed that the largest change did not exceed 2% and therefore was negligible.

Since the $900 \times 175 \text{ mm}^2$ region of interest exceeds the calibrated measurement volume of the sensor, a smaller region of interest was selected on the panel surface where the structure was likely to give rise to variations in the resulting strain field, as shown in Figure 74-b. The SMS was translated along the panel to three positions to generate overlapping views of the region of interest, for each of which a full cycle of loads and measurements was acquired. In this test, the load F was applied from a maximum tension of 1950 kN to a maximum compression of -1135 kN with an uncertainty of about ± 3 kN.

A common practice in preparing the speckle pattern to be used for image correlation techniques is spraying paint directly onto the surface. The advantages of this approach are that it can be done quickly and that the speckles adhere strongly to the surface. However, paint spraying was not practical and not allowed in the present test. Alternatively, the speckles were printed on adhesive papers before the test date and applied to the surface on the test date. The speckle pattern created by this method and applied to the skin surface of the wing cover is shown in Figure 76. The adhesive layer is very thin, sticky and stretchable, thus ensuring that the speckle pattern deforms with the surface even in large deformation. The adhesive paper is a commonly-available photo transfer paper which contains a transparent layer to print the feature and an adhesive layer to stick to the surface. In the first preparation step, several synthetic speckle patterns with different speckle sizes and distributions were generated on the computer using the algorithm described in Section 4.3.3 and printed on a 600dpi laser printer to draft papers. Each draft pattern was placed at the assumed location of the specimen in the field of view of the scanner, and its image was taken by the camera. The optimum speckle pattern was chosen from all of the recorded speckle images so that an average speckle contains 5-7 pixels. Then, the optimum pattern was printed to an A4-size photo transfer paper. To cover an area larger than an A4-size paper, additional patterns with the same speckle size but different random distribution were also created and printed to transfer papers. Finally, on the test date the transfer papers were applied to the wing skin surface within 30 minutes. The patterns can be removed after the test with warm water.

6.2.3 Camera views alignment

The proposed shape and deformation measurement technique was applied for all views at the same loading state, resulting in point clouds and displacement fields defined in three different coordinate systems. In an additional alignment stage, the coordinate transformations of view 1 and 3 with respect to view 2 were estimated by using their overlapping speckled areas as the markers. On the texture images for the undeformed state (i.e. simply from the original shape measurement data), several pairs of approximately matched points were selected within the overlapping area of view 1 and view 2. The 2D DIC technique was used to refine the image coordinates of these matched points. Then, their corresponding 3D coordinates were extracted from the original point clouds.

Theoretically, there exists a rigid-body transformation between these two sets of 3D coordinates, which can be estimated by the singular value decomposition technique (SVD) as presented in [133]. The obtained transformation simply relates the two positions of the SMS and is therefore common to all loading states and all data points. Hence, it can be applied to all 3D deformed coordinates of view 1 in order to bring them into the coordinate system of view 2. The same process was used to bring view 3 into the coordinate system of view 2.

6.2.4 Measured displacement fields

The results of 3D displacement fields are displayed in Figure 77, Figure 78 and Figure 79 with respect to the X -, Y - and Z -component, respectively. It is noted that the displacement fields are plotted on top of the deformed shapes which are defined in the coordinate system of view 2. The correlation window size was chosen to be 33×33 pixels, and the separation between image sample points was 32 pixels. Each displayed displacement field was interpolated to the single pixel level, and therefore contained around 3 million data points. The results are presented for several states of a fatigue loading cycle, which are the unloaded state ($F = 0$ kN), four tension states ($F = 524, 985, 1445$ and 1955 kN) and five compression states ($F = -206, -409, -673, -912$ and -1135 kN).

It can be seen that the displacement in the X -direction, which is almost the loading direction, is dominant as expected for a compression test of a relatively long panel. The magnitude of the X -displacement is larger towards the loading block (on the right) and

smaller towards the middle of the panel (on the left), which is also reasonable for a uniaxial test with two-end loading. The Y - and Z -displacement increase spatially towards the cracked stringer B which is less able to carry stress than stringer A. The deformation also increases towards the left of the area where the skin is least supported by the stringers.

Slight discrepancies among the three camera views can be observed from the displacement fields. The causes may be (i) the view alignment error mainly due to mismatching of the overlapping speckle regions, (ii) changes in testing condition across different views, such as vibration and lightning, and (iii) the uncertainty of the loading machine when repeated for every view, which is however less than 1% of the applied loads.

6.2.5 Measured strain fields

Computing strain fields from displacement fields is a well-established problem in finite element analysis, experimental mechanics and image processing. Some methods to compute a strain field from a discrete displacement field obtained by digital image correlation were presented by Sutton et al [62], Geers et al [134] and Hild et al [135]. A 2D/3D strain computation software package written in MATLABTM was also introduced by Teza et al [136] for imaging analysis of landslides.

For the present test, a simpler method was developed to compute an infinitesimal strain field based on the formula of Cauchy's infinitesimal strain tensor,

$$\varepsilon_{ij} = \frac{1}{2}(d_{j,i} + d_{i,j}) \quad (5.1)$$

where ε_{ij} is the strain tensor, d_j is the displacement tensor and $d_{j,i}$ represents the partial derivative of the displacement (i.e., $d_{y,x} = \partial d_y / \partial x$). The assumption of this formula is that the higher-order partial derivatives are negligible, which is applicable for the present test of fairly homogenous panel undergoing relatively small deformation. Equation (5.1) can be written explicitly for the three in-plane strain components,

$$\varepsilon_{xx} = \frac{\partial d_x}{\partial x}, \varepsilon_{yy} = \frac{\partial d_y}{\partial y}, \text{ and } \varepsilon_{xy} = \frac{1}{2}\left(\frac{\partial d_y}{\partial x} + \frac{\partial d_x}{\partial y}\right), \quad (5.2)$$

where Oxy is a coordinate system attached to the skin surface with the x -axis going along the loading axis, ε_{xx} is the longitudinal strain, ε_{yy} is the transverse strain, and ε_{xy} is the shear strain. The factor of $\frac{1}{2}$ in the definition of shear strain is commonly omitted in engineering shear strain. The strain calculation includes the following two steps:

1. Converting the in-plane displacements to the frame Oxy : The global frame XYZ in which the measured displacements are defined is not necessarily attached nor aligned to the panel surface, and thus cannot be used to represent surface strains. Instead, the frame Oxy is defined so that the y -axis is parallel to the line connecting strain gauge 1 and 2 (as shown in Figure 76), the x -axis is the symmetry line of stringer A and B, and the origin O is arbitrarily located near the centre of the view 2. This frame is associated with some markers physically defined within the speckle pattern. These markers are visible to the cameras, so their global XYZ coordinates can be extracted from the 3D shape data. Therefore, a rigid body transformation that aligns the two frames can be estimated and then applied to all data points in order to bring them into the in-plane frame Oxy .

2. Computing the partial derivatives $\frac{\partial d_x}{\partial x}$, $\frac{\partial d_y}{\partial y}$, $\frac{\partial d_x}{\partial y}$ and $\frac{\partial d_y}{\partial x}$: Displacement fields are defined on a discrete and generally non-regular grid of sample points. A common approach in finite element analysis to computing a local partial derivative of displacement is to assume a linear shape function that models the deformation of an element bounded by three/four neighbouring sample points. The derivatives can then be determined by differentiating the shape function and solving a set of linear equations for every element. For the present case of nearly 3 million elements, such a repetitive implementation is not computationally economical. Alternatively, the high density of the data points (which is 1,000 points in 300 mm) suggests that finite differences computed from neighbouring data points can be used to approximate the partial derivatives. In this work, a MATLAB function developed by Phase Vision was used to compute the partial derivatives. The derivative $\frac{\partial d_j}{\partial x}$ (where $j = x$ or y) at a given point (x,y) was estimated from the d_j values over a square region of size $N_s \times N_s$ (with $N_s=7$ pixels

in this experiment) centred at (x,y) . A gradient estimator with reduced variance compared to a simple finite difference operator is obtained by least squares fitting a first-order polynomial to the displacement data along each row of the square and then averaging the N_s , resulting best-fit gradients over all the rows.

The derivative $\frac{\partial d_j}{\partial y}$ (where $j = x$ or y) with respect to y was carried out in the same way but with the least squares fitting carried out along the columns of the square and the gradients averaged over the columns.

The resulting ε_{xx} and ε_{yy} strain fields for the cases of maximum tension ($F = 19955$ kN) and maximum compression ($F = -1135$ kN) are shown in Figure 80 as examples. For both cases, it is observed that (i) the longitudinal strain ε_{xx} increases in magnitude towards the cracked stringer in the bottom and (ii) the transverse strain ε_{yy} increases in magnitude towards the panel centre. The longitudinal strain has much higher value than the transverse strain, as the deformation is mostly along the loading axis. The presence of the crack also appears to affect the strain distribution, as visualised by the deflection of the equi-strain lines near the crack tip.

To compare against the strain gauges, strain values of data points lying on the cross-section line which connects the two strain gauges are extracted from the longitudinal strain fields. The ε_{xx} strain results for all of the loading cases are shown in Figure 81, where the readings of the strain gauges are also incorporated for comparison. The exact readings of the strain gauges are given in Table 5 with the uncertainty of about 1 microstrain. It can be seen that the strains measured by the proposed SMS-DIC technique have a linear variation along the cross-section that is very close to that of the strain gauges. The maximum error between the two methods is approximately 100 microstrain. As compared to the stated accuracy of up to 50 microstrain of the well-known VIC-2D/3D digital image correlation system [16], the currently achieved strain accuracy by the proposed technique is acceptable. Possible sources of the strain error include (i) the approximation method of the partial derivatives (which could have been improved by reducing the finite difference step and incorporating a higher-order shape function), and (ii) the inherent error in the measured displacement fields (which may have been affected by insufficient calibration or vibration of the test jig on which the scanner was placed). Also, it is observed that the data curves by the proposed technique

seem to be offset from the strain gauge lines by approximately 50 microstrain. This offset suggests a systematic source of error during this experiment, which could possibly be the calibration error and the vibration of the test jig as mentioned earlier. Another possible cause is the small force applied by the loading machine to the specimen to keep it stable before the test, which was not recorded by the strain gauges but by the proposed system.

6.3 Buckling test of composite wing panel

6.3.1 Test description

A350 is the next generation of long-range and wide-body aircrafts developed and manufactured by Airbus. It will be the first Airbus aircraft to have both wing and fuselage structures made primarily of carbon fibre-reinforced plastic (CFRP) [137]. The Airbus Centre of Excellence in Bristol is in charge of designing, manufacturing and testing the wing structure of the aircraft. To support one of their structural tests, the proposed SMS-DIC technique was applied to measuring 3D displacement fields of a full-scale lower wing cover of an A350XWB under compressive loading.

An aircraft wing can bend upwards or downwards during a flight due to the interaction of many forces, such as aerodynamic lift and aircraft weight. This causes the lower (as well as upper) cover to be stretched or compressed. Being under compression is usually more dangerous to the panel than being under tension, as it is prone to buckling failure. Buckling is a stability problem which causes a compressed structure to deform into undesired shape and lose its integrity. It is very sensitive to geometrical imperfections that are present in any practical structure, and may occur at low external loads and in the elastic range of the material. When buckling occurs, although loaded in-plane the panel may exhibit out-of-plane deformation in many different mode shapes. An example buckling mode shape is illustrated in Figure 82. Buckling phenomena of composite panels are even more complicated than those of metallic ones, due to the inhomogeneous and anisotropic nature of the composite materials. Delamination or disbonding of adjacent layers may propagate in the presence of buckling and lead to catastrophic failures.

The tested specimen is depicted in Figure 83, which is a $1.8 \times 1.3 \text{ m}^2$ wing cover section comprising a relatively flat skin stiffened by two ribs and five stringers. For testing

purposes, a disbond of the middle stringer from the skin was created in the central area. The specimen was mounted on a test rig supplied by J.R. Dare Ltd that has a load capacity of 2,000 tonnes. Compressive loads were applied to the opposite ends of the panel through two loading blocks. A steel support frame was attached to the specimen to keep it standing straight and steady. There were also four horizontal tie rods to hold the two unloaded edges of the panel. At the initial state, there was a clearance of approximately 10 cm between the upper loading block and the support frame. The maximum displacement of the upper loading block was controlled so that it did not exceed this clearance.

The SMS was used to measure the 3D displacement field on the back of the specimen. Besides, several acoustic sensors were also attached to the back in order to monitor the propagation process of the disbond. Two high-speed cameras were located in the back to record the deformation process for qualitative assessment of the buckling failure. Various strain gauges were also applied to the back surface at critical locations to monitor strains. Meanwhile, the 3D deformation of the front surface was monitored by a stereo digital image correlation system. For this purpose, the front surface was prepared with a random speckle pattern.

6.3.2 Test preparation and execution

A Phase Vision's SMS800 system with the camera-projector baseline of 800 mm was used for the buckling test. In the initial test plan, the SMS was supposed to observe an area of $1.2 \times 1.2 \text{ m}^2$ with a stand-off distance of about 4 m, as shown in Figure 84-a, in order to cover most of the panel and the support frame. The support frame was prepared with random speckles so that its rigid-body movement can be tracked and subtracted from the measured displacement of the specimen. However, due to a technical incident in the test site, the plan had to change and the SMS was moved forward to a stand-off distance of approximately 1 m. The measured field of view was therefore reduced to an area of $300 \times 300 \text{ mm}^2$, which was chosen to cover the stringer disbond region in the centre of the specimen as shown in Figure 84-b. The scanner was rotated to the side by 90° to minimise optical obstruction caused by the two vertical pillars of the support frame. The projector was positioned higher than the camera so that the hot air coming out of the projector's bulb can move upwards easily for better heat dissipation. To assist

the image correlation process, the measured area was prepared with a random speckle pattern using the adhesive transfer paper technique introduced in Section 6.2.2.

The SMS was recalibrated on-site using a planar circle pattern as the reference artefact, as presented in Figure 85. The global coordinate system XYZ was defined by three distinguishable markers on the circle pattern when placed at the assumed location of the specimen. In the present arrangement, the X -axis pointed downward (nearly along the loading axis), the Y -axis pointed to the right of the specimen, and the Z -axis pointed towards the scanner (almost in the out-of-plane direction). The artefact mounted on a tripod was displaced and rotated at 15 different poses within the measurement volume. The centres of the circles were detected on the camera images and their coordinates were refined by a bundle adjustment algorithm. This quick calibration technique had been implemented in the measurement software of the SMS. The whole calibration process, including image acquisition and processing, took around 30 minutes. A RMS calibration error of approximately $30\text{ }\mu\text{m}$ (or nearly $1/10,000$ of the measurement volume side) was achieved.

The test execution was divided into two stages. The first stage employed all measuring equipment except for the SMS. The test was repeated in the second stage where only the SMS was used for measurement. The purpose of this was to keep the strong SMS projector light from disturbing the recording of the high-speed cameras. For each stage, there were two set of runs: *settling* runs and *failure* runs. In settling runs, the load was increased from 0 kN to 700 kN in increments of 87.5 kN to ensure that the panel is positioned properly. The load was then decreased to 0 kN. In the failure runs, the load was increased slowly from 0 kN towards the buckling load predicted by a finite element analysis. For the second stage of this test, the failure runs consisted of the compressive loads of 0, 211, 530, 1028, 1570, 2012, 2499 and 3008 kN. Complete buckling failure did not occur at the largest load. At each loading condition, the loading was ramped and held so that the SMS could complete a measurement. The shape data were achieved nearly in real time, but the deformation data were calculated off-line after the test.

6.3.3 Results of displacement fields

A texture image of the speckled specimen as captured by the camera at the reference (undeformed) state is presented in Figure 86-a, showing the geometrical complexity of the scene. The T-profile stringer connected to the skin contains four bolts and nuts as

seen on the top of the image. The stringer itself is disbonded from the skin in the central region, which is expected to cause discontinuous displacement field across the stringer edges. The flange of the stringer rising towards the camera can introduce different magnification from the base and thereby different image displacement as processed by digital image correlation. Four acoustic sensors with wirings are also visible, so is a metal tie rod running across. The projector light is obstructed by the tie rod, creating three shadow stripes on the skin and the stringer. Despite the complexity, the components have been identified and separated by the automatic image segmentation algorithm which utilises the knowledge of the 3D scene from the measured point cloud. The label map of 19 continuous regions detected in the view is presented in Figure 86-b. It can be seen that the bolts, nuts and sensor wires haven't been filtered out due to their low fringe visibilities and high phase errors. The tie rod and the acoustic sensors are kept in the result as their phase qualities are still within acceptable thresholds. However, the rod's shadow has been masked out completely as no fringes can be projected onto this region.

The measurement results for the case of the maximum applied compressive load of 3008 kN are given in Figure 87. The image displacement fields show that most of the movement is observed in the vertical direction of the loading with the vertical displacement component u increasing towards the image bottom. The 3D displacement fields (i.e., d_x , d_y and d_z in Figure 87-e, -d and -e, respectively) confirm that deformation in the X -direction is much larger than that in the Y -direction, and further show that the very significant deformation has also occurred in the Z -direction. This out-of-plane deformation is expected for a compression test when buckling has occurred. The 3D displacement fields reveal two 'hot spots' of large buckling deformation on the bases of the stringer which have been detached from the skin due to the disbond. The displacement magnitude field is displayed in Figure 87-f as well as in Figure 88 as a 3D representation. It can be seen from the results that measurement data have been achieved even on the narrow edge of the stringer flange. The displacement data of one continuous region is distinguishable clearly from adjacent ones, particularly along their boundaries.

The whole buckling sequence is presented by the out-of-plane displacement fields shown in Figure 89. As the applied compressive load increases, the stringer tends to

buckle before the skin does. The largest out-of-plane deformation is observed on the right base of the stringer, which keeps increasing with the applied load. The deformation of the skin in particular, as well as the whole panel in general, is not clearly visible in this representation due to the limited range of the colour bar. It would be interesting to compare this displacement field of the skin's back surface measured by the SMS-DIC technique with that of the skin's front surface measured by the stereo-DIC system. However, the author was not authorised to access the DIC measurement data.

6.4 Summary

Two applications of the proposed SMS-DIC technique to structural testing at Airbus UK facility have been presented. The first application is a static fatigue test of a metallic wing panel of an A380 aircraft. It has been shown that the proposed technique was able to obtain both displacement and strain fields of the panel. The measured strain results are in acceptable agreement with those of strain gauges attached to the panel, with a maximum discrepancy of about 100 microstrain. The second application is a buckling test of a composite wing cover of an A350XWB aircraft. The complex geometry, deformation and optical access of the specimen introduced several challenges to the deployment of the system. However, the obtained displacement fields have been able to show the structural behaviour of a disbanded stringer as it develops with the buckling failure. This therefore has demonstrated the performance of the proposed technique in measuring discontinuous surfaces in industrial environment.

6.5 Tables

Table 5: Strains measured by three strain gauges at various loads. The strain gauges are located as shown in Figure 76. The x -axis is orientated along the loading axis, and the y -axis is perpendicular to the loading axis. Uncertainty is approximately $1 \mu\text{m/m}$.

F (kN)	$\varepsilon_{xx}^{(1)}$ ($\mu\text{m/m}$)	$\varepsilon_{xx}^{(2)}$ ($\mu\text{m/m}$)	$\varepsilon_{xx}^{(3)}$ ($\mu\text{m/m}$)	$\varepsilon_{yy}^{(3)}$ ($\mu\text{m/m}$)	$\varepsilon_{xy}^{(3)}$ ($\mu\text{m/m}$)
0	4	6	4	0	0
524	433	442	417	9	539
985	809	830	779	17	1008
1445	1185	1221	1140	24	1474
1955	1612	1663	1548	33	1997
-206	-170	-171	-165	-4	-216
-409	-335	-342	-327	-8	-425
-673	-548	-561	-536	-14	-694
-912	-740	-759	-725	-21	-937
-1135	-919	-945	-904	-25	-1168

6.6 Figures

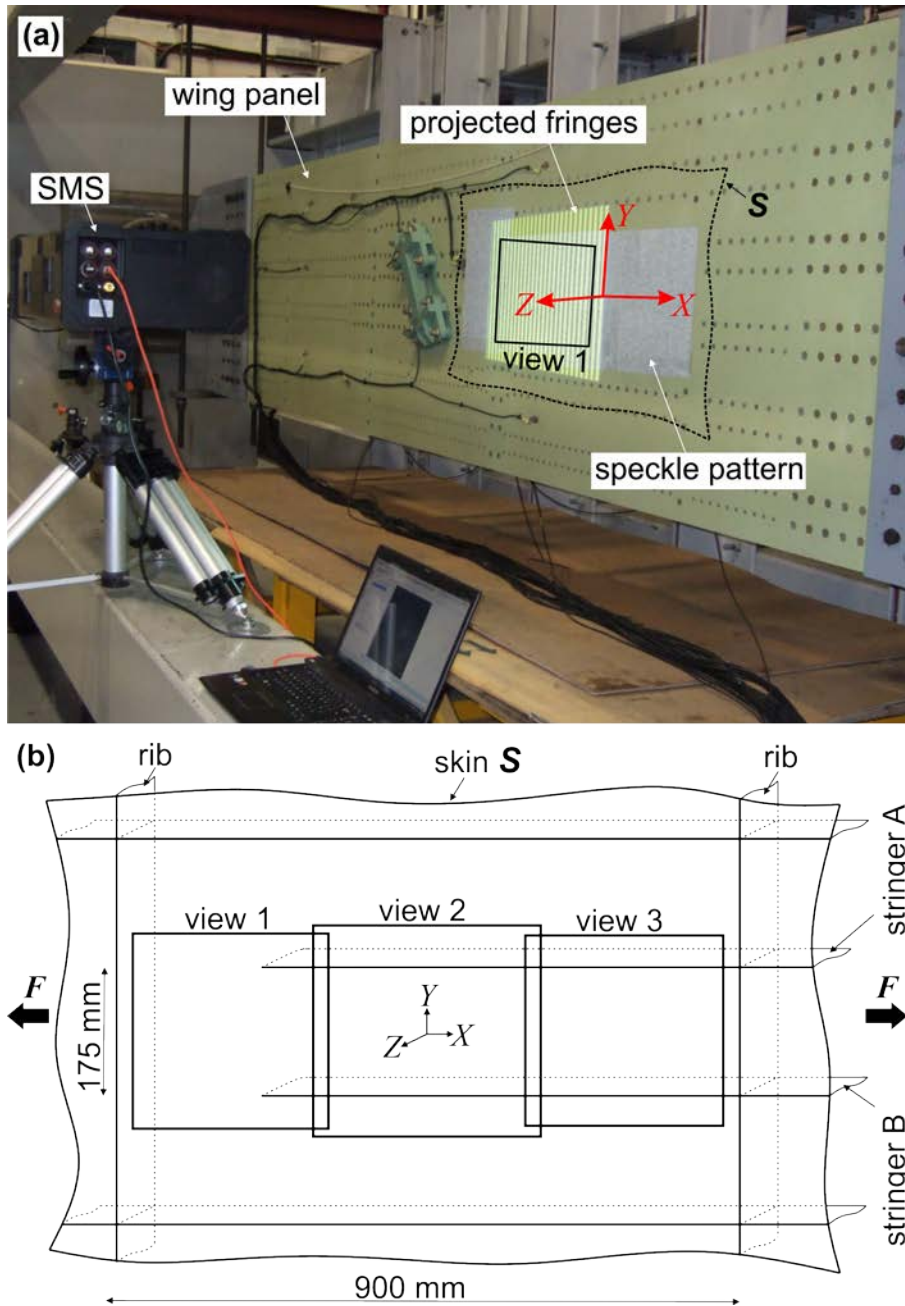


Figure 74: (a) Arrangement of the fatigue test. (b) Skin area S containing two different stringers as observed by three different SMS's views.

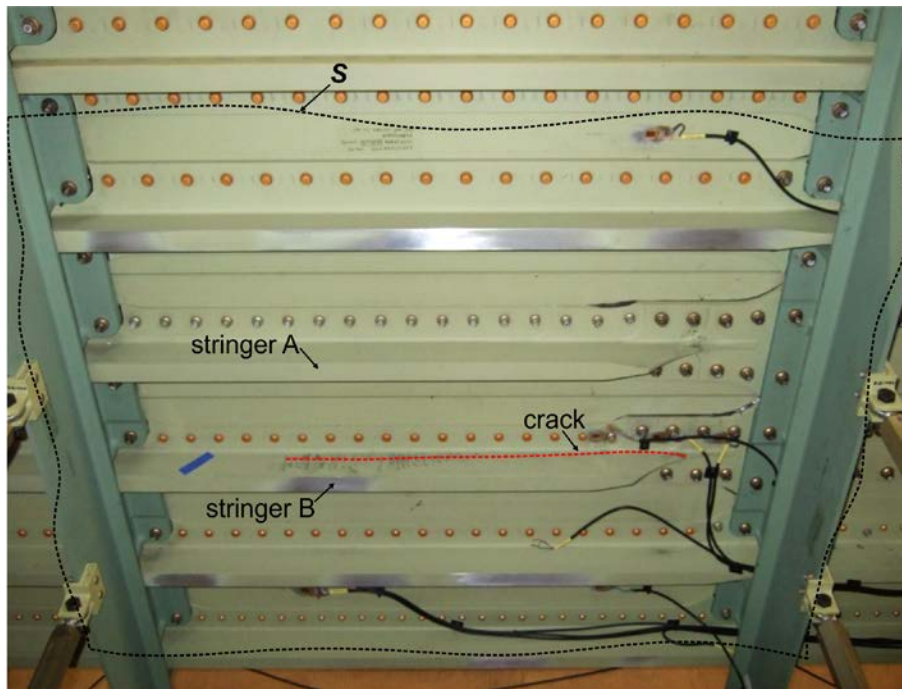


Figure 75: The back of the measured area. The area S shown in Figure 74-b is presented by the dashed lines. Stringer B contains a long crack propagating from the right to the left.

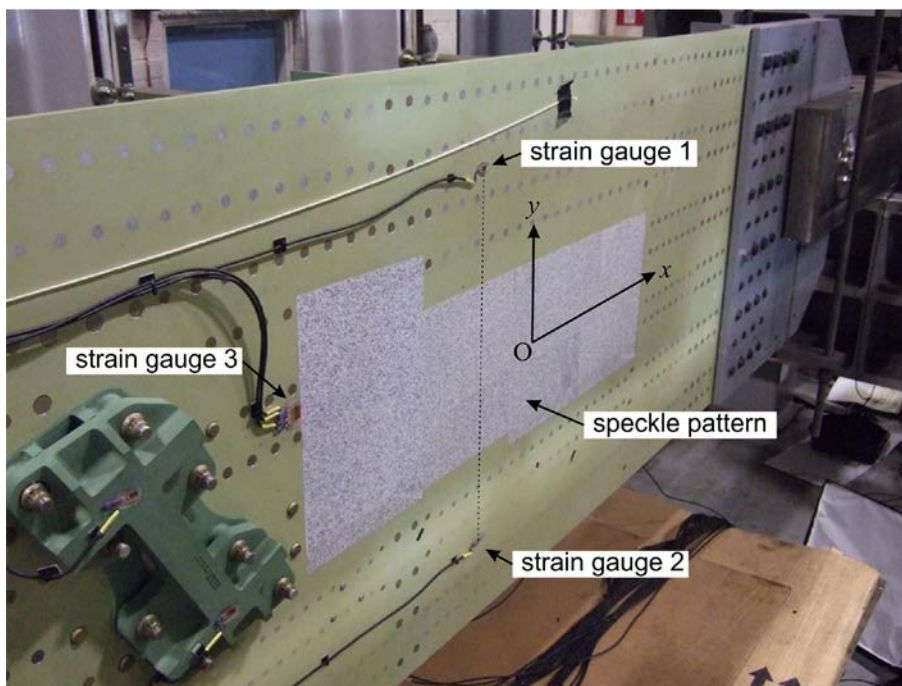


Figure 76: Speckle pattern applied to the skin using adhesive paper. Three available strain gauges measure in-plane strains. Presented strains are defined in the frame Oxy .

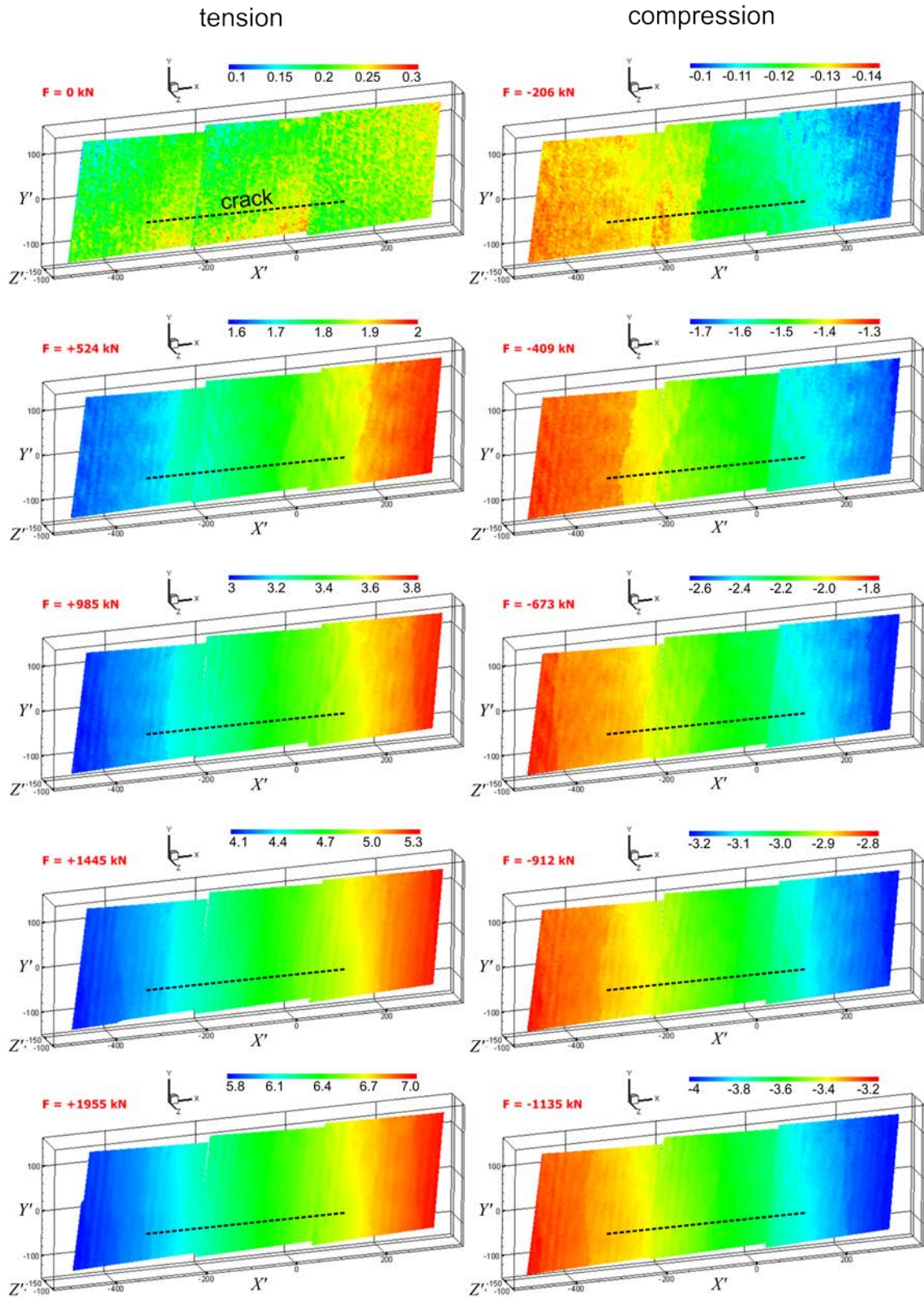


Figure 77: Measured displacement field in the X -direction, d_x , for a load cycle, expressed in mm. The results of the 3 views are combined and displayed in the same global coordinate system.

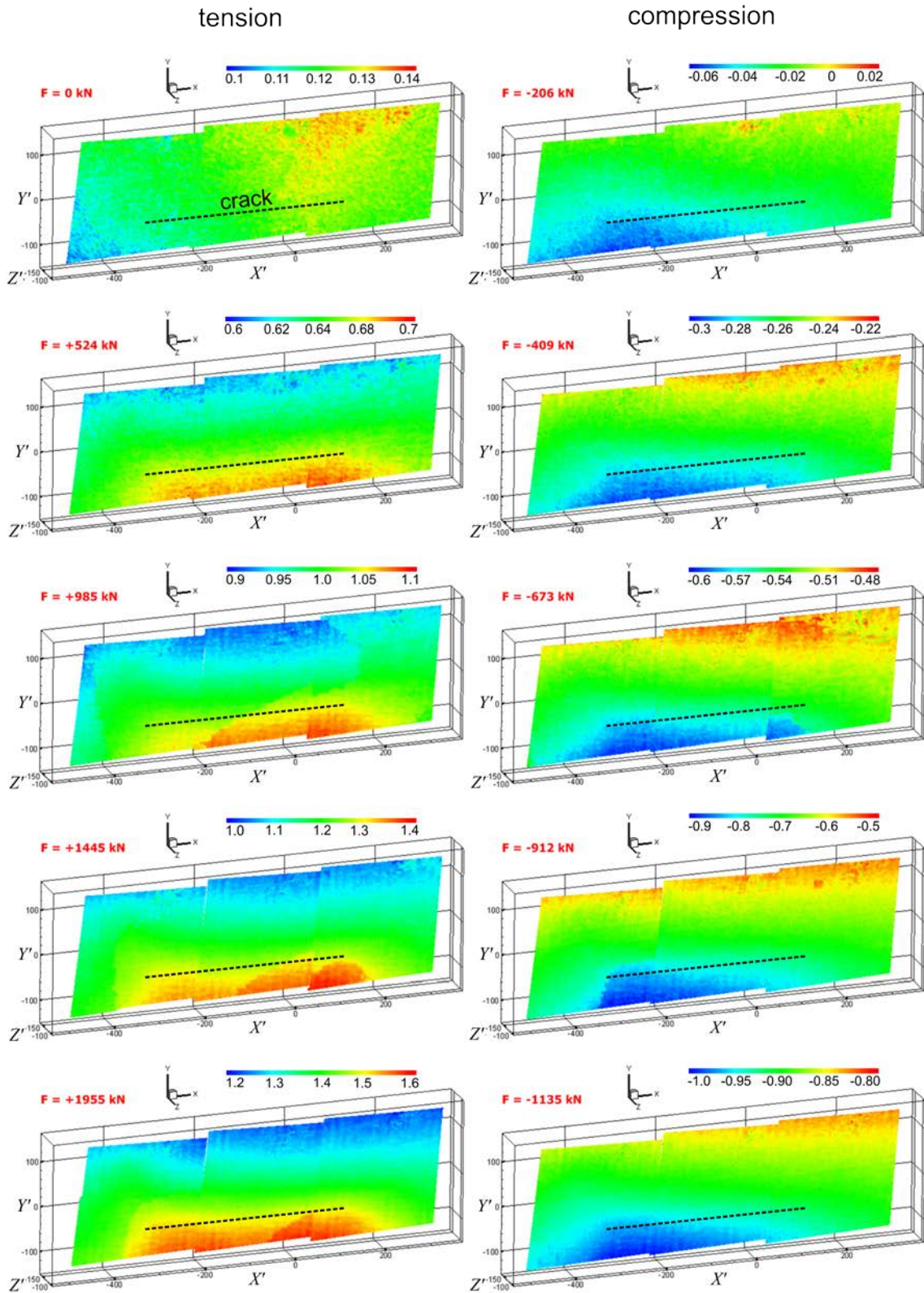


Figure 78: Measured displacement field in the Y -direction, d_Y , for a load cycle, expressed in mm. The results of the 3 views are combined and displayed in the same global coordinate system.

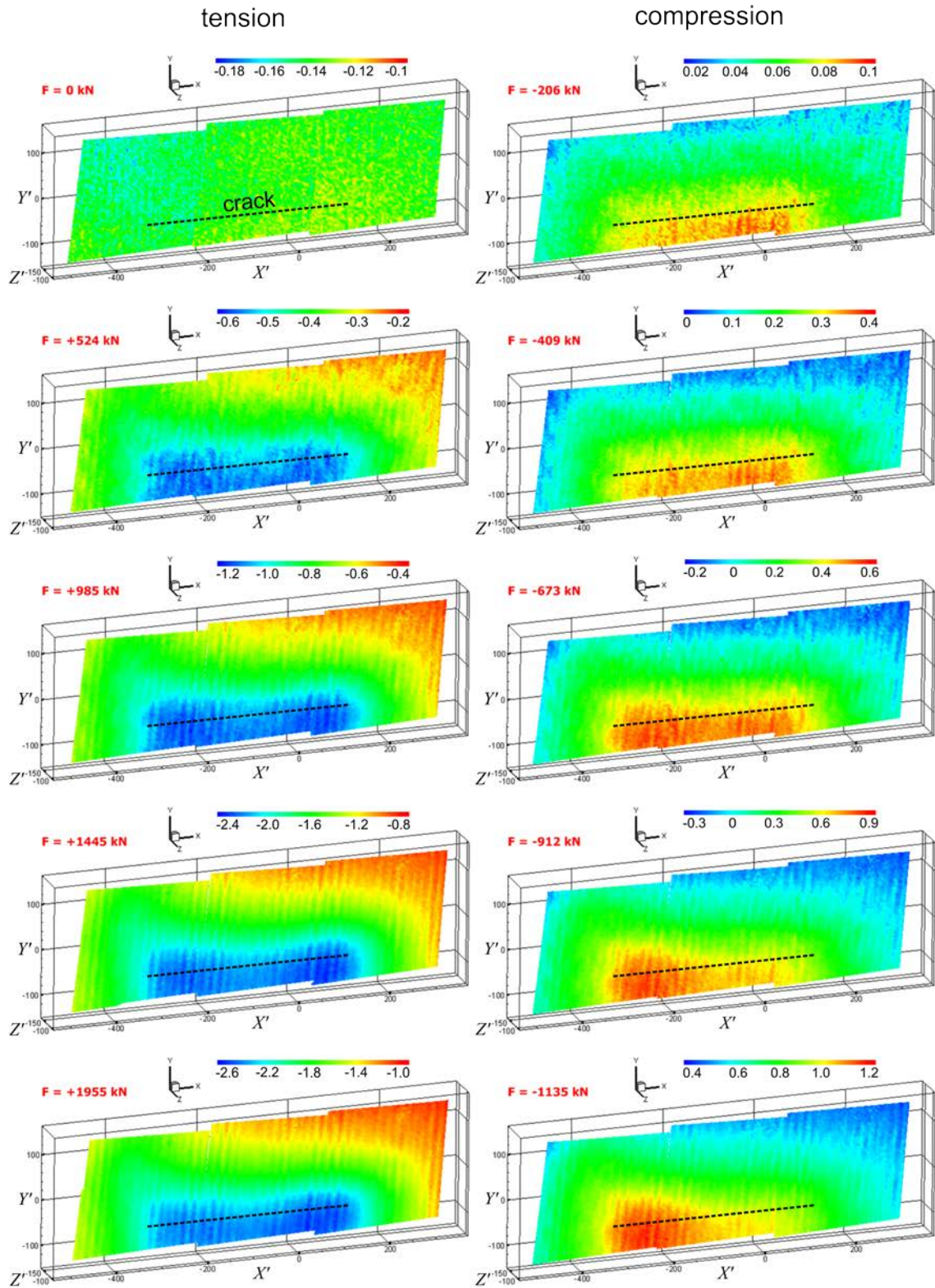


Figure 79: Measured displacement field in the Z-direction, d_z , for a load cycle, expressed in mm. The results of the 3 views are combined and displayed in the same global coordinate system.

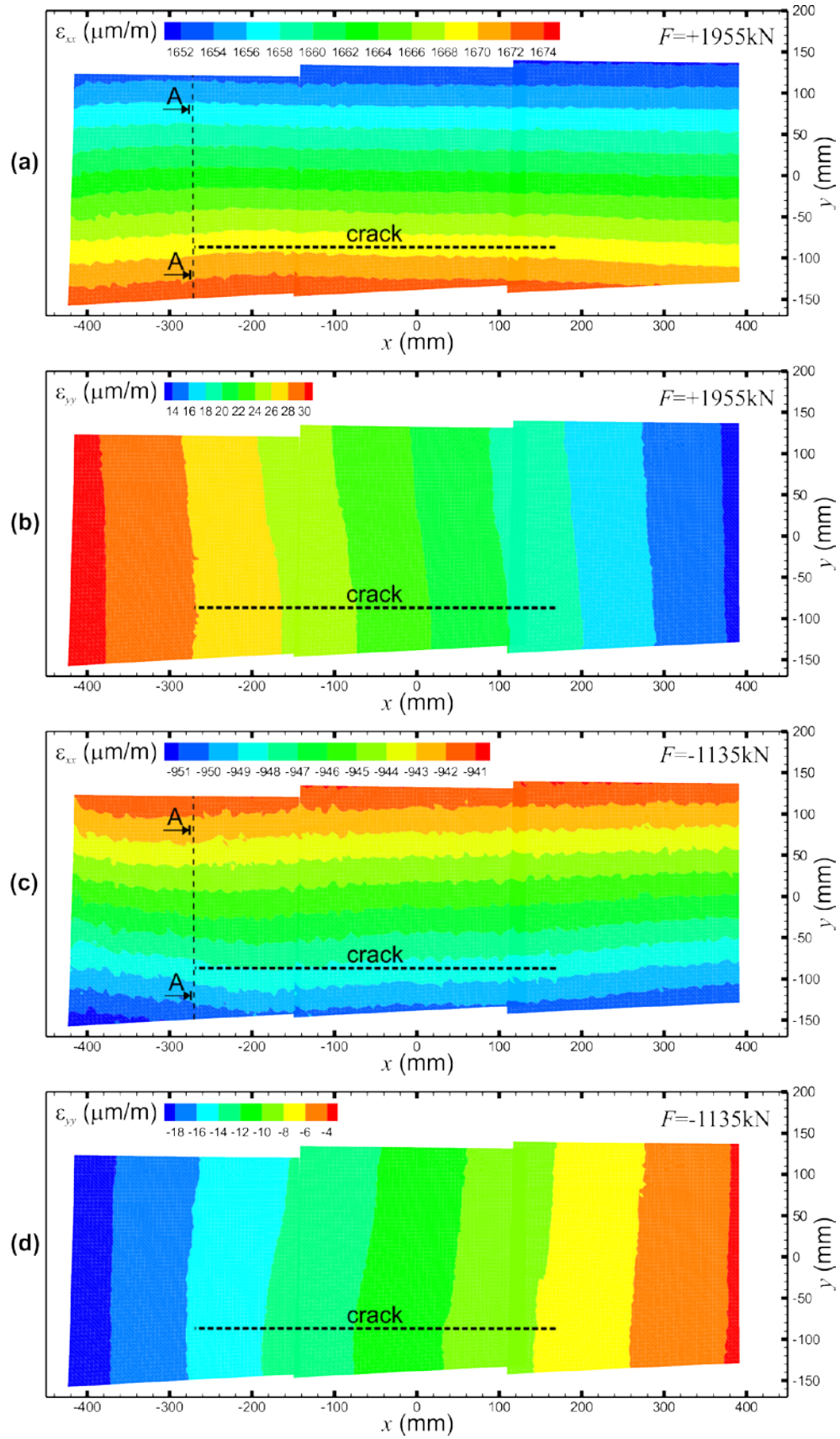


Figure 80: Estimated in-plane strain fields for the cases of maximum tension (a&b) and maximum compression (c&d). The x -axis is aligned with the loading axis.

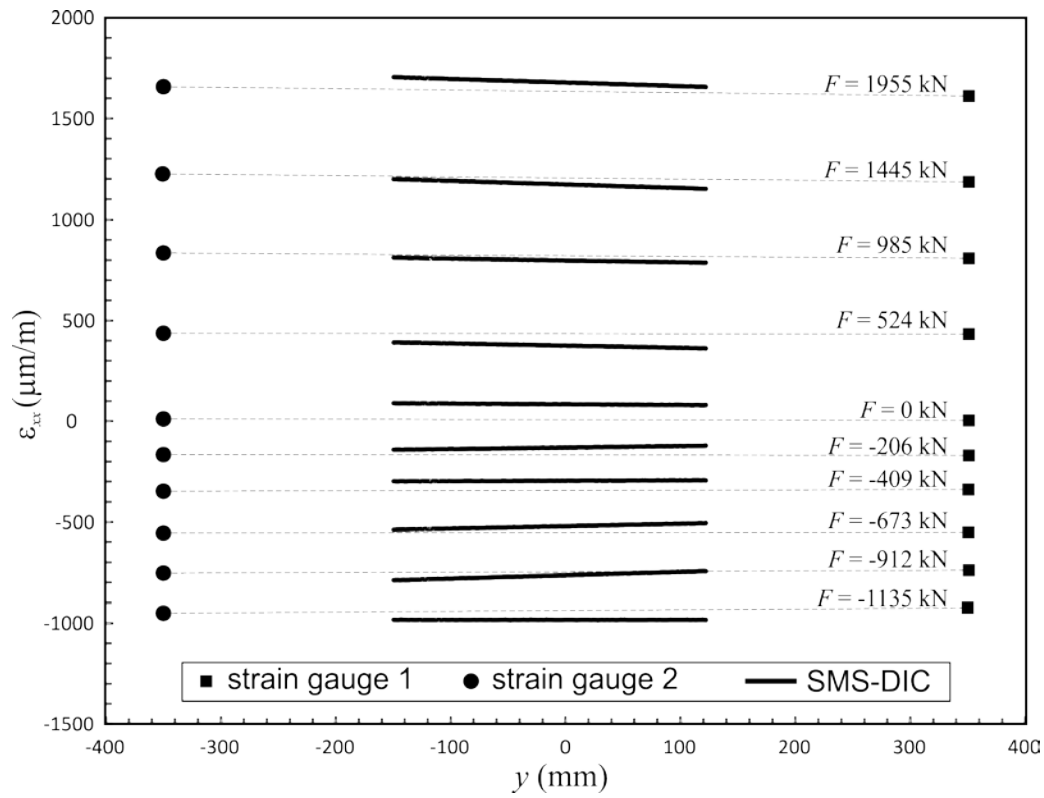


Figure 81: Longitudinal strain ϵ_{xx} estimated for all load cases along cross section A-A in Figure 80 which goes through strain gauges 1 and 2.

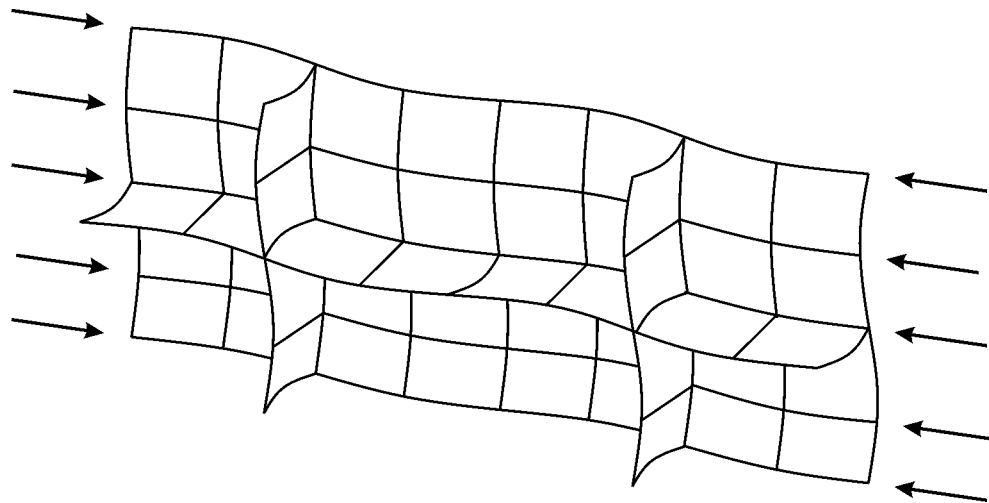


Figure 82: Buckling mode of a panel under compressive loads.

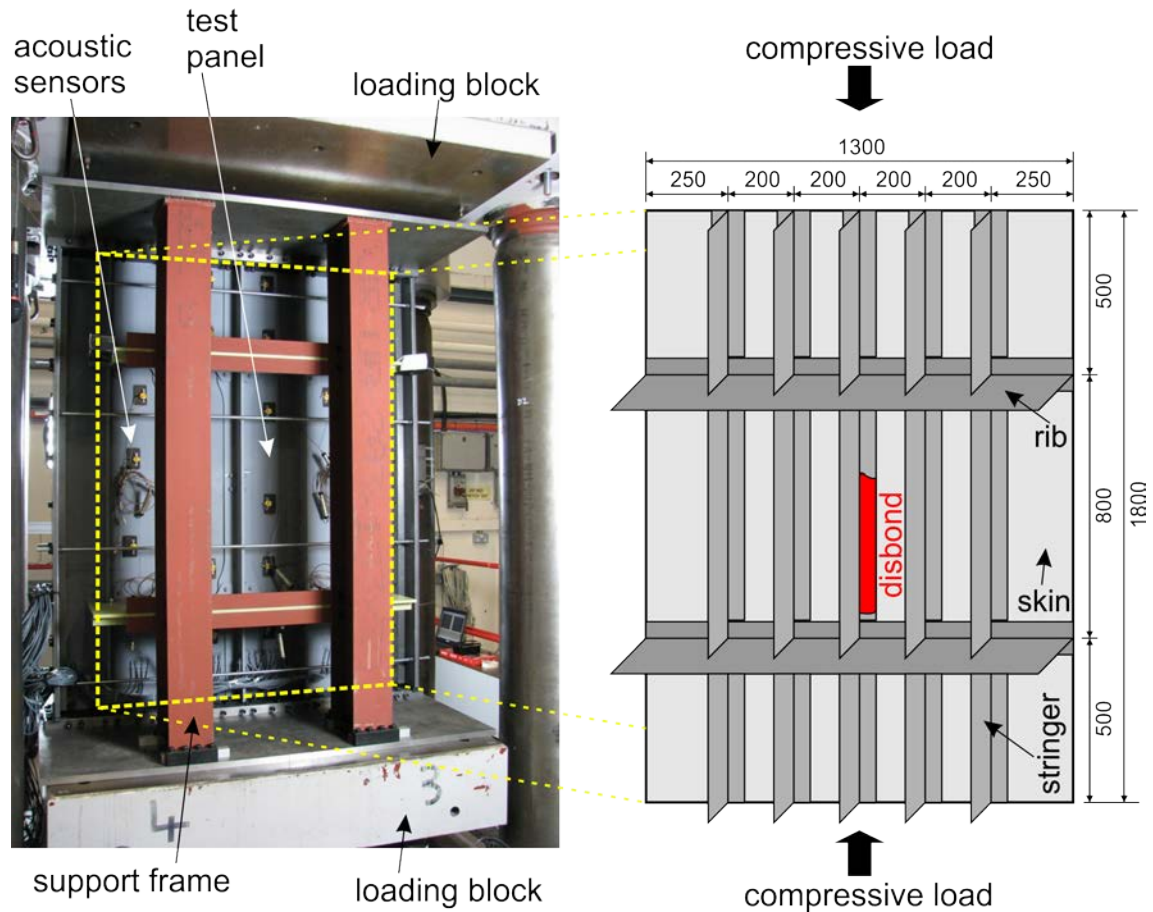


Figure 83: Buckling test specimen of an A350XWB's lower wing cover. Dimensions are expressed in mm.

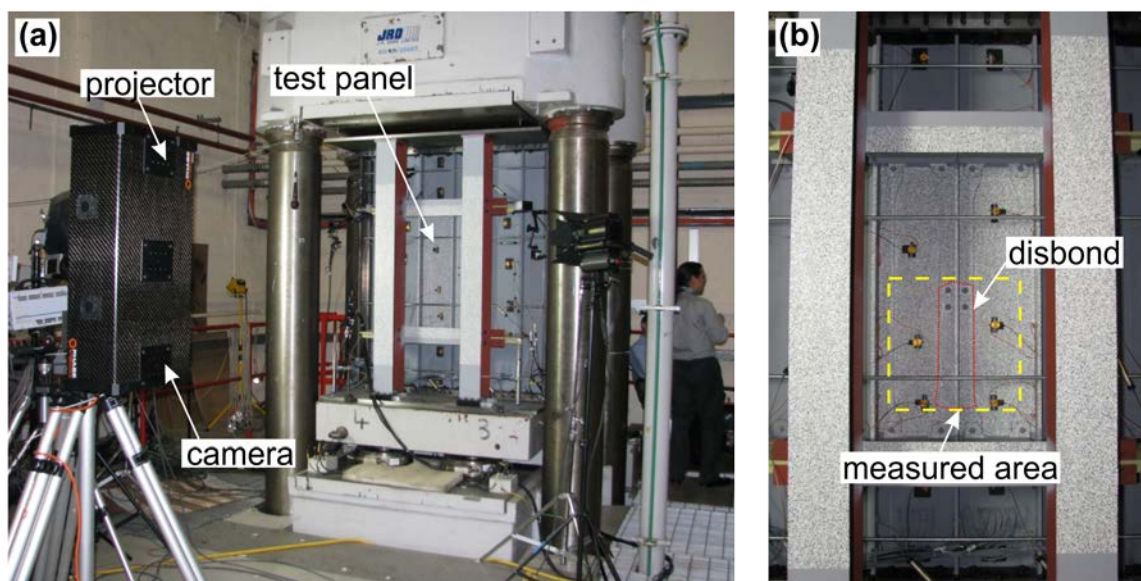


Figure 84: (a) Arrangement of the buckling test, and (b) field of view of the SMS.

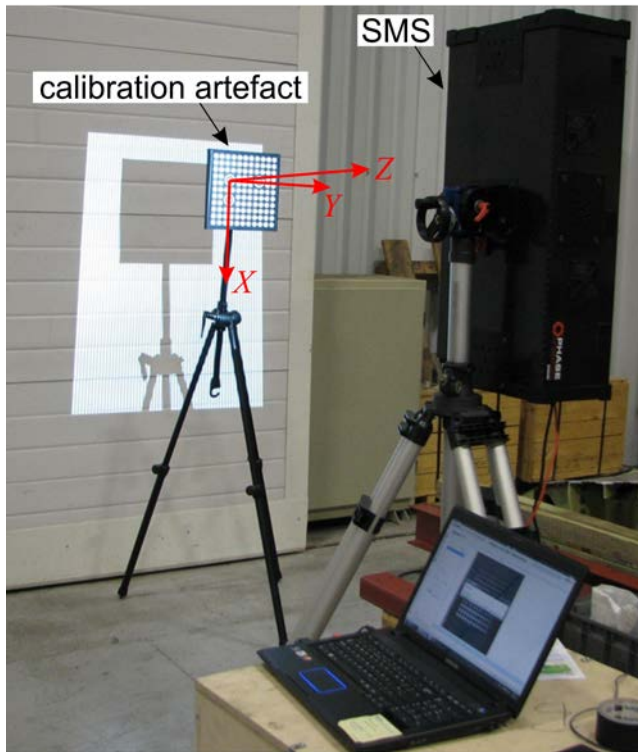


Figure 85: On-site calibration of the SMS using circle pattern artefact.

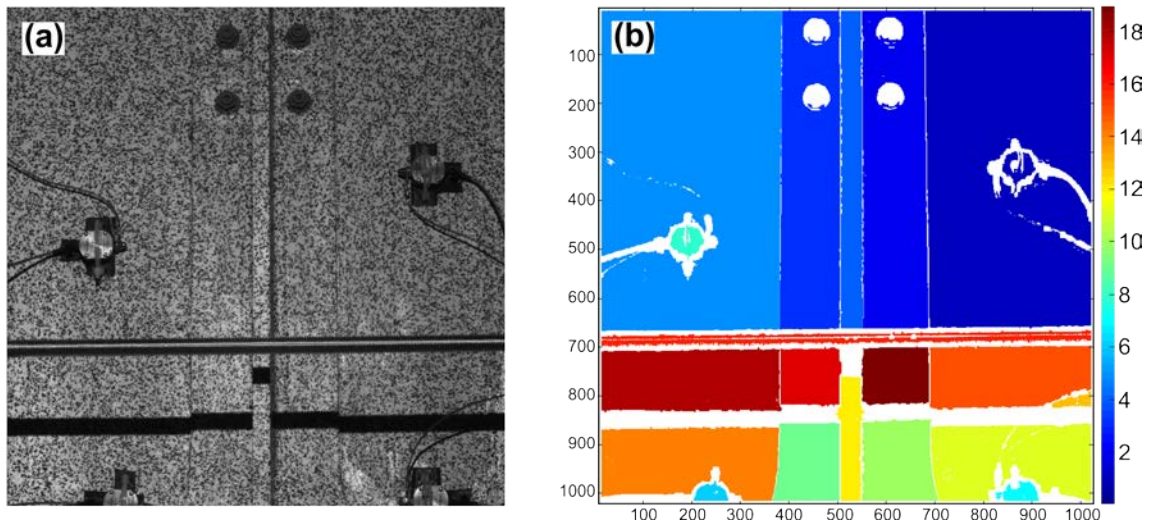


Figure 86: (a) Texture image of the measured area for reference state. (b) Label map of continuous regions for reference state.

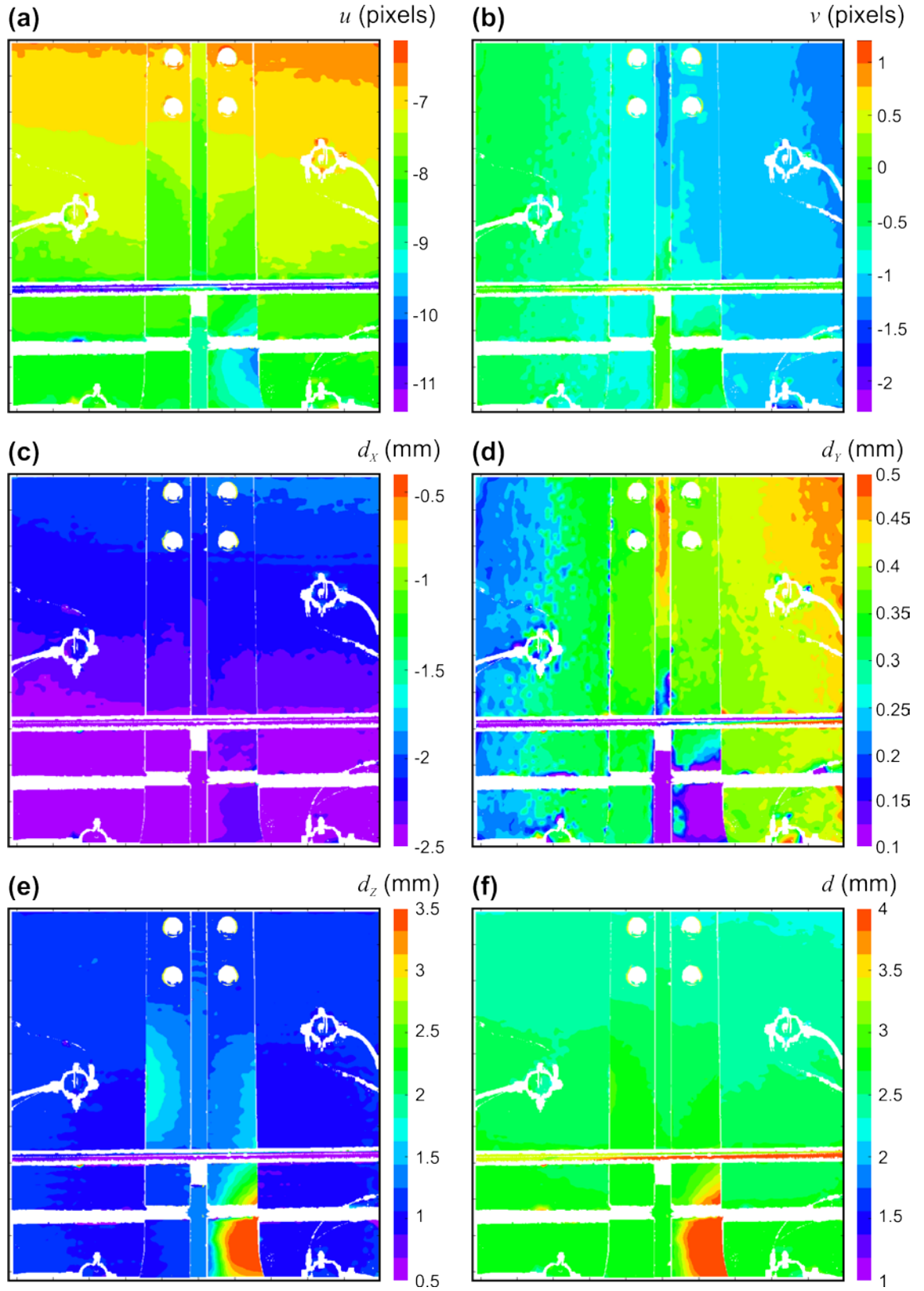


Figure 87: Vertical and horizontal image displacement fields (a&b), X-, Y- and Z-components of 3D displacement fields (c-e), and 3D displacement magnitude field measured for the case of maximum applied compressive load of 3008 kN.

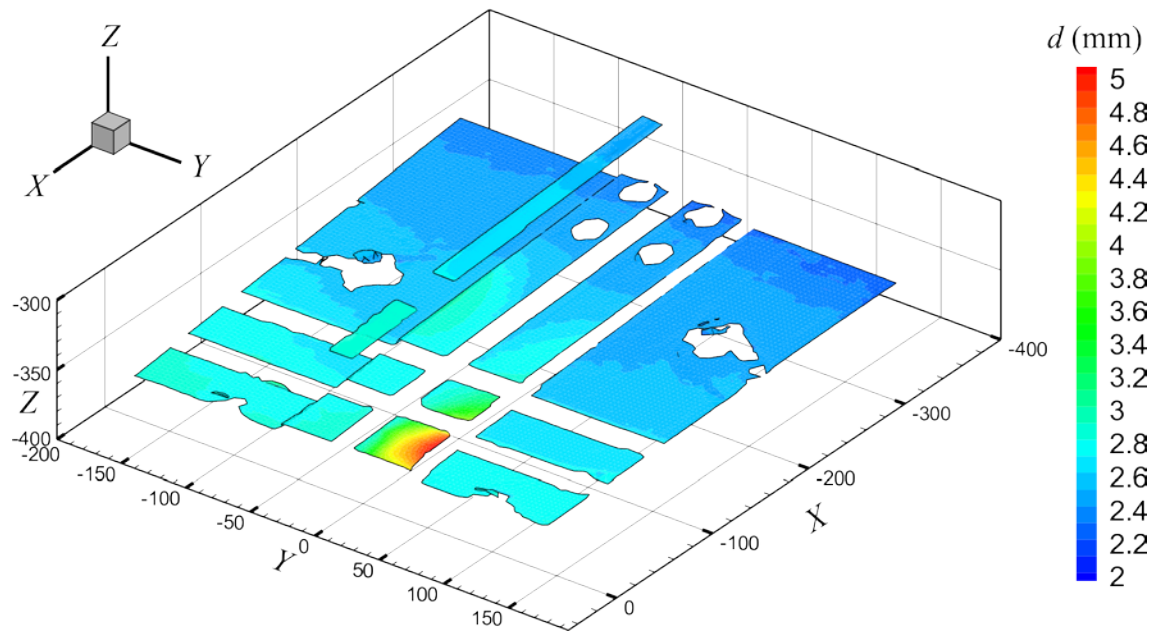


Figure 88: Displacement magnitude field measured for the case of maximum applied compressive load of 3008 kN, visualised in 3D on top of the undeformed shape.

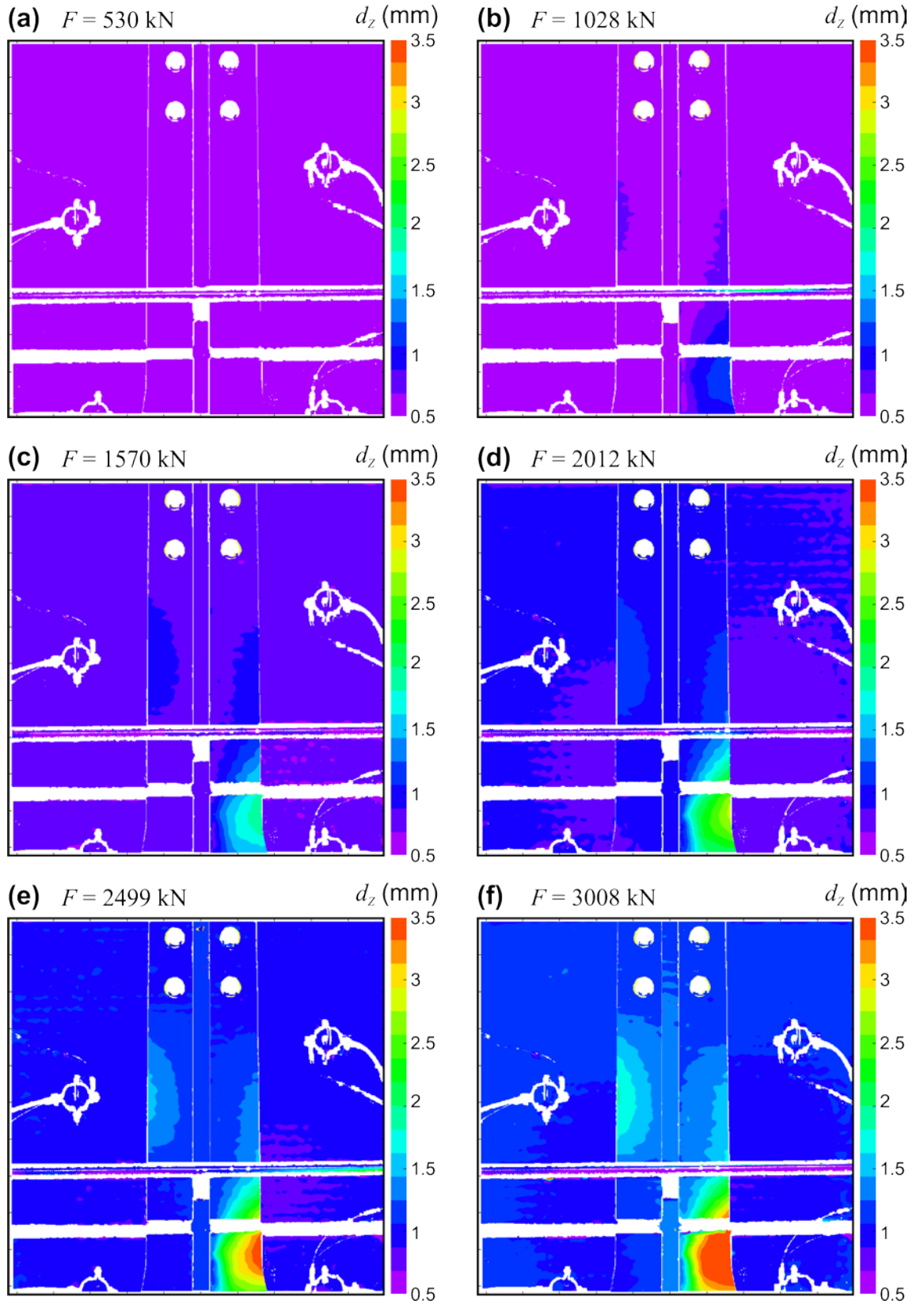


Figure 89: Out-of-plane displacement fields measured for the whole compression process.

Chapter 7

Fourier domain ranging technique for shape measurement with multiple reflections

7.1 Overview

Many optical techniques have been developed for fast, accurate, automated and non-contact measurement of surface profiles. One of the most popular methods is the fringe projection technique [1–3]. In this technique, as described earlier in this thesis, a fringe pattern consisting of parallel lines with sinusoidal intensity profile is projected onto an object surface, and its images are recorded by a camera placed at a different viewing angle. The spatial distortion of the fringes encodes the wanted information of the object shape, which can be extracted from the recorded images. The use of actively-generated surface features (e.g. fringes) enables highly-accurate feature detection without physical surface preparation. The assumption is that the surface is mostly diffusely scattering for the fringes to be identified correctly on the camera images. However, many mechanical components have complex and/or shiny surface finishes which may cause various problems for the fringe projection and other triangulation-based optical techniques. Some of the problems and available solutions are presented in this section, followed by the descriptions of the multiple-reflection problem which is the focus of this chapter. The next sections introduce a novel method called Fourier domain ranging (FDR) to rectify the multiple-reflection problem and improve the applicability of the fringe projection technique. Experimental results are presented to demonstrate the performance of the FDR technique.

7.1.1 Surface reflection

When a point on a surface is illuminated, it reflects the incident light in various directions. Light rays that are reflected to the camera sensor(s) produce images of the surface. The intensity at an image point depends strongly on the reflectance properties of the corresponding point on the surface. There are two approaches to study the surface reflectance: *physical optics* and *geometrical optics*. Physical optics models [138] are based on the propagation of light as treated as an electromagnetic wave. The reflection

is modelled from the interaction of incident light waves and the surface material by using Maxwell's equations with boundary conditions imposed on the reflecting surface. These models are general and applicable to all types of surfaces varying from perfectly smooth to rough. Geometrical optics models [139–141], on the other hand, are simpler in mathematical formulation and are thus popular in the computer graphics and computer vision communities. However, the assumption that the wavelength of the incident light is much smaller than the dimensions of the surface imperfections restricts their range of application [142].

A unified reflectance model was developed for machine vision by Nayar et al [143], which describes the reflection of monochromatic light from smooth to rough surfaces. As illustrated in Figure 90, the radiance at a point on the reflecting surface in the direction of a sensor is the sum of three primary components:

- Diffuse lobe: represents the internal scattering mechanism in which incident light rays penetrate the surface and interact with microscopic inhomogeneities in the surface material. The light is repeatedly reflected and refracted, until some of the scattered rays find their way to the surface in various directions. The surface radiance is therefore constant in all directions and independent of the viewing direction, which is known as a Lambertian reflection. The diffuse lobe is distributed evenly around the surface normal. If the surface material is homogenous as in the case of metals and crystals, the diffuse lobe may be ignored. For inhomogeneous materials such as plastics and paints, the diffuse lobe is very significant [144]. Many optical techniques assume the Lambertian model, such as the shape-from-shading [145, 146] and the photometric stereo methods [147, 148].
- Specular lobe: represents the single reflection of incident light. It tends to be distributed around the specular direction and has off-specular peaks for relatively large surface roughness. The magnitude of the lobe increases with the viewing angle θ_v . If the surface roughness is small compared to the wavelength of the incident light, the specular lobe is negligible. There are a limited number of papers [149] addressing optical measurement for surfaces with specular lobe reflectance properties.

- **Specular spike:** represents the mirror-like reflection which is dominant in the case of very smooth surfaces. It is concentrated in a small region around the specular direction. As the surface roughness increases, the specular spike shrinks rapidly in magnitude and broadens towards the specular lobe form. Some techniques make use of detectable specular spikes to estimate surface orientations based on the law of reflection, such as the parabolic-mirror sensing [142] and the deflectometry techniques [150].

It can be concluded that the reflectance property of a surface is governed by (i) the inhomogeneity of its material, and (ii) the surface roughness. Additionally, the intensity of a captured image depends on (iii) the incident angle and (iv) the angle of reflection, i.e. the relative orientation of the surface with respect to the light source and the camera. Depending on these four quantities, hotspots/highlights may arise due to the specular components and induce errors in an optical measuring system like the present fringe-projection SMS. When a surface region with high magnitude of reflectance is observed by a camera, it can cause the image intensity variation to exceed the dynamic range of the camera sensor. Typical commercial CMOS and CCD sensors are 8-bit (or 256 grey levels), whilst more modern cameras like the ones used in current the Phase Vision SMS have 12-bit sensors with 4096 grey levels. A solution may be to reduce the camera lens aperture so that the intensity of the hotspot can fit in the dynamic range. However, this will also reduce the intensity of other image regions and cause under-sampling effects. Another solution is to change slightly the orientation of the object with respect to the sensors, i.e. varying the afore-mentioned quantities (iii) and (iv). However, this usually has to be done in a trial-and-error manner, and is not always beneficial. Another common practice to suppress hotspot effects is to cover the surface with paint or developer powder, which effectively increases the surface inhomogeneity and roughness – i.e. quantities (i) and (ii). Besides being laborious and time-consuming for routine inspections, this approach induces potential errors due to the coating thickness.

7.1.2 Measurement of specular surfaces

Structured-light techniques that are based on the principle of triangulation between an incident light ray emanating from a projector and a reflective light ray coming to a camera, such as fringe projection and laser scanning, generally fail to measure surfaces with high specular reflectance. This is because specularly-reflected light rays are in

restricted direction and do not always reach the camera. What the camera sees may not be the image of the surface but that of the surrounding scene. Even if the specular direction coincides with the camera viewing direction, the camera can only see the image of the light source rather than that of the surface. In most cases, the high specularity causes the following two assumptions of the triangulation to be invalid [151]: (i) the 3D position of a surface point depends only on its image point location, and (ii) the 3D position is independent of the surface facet orientation. Therefore, alternative techniques have been developed to inspect highly-specular surfaces, such as glossy-finished metallic components and automotive windscreens.

Humans typically inspect a specular surface visually by analysing a surrounding feature reflected on the surface and looking for deformation of the feature [150]. Bumps, dents and waves on a car body, which are almost invisible on diffuse surfaces, can easily be detected on specular surfaces by looking for locally distorted reflection of a nearby brick wall, for example. Deflectometry techniques mimic this behaviour of humans to measure curvatures of very shiny surfaces. Perard and Beyerer [152] introduced a deflectometry technique that uses an LCD screen to generate Gray-coded features which are reflected on the specular surface to a camera. An illustration of their back-ray-tracing principle is given in Figure 91. The relationship of the reverse incident light ray \mathbf{r} and the reverse reflective light ray \mathbf{s} with the surface normal \mathbf{n} can be expressed by the reflection law as

$$\mathbf{r} = \mathbf{s} - 2\mathbf{n}\mathbf{n}^T\mathbf{s}. \quad (6.1)$$

By establishing the relationship of the camera position \mathbf{O} , the measured point \mathbf{S} and the corresponding point \mathbf{L} on the screen, the equation can be rewritten as

$$\mathbf{l} - \rho(\mathbf{s} - 2\mathbf{n}\mathbf{n}^T\mathbf{s}) - \sigma\mathbf{s} = \mathbf{0} \quad (6.2)$$

Provided that the camera and the screen have been calibrated, the ray vector \mathbf{s} is known for each camera pixel. The location of its corresponding screen point \mathbf{L} can be detected and location vector \mathbf{l} can be known. The four remaining unknowns are therefore the normal vector \mathbf{n} (containing two scalars) and the two scalar distances σ and ρ . Equation (6.2), however, contains only three scalar equations corresponding to three coordinate axes. So, an additional equation is introduced in the form of a Bézier surface

model based on the spatial smoothness condition of the surface. The surface reconstruction task is fundamentally fitting the surface model to all camera pixels. The authors presented experimental results of a polished metal plate. Hung et al [153] proposed a similar technique called *grid reflection* that uses a grid as the reference feature. Later, sinusoidal fringes were used with phase-shifting technique by Kammel and Léon [150] to improve the feature detection accuracy. Instead of creating the pattern on a LCD screen, Höfling et al [154] presented a *phase reflection* technique in which fringe patterns are projected onto a white screen, allowing easy adjustment of measured field of view. There were also many other variants of the deflectometry techniques [155–157] which demonstrated good performance on measuring automotive windshields and shiny painted doors. An excellent survey of other state-of-the-art 3D reconstruction methods for transparent and specular objects was provided by Ihrke et al [158].

Although many papers have addressed the mirror-like specularity, very few methods on the hybrid effect of diffuse and specular reflections can be found in literature. In the laser rangefinder system presented by Baba et al [151], a shield mask consisting of parallel thin plates is located in between the lens and the image sensor to adjust the defocus of specularly-reflected light rays whilst letting diffusely-reflected rays pass through as normal. The measurement performance was demonstrated on various types of materials with different specular-to-diffuse-reflection ratios, such as metal and ceramic. Curless and Levoy [159] suggested that the negative effect of specular components to laser speckles can be reduced by analysing the time evolution of the reflected light imaged onto the sensor.

7.1.3 Multiple-reflection problem

In the case of specular surfaces with concave profile, a reflective light ray at a surface point may become the incident ray to another point. As explained in Figure 92 for a typical fringe projection system, a point C on the camera image is suffered from multiple reflections of two signals: one coming from projector point P_1 and reflecting only once on the surface at point S_1 ; and the other coming from projector point P_2 , reflecting twice on the surface first at S_2 and then at S_1 , before reaching the camera. Thus, the obtained image intensity at camera point C is the sum of both the diffuse component of signal 1 and the specular component of signal 2. Only signal 1 carries the

correct coordinate information about the measured point S_1 . The use of traditional phase estimation techniques on the superimposed signals generally result in incorrect phase gradients and thus incorrect triangulated surface points.

There are a limited number of papers in the literature addressing the multiple-reflection problem for structured-light techniques. Nygard and Wernersson [160] proposed a method for moving laser-scanning range cameras that checks for consistency across multiple views of the measured data disrupted by multiple reflections. Their method also enables detection of the position and orientation of the reflective surface which causes multiple reflections on the measured diffuse surface. Cheng et al [161] introduced a method that projects time-varying binary-coded patterns on a microscopic object surface of interest. Image pixels corresponding to multiple reflections are detected as temporal changes in pre-defined binary codewords, and suitable segments in the patterns are then corrected to retrieve the corrupted data.

This chapter presents a new method to tackle the multiple reflection problem on the platform of the fringe projection SMS being developed at Loughborough University and Phase Vision Ltd. The method involves two key tasks: (i) to detect all single-reflected and multiple-reflected signals at once, and (ii) to pick out the correct signal for the subsequent triangulation. The first task is done by using a Fourier transform method developed based on the previous work of Huntley and Saldner [96]. In terms of implementation, the method is merely a software upgrade to the present Phase Vision SMS; thus, no additional hardware costs are incurred. The method has been tested on simple specimens to prove its principle, as well as on practical mechanical components.

7.2 Fourier domain ranging technique

The description of the proposed Fourier domain ranging (FDR) technique is given in this section. The section starts with a review of available Fourier transform methods for fringe projection, including a mathematical summary of the Fourier domain ranging method by Huntley and Saldner [96] which sets the foundation for the present FDR. Improvements to the method for multiple-peak detection are then discussed, followed by its application to correcting the point-cloud triangulation for multiple reflections.

7.2.1 Review of Fourier transform methods for phase estimation

The Fourier transform has been applied extensively to estimating phase with interferometry and fringe projection techniques, since the first work of Takeda et al [162]. In these techniques, sinusoidal fringes are projected onto the object surface, and their deformation as recorded on an image sensor encodes the wanted information of the object shape. The fringe deformation is typically quantified by the change (either spatial or temporal) in phase of the fringes. Many phase estimation methods [100, 21] work out the phase directly from the intensity of the captured images, i.e. in the spatial domain. On the other hand, the general idea of Fourier transform methods is to calculate the Fourier transform of the signal, filter the signal in the frequency domain, detect the signal peaks which correspond to its phase values, and calculate an inverse Fourier transform to convert the results back into the spatial domain [163]. An advantage of the Fourier transform methods is that they are easy to apply as they do not require finding fringe centres and fringe orders [164]. Additionally, the transform offers high accuracy in the presence of noise, as the signal is concentrated around the peaks [96].

Huntley and Saldner [96] introduced the Fourier transform ranging (also known as Fourier domain ranging) method in which the Fourier transform is done in one dimension along the time axis instead of two dimensions along spatial axes as in common methods. Besides better computational performance, this method allows processing of each image pixel independently of other pixels, so it is useful for measuring discontinuous surfaces. In this method, both the phase and the pitch of the fringes generated on the projector SLM are varied in time. At the initial time that the number of $t=1$ fringe is projected, the fringe phase ranges from $-\pi$ to π across the projector's field of view. For subsequent time values ($t=2,3,\dots,s$), the number of fringes is also set to t so that the phase range increases to $(-t\pi, t\pi)$, where s is the maximum number of fringes used. For each value of t , a number of q phase-stepped images are acquired, with the phase step index $p=1,2,\dots,q$. The Fourier transform is applied along the time axis t on the complex signal computed by a phase-stepping technique. The authors provided a quantitative comparison in computational time and phase gradient errors of the method against other intensity-based methods such as the reverse exponential phase unwrapping. They concluded that the Fourier transform ranging gives lower random errors which fall off by $1/s^{3/2}$ rather than $1/s(\log_2 s)^{1/2}$, although it requires more computational effort with the complexity of $O(s\log_2 s)$ rather than $O(\log_2 s)$. In

practice, the maximum number of fringes s may reach 100 without negative effects of under-sampling [165]. That means the random errors can be reduced by 1000 times and reach the level of $1/10^5$, although the computing time can be at most 100 times longer than the reverse exponential technique. For applications that processing time is not a critical factor, the Fourier domain ranging technique may be a good solution.

The mathematical description of the Fourier domain ranging technique [96] is summarised as follows. A set of qs fringe images are acquired in the sequence described in the previous paragraph. The intensity at each image pixel can be represented as a sinusoidal function [166],

$$I(p, t) = I_0(1 + V \cos(\omega t + 2\pi(p-1)/q)), \quad (6.3)$$

where $p=1,2,\dots,q$ is the phase shift index and $t=1,2,\dots,s$ is the time-varying fringe spatial frequency. I_0 is the constant mean intensity and V is the constant fringe visibility. The variable ω is the phase gradient (with respect to time t) to be sought as it encodes the depth information. If the qs fringe images are acquired with vertical fringes, ω (specifically denoted as ω_x) varies from $-\pi$ at the left to π at the right of the projector's field of view, and defines a vertical plane going through the scattering point to be measured. The process can be repeated with another qs horizontal fringes to provide a second phase gradient ω_y which varies from $-\pi$ at the bottom to π at the top of the projector's field of view and defines another horizontal plane containing the scattering point. The intersection of these two planes is a light ray coming from the projector that contains the scattering point. By triangulating this projector's light ray with the camera's light ray emanating from the image pixel under consideration, the 3D coordinate of the scattering point can be determined. Therefore, the key task is to estimate the value of the phase gradient ω at each pixel and for each of the two fringe orientations.

Using the four-frame phase-stepping algorithm (i.e. $q=4$), a complex signal can be constructed,

$$I_s(t) = [I(1, t) - I(3, t)] + i[I(4, t) - I(2, t)]. \quad (6.4)$$

The two-dimensional discrete Fourier transform of the original signal in Equation (6.3) can be reduced to a one-dimensional Fourier transform of the complex signal by

$$H(k) = \sum_{t=1}^s I_s(t) \exp[-2\pi i k(t-1)/s], \quad (6.5)$$

where k denotes the temporal frequency along the t (time) axis, which is related to the phase gradient ω through the equation

$$\omega = \frac{2\pi k}{s}. \quad (6.6)$$

Thus, the aim becomes to find the value $k = \kappa$ which maximises $|H(k)|$. This can be done by a two-stage process:

1. Obtain an initial estimate of k by evaluating Equation (6.5) with a 1D Fast Fourier Transform (FFT) on the complex signal I_s and finding the integral value $k=k_0$ that maximises $|H(k)|$.
2. Using the initial estimate $k=k_0$ as the starting point, obtain a refined estimate $k=\kappa$ by a Newton-Raphson optimisation of the continuous Fourier transform of I_s where k is no longer constrained to be integral. The optimisation scheme presented in [101] can be used for the peak detection.

7.2.2 Improved Fourier domain ranging

Huntley [166] recently proposed a few changes to the two-stage peak-detection process presented in the previous section to improve the overall data processing speed of the Fourier domain ranging technique. He observed that the integral value of the temporal frequency $k=k_0$ is in many cases too far from the true value $k=\kappa$. This causes the Newton-Raphson nonlinear optimisation to fail or converge very slowly towards the true value. Thus, he proposed a modified approach that involves using two integral values k_1 and k_2 bounding the peak of the FFT to predict a new starting point k_i that is much closer to the true value so that only one iteration is generally required.

The initial estimate k_i can be determined by using the following linear interpolation

$$k_i = \frac{\phi_2 k_1 - \phi_1 k_2}{\phi_2 - \phi_1}, \quad (6.7)$$

where ϕ_1 and ϕ_2 are the phase values at which the integral peak-bounding frequencies k_1 and k_2 are specified. This simple relationship is based on his observation that the phase value reaches zero at the position of the true peak if the fringe sequence is instead defined in the range $t=0,1,2,\dots,s-1$. The fringe pattern for $t=0$ and $p=1$ corresponds to the uniformly bright texture image which is always captured by the SMS on a routine basis. The fringe pattern for $t=0$ and $p=3$, which corresponds to the uniformly dark illumination, is the only additional frame that needs to be acquired. The frames corresponding to $p=2$ and $p=4$ (both with $t=0$) do not need to be acquired, since they are set to zero so as to remove the imaginary part of the complex signal for the case of $t=0$ for more convenient manipulations. So, the total number of needed fringe images is $(4s-2)$ instead of $(4s+1)$ as for the original Fourier domain ranging method.

Simulated data were used to demonstrate the performance of the improved Fourier domain ranging method. The simulated intensity profile of one pixel was generated using Equation (6.3) for $p=1,2,3,4$ and $t=0,1,2,\dots,63$ (i.e. $q=4$ phase-stepping frames and $s=64$ fringe pitch values). The frequency k at the peak was set to a reference value $\kappa=3.3$, and the phase gradient ω was defined following Equation (6.6). The intensity was disturbed with random numbers with standard deviation of $\sigma_e=0.01$ and uniform distribution to simulate the random errors due to noise. The complex signal was then constructed by using Equation (6.4). The computed Fourier transform of the complex signal in the region of the peak is presented in Figure 93. It should be noted that only the discrete Fourier transform is available in practice, whereas the continuous Fourier transform is provided for reference purposes. It can be seen that the ideal peak position is bounded by $k=3$ (which gives maximum discrete Fourier transform value) and $k=4$, within which the phase ϕ varies linearly. The property that phase value ϕ vanishes at the peak position can also be seen in this example. The linear interpolation defined by Equation (6.7) gives a very good initial estimate of the peak position. The results of Newton-Raphson optimisation for peak location k and the corresponding phase gradient ω are summarised in Table 6, in comparison with the original FDR technique [96] and a temporal phase unwrapping technique based on least-square fitting. It can be seen that

the improved FDR gives superior performance in terms of both accuracy and computational time.

The above-described FDR technique by Huntley [166] was applicable to detecting only one peak and was tested only on simulated data. In this thesis, his FDR is adopted and extended to multiple peaks where their interferences can strongly affect the peak detection accuracy. The technique is also tested on both simulated data and real specimens with noise effects taken into account. Nevertheless, the key contribution of this thesis is the application of the multiple-peak FDR algorithm to the practically-challenging multiple-reflection problem. Details of the technique are provided in the following section.

7.2.3 Application to multiple reflection problem

The geometric model of the fringe projection SMS in the presence of multiple reflections is depicted in Figure 94. For a pixel on the camera image, a pair of phase gradients (ω_x, ω_y) can be estimated from the intensity signals from the sets of vertical and horizontal fringe patterns by using a temporal phase unwrapping technique or the FDR technique. The ω_x value measured at a pixel defines the unwrapped phase value from the vertical fringes and therefore defines a plane in the space in front of the projector on which the scattering point, which is imaged onto that pixel, must lie. Points on this plane can be projected back onto the image plane of the projector and in effect define a vertical line in the SLM through which the light falling onto that pixel must have travelled. Similarly the ω_y value defines a horizontal line on the SLM image plane. In the normal condition of single reflection, at most one pair of peaks, $(\omega_x^{(1)}, \omega_y^{(1)})$, can be found, which thus specifies a unique position on the projector SLM from which the direct projector light ray emanates and intersects with the camera light ray at the measured scattering point. However, if the signal reaching this pixel is contaminated with specular reflection on a nearby reflective surface (or a reflective part of the same inspected surface), it is influenced by an additional indirect light ray that emanates from a second point $(\omega_x^{(2)}, \omega_y^{(2)})$ on the projector SLM. More indirect reflections will involve more phase gradients.

If multiple reflections are present, the signal from the second location on the SLM will be added on an intensity basis to the first signal. The Fourier transform will however

separate out the two signals, provided that $\omega_x^{(1)}$ is sufficiently distinct from $\omega_x^{(2)}$ (on the vertical fringes) and likewise $\omega_y^{(1)}$ is sufficiently distinct from $\omega_y^{(2)}$ (on the horizontal fringes). This allows the possibility, in this simple case of one direct ray and one indirect ray, of identifying from the intensity signals from each fringe orientation a pair of peaks. However, there remains ambiguity as to how the peaks from the two orientations should be paired. Therefore, the main tasks are (i) to identify all valid peaks in the Fourier transform of the signal from each fringe orientation, (ii) to compute all possible phase gradient pairs for each image pixel, and (iii) to identify the correct pair which corresponds to the direct light ray. In this work, the first two tasks are done based on the improved FDR technique with modification to deal with multiple peak detection. The third task is achieved by exploiting the fact that the direct (and correct) projector's light ray must intersect (within a certain tolerance) with the camera light ray. The procedures of these two tasks are described as follow.

Detecting multiple peaks of Fourier transform

Let us consider a complex signal $I_s(t)$ generated to simulate the mixing of two signals with unique phase gradient values $(\omega_x^{(1)}, \omega_y^{(1)})$ and $(\omega_x^{(2)}, \omega_y^{(2)})$ as would be observed when integrating light rays from two different points on the projector SLM. Figure 95 shows a plot of $I_s(t)$ observed at a single pixel on the camera sensor when vertical fringes are used. A total of 32 vertical fringes are used to generate this signal with the fringe pitch varying in a linear sequence $t=0,1,2,\dots,31$. The contained signal frequencies are set to $\omega_x^{(1)}=1.35$ rad and $\omega_x^{(2)}=0.68$ rad, which correspond to two distinguishable peaks in the Fourier transform of $I_s(t)$. Both of the peaks can be detected with the improved FDR technique following the procedure below.

1. Detecting the strongest peak: The FFT is applied to the complex signal $I_s(t)$ to obtain its amplitudes $|H|$ and phases ϕ at s integral values of the frequencies k_x . Figure 96 shows the FFT result of this simulated signal where $s=32$. The integral frequency which gives the largest signal amplitude is determined. The corresponding phase values of this frequency and one neighbour are used to calculate the initial non-integral estimate of the peak position following Equation (6.7). There might be a jump of π between the two phase values, which should be removed before the interpolation. Then, the Newton-Raphson optimisation is used to refine the initial estimate, resulting in the frequency $k_x^{(1)}$

of the strongest peak (namely, peak 1). The corresponding phase gradient $\omega_x^{(1)}$ is thus achieved by using Equation (6.6).

2. Removing the strongest peak: A complex signal corresponding to the detected peak 1 can be reconstructed as

$$I_s^{(1)}(t) = A_x^{(1)} \left[\cos(\omega_x^{(1)} t) + i \sin(\omega_x^{(1)} t) \right], \quad (6.8)$$

where $A_x^{(1)}$ is the signal amplitude. The reconstructed complex signal of peak 1 in this simulation is shown in Figure 97. To remove peak 1, the signal $I_s^{(1)}$ is subtracted from the original signal I_s , giving a signal I_s' that contains remaining weaker peaks. Figure 98 shows the remaining signal I_s' after peak 1 has been removed.

3. Detecting the next peak(s): Steps 1 and 2 are repeated with the original signal I_s being replaced by the remaining signal I_s' in order to detect the second strongest peak (namely, peak 2) which corresponds to the phase gradient $\omega_x^{(2)}$. The Fourier transform of the remaining signal I_s' from which peak 2 is detected is shown in Figure 99. The process continues for subsequent peaks until the amplitude $|H|$ falls below a predefined threshold of signal strength. Figure 100 shows the amplitude and phase of the signal after peak 2 is removed, where the highest peak is not considerably higher than the others and is thus not counted as a valid peak.
4. Refining detected peaks: In situations that two or more peaks are tightly clustered and the frequency resolution is not sufficiently high, the linear interpolation in Equation (6.7) may not give a good estimate of the first peak. To improve this estimate, a refinement step is included, which is essentially a repetition of all of the previous steps. Before the refinement, signals of all the previously-detected peaks rather than peak 1 are removed from the original signal. This is to suppress their cross-talk effects on peak 1 so that the location of peak 1 (and thereby all the other peaks) can be computed more accurately. This refinement step (i.e., step 4) can be iterated several times, but one iteration is typically enough.

When horizontal fringes are used, the whole procedure is repeated in order to obtain the phase gradients $\omega_y^{(1)}$ and $\omega_y^{(2)}$.

Selecting correct triangulation light rays

Let us assume that two phase gradients $\omega_x^{(1)}$ and $\omega_x^{(2)}$ are detected from the vertical fringe patterns, together with two phase gradients $\omega_y^{(1)}$ and $\omega_y^{(2)}$ from the horizontal fringe patterns. Thus, there are a total of four combinations $(\omega_x^{(1)}, \omega_y^{(1)})$, $(\omega_x^{(1)}, \omega_y^{(2)})$, $(\omega_x^{(2)}, \omega_y^{(1)})$ and $(\omega_x^{(2)}, \omega_y^{(2)})$ corresponding to four points on the projector SLM from which the projector light ray, whose scattered light is detected at the camera pixel of interest, could have emanated. As illustrated in Figure 94, only one projector light ray travels directly to the measured scattering point at which it intersects with the camera light ray, whereas the other projector light rays go in wrong directions. In this work, the closest distance ε_1 between the camera and project rays is used to assess how well they intersect. This closest-approach triangulation has been described in Section 2.4 and particularly in Figure 12. The correct light ray is selected as the one which gives the lowest distance ε_1 .

Software implementation

The present FDR technique for shape measurement in the presence of multiple reflections has been implemented in MATLABTM. The results presented in this chapter were obtained with the MATLAB code. The code has recently been converted into the C++ language for better computational performance and integration with the current Phase Vision SMS software. The FDR code can be considered as an add-on module of the measurement software, which users can select in the graphical user interface (GUI) as an alternative to the reverse exponential phase unwrapping module.

The data flow diagram of the FDR software implementation is illustrated in Figure 101. A unified input file is created in the extensible markup language (XML) to store all setting parameters of a measurement task, such as sensor calibration parameters, number of fringes to be projected s , switch flag of the phase estimation algorithm used (e.g. FDR or temporal phase unwrapping) and threshold values. This file is a copy of a typical input file used for all the measurements presented in the previous chapters, with additional information nodes specifying the settings of the FDR technique. The input file can be easily modified by using either a text editor or the SMS GUI. The acquisition

module parses the XML input file for relevant setting parameters and generates the fringe patterns accordingly. It also controls the process of projecting those fringe patterns onto the object and acquiring their images with the camera(s). The acquired fringe images are stored on the computer hard-disk and then passed to the FDR module for processing. For each of the vertical and horizontal fringe pattern sets, a number of s complex signals are computed for the whole sequence of acquired images, each of which is stored as two images containing the real and imaginary components. By pre-computing the complex signals, a half of the memory space can be released, i.e. only $2s$ images of the complex signals rather than $4s$ fringe images are loaded to the memory. The complex signals are multiplied with a suitable window function (e.g. rectangular, Hann and Hamming [167]) to reduce spectral leakage in the Fourier transform. Then, a number of N_p phase gradient maps $\omega_x^{(m)}$, where $m=1,2,\dots,N_p$ and N_p is the maximum number of peaks needed, are computed by the FDR phase estimation algorithm for the vertical fringes. There are also N_p phase gradient maps $\omega_y^{(n)}$, where $n=1,2,\dots,N_p$, computed for horizontal fringes. Each pair $(\omega_x^{(m)}, \omega_y^{(n)})$ of the phase gradient maps are then passed to a point-cloud triangulation function (written in C and compiled as a dynamic-link library DLL which can be called by most programming languages), and the corresponding 3D coordinates and triangulation errors are obtained. These triangulation results are saved on the computer hard-disk instead of in random access memory (RAM), because the total of N_p^2 pairs may cause memory overflow if N_p is sufficiently large. However, for a small value of N_p the results are kept in the memory to increase the processing speed. Finally, an optimum pair is selected for each pixel as the one with the lowest triangulation error, and the corresponding optimum 3D point cloud results are obtained.

7.3 Experimental results

7.3.1 Proof-of-principle specimen

A specimen has been constructed consisting of a pair of planar surfaces arranged in a 'V' formation, as shown in Figure 102-a. One of the surfaces is made of plastic and has a diffuse white finish, and the other is a mirror. The diffuse plastic plate has dimensions of $500 \times 300 \text{ mm}^2$, which is larger than the mirror (dimensions of $200 \times 200 \text{ mm}^2$). The arrangement of the specimen and the scanner, as depicted in Figure 102-b, was chosen so that the lower half of the plate surface was illuminated both by rays following a

direct path from the projector to the surface and by rays reflecting from the mirror surface, i.e. the lower half was affected by multiple reflections. The upper half of the plate surface remained illuminated only by direct light rays. If the FDR technique worked perfectly, there should be no difference in the measured shape of the lower half measured with and without the mirror.

The specimen was inspected using the Phase Vision shape measurement system SMS1200 which has a camera-projector baseline distance of 1200 mm, a 4-megapixel and 12-bit camera and a powerful digital projector. The scanner was calibrated to obtain a measurement area of $600 \times 600 \text{ mm}^2$ (which covers the entire surfaces of the specimen) and a calibration error of approximately $60 \text{ }\mu\text{m}$ (or $1/10,000$ of the side of the measurement area). The calibrated global coordinate system was located at nearly 2.5 m away from the scanner and had the Z-axis pointing towards the scanner. A forward linear sequence ($t=0,1,2,\dots,s-1$) of sinusoidal fringe patterns was projected onto the specimen surfaces for each of the orthogonal vertical and horizontal fringe orientations, with the maximum fringe density of $s=64$ fringes across the projected field of view. The four-frame phase stepping algorithm was used.

Some acquired fringe images are shown in Figure 103, including the first and the last two images of the acquisition process. Both of the vertical and horizontal fringe images clearly show a simple fringe pattern in the upper half and a more complex pattern, formed by the superposition of the directly illuminated and reflected rays, in the lower half of the white surface. All of the acquired images were archived to hard-disk and subsequently analysed by the FDR technique as well as the reverse exponential phase unwrapping technique.

The results of phase gradients estimated by the FDR technique are shown in Figure 104. It can be seen that only one phase gradient value is detected for each of the pixels in the upper half of the white surface, whereas two phase gradients are detected in the lower half, for each of the fringe orientations. It is interesting that two phase gradients for each fringe orientation are also achieved on the mirror surface and appear to be symmetrical with those achieved on the lower half of the white surface. This is because the former are a virtual image of the latter. The corresponding phase amplitudes are presented in Figure 105, showing that the signal strengths of the strongest (primary) peaks are about twice those of the secondary peaks. Although the amplitudes indicate high strengths

(and thus reliabilities) of the detected signals, they do not necessarily specify which signal corresponds to a correct scattering point. The triangulation error ε_1 , which is the criterion to select correct scattering points, is displayed in Figure 106-a to -d for each of the four pairs of phase gradients $(\omega_x^{(1)}, \omega_y^{(1)})$, $(\omega_x^{(1)}, \omega_y^{(2)})$, $(\omega_x^{(2)}, \omega_y^{(1)})$ and $(\omega_x^{(2)}, \omega_y^{(2)})$. The label map of optimum ε_1 is shown in Figure 106-e, which assigns to each pixel the index of the pair having the lowest triangulation error ε_1 . The triangulation error map of the selected optimum result is thus given in Figure 106-f, which shows relatively low errors over almost the entire surfaces. However, some pixels near the hinge with the mirror give high errors, which is due to the fact that the travel distances of direct and indirect light rays to a scattering point are so similar that the two corresponding peaks could not be distinguished clearly (i.e., the peak cross-talk effect). For pixels lying right next to the hinge, their errors return to normally low values although the peak cross-talk still is present. This is because the frequencies of the peaks are identical and choosing either peak gives the same correct result.

The final results of optimum phase gradients and 3D coordinates of scattering points are shown in Figure 107. It can be seen that the lower half of the white surface, which was corrupted by multiple reflections, has been successfully recovered. The measured data are continuous across the boundary with the unaffected upper half, showing that the FDR technique can deal with both single-reflection and multiple-reflection situations. The pixels with relatively high errors near the hinge of the white surface and the mirror surface can be improved further by (i) using additional refinement steps in the Newton-Raphson optimisation, and (ii) increasing the projected fringe density s . A parametric study of these two issues is discussed in the next sections.

Effect of the number of refinement iterations

The above-mentioned results were obtained with only one iteration of the refinement step (i.e. step 4) presented in Section 7.2.3. To study the effect of the number of refinement iterations on the measurement precision, two additional computation cases were carried out: one with no refinement iteration and the other with two iterations. The resulting triangulation errors ε_1 for the three cases are presented in Figure 108 for comparison. The results show that two improvements on ε_1 can be achieved by increasing the number of iterations. Firstly, the ripples present over the entire multiple-reflecting lower half of the white surface reduce as the iteration number increases. This

is due to the increasing peak detection accuracy. Secondly, more pixels are recovered in the region near the mirror, which are influenced by the peak cross-talk. However, the second improvement is not significant, as the available signal content is restricted by the frequency resolution.

Effect of the number of fringes s

The frequency resolution has a strong effect on the phase gradient error and thus the triangulation error. In this experiment, four values of fringe densities which are $s=8$, $s=16$, $s=32$ and $s=64$ were tested and their corresponding triangulation errors ε_1 are shown in Figure 109. It can be seen that ε_1 in the multiple-reflecting region decreases significantly with the fringe density s with the large errors becoming progressively confined to the ‘hinge’ region. This is to be expected since, as the hinge region is approached, the two locations on the projector’s SLM through which the direct and reflected illuminating beams pass become progressively closer to one another. The datasets with a large s value result in a narrower Fourier domain peak and therefore can reach closer in to the hinge before the two peaks begin to overlap. Therefore, a fringe density larger than the value of 64 used in this experiment is expected to improve the measurement precision of the FDR technique still further. A trade off of this is the longer acquisition time and larger fringe data set for the computer to handle. For the current fringe density of $s=64$, there are a total of $2 \times 4 \times 64 = 512$ fringe images (each of which has 4 megapixel resolution and 12-bit intensity scale) that require approximately 4 GB of storage.

Point-cloud measurement accuracy in comparison with the reverse exponential phase unwrapping technique

An accuracy measure ε_2 was computed for each scattering point on the white surface as the geometric deviation of its estimated 3D coordinates from a plane of best fit. Two best fit planes were computed for the scattering points within two regions of interrogation ROI1 and ROI2 defined in Figure 110. ROI1 lies in the single-reflecting upper half of the white surface, whereas ROI2 lies in the multiple-reflecting lower half. They were selected to contain meaningful point cloud results estimated by the reverse exponential phase unwrapping technique, for the purpose of comparison.

The errors ε_2 of the estimated point clouds from the best fit planes are shown in Figure 111 for both the FDR and the reverse exponential phase unwrapping techniques. It can be seen that the single-reflecting region ROI1 gives comparable errors for both techniques. The RMS error in ROI1 is 0.405 mm for the FDR technique and 0.417 mm for the reverse exponential technique. The residual errors indicate that there is some curvature to the plate, which explains why the obtained plane-fitting error ε_2 is higher than the expected error (about 60 μm for the present calibration) for the scanner. The multiple-reflecting region ROI2, on the contrary, gives very different errors. The RMS error in ROI2 is 0.538 mm for the FDR technique, which is slightly higher than that in ROI1. It is noted that the FDR result presented in Figure 111 was obtained without the peak refinement step; thus, the ripple in ROI2 is expected as explained previously in Figure 108. Nonetheless, the RMS error of 2.726 mm in ROI2 obtained by the reverse exponential technique, which implicitly assumes single-scattering only, is still about 5 times larger with significant peaks and troughs in the deviations of the measured point cloud from the best fit surface.

7.3.2 Practical shiny metallic components

In addition to the proof of principle experiments described above, the FDR technique has been applied to several practical mechanical components with shiny surface finishes. Two applications are presented in this section, which are for a cast-alloy cover of an automotive engine block and an aluminium-alloy rib of an aircraft wing. The former is partially shiny, whereas the latter is entirely shiny.

A texture image of the engine block is shown in Figure 112-a. The surface contains a rough and diffuse region and a fairly-shiny polished region near the clamp seen in the bottom of the image. The shiny region reflected the projector light onto the edge of the diffuse region, causing multiple reflections along the edge. This multiple-reflecting region can be seen in Figure 112-b as the corrupted data when estimated using the reverse exponential technique. Figure 113 presents the estimated point cloud by the FDR technique, showing that the corrupted data have been successfully recovered. However, the triangulation error ε_1 in this area is relatively high as compared to the rest of the surface. This is possibly caused by the peak cross-talk effect as the multiple-reflecting area is very close to the shiny region.

The application results of the wing rib are presented in Figure 114. As shown in the texture image, both the rib body and the rib foot have very a shiny surface finish. To reduce the effect of specular components, the rib was placed at an oblique angle with respect to the scanner so that the main specular direction does not point towards the camera and most of the projector light does not over-saturate the acquired images. The results of point cloud and triangulation error show that more than three quarters of the wing rib have been measured successfully with the FDR technique. However, there persist many pixels that are automatically masked out due to their low fringe modulations caused by over-saturation. Furthermore, the multiple reflections in the angle region near the rib foot are particularly challenging as the light reflects back and forth many times before reaching the camera, causing very significant triangulation errors.

7.4 Summary

A novel technique based on the Fourier domain ranging algorithm introduced by Huntley and Saldner [96] has been developed to measure partially reflective surfaces in the presence of multiple reflections. For the first time, the improved phase estimation algorithm by Huntley [166] has been extended to detect multiple signals and fully tested on both simulated and real data. A key contribution of this thesis is the introduction of a procedure to accurately detect multiple signals and select the optimum signal based on triangulation errors, thus allowing measurement data corrupted by the multiple reflection effect to be recovered easily. The algorithm has been implemented in both MATLAB and C++ for employment in industrial applications.

Validating experiments were carried out on a simple plate-and-mirror specimen, as well as an automotive engine block and an aircraft wing rib both with shiny surface finishes. The results of the first specimen have shown that the FDR technique is able to recover 3D coordinates of almost all scattering points that are influenced by multiple reflections. The parametric study has shown that increasing fringe density and peak refinement iteration may increase the measurement precision at the costs of acquisition and computing time. The comparison with the reverse exponential phase unwrapping technique has shown that the FDR technique provides superior measurement accuracy in the presence of multiple reflections, where the errors from a plane of best fit are reduced by approximately 5 times. Moreover, the good performance of the FDR

technique has been demonstrated by the experimental results of the engine block which contains a diffuse part next to a reflective part. However, for the entirely reflective surface of the wing rib the FDR can only recover around three quarters of surface scattering points.

7.5 Tables

Table 6: Comparison of phase gradients of simulated signal by several phase estimation techniques. The improved Fourier domain ranging technique shows the best accuracy.

	Phase frequency k	Phase gradient ω		Execution time (s)
		Mean (rad)	Std (10^{-5} rad)	
Reference	3.3	0.3240		
Temporal phase unwrapping with least square fitting [96]	3.2228	0.3164	2.3763	2.626
Original FDR [96]	3.2218	0.3163	2.3999	4.967
Improved FDR [166]	3.3002	0.3240	2.4327	1.052

7.6 Figures

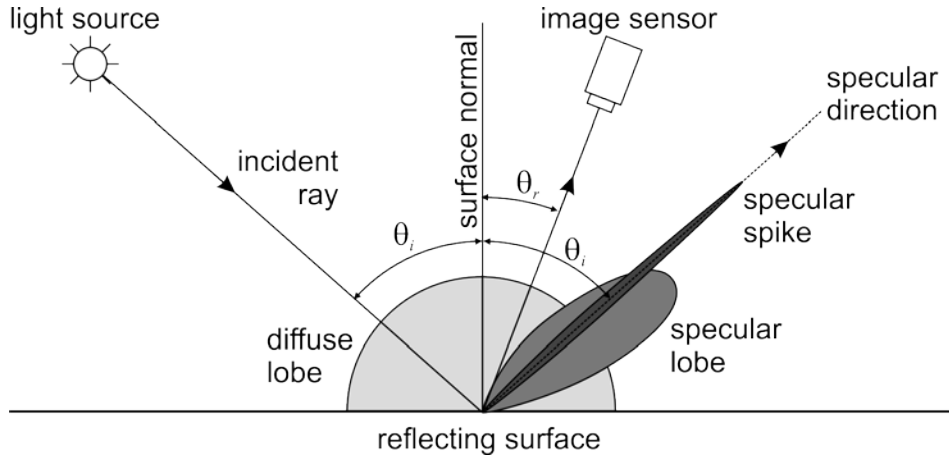


Figure 90: Polar plot of three surface reflection components as functions of the image sensor angle for a fixed incident angle.

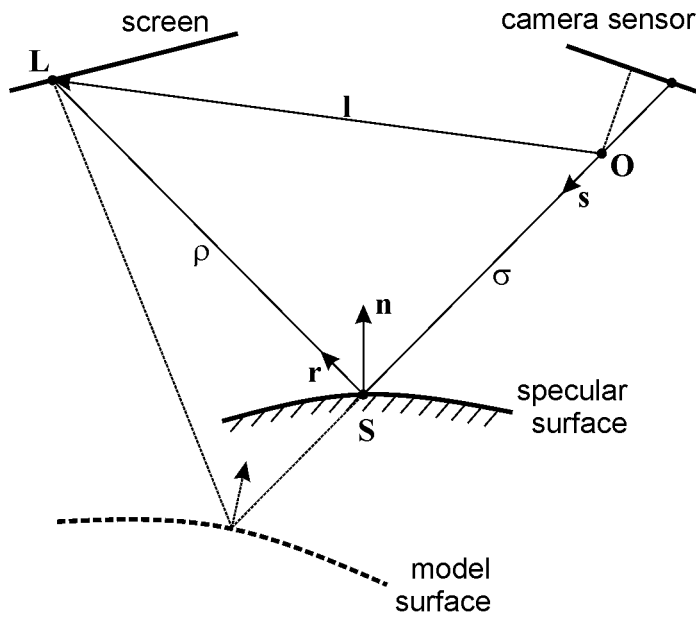


Figure 91: 2D representation of the back-ray-tracing principle of deflectometry technique. O is the camera lens pinhole. S is the reflection point to be determined on the surface. L is a point on the screen. \mathbf{n} is the normal vector of the surface at S . \mathbf{s} and \mathbf{r} are unit vectors specifying the reverse reflective and incident rays, respectively. \mathbf{l} is the vector specifying the location of L with respect to the camera position O . σ and ρ represents the distances from the camera O and the screen point L , respectively, to S .

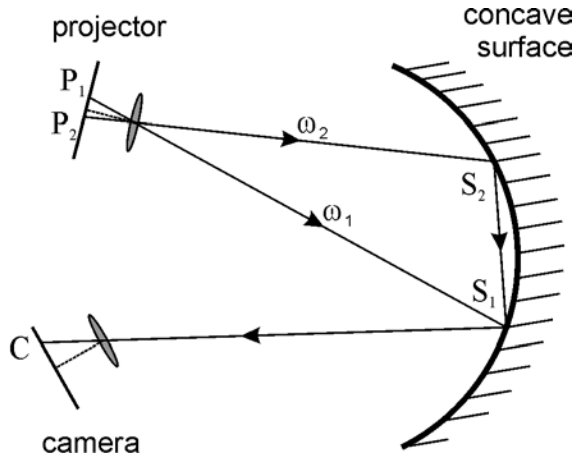


Figure 92: Multiple reflections of two signals emanating from two different projector points but superimposing on one camera point.

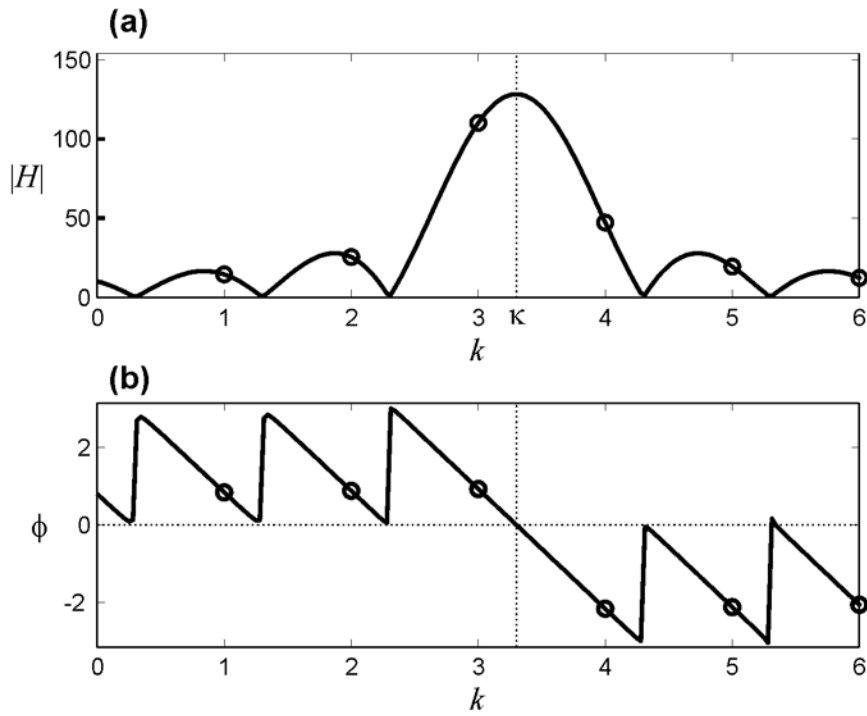


Figure 93: Amplitude (a) and phase (b) of Fourier transform of simulated signal I_s for a single pixel in the neighbourhood of the signal peak (at $\kappa = 3.3$). The open circles are computed from the discrete Fourier transform, whereas the continuous curves are the continuous transform.

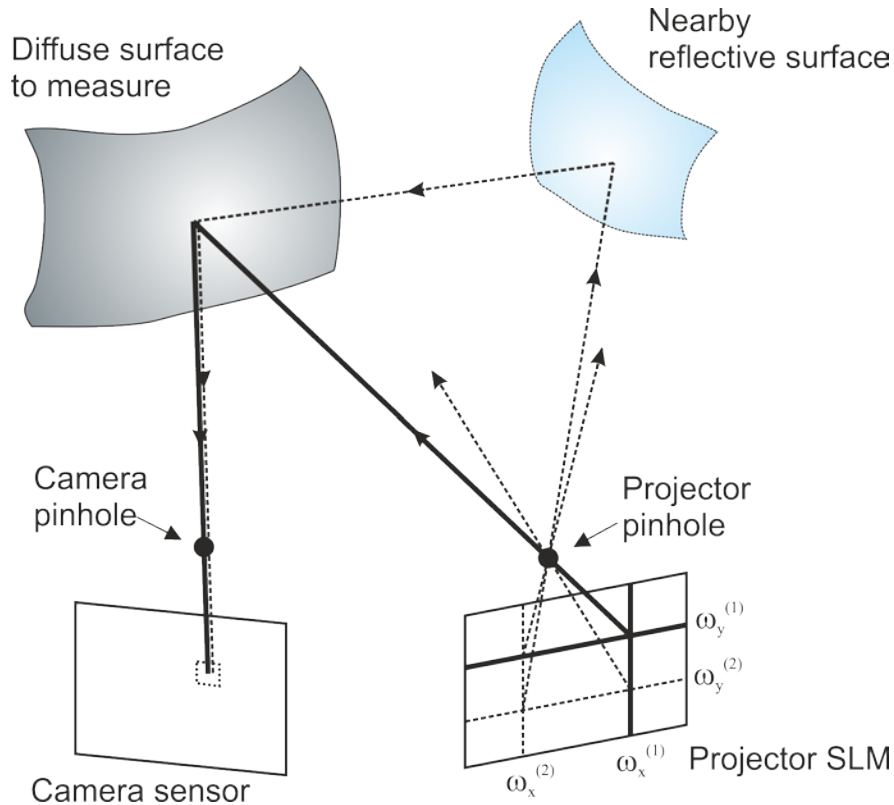


Figure 94: Model of two signals causing multiple reflections at a measured point. The correct direct signal emanates from point $(\omega_x^{(1)}, \omega_y^{(1)})$ on the projector SLM and reflects only once on the measured surface before reaching the camera sensor. The indirect signal emanates from point $(\omega_x^{(2)}, \omega_y^{(2)})$ on the projector SLM and reflects on both the reflective surface and the measured surface before reaching the camera.

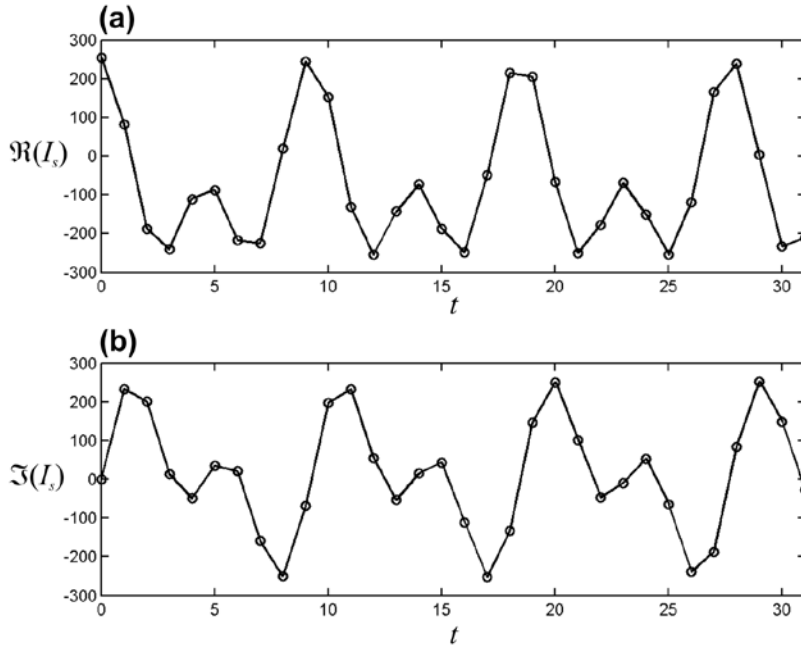


Figure 95: Real (a) and imaginary (b) components of simulated complex signal $I_s(t)$ at a point on the measured surface which scatters light received from two light rays.

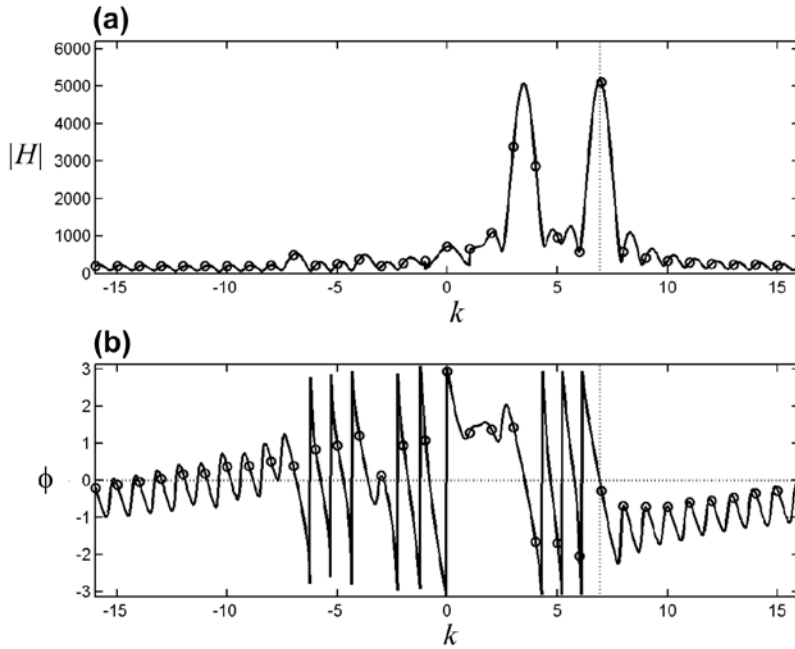


Figure 96: Amplitude (a) and phase (b) of Fourier transform of the complex signal $I_s(t)$ shown in Figure 95. The strongest peak is located at $k_x^{(1)}=6.90$ and the weaker is at $k_x^{(2)}=3.45$, corresponding to signal frequencies of $\omega_x^{(1)}=1.35$ rad and $\omega_x^{(2)}=0.68$ rad.

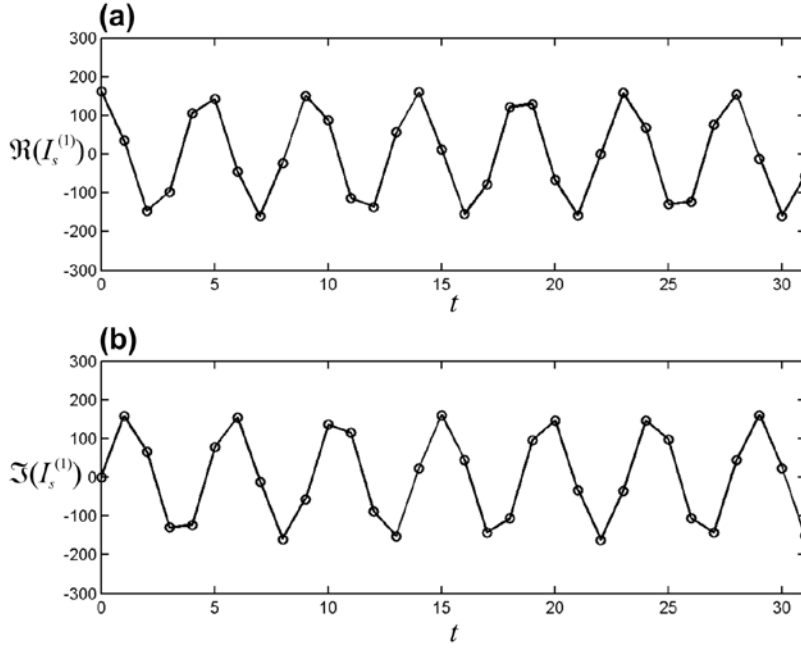


Figure 97: Complex signal $I_s^{(1)}$ corresponding to the detected peak 1 shown in Figure 96. The frequency of the signal is $\omega_x^{(1)}=1.35$ rad.

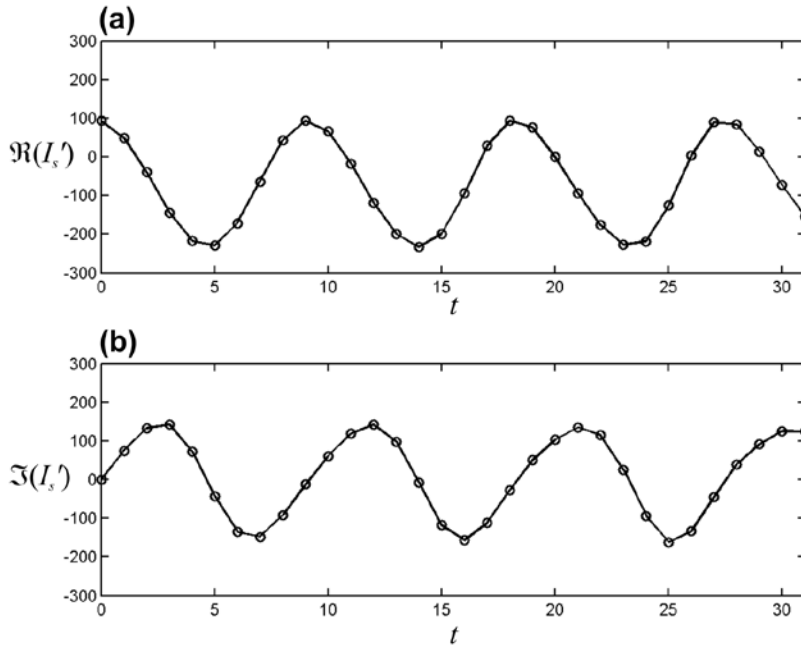


Figure 98: Remaining complex signal $I_s'(t)$ after removing the detected peak 1 (by subtracting the original signal shown in Figure 95 by the signal of peak 1 shown in Figure 97).

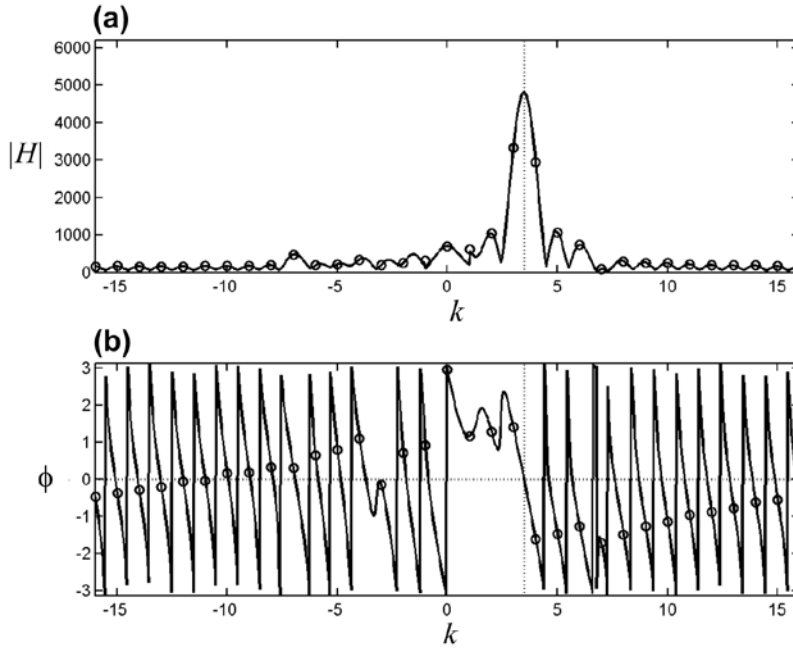


Figure 99: Amplitude and phase of the remaining complex signal $I_s'(t)$ shown in Figure 98. The peak 2 is identified at $k_x^{(2)}=3.45$ corresponding to $\omega_x^{(2)}=0.68$ rad.

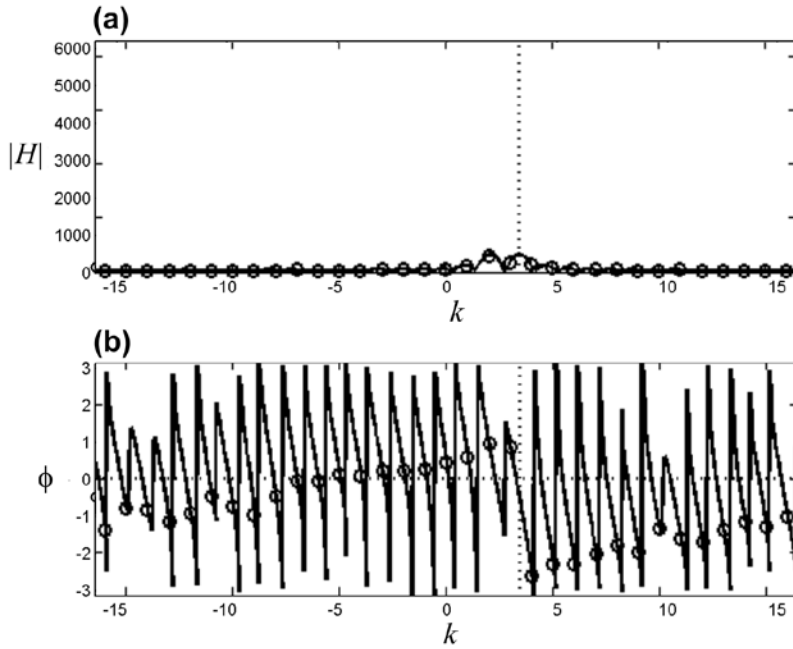


Figure 100: Amplitude and phase of the remaining complex signal $I_s''(t)$ after peak 2 is removed. No valid tertiary peak is detected as the signal amplitude is not sufficiently high.

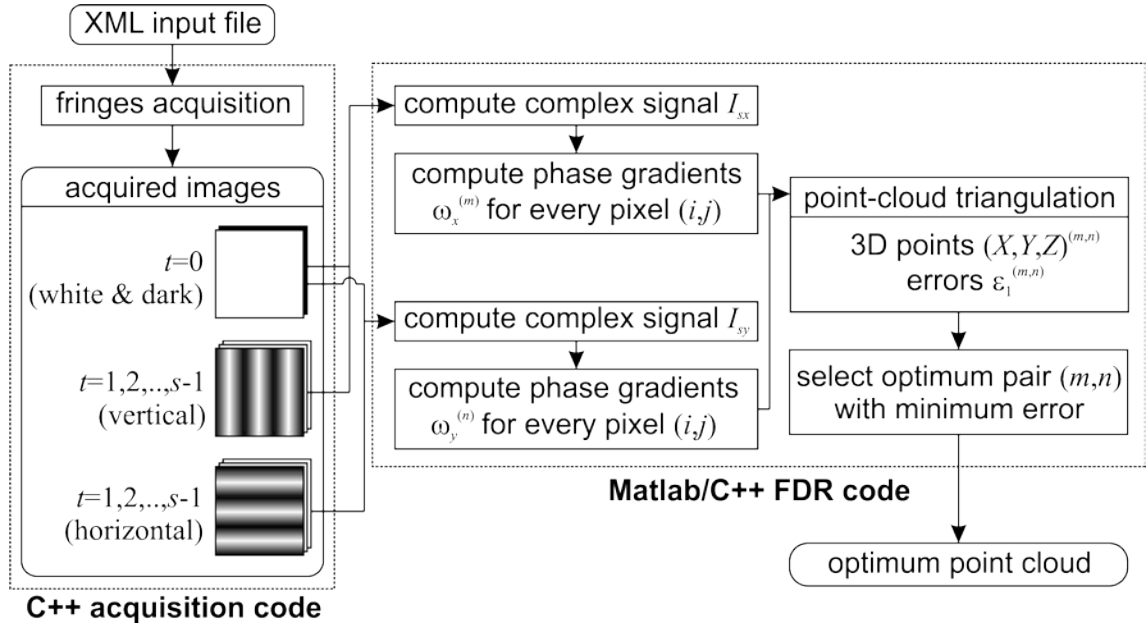


Figure 101: Data flow diagram of the FDR code.

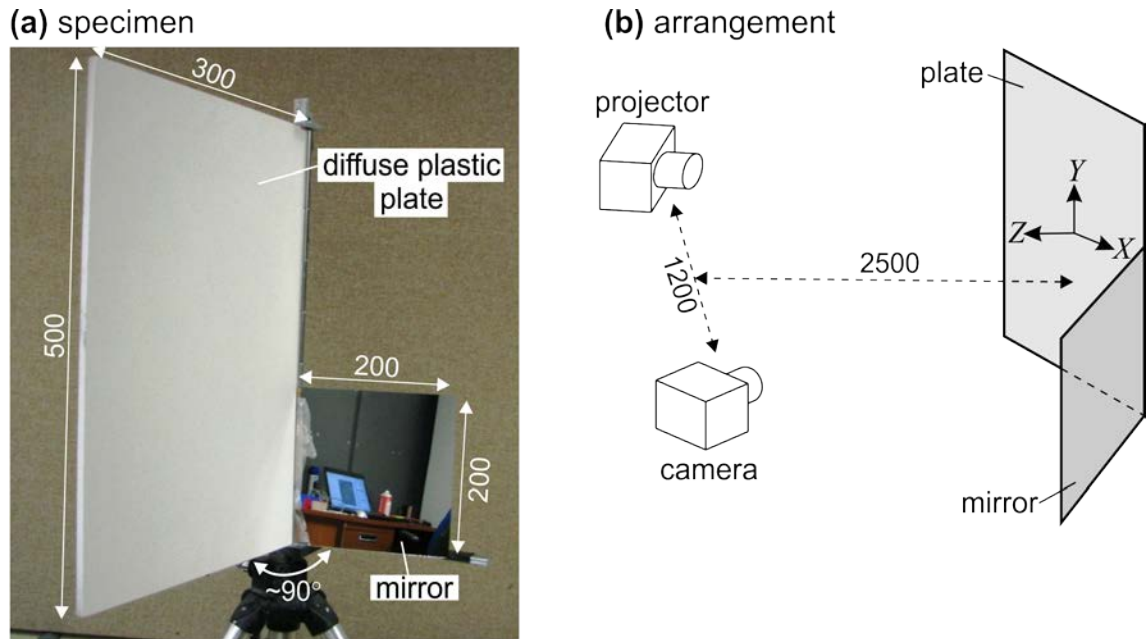


Figure 102: Specimen (a) and arrangement (b) of proof-of-principle experiment. The measured surface is a diffuse flat plate placed next to a mirror. A SMS1200 scanner with 4Mpixel camera was used. All dimensions are expressed in mm and are not to scale.

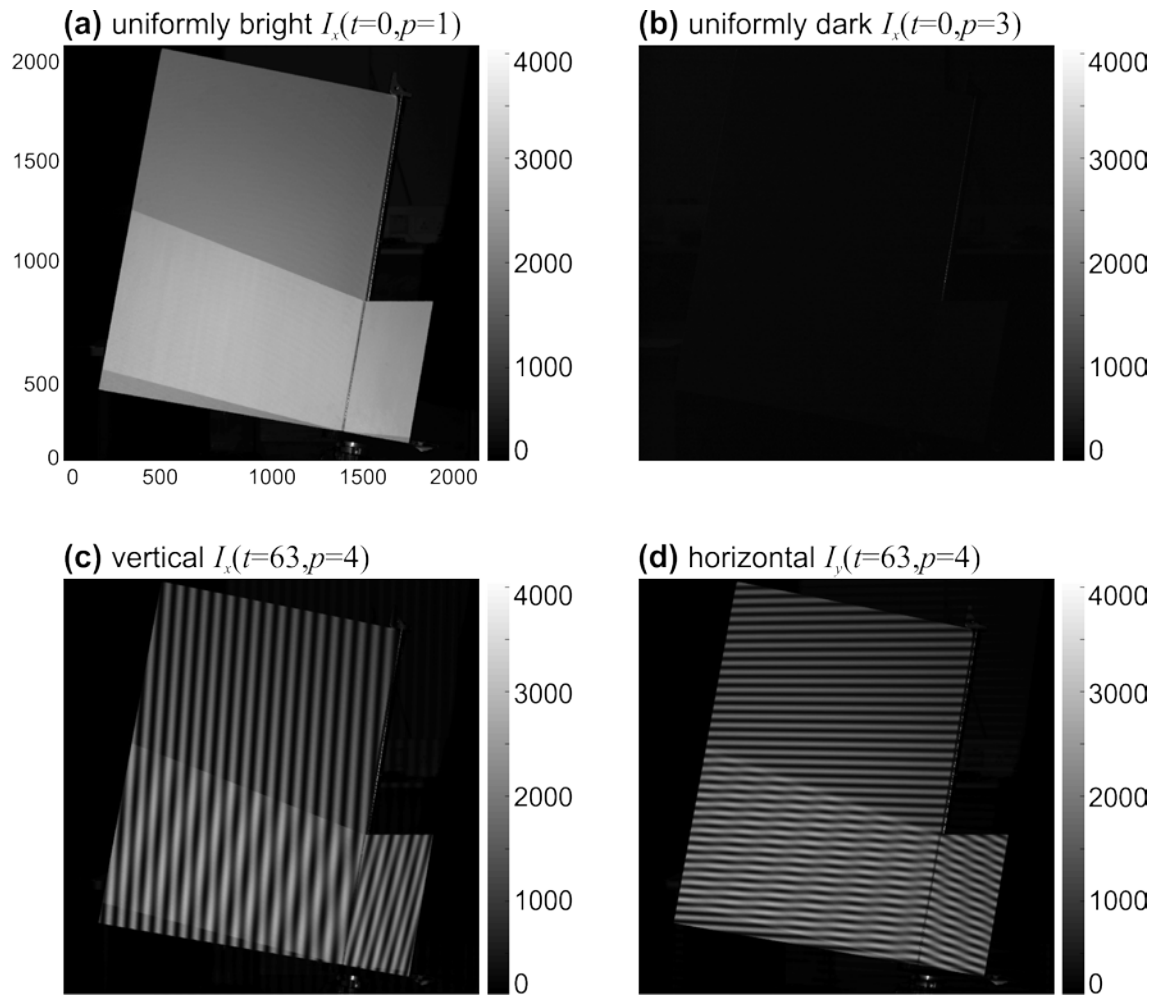


Figure 103: Some acquired fringe images of the plate-and-mirror specimen. (a) Image of uniformly-bright vertical fringes. (b) Image of uniformly-dark vertical fringes. (c) Image of last vertical fringe pattern. (d) Image of last horizontal fringe pattern. Disrupted fringes in the bottom half of the plate indicate multiple-reflection effect.

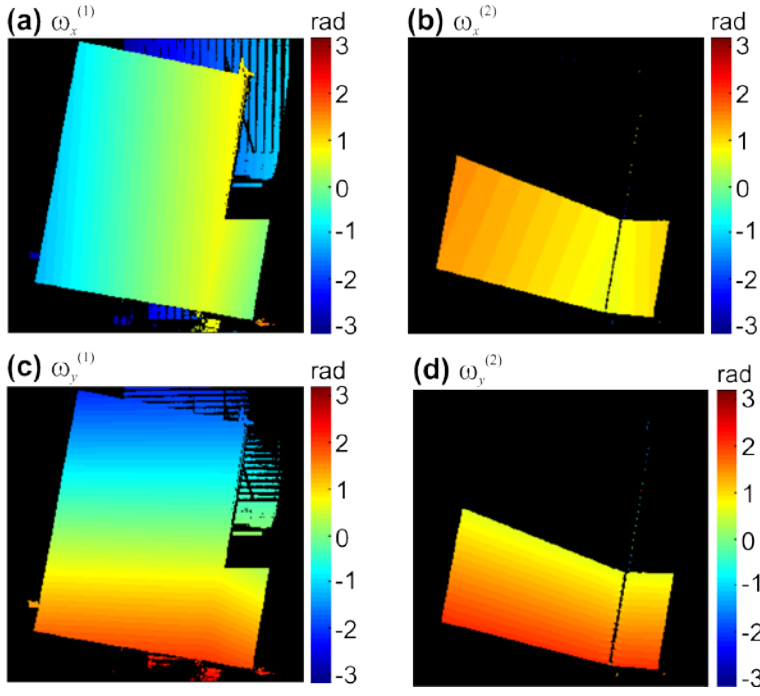


Figure 104: Phase gradients of two strongest signals (1 and 2) computed for vertical fringes (a&b) and horizontal fringes (c&d). The number of fringes is $s=64$ for each fringe orientation.

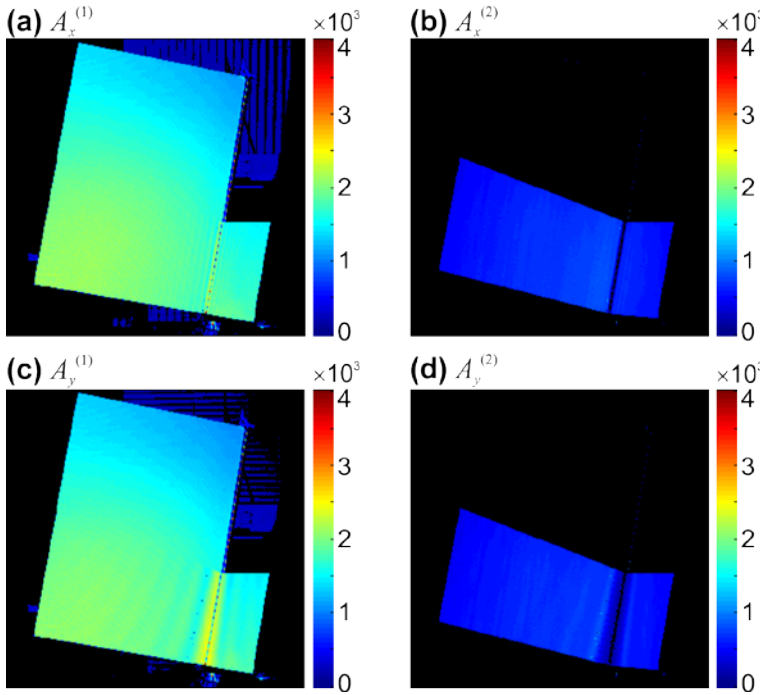


Figure 105: Amplitudes of two strongest signals (1 and 2) computed for vertical fringes (a&b) and horizontal fringes (c&d). $s=64$ for each fringe orientation.

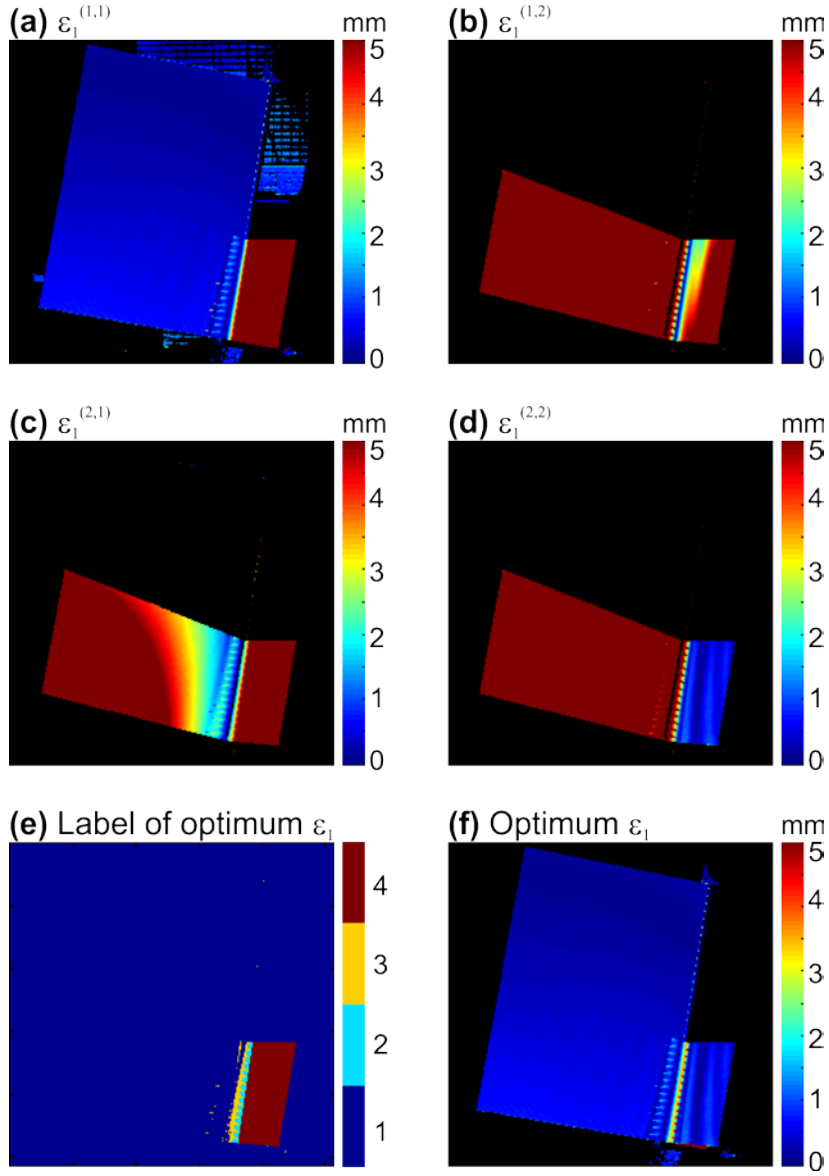


Figure 106: Triangulation error maps corresponding to four phase gradient pairs: (a) pair 1 ($\omega_x^{(1)}, \omega_y^{(1)}$), (b) pair 2 ($\omega_x^{(1)}, \omega_y^{(2)}$), (c) pair 3 ($\omega_x^{(2)}, \omega_y^{(1)}$) and (d) pair 4 ($\omega_x^{(2)}, \omega_y^{(2)}$). (e) Map to label an optimum pair (i.e., pair giving the lowest error) for every pixel. (f) Triangulation error of optimum result. $s=64$ for each fringe orientation.

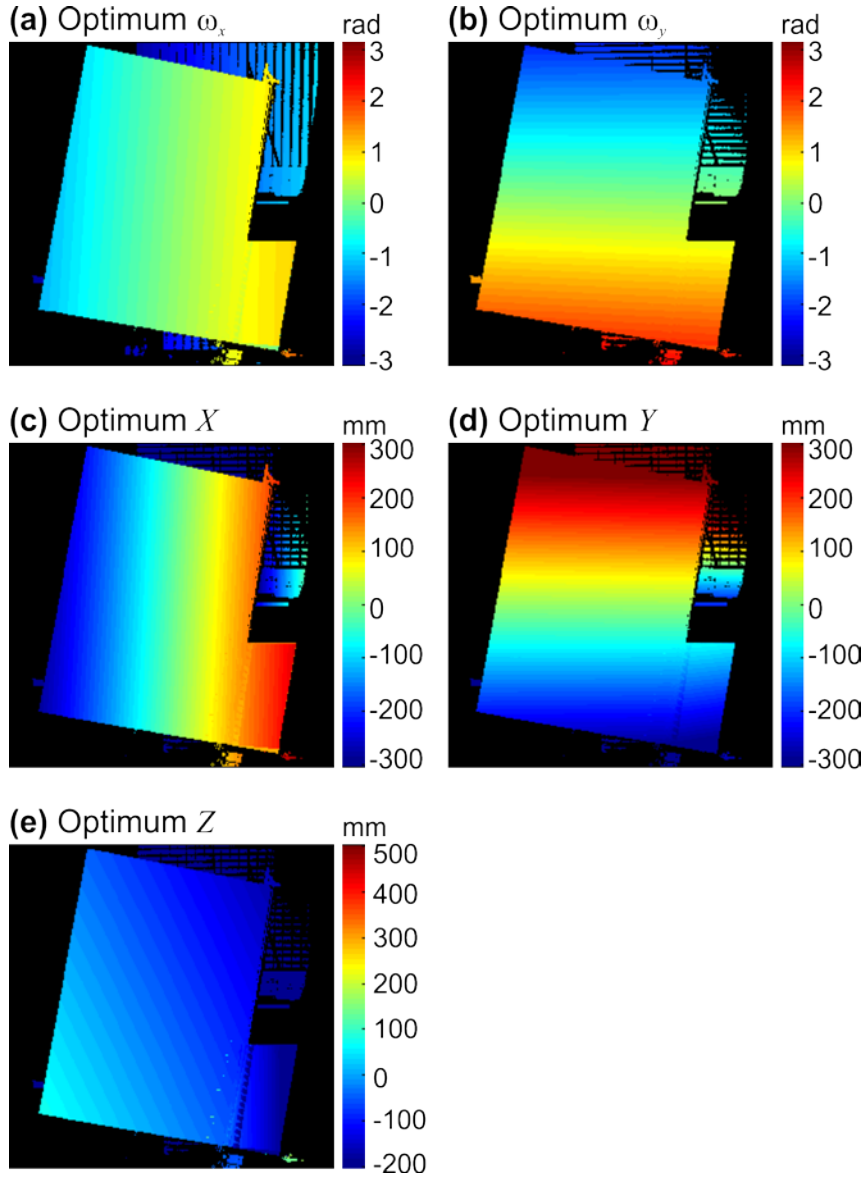


Figure 107: Optimum results of phase gradients for vertical fringes (a), phase gradients for horizontal fringes (b), X-components of scattering points (c), Y-components of scattering points (d), and Z-components of scattering points (e). $s=64$ for each fringe orientation.

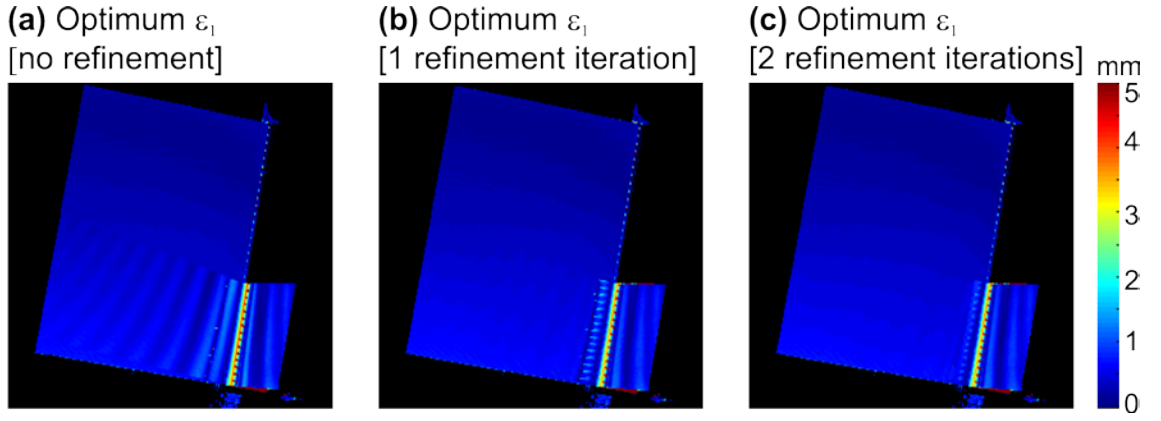


Figure 108: Variation of optimum triangulation error ε_1 with number of refinement iterations.

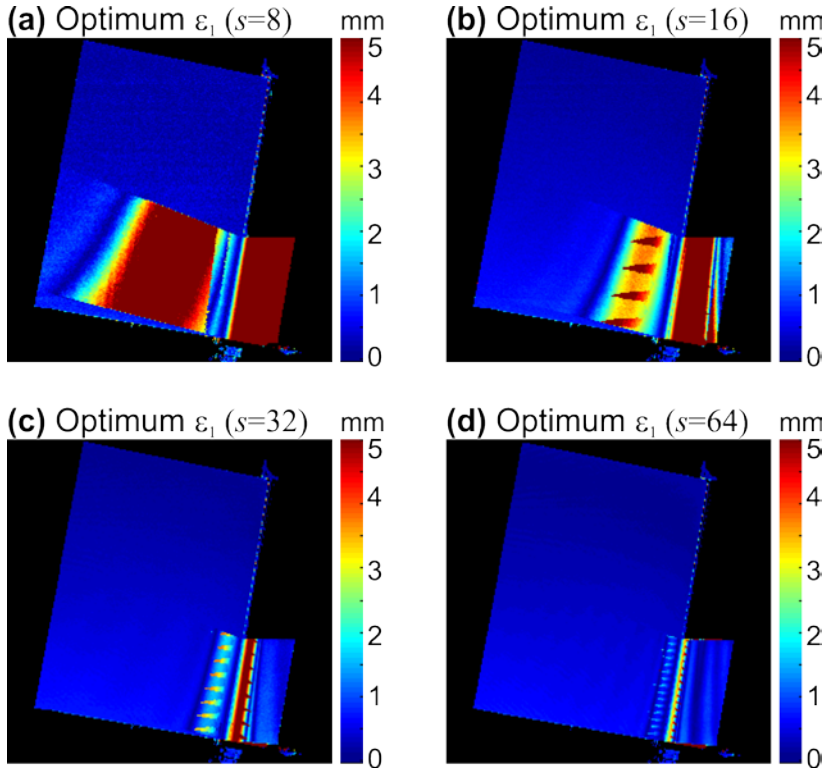


Figure 109: Variation of optimum triangulation error ε_1 with maximum number of fringes s .

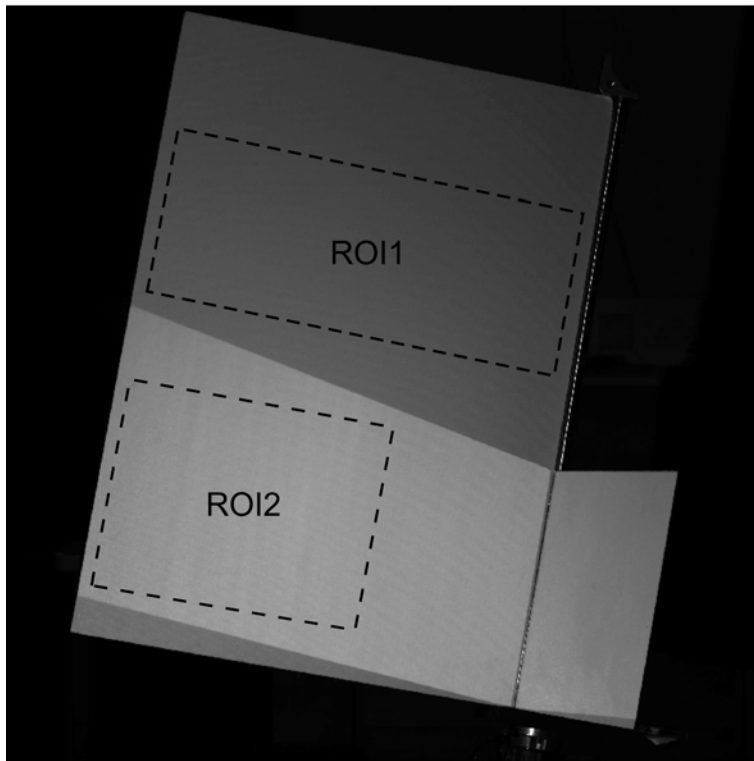


Figure 110: Regions of interrogation used to compute best fit planes shown in Figure 111. ROI1 receives only direct reflection (i.e. not affected by multiple reflections), whereas ROI2 receives both direct and indirect reflections (i.e. affected by multiple reflections).

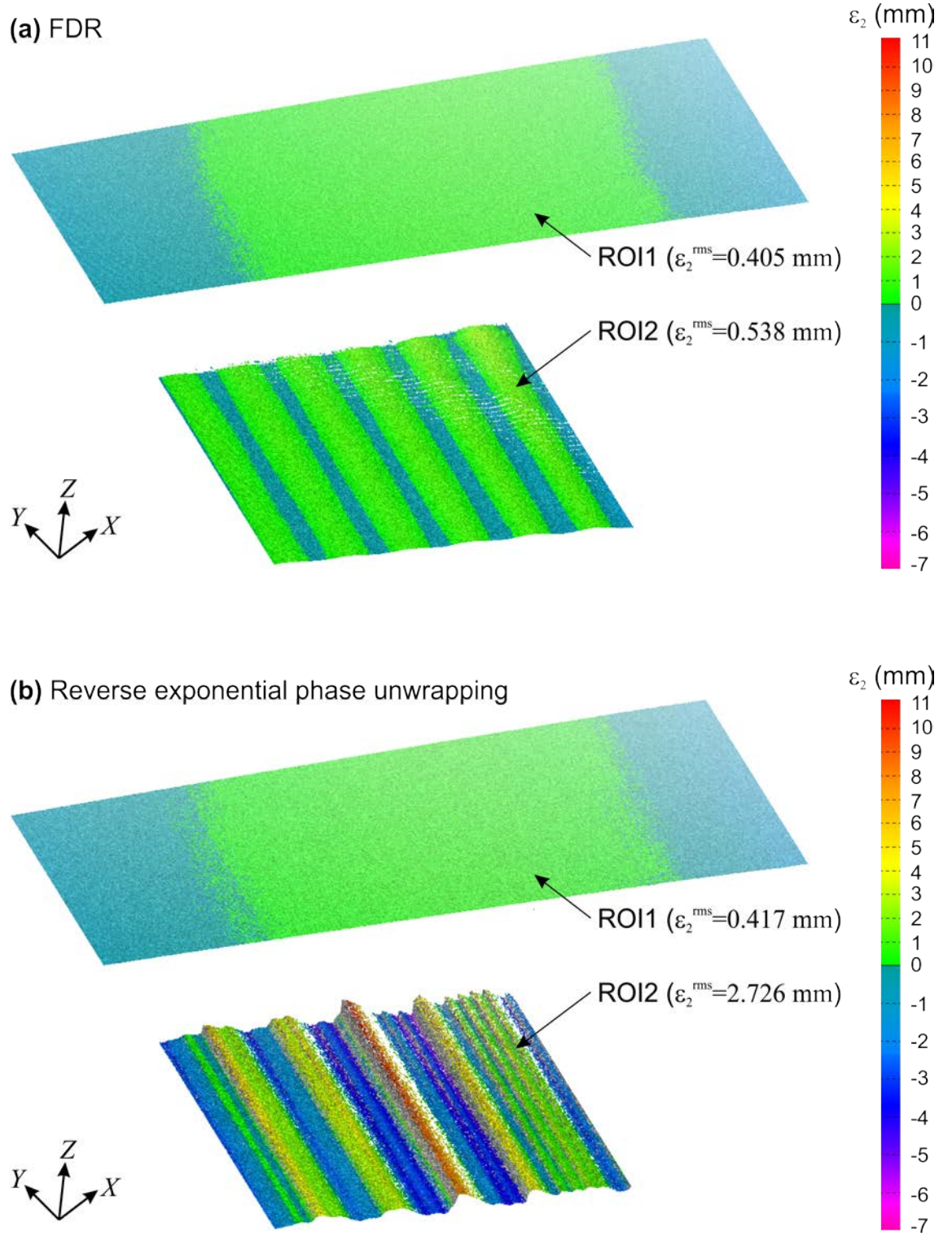


Figure 111: Comparison of resulting scattering points in regions ROI1 and ROI2 estimated by the Fourier domain ranging (a) and the reverse exponential phase unwrapping (b) techniques. The colour bar represents deviation ε_2 from the planes of best fit. ROI1 and ROI2 are defined in Figure 110.

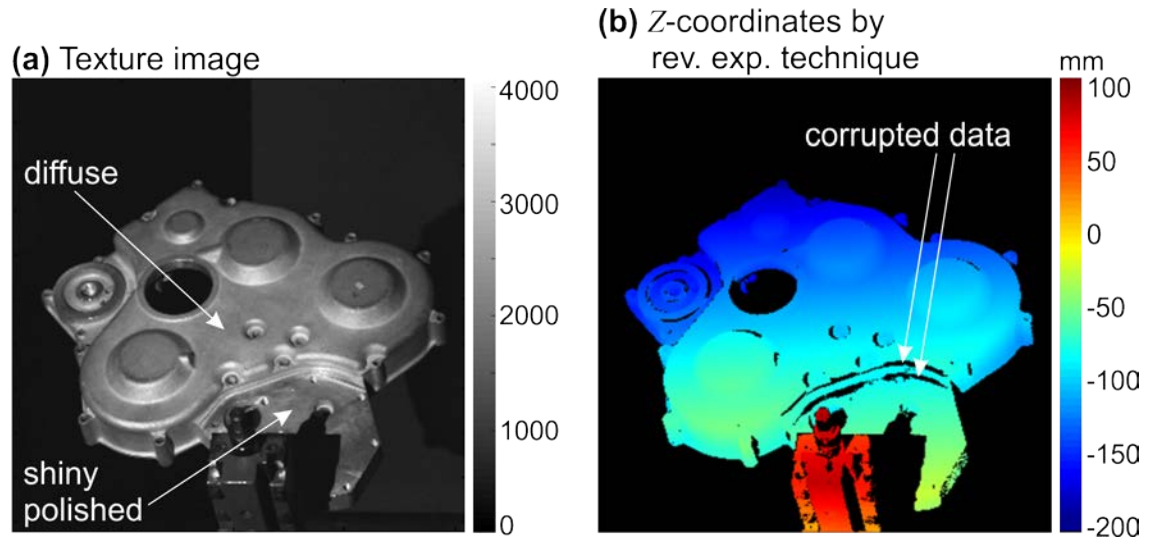


Figure 112: Metallic engine block cover containing a shiny-polished part. (a) Texture image for uniformly bright illumination. (b) Depth range map computed by the reverse exponential phase unwrapping technique, showing masked-out regions with excessively high ε_1 due to multiple reflections.

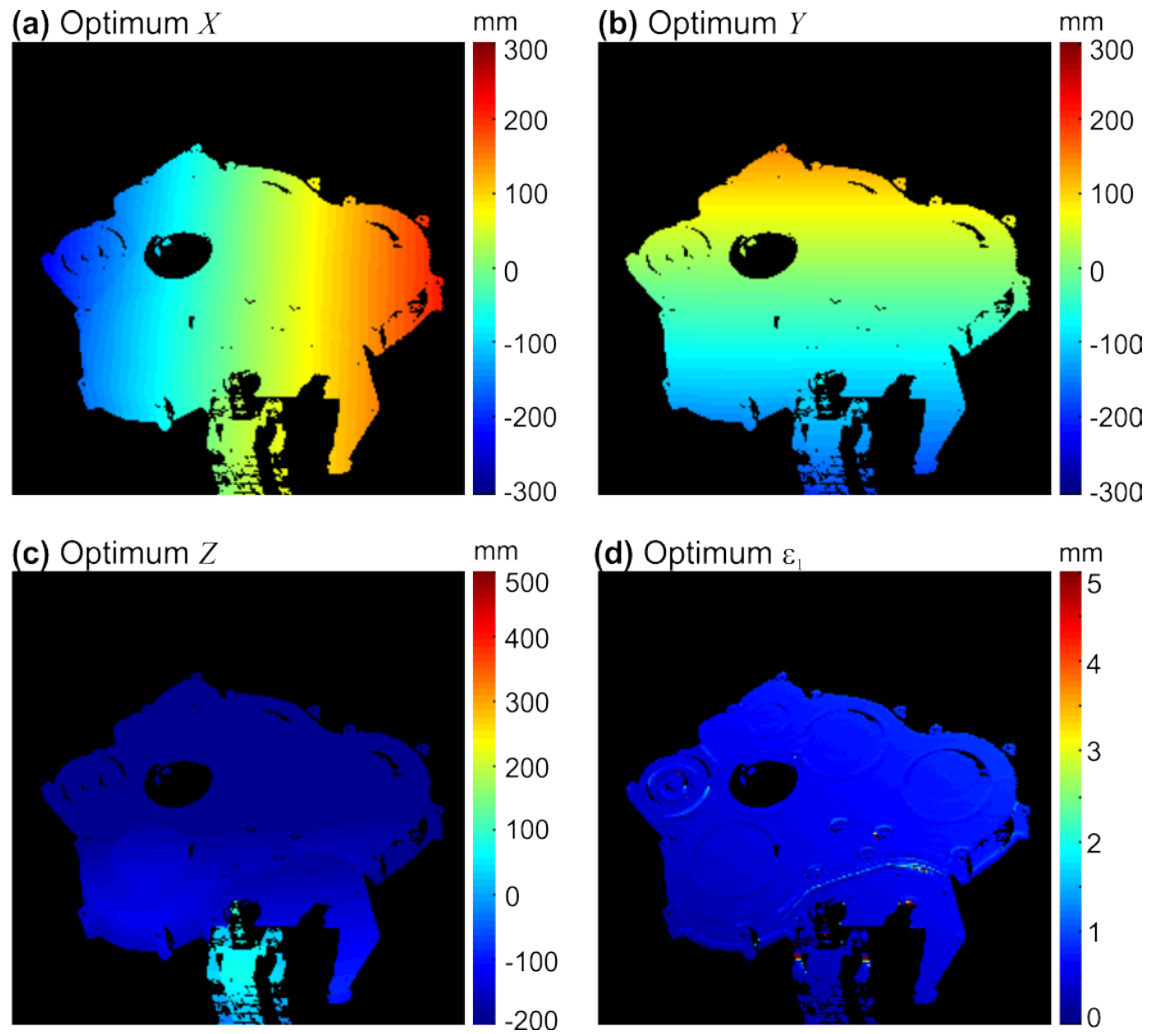


Figure 113: Scattering points of engine block computed by the FDR technique.

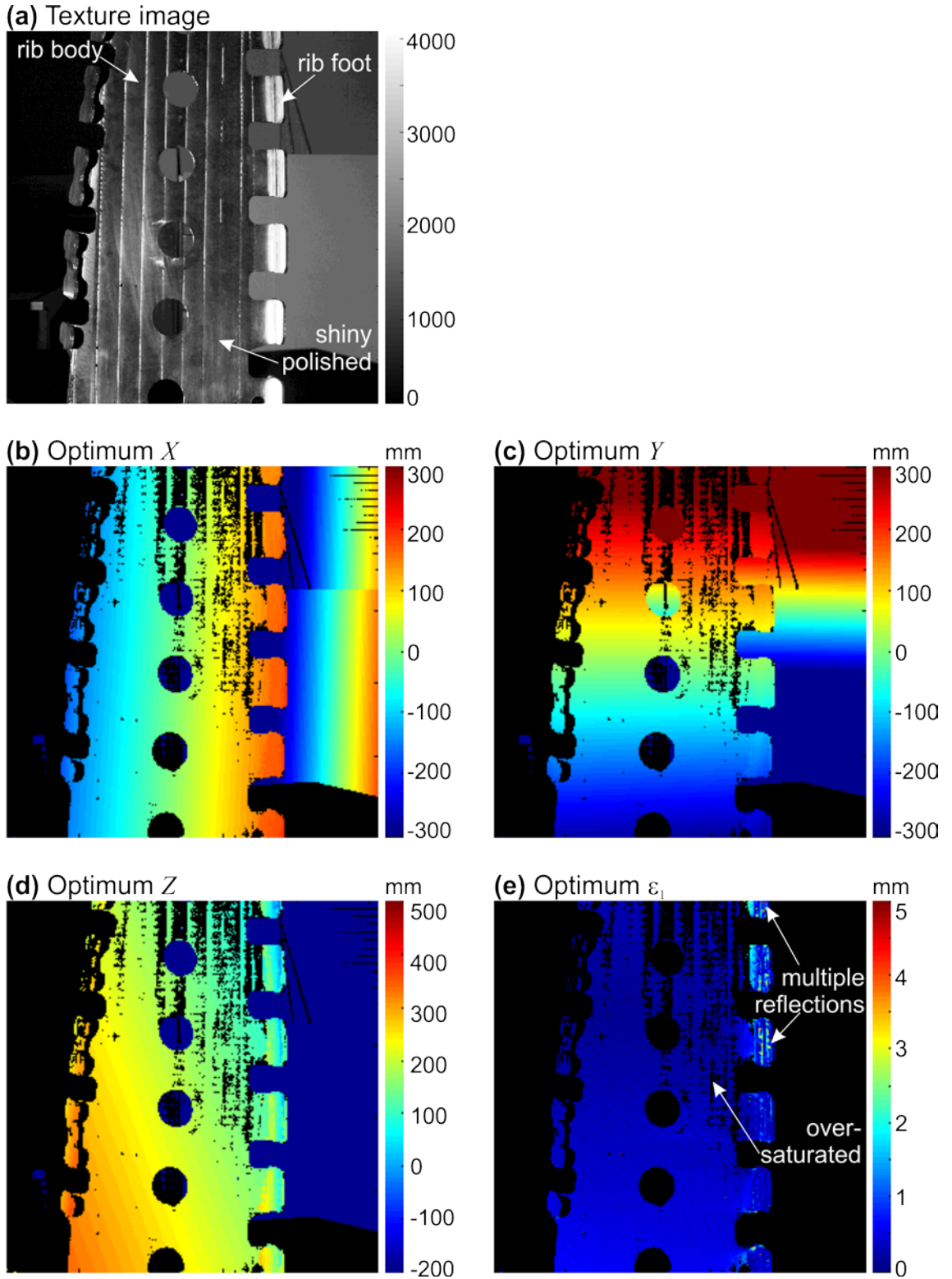


Figure 114: Measurement results of a very shiny aluminium-alloy wing rib obtained by the FDR technique. Over-saturated pixels with excessively high triangulation error ε_1 have been automatically masked out. Most pixels affected by multiple reflections have been recovered although their ε_1 errors are relatively high.

Chapter 8

Conclusions and further work

Optical measurement techniques have been developed rapidly over the last twenty years and have been used in a wide range of industrial applications. One of the most popular optical techniques for measuring the 3D shapes of medium-to-large-scale surfaces is the *fringe projection* technique, whilst the *digital image correlation* (DIC) technique has become a standard in measuring deformation fields. A shape measurement system (SMS) based on the principle of fringe projection has been developed at Loughborough University and its spin-out Phase Vision Ltd. In this SMS, a set of sinusoidal fringes with time-varying fringe pitch are generated on the spatial light modulator (SLM) of a projector and are projected onto the surface to be measured. A digital camera located at a distance from the projector is used to capture the images of the fringe patterns. The temporal change in phase of the fringes as observed at each image pixel encodes the 3D coordinates of a scattering point on the object surface. This phase gradient is estimated unambiguously by a temporal phase unwrapping technique used in conjunction with a phase-shifting algorithm. Both vertical and horizontal fringe orientations are used; and a pair of phase gradients is estimated at each pixel of the camera image, which corresponds to a point on the projector SLM. The 3D coordinates of the scattering point can be determined by intersecting a ray coming from the camera pixel and a ray coming from the projector point, following an optimisation scheme to minimise their closest distance. Each image pixel is processed independently of each other, allowing the SMS to measure discontinuous surfaces as easily as smooth ones. The photogrammetry-based calibration technique is able to provide an accuracy as small as 1 part in 20,000 of the measure volume side. The SMS can easily be expanded to contain multiple cameras and multiple projectors due to its modular hardware and software design; and multiple views of an object can be achieved for up to 360° coverage and are automatically defined in a global coordinate system.

This thesis has focused on extending the feasibility and accuracy of the SMS so that it can be applied in industrial environments. Summaries and conclusions of the main findings of the thesis are discussed as follows.

8.1 Conclusions

An automated positioning system for the calibration artefacts has been developed to replace the manual system. The system consists of a robot arm with pan and tilt degrees of freedom to hold and rotate to an artefact clamp, a control box connected to the SMS computer and self-developed C++ monitoring code integrated within the SMS software. The positioning system has been successfully implemented and used for the calibration of most Phase Vision scanners, although now an alternative method based on lightweight planar artefacts are routinely used in place of the ball bar. It has been providing the advantages of shorter calibration time, less laborious operation, higher repeatability and higher traceability as compared to the original manual system. As an additional advantage, an algorithm has been developed to estimate the whereabouts of the artefact from the knowledge of the assigned pan and tilt angles. The subsequent artefact detection process can thus benefit from this, as detection regions are reduced significantly to the vicinities of the predicted locations.

A technique has been introduced to combine the strengths of the digital image correlation and the fringe projection techniques for simultaneous measurements of both shape and deformation. The proposed technique offers two unique advantages over available combined fringe-projection and DIC techniques: (i) the ability to detect geometrical discontinuities and automatically adjust the image correlation along the discontinuities, and (ii) the ability to extend to multiple sensors. The general idea for achieving a 3D displacement field is to track the movement of a dense point cloud measured with the fringe projection technique. The tracking is done on the camera images by using the 2D digital image correlation technique which traces a random speckle pattern previously-applied to the measured surface. As the main contribution, a new image correlation algorithm guided by the point cloud data of the structured-light fringe projection has been proposed to deal with geometrical discontinuities on the surface which strongly affect the accuracy of conventional image correlation techniques within correlation windows straddling the discontinuities. Experimental results have demonstrated the capability of the combined SMS-DIC technique in measuring a discontinuous plate that contains a hole and a step under rigid-body translation. A measurement of nearly 1 million points with a spatial resolution of 1 pixel, an accuracy of 1/7,000 and a precision of 1/24,000 of the measurement volume side length has been

reported. The technique provides 3D displacement fields, yet requires only the most basic SMS hardware of a single camera and a single projector without any additional hardware costs. However, it may be restricted to applications with relatively low strain rates.

The combined SMS-DIC technique can be easily expanded to multiple cameras and multiple projectors to achieve up to 360° measurements of both shape and deformation fields. Due to the calibration technique, measured point clouds of all the views are automatically defined in a unified coordinate system; and thus no extra point cloud alignment is needed. A simple procedure to combine estimated point clouds and deformation fields to a single model has been introduced. Experimental results have been reported on an aluminium sheet bent into a top hat profile which was loaded under central-point bending. A displacement accuracy of 1/12,000 of the measurement volume diagonal has been achieved. Comparison with a finite element model and the output of a standard DIC system has shown that the combined SMS-DIC technique was able to provide accurate measurements of the whole surface, including around its discontinuities where standard DIC often fails.

Two applications of the SMS-DIC technique in the industrial environments of the aircraft manufacturer Airbus UK have been reported. The first application is a static fatigue test of an A380's metallic wing cover, of which the test results have shown that the SMS-DIC technique is able to obtain very dense displacement fields and strain fields. The achieved strain fields were in good agreement with those measured with strain gauges, where a discrepancy of 100 microstrain has been reported. The second application is a buckling test of an A350's composite wing panel. The experimental results have demonstrated the ability of the SMS-SIC to measure such a complex object that contains severe geometrical and displacement discontinuities.

A novel technique based on the Fourier domain ranging (FDR) method has been developed to recover shape measurement data corrupted by the multiple-reflection problem in which a scattering point receives light from both a direct ray coming straight from the projector and an indirect ray reflected from a nearby shiny surface. The general idea of the technique is to detect in the frequency domain of the intensity at a given pixel multiple signals that correspond to multiple projector light rays, and to select the light ray which intersects with the camera light ray with the lowest triangulation error.

The key novelty is the extension of Huntley's FDR method [166] to detecting multiple peaks and application to selecting the correct triangulation light rays. The technique has been implemented in both MATLAB and C++ and is available for industrial applications as an add-on feature of the SMS software. Good performance of the FDR technique has been demonstrated by a proof-of-principle experiment on a specimen that contains a diffuse flat plate placed next to a mirror in a 'V' formation. Its accuracy was shown to be better than that of the reverse exponential phase unwrapping technique (which is used routinely on the Phase Vision scanners) by 5 times. The parametric study has revealed that its precision and robustness can be further improved by increasing the density of the projected fringes at the cost of longer acquisition time and larger data storage. The FDR technique has also applied to a partial-shiny automotive engine block and a fully-shiny aircraft wing rib. Good results have been reported for the former specimen, whereas relatively high errors still persist for the latter specimen.

8.2 Further work

For better accuracy and application range of the combined SMS-DIC technique, several improvements can be suggested for future research and implementation work:

- A higher-order deformation model of correlation window should be introduced to the correlation algorithm presented in Section 4.3.2. This is to compensate for large and complicated structural and perspective deformations.
- In the current software implementation, the core module of image correlation is done in a sequential procedure. For better computational performance, future implementations should make use of the independency of one image pixel on another and re-structure the procedure so that pixels are analysed in parallel. Also, the iterative nature of the correlation peak optimisation suggests that the code should be implemented in C/C++ rather than MATLAB.
- High-contrast speckle pattern applied to the object surface is essential for image correlation. However, low fringe visibility was observed on dark speckles which induced additional uncertainty in the estimate phases. Further investigations should be done to quantify this effect.

Future developments of the Fourier domain ranging technique are needed to address the following issues:

- The current implementation uses the triangulation error as an objective function to select the optimum signal. In future work, it is suggested that additional measures such as the peak's strength and width are incorporated in the objective function to achieve a higher measurement precision.
- Future study on the specular and diffuse components of the measured surface is suggested to understand their effects to the acquired signal strengths and thus the measurement uncertainties.
- Parallel computation may be implemented to improve computation speed, as each pixel is processed independently of another.
- To reduce the negative effect of peak cross-talk in which the detected frequencies are too close to each other for one of the fringe orientations, the fringes can be re-orientated (e.g. in $\pm 45^\circ$ orientation) so that the resulting frequencies are separable. Instead of rotating the scanner with respect to the object, the generated fringes can be rotated on the projector SLM and projected onto the object. Thus, two more sets of fringes can be obtained easily in addition to the vertical and horizontal sets.
- The FDR technique can be used in combination with a technique to dynamically adjust the fringe modulation to ensure that received intensities at all image pixels are maintained within the dynamic range of the camera sensor. By doing this, the over-saturating effect of specular components can be reduced significantly. Such a technique has been developed and patented by Phase Vision Ltd, but has not yet been combined with the FDR.

References

1. Huntley, J. M. (2000) Optical shape measurement technology: past, present, and future. *Proc. SPIE* **4076**, 162–173.
2. Chen, F., Brown, G. M. and Song, M. (2000) Overview of three-dimensional shape measurement using optical methods. *Opt. Eng.* **39**, No.1, 10–22.
3. Huntley, J. M., Ogundana, T., Burguete, R. L. and Coggrave, C. R. (2007) Large-scale full-field metrology using projected fringes: some challenges and solutions. *Proc. SPIE* **6616**, 66162C–10.
4. Osten, W. (2000) Application of optical shape measurement for the nondestructive evaluation of complex objects. *Opt. Eng.* **39**, No.1, 232–243.
5. Fechteler, P., Eisert, P. and Rurainsky, J. (2007) Fast and high resolution 3D face scanning. *The 14th International Conference on Image Processing*, San Antonio, Texas, USA, III – 81 – III – 84.
6. Shoup, T. E. (1976) Optical measurement of the center of rotation for human joints. *Journal of Biomechanics* **9**, No.4, 241–242.
7. Saumarez, R. C. (1986) Automated optical measurements of human torso surface movements during breathing. *J Appl Physiol* **60**, No.2, 702–709.
8. Huan-Xiang, S. and Ping, Z. (2010) Measuring mould boundary by optical scanners and three coordinate measuring machine. *2010 International Conference on Computer, Mechatronics, Control and Electronic Engineering (CMCE)*, Shanghai, China, 508–511.
9. Peiponen, K.-E., Myllylä, R. and Priezhev, A. V. (2009) *Optical measurement techniques: innovations for industry and the life sciences*, Springer.
10. Bosch, J. A. (1995) *Coordinate measuring machines and systems*, M. Dekker.
11. Athappan, N. (1991) *Coordinate measuring machine: a survey of current issues and suggestions*, University of Texas at El Paso.

12. Nakamura, O., Goto, M., Toyoda, K., Tanimura, Y., Kurosawa, T. and Uehara, K. (1991) Development of a coordinate measuring system with tracking laser interferometers. *CIRP Annals - Manufacturing Technology* **40**, No.1, 523–526.
13. Blais, F. (2004) Review of 20 years of range sensor development. *J. Electron. Imaging* **13**, No.1, 231.
14. GOM (2010) ATOS - High resolution, optical 3D scanner. Available at: <http://www.gom.com/metrology-systems/system-overview/atos.html> (Accessed 17 February, 2011).
15. GOM (2010) TRITOP - Optical 3D coordinate measuring machine. Available at: <http://www.gom.com/metrology-systems/system-overview/tritop.html> (Accessed 17 February, 2011).
16. Correlated Solutions (2010) Vic-3D. Available at: <http://www.correlatedsolutions.com/index.php/products/vic-3d-2010/vic3d> (Accessed 17 February, 2011).
17. Coggrave, C. R. (2001) *Temporal phase unwrapping: development and application of real-time systems for surface profile and surface displacement measurement*, PhD thesis, Loughborough University, UK.
18. Ogundana, O. (2007) *Automated calibration of multi-sensor optical shape measurement system*, PhD thesis, Loughborough University, UK.
19. Coggrave, C. R. and Huntley, J. M. (1999) High-speed surface profilometer based on a spatial light modulator and pipeline image processor. *Opt. Eng.* **38**, No.9, 1573–1581.
20. Coggrave, C. R. and Huntley, J. M. (2000) Optimization of a shape measurement system based on spatial light modulators. *Opt. Eng.* **39**, No.1, 91–98.
21. Saldner, H. O. and Huntley, J. M. (1997) Temporal phase unwrapping: application to surface profiling of discontinuous objects. *Appl. Opt.* **36**, No.13, 2770–2775.
22. Nguyen, T. N., Huntley, J. M., Burguete, R. and Coggrave, C. R. (2009) Combining digital image correlation and projected fringe techniques on a multi-camera multi-projector platform. *J. Phys.: Conf. Ser.* **181**, No.1, 012076.

23. Nguyen, T. N., Huntley, J. M., Burguete, R. and Coggrave, C. R. (2009) Combining digital image correlation and projected fringe techniques on a multi-camera multi-projector platform. *4th International Conference on Optical Measurement Techniques for Structures and Systems (OPTIMESS)*, Antwerp, Belgium.
24. Nguyen, T. N., Huntley, J. M., Burguete, R. L. and Russell Coggrave, C. (2011) Shape and displacement measurement of discontinuous surfaces by combining fringe projection and digital image correlation. *Opt. Eng.* **50**, 101505.
25. Nguyen, T. N., Huntley, J. M., Burguete, R. L. and Coggrave, C. R. (2012) Multiple-view shape and deformation measurement by combining fringe projection and digital image correlation. *Strain* **48**, No.3, 256–266.
26. Haralick, R. M. and Shapiro, L. G. (1991) *Computer and Robot Vision, Vol. 1*, Addison-Wesley.
27. Groover, M. P. (1986) *Industrial robotics: technology, programming, and applications*, McGraw-Hill.
28. Matthies, L., Kelly, A., Litwin, T. and Tharp, G. (1995) Obstacle detection for unmanned ground vehicles: a progress report. *Proceedings of the IEEE Intelligent Vehicles '95 Symposium*, 475–486.
29. Buluswar, S. D. and Draper, B. A. (1998) Color machine vision for autonomous vehicles. *Int. J. Eng. Appl. Artif. Intell.* **1**, 245–256.
30. Hu, W., Tan, T., Wang, L. and Maybank, S. (2004) A survey on visual surveillance of object motion and behaviors. *IEEE Transactions on Systems, Man, and Cybernetics, Part C: Applications and Reviews* **34**, No.3, 334–352.
31. Remagnino, P. (2002) *Video-based surveillance systems: computer vision and distributed processing*, Springer.
32. Agin, G. J. (1980) Computer vision systems for industrial inspection and assembly. *Computer* **13**, No.5, 11–20.
33. Pun, T., Gerig, G. and Ratib, O. (1994) Image analysis and computer vision in medicine. *Comput Med Imaging Graph* **18**, No.2, 85–96.

34. Freeman, W. T., Tanaka, K., Ohta, J. and Kyuma, K. (1996) Computer vision for computer games. *Proceedings of the Second International Conference on Automatic Face and Gesture Recognition*, Killington, VT, USA, 100–105.
35. Freeman, W. T. et al. (1998) Computer vision for interactive computer graphics. *IEEE Computer Graphics and Applications* **18**, No.3, 42–53.
36. Zhang, R., Tsai, P.-S., Cryer, J. E. and Shah, M. (1999) Shape-from-shading: a survey. *IEEE Transactions on Pattern Analysis and Machine Intelligence* **21**, No.8, 690–706.
37. Kleffner, D. A. and Ramachandran, V. S. (1992) On the perception of shape from shading. *Perception & Psychophysics* **52**, 18–36.
38. Nayar, S. K. (1992) Shape from focus system. *IEEE Computer Society Conference on Computer Vision and Pattern Recognition*, 302–308.
39. Hartley, R. I. and Sturm, P. (1997) Triangulation. *Computer Vision & Image Understanding* **68**, No.2, 146–157.
40. Hartley, R. and Zisserman, A. (2004) *Multiple view geometry in computer vision*, 2nd edn, Cambridge University Press, Cambridge.
41. Chu, T. C., Ranson, W. F. and Sutton, M. A. (1985) Applications of digital-image-correlation techniques to experimental mechanics. *Experimental Mechanics* **25**, 232–244.
42. Tsai, R. (1987) A versatile camera calibration technique for high-accuracy 3D machine vision metrology using off-the-shelf TV cameras and lenses. *IEEE Journal of Robotics and Automation* **3**, No.4, 323–344.
43. Heikkilä, J. (1997) *Accurate camera calibration and feature based 3-D reconstruction*, University of Oulu, Finland.
44. Zhang, Z. (2000) A flexible new technique for camera calibration. *IEEE Transactions on Pattern Analysis and Machine Intelligence* **22**, No.11, 1330–1334.
45. Faugeras, O. D., Luong, Q.-T. and Maybank, S. J. (1992) Camera self-calibration: theory and experiments. In: *Computer Vision - ECCV'92, Lecture Notes in Computer Science*. Springer: 321–334.

46. Scharstein, D. and Szeliski, R. (2002) A taxonomy and evaluation of dense two-frame stereo correspondence algorithms. *International Journal of Computer Vision* **47**, No.1-3, 7–42.
47. Kanade, T. and Okutomi, M. (1994) A stereo matching algorithm with an adaptive window: theory and experiment. *IEEE Transactions on Pattern Analysis and Machine Intelligence* **16**, No.9, 920–932.
48. Devernay, F. and Faugeras, O. D. (1994) Computing differential properties of 3-D shapes from stereoscopic images without 3-D models. *Proceedings of the IEEE International Conference on Computer Vision and Pattern Recognition* **21**, No.2304, 208–213.
49. Veksler, O. (2005) Stereo correspondence by dynamic programming on a tree. *IEEE Computer Society Conference on Computer Vision and Pattern Recognition* **2**, 384–390.
50. Pollefeys, M. (2002) *Visual 3D modeling from images*, University of North Carolina, Chapel Hill, USA.
51. Triggs, B., McLauchlan, P. F., Hartley, R. I. and Fitzgibbon, A. W. (1999) Bundle adjustment - a modern synthesis. *International Workshop on Vision Algorithms: Theory and Practice*, London, UK.
52. PhotoModeler - accurate and affordable 3D photogrammetry measurement and scanning. Available at: <http://www.photomodeler.com> (Accessed 27 February, 2012).
53. Bouguet, J.-Y. and Perona, P. (1998) 3D photography on your desk. *Sixth International Conference on Computer Vision*, Bombay, India, 43–50.
54. Phase Vision, Shape measurement system. Available at: <http://www.phasevision.com> (Accessed 21 September, 2011).
55. Peters, W. H. and Ranson, W. F. (1982) Digital image techniques in experimental stress analysis. *Opt. Eng.* **21**, 427–431.
56. Bruck, H., McNeill, S., Sutton, M. and Peters, W. (1989) Digital image correlation using Newton-Raphson method of partial differential correction. *Experimental Mechanics* **29**, No.3, 261–267.

-
57. Vendroux, G. and Knauss, W. G. (1998) Submicron deformation field measurements: Part 2. Improved digital image correlation. *Experimental Mechanics* **38**, No.2, 86–92.
 58. Hung, P.-C. and Voloshin, A. S. (2003) In-plane strain measurement by digital image correlation. *J. of the Braz. Soc. of Mech. Sci. & Eng.* **XXV**, No.3, 215–221.
 59. Yoneyama, S., Kikuta, H., Kitagawa, A. and Kitamura, K. (2006) Lens distortion correction for digital image correlation by measuring rigid body displacement. *Opt. Eng.* **45**, No.2, 023602.
 60. Scrivens, W. A., Luo, Y., Sutton, M. A., Collette, S. A., Myrick, M. L., Miney, P., Colavita, P. E., Reynolds, A. P. and Li, X. (2006) Development of patterns for digital image correlation measurements at reduced length scales. *Experimental Mechanics* **47**, No.1, 63–77.
 61. Sutton, M., McNeill, S., Helm, J. and Chao, Y. (2000) Advances in two-dimensional and three-dimensional computer vision. In: *Photomechanics*, Topics in Applied Physics (P. K. Rastogi, Ed.). Springer, Berlin: 323–372.
 62. Sutton, M. A., Orteu, J.-J. and Schreier, H. (2009) *Image correlation for shape, motion and deformation measurements: basic concepts, theory and applications*, Springer, New York.
 63. Press, W. H., Teukolsky, S. A., Vetterling, W. T. and Flannery, B. P. (2002) *Numerical Recipes in C++: The Art of Scientific Computing*, 2nd edn, Cambridge University Press.
 64. Schreier, H. W., Garcia, D. and Sutton, M. A. (2004) Advances in light microscope stereo vision. *Experimental Mechanics* **44**, No.3, 278–288.
 65. Helm, J. D., McNeill, S. R. and Sutton, M. A. (1996) Improved three-dimensional image correlation for surface displacement measurement. *Opt. Eng.* **35**, No.7, 1911–1920.
 66. Garcia, D., Orteu, J. . and Penazzi, L. (2002) A combined temporal tracking and stereo-correlation technique for accurate measurement of 3D displacements: application to sheet metal forming. *Journal of Materials Processing Technology* **125-126**, 736–742.

-
67. Luo, P., Chao, Y., Sutton, M. and Peters, W. (1993) Accurate measurement of three-dimensional deformations in deformable and rigid bodies using computer vision. *Experimental Mechanics* **33**, No.2, 123–132.
 68. Luo, P.-F., Chao, Y. J. and Sutton, M. A. (1994) Application of stereo vision to three-dimensional deformation analyses in fracture experiments. *Opt. Eng.* **33**, No.3, 981–990.
 69. Kahn-Jetter, Z. and Chu, T. (1990) Three-dimensional displacement measurements using digital image correlation and photogrammic analysis. *Experimental Mechanics* **30**, No.1, 10–16.
 70. Tournas, L., Tsakiri, M. and Kattis, M. (2006) Displacement monitoring at the micron level using digital photogrammetry. *3rd IAG / 12th FIG Symposium*, Baden, Austria.
 71. Peters, W. H., Sutton, M. A., Ranson, W. F., Poplin, W. P. and Walker, D. M. (1989) Whole-field experimental displacement analysis of composite cylinders. *Experimental Mechanics* **29**, No.1, 58–62.
 72. Meng, L. B., Jin, G. C., Yao, X. F. and Yeh, H. Y. (2006) 3D full-field deformation monitoring of fiber composite pressure vessel using 3D digital speckle correlation method. *Polymer Testing* **25**, No.1, 42–48.
 73. GOM, ARAMIS Software. Available at: <http://www.gom.com/3d-software/aramis-software.html> (Accessed 27 February, 2012).
 74. Dantec, Digital Image Correlation System (Q-400). Available at: <http://www.dantecdynamics.com> (Accessed 27 February, 2012).
 75. Synnergren, P. and Sjodahl, M. (1999) A stereoscopic digital speckle photography system for 3-D displacement field measurements. *Optics and Lasers in Engineering* **31**, No.6, 425–443.
 76. Becker, T., Splitthof, K., Siebert, T. and Kletting, P. (2006) Error estimations of 3D digital image correlation measurements. *Proceedings of SPIE* **6341**, No.1, 63410F–6.
 77. Matumoto, S., Miwata, Y. and Kuwabata, T. (1995) Development of three-dimensional displacement measurement method using CCD cameras. *JSAE Review* **16**, No.1, 105.

-
78. Rastogi, P. K. (2001) *Digital speckle pattern interferometry and related techniques*, Wiley.
 79. Saldner, H. O. (1997) Profilometry using temporal phase unwrapping and a spatial light modulator-based fringe projector. *Opt. Eng.* **36**, 610.
 80. Huntley, J. M. (1998) Automated fringe pattern analysis in experimental mechanics: a review. *The Journal of Strain Analysis for Engineering Design* **33**, No.2, 105 –125.
 81. Schreiber, W. and Notni, G. (2000) Theory and arrangements of self-calibrating whole-body three-dimensional measurement systems using fringe projection technique. *Opt. Eng.* **39**, No.1, 159–169.
 82. Fitzgibbon, A., Pilu, M. and Fisher, R. B. (1999) Direct least square fitting of ellipses. *IEEE Transactions on Pattern Analysis and Machine Intelligence* **21**, No.5, 476 –480.
 83. Abdel-Aziz, Y. I. and Karara, H. M. (1971) Direct linear transformation from comparator coordinates into object space coordinates in close-range photogrammetry. *Proceedings of the Symposium on Close Range Photogrammetry* **1**, 1–18.
 84. Chen, L., Armstrong, C. W. and Raftopoulos, D. D. (1994) An investigation on the accuracy of three-dimensional space reconstruction using the direct linear transformation technique. *Journal of Biomechanics* **27**, No.4, 493–500.
 85. Ogundana, O. O., Coggrave, C. R., Burguete, R. L. and Huntley, J. M. (2007) Fast Hough transform for automated detection of spheres in three-dimensional point clouds. *Opt. Eng.* **46**, No.5, 051002–11.
 86. Huntley, J. M. (2006) *Bundle adjustment method based on object-side ray tracing*, Phase Vision Ltd, Loughborough, UK.
 87. Huntley, J. M. and Coggrave, C. R. (2007) *Development of automated calibration sequence based on an analytical model for the best set of rotation angles*, Phase Vision Ltd, Loughborough, UK.
 88. Weber, H., Lichtenberger, R. and Wolf, T. (2000) The combination of speckle correlation and fringe projection for the measurement of dynamic 3-D

- deformations of airbag caps. In: *IUTAM Symposium on Advanced Optical Methods and Applications in Solid Mechanics*. Springer: 619–626.
89. Tay, C. J., Quan, C., Wu, T. and Huang, Y. H. (2004) Integrated method for 3-D rigid-body displacement measurement using fringe projection. *Opt. Eng.* **43**, No.5, 1152–1159.
90. Quan, C., Tay, C. J. and Huang, Y. H. (2004) 3-D deformation measurement using fringe projection and digital image correlation. *Optik* **115**, No.4, 164–168.
91. Klein, J., Lointier, P., Chalvidan, V. and Hild, F. (2004) Mesure de forme et de champ de déplacement par association de la projection de franges et de la corrélation d'images. *5ème Colloque Méthodes et Techniques Optiques pour l'Industrie*, Saint-Etienne, France.
92. Jin, H. and Bruck, H. A. (2005) Theoretical development for pointwise digital image correlation. *Opt. Eng.* **44**, No.6, 067003–14.
93. Réthoré, J., Hild, F. and Roux, S. (2008) Extended digital image correlation with crack shape optimization. *Int. J. Numer. Meth. Eng.* **73**, No.2, 248–272.
94. Sjö Dahl, M. (2010) Image and complex correlation near discontinuities. *Strain* **46**, No.1, 3–11.
95. Poissant, J. and Barthelat, F. (2009) A novel subset splitting procedure for digital image correlation on discontinuous displacement fields. *Exp. Mech.* **50**, No.3, 353–364.
96. Huntley, J. M. and Saldner, H. O. (1997) Error-reduction methods for shape measurement by temporal phase unwrapping. *J. Opt. Soc. Am. A* **14**, No.12, 3188–3196.
97. Shapiro, L. G. and Stockman, G. C. (2001) *Computer vision*, Prentice Hall.
98. Dillencourt, M. B., Samet, H. and Tamminen, M. (1992) A general approach to connected-component labeling for arbitrary image representations. *J. ACM* **39**, No.2, 253–280.
99. Gonzalez, R. C. and Woods, R. E. (2008) *Digital Image Processing*, 3rd edn, Pearson Education.

100. Huntley, J. M. (1989) Speckle photography fringe analysis: assessment of current algorithms. *Appl. Opt.* **28**, No.20, 4316–4322.
101. Huntley, J. M. (1986) An image processing system for the analysis of speckle photographs. *J. Phys. E: Sci. Instrum.* **19**, No.1, 43–49.
102. Harold, E. R. and Means, W. S. (2004) *XML in a Nutshell*, third edn, O'Reilly Media.
103. JDOM. Available at: <http://www.jdom.org> (Accessed 9 March, 2012).
104. Innovmetric, PolyWorks: 3D scanner software. Available at: <http://www.innovmetric.com/polyworks> (Accessed 11 March, 2012).
105. Geomagic, Reverse engineering and 3D inspection software. Available at: <http://www.geomagic.com> (Accessed 11 March, 2012).
106. Tecplot 360. Available at: <http://www.tecplot.com> (Accessed 11 March, 2012).
107. MeshLab. Available at: <http://meshlab.sourceforge.net> (Accessed 11 March, 2012).
108. Innovmetric, PolyWorks Reference Guide Version 11.0. Available at: http://www.duwe-3d.de/mediathek/pdf/pdf-en/pif-format-en.pdf/at_download/file (Accessed 12 March, 2012).
109. Tecplot (2011) Data Format Guide. Available at: <http://download.tecplot.com/360/2011/dataformat.pdf> (Accessed 12 March, 2012).
110. Di Angelo, L., Di Stefano, P. and Giaccari, L. (2011) A new mesh-growing algorithm for fast surface reconstruction. *Computer-Aided Design* **43**, No.6, 639–650.
111. Lecompte, D., Smits, A., Bossuyt, S., Sol, H., Vantomme, J., Van Hemelrijck, D. and Habraken, A. M. (2006) Quality assessment of speckle patterns for digital image correlation. *Opt. Laser Eng.* **44**, No.11, 1132–1145.
112. Lane, C., Burguete, R. L. and Shterenlikht, A. (2008) An objective criterion for the selection of an optimum DIC pattern and subset size. *SEM XI International Congress & Exposition on Experimental & Applied Mechanics*, Orlando, Florida USA.

-
113. Schmidt, T., Tyson, J. and Galanulis, K. (2003) Full-field dynamic displacement and strain measurement using advanced 3D image correlation photogrammetry: part I. *Exp. Tech.* **27**, No.3, 47–50.
 114. Cheng, X.-X., Su, X.-Y. and Guo, L.-R. (1991) Automated measurement method for 360° profilometry of 3-D diffuse objects. *Appl. Opt.* **30**, No.10, 1274–1278.
 115. Guo, H. and Chen, M. (2003) Multiview connection technique for 360-deg three-dimensional measurement. *Opt. Eng.* **42**, No.4, 900–905.
 116. Sansoni, G. and Docchio, F. (2004) Three-dimensional optical measurements and reverse engineering for automotive applications. *Robot* **20**, No.5, 359–367.
 117. Reich, C., Ritter, R. and Thesing, J. (2000) 3-D shape measurement of complex objects by combining photogrammetry and fringe projection. *Opt. Eng.* **39**, No.1, 224–231.
 118. Degenhardt, R., Kling, A., Bethge, A., Orf, J., Kärger, L., Zimmermann, R., Rohwer, K. and Calvi, A. (2010) Investigations on imperfection sensitivity and deduction of improved knock-down factors for unstiffened CFRP cylindrical shells. *Compos. Struct.* **92**, No.8, 1939–1946.
 119. Hühne, C., Rolfes, R., Breitbach, E. and Teßmer, J. (2008) Robust design of composite cylindrical shells under axial compression - simulation and validation. *Thin Walled Struct.* **46**, No.7-9, 947–962.
 120. Harvent, J., Bugarin, F., Orteu, J.-J., Devy, M., Barbeau, P. and Marin, G. (2008) Inspection de pièces aéronautiques pour la détection de défauts de forme à partir d'un système multi-caméras. *Journées COFREND 2008*, Toulouse-Labège, France.
 121. Ogale, A. S. and Aloimonos, Y. (2005) Shape and the stereo correspondence problem. *Int. J. Comput. Vision* **65**, No.3, 147–162.
 122. Barber, C. B., Dobkin, D. P. and Huhdanpaa, H. (1996) The quickhull algorithm for convex hulls. *ACM Trans. Math. Softw.* **22**, 469–483.
 123. Adrian, R. J. (1991) Particle-imaging techniques for experimental fluid mechanics. *Annual Review of Fluid Mechanics* **23**, No.1, 261–304.

-
124. Adrian, R. J. (2005) Twenty years of particle image velocimetry. *Experiments in Fluids* **39**, No.2, 159–169.
 125. V-STARS, *Demonstration of V-STARS for Northrop Grumman - Stuart, FL*
Available at: www.geodetic.com/f.ashx/reports/aerospace/Flap_Jig_Measurement.pdf (Accessed 30 May, 2012).
 126. Acar, E., Haftka, R. T., Kim, N. and Buchi, D. (2010) Effects of structural tests on aircraft safety. *AIAA Journal* **48**, No.10, 2235–2248.
 127. Airbus, Test programme and certification. Available at:
<http://www.airbus.com/company/aircraft-manufacture/how-is-an-aircraft-built/test-programme-and-certification/> (Accessed 30 May, 2012).
 128. Sharpe, Jr. and William, N. (2008) *Springer Handbook of Experimental Solid Mechanics*, Springer.
 129. Eaton-Evans, J., Dulieu-Barton, J. M. and Burguete, R. L. (2009) *Modern Stress and Strain Analysis: A State of the Art Guide to Measurement Techniques*, Eureka magazine.
 130. Du, Y., Díaz, F. A., Burguete, R. L. and Patterson, E. A. (2010) Evaluation using digital image correlation of stress intensity factors in an aerospace panel. *Experimental Mechanics* **51**, 45–57.
 131. Featherston, C. A., Mortimer, J., Eaton, M. J., Burguete, R. L. and Johns, R. (2010) The dynamic buckling of stiffened panels – a study using high speed digital image correlation. *Applied Mechanics and Materials* **24-25**, 331–336.
 132. Patterson, E. A., Hack, E., Brailly, P., Burguete, R. L., Saleem, Q., Siebert, T., Tomlinson, R. A. and Whelan, M. P. (2007) Calibration and evaluation of optical systems for full-field strain measurement. *Optics and Lasers in Engineering* **45**, No.5, 550–564.
 133. Sjö Dahl, M. and Oreb, B. F. (2002) Stitching interferometric measurement data for inspection of large optical components. *Opt. Eng.* **41**, No.2, 403–408.
 134. Geers, M. G. D., De Borst, R. and Brekelmans, W. A. M. (1996) Computing strain fields from discrete displacement fields in 2D-solids. *International Journal of Solids and Structures* **33**, No.29, 4293–4307.

-
135. Hild, F., Raka, B., Baudequin, M., Roux, S. and Cantelaube, F. (2002) Multiscale displacement field measurements of compressed mineral-wool samples by digital image correlation. *Applied Optics* **41**, No.32, 6815–6828.
 136. Teza, G., Pesci, A. and Galgaro, A. (2008) Grid_strain and grid_strain3: Software packages for strain field computation in 2D and 3D environments. *Computers & Geosciences* **34**, No.9, 1142–1153.
 137. Airbus, A350 XWB - Shaping efficiency. Available at:
<http://www.airbus.com/aircraftfamilies/passengeraircraft/a350xwbfamily>
(Accessed 7 June, 2012).
 138. Beckmann, P. and Spizzichino, A. (1987) *The Scattering of Electromagnetic Waves from Rough Surfaces*, Artech Print on Demand.
 139. Hering, R. G. and Houchens, A. F. (1967) Bidirectional reflectance of rough metal surfaces. *AIAA Journal* **67**, 319.
 140. Healey, G. and Binford, T. O. (1988) Local shape from specularity. *Computer Vision, Graphics, and Image Processing* **42**, No.1, 62–86.
 141. Torrance, K. E. and Sparrow, E. M. (1967) Theory for off-specular reflection from roughened surfaces. *Journal of the Optical Society of America* **57**, No.9, 1105–1114.
 142. Ryu, Y. K. and Cho, H. S. (1996) New optical sensing system for obtaining the three-dimensional shape of specular objects. *Opt. Eng.* **35**, No.5, 1483–1495.
 143. Nayar, S. K., Ikeuchi, K. and Kanade, T. (1991) Surface reflection: physical and geometrical perspectives. *IEEE Transactions on Pattern Analysis and Machine Intelligence* **13**, No.7, 611–634.
 144. Tominaga, S. (1991) Surface identification using the dichromatic reflection model. *IEEE Transactions on Pattern Analysis and Machine Intelligence* **13**, No.7, 658–670.
 145. Zhang, R., Tsai, P.-S., Cryer, J. E. and Shah, M. (1999) Shape from shading: a survey. *IEEE Trans. Pattern Anal. Mach. Intell.* **21**, No.8, 690–706.
 146. Horn, B. K. P. (1989) Shape from shading. In: *Shape from Shading (Artificial Intelligence)* (B. K. P. Horn, Ed.). MIT Press, Cambridge, MA, USA: 123–171.

-
147. Woodham, R. J. (1980) Photometric method for determining surface orientation from multiple images. *Opt. Eng.* **19**, No.1, 139–144.
 148. Ikeuchi, K. (1981) Determining surface orientations of specular surfaces by using the photometric stereo method. *IEEE Transactions on Pattern Analysis and Machine Intelligence* **PAMI-3**, No.6, 661 –669.
 149. Baba, M., Narita, D. and Ohtani, K. (2002) 360° shape measurement system for objects having from Lambertian to specular reflectance properties utilizing a novel rangefinder. *Journal of Optics A: Pure and Applied Optics* **4**, No.6, S295–S303.
 150. Kammel, S. and León, F. P. (2008) Deflectometric measurement of specular surfaces. *IEEE Transactions on Instrumentation and Measurement* **57**, No.4, 763–769.
 151. Baba, M., Ohtani, K., Imai, M. and Konishi, T. (2001) New laser rangefinder for three-dimensional shape measurement of specular objects. *Opt. Eng.* **40**, No.1, 53–60.
 152. Perard, D. and Beyerer, J. (1997) Three-dimensional measurement of specular free-form surfaces with a structured-lighting reflection technique. *Society of Photo-Optical Instrumentation Engineers (SPIE) Conference Series*, 74–80.
 153. Hung, Y. Y., Chen, F. and Tang, S. H. (1993) Reflective computer vision technique for measuring surface slope and plate deformation. *SEM Proc.* 948–953.
 154. Höfling, R., Aswendt, P. and Neugebauer, R. (2000) Phase reflection – a new solution for the detection of shape defects on car body sheets. *Opt. Eng.* **39**, No.1, 175–182.
 155. Werling, S., Mai, M., Heizmann, M. and Beyerer, J. (2009) Inspection of specular and partially specular surfaces. *Metrol. Meas. Syst.* **XVI**, No.3, 415–431.
 156. Skydan, O. A., Lalor, M. J. and Burton, D. R. (2007) 3D shape measurement of automotive glass by using a fringe reflection technique. *Measurement Science and Technology* **18**, No.1, 106–114.

-
157. Knauer, M. C. (2004) Phase measuring deflectometry: a new approach to measure specular free-form surfaces. *Optical Metrology in Production Engineering*, 366–376.
 158. Ihrke, I., Kutulakos, K. N., Lensch, H. P. A., Magnor, M. and Heidrich, W. (2010) Transparent and specular object reconstruction. *Computer Graphics Forum* **29**, No.8, 2400–2426.
 159. Curless, B. and Levoy, M. (1995) Better optical triangulation through spacetime analysis. *Proc. ICCV '95*, Los Alamitos, CA, USA, 987.
 160. Nygard, J. and Wernersson, A. (1994) Specular objects in range cameras: reducing ambiguities by motion. *Proceedings of the 1994 IEEE International Conference on Multisensor Fusion and Integration for Intelligent Systems*, Las Vega, NV, USA, 320–328.
 161. Chung, R., Lam, E. Y. and Fung, K. S. M. (2008) Handling of multi-reflections in wafer bump 3D reconstruction. *IEEE International Conference on Systems Man and Cybernetics*, 1558–1561.
 162. Takeda, M., Ina, H. and Kobayashi, S. (1982) Fourier-transform method of fringe-pattern analysis for computer-based topography and interferometry. *J. Opt. Soc. Am.* **72**, No.1, 156–160.
 163. Su, X. and Chen, W. (2001) Fourier transform profilometry:: a review. *Optics and Lasers in Engineering* **35**, No.5, 263–284.
 164. Macy, W. W. (1983) Two-dimensional fringe-pattern analysis. *Applied Optics* **22**, No.23, 3898–3901.
 165. Nguyen, T. N., Coggrave, C. R. and Huntley, J. M. (2009) *Novel techniques to reduce errors due to multiple scattering and spatial intensity gradient effects*, Phase Vision Ltd, Loughborough, UK.
 166. Huntley, J. M. (2009) *Modifications to the Fourier transform ranging technique*, Phase Vision Ltd, Loughborough, UK.
 167. Wikipedia contributors (2012) Window function. *Wikipedia, the free encyclopedia*. (Accessed 22 June, 2012).